THE UNIVERSITY OF MICHIGAN
ANN ARBOR, MICHIGAN

FREQUENCY CONVERSION AND NOISE IN MILLIMETER-WAVE TRANSIT-TIME DEVICES

by

R. O. Grondin

Technical Report No. 157

Electron Physics Laboratory
Department of Electrical and Computer Engineering

April 1983

ABSTRACT

A theoretical study of frequency conversion and noise in millimeter-wave transit-time devices is made. In particular the performance of BARITT devices as mixers and detectors in the 30- to 100-GHz range is studied. Additionally, some potential limitations in the basic model of a transit-time device are also investigated.

The performance of BARITT mixers is based on a matrix formulation of frequency conversion and noise in a transit-time device. This matrix formulation is developed by extending conventional Schottky-barrier mixer models. Additionally, various burnout mechanisms and video detection are also considered. The BARITT is found to be a much more durable and burnout resistant device than the Schottky-barrier diode. The results obtained here indicate that it will probably be competitive with Schottky-barrier diodes in low-noise video detection and mixing applications. However, the BARITT device may be very useful in applications where high burnout capability and reasonable sensitivity are needed.

As the BARITT is a transit-time device the possibility of negative-resistance effects must be considered. Short highly doped BARITTs are found to be potentially useful as self-oscillating mixers at frequencies in the 30- to 40-GHz range. Such devices could also be used in an active mode of video detection where the device simultaneously functions as a video detector and reflection amplifier in this range as well. Longer lightly doped devices can have negative resistances in the IF band and as a result can exhibit conversion gain although stability cannot be guaranteed.

A Monte Carlo model of electron transport in GaAs is used to study the validity of the drift-diffusion approximation and the assumption of white velocity fluctuation noise spectra. Both are found to become invalid at sufficiently high frequencies. The characteristics present when the drift-diffusion approximation becomes questionable are shown to represent both performance limitations for some modes of transit-time devices and sources for new potentially advantageous device designs as well.

TABLE OF CONTENTS

	Page
CHAPTER I. INTRODUCTION	1
1.1 Historical Background	1
1.2 Fundamental Principles of Transit-Time Devices	5
1.2.1 IMPATT Diode	9
1.2.2 TUNNETT Diode	17
1.2.3 BARITT Diode	18
1.2.4 Schottky and Mott Barriers	22
1.3 State of the Art for Transit-Time Device Oscillators	28
1.4 State of the Art for 30- to 110-GHz Mixers	31
1.5 Outline of Present Study	37
CHAPTER II. FREQUENCY CONVERSION IN TWO-TERIMINAL JUNCTION DEVICES	39
2.1 Introduction	39
2.2 Frequency Conversion in Two-Terminal Junction Devices	41
2.2.1 General Frequency Converter	41
2.2.2 Injection Region	45
2.2.3 Drift Region	48
2.3 Complete Frequency Converter	53
2.3.1 Augmented Network	53
2.3.2 Calculating Port Impedances	54
2.3.3 Calculating Conversion Loss	56
2.4 Upper-Sideband Downconverter	58
2.4.1 Reduction to a Two-Port	58
2.4.2 Optimum Three-Frequency Mixer	63
2.4.3 Stability of the Upper-Sideband Downconverter	66

Page

2.5 Summary 68

CHAPTER III. NOISE CORRELATION IN TWO-TERMINAL JUNCTION DEVICES 69

3.1 Introduction 69

3.1.1 Introduction 69
3.1.2 Mathematical Introduction 70
3.1.3 Origin of the Noise Correlation 71

3.2 Poisson Point Process Model of Injection Region Noise 72

3.2.1 Poisson Point Process 72
3.2.2 Connection with Deterministic Injection Region Models 74

3.3 Correlation Matrix 75

3.3.1 Injection Region Correlation Matrix 75
3.3.2 Drift Region and Noise Correlation Matrix 75
3.3.3 Velocity Fluctuation and Thermal Noise 81

3.4 Applications of Correlation Matrices 86

3.4.1 Applications in Mixers 86
3.4.2 Applications to Oscillators and Amplifiers 89

3.5 Summary 90

CHAPTER IV. VIDEO DETECTOR STUDIES 91

4.1 Introduction 91

4.1.1 The Basic Semiconductor Equations 91
4.1.2 Modeling Methods 93
4.1.3 Device Design and Specification 98

4.2 Intrinsic Diode Properties 98

4.2.1 Introduction 98
4.2.2 Dc Studies 98
4.2.3 Small-Signal Impedance Studies 107

4.3 Video Detectors 119

4.3.1 Introduction 119
4.3.2 Analysis 122
4.3.3 Results 126

Page

4.4 Discussion and Summary 137

4.4.1 Discussion 137
4.4.2 Summary 139

CHAPTER V. MIXER STUDIES 141

5.1 Introduction 141
5.2 Schottky-Barrier Mixer Diodes 143
5.3 BARITT Mixers 153

5.3.1 Introduction 153
5.3.2 The Optimal Conversion Loss Survey 153
5.3.3 Self-Oscillating BARITT Mixers 164
5.3.4 Noise Minimization Studies 173

5.4 Summary 192

CHAPTER VI. MONTE CARLO STUDIES OF NOISE AND TRANSPORT IN GaAs 194

6.1 Introduction 194
6.2 The Monte Carlo Model and Method 194

6.2.1 The Monte Carlo Method 194
6.2.2 The Physical Model 200

6.3 Dynamic Transport Transients and Consequences for GaAs Transit-Time Device Properties 201

6.3.1 Introduction 201
6.3.2 Transient Carrier Dynamics 202
6.3.3 Efficiency Enhancement and Degradation Through Transient Carrier Transport 215
6.3.4 Premature Collection at Millimeter-Wave Frequencies 218
6.3.5 Carrier Inertial Effects in Undepleted Regions 224

6.4 The Theory and Practice of Monte Carlo Noise Experiments 227

6.4.1 Introduction 227
6.4.2 Physical and Mathematical Background 228
6.4.3 Statistical Procedures 231
6.4.4 An Example of a Time Series Analysis 241
6.4.5 General Discussion 253
6.4.6 Hot Carrier Noise in Mixer Diodes 255

6.5 Summary and Conclusions 256

	Page
CHAPTER VII. CONCLUSIONS AND SUGGESTIONS FOR FUTURE STUDY	258
7.1 Introduction	258
7.2 Conclusions	258
7.3 Suggestions for Future Studies	261
APPENDIX A. MATERIAL PARAMETERS	263
A.1 Silicon Parameters	263
A.2 Gallium Arsenide Parameters	264
APPENDIX B. DOCUMENTATION OF COMPUTER PROGRAM	266
APPENDIX C. NOISE FACTOR MINIMIZATION	273
LIST OF REFERENCES	280

LIST OF ILLUSTRATIONS

Figure		Page
1.1	Simple Waveforms for Transit-Time Device Modeling. (a) Terminal Voltage Waveform, (b) Injected Current Waveform and (c) Induced Current Contribution to the Terminal Current. (Elta and Haddad[10])	6
1.2	Separation of a Transit-Time Device into Injection and Drift Regions.	7
1.3	The Negative Conductance-RF Voltage Amplitude Characteristic of a GaAs IMPATT Driven into Premature Collection Mode Operation.	12
1.4	Physical Basis for Charge-Limited Domain or Surfing Mode Operation. (a) Effect of the Drifting Carrier Pulse Space-Charge on the Electric Field Profile and (b) Resulting Velocity Modulation.	13
1.5	BARITT Device Structure and Operation. (a) MSM BARITT Structure and (b) Electric Field Profile as a Function of Terminal Voltage.	19
1.6	Effect of Injection into a Low-Field Region on the Induced Current in a BARITT Device. (Nguyen-Ba and Haddad[65])	21
1.7	Device Structure for Schottky (N_d High) and Mott (N_d Low) Devices.	23
1.8	Electric Field Profiles in (a) Schottky and (b) Mott Devices as a Function of Terminal Voltage.	24
1.9	(a) Current-Voltage and (b) Capacitance-Voltage Characteristics of a Schottky Diode. (c) Capacitance-Voltage Characteristic of a Mott Device.	25
1.10	Equivalent Circuits of Various Semiconductor Diodes. (a) Schottky Diode, (b) Mott Barrier Diode and (c) BARITT Device.	27
1.11	State of the Art for Si Transit-Time Device Oscillators.	29
1.12	State of the Art for GaAs Transit-Time Device Oscillators.	30
2.1	General Frequency Converter.	42

Figure | Page

2.2 (a) Equivalent Circuit for the Injection Region of BARITT, TUNNETT, Tunnel, Schottky and Mott Diodes (Any Device with Negligible Avalanching) and (b) Equivalent Circuit for IMPATT and MITATT Device Injection Regions. 46

2.3 General Transit-Time Device Drift Region Equivalent Circuit. 50

2.4 A Complication in Transit-Time Device Frequency Converters. Frequency Conversion in the Injection Region Produces Additional Particle Current at any Frequency of Interest, for Example, the Sources $Y_{B_{10}} \delta V_o$ and $Y_{B_{1-1}} \delta V_{-1}$. This Modifies the Drift Region Response even Though the Drift Region Is Linear. 51

2.5 The Equivalent Circuit Describing the Transformation from the Injection Region to the Intrinsic Diode Terminals at the mth Sideband Frequency. 52

2.6 Formation of the Augmented Network. Here the Intrinsic Diode Conversion Admittance Matrix Is Represented as a Multiport. (Siegel and Kerr[117]) 55

2.7 Y Parameters for a Reduced Frequency Converter Network for a Known Image Termination. 67

3.1 Equivalent Circuit for the Transformation of the Injection Region Noise Current Source to the Intrinsic Diode Terminal Plane at the kth Sideband Frequency. 77

3.2 Injection Region Noise in the Mixer Prior to Its Transformation to the Intrinsic Diode Terminal Plane. 79

3.3 Injection Region Noise Current in the Mixer After Its Transformation to the Intrinsic Diode Terminal Plane. 80

3.4 Thermal and Velocity Fluctuation Noise Current Sources Combined into the Noise Current Source δI_N. The Problem Is now Ready for Solution Using the Correlation Matrices and the Augmented Network Conversion Impedance Matrix. 82

3.5 Thermal and Velocity Fluctuation Equivalent Noise Voltage Sources in the Mixer. 87

4.1 Sign Conventions. 94

Figure | Page

4.2 Optimum Device Length and VBDMAR as a Function of Doping for Si and GaAs BARITTs. 105

4.3 Thermal Time Constant as a Function of Length or Mesa Height for Mesa Structures. 106

4.4 Diameter for 50-Ω Match of Real Part of Impedance at 300 MHz for BARITTs 6 and 12 as a Function of Current Density. 110

4.5 Diode Conductance G and Susceptance B as a Function of Frequency for BARITT 1. (J_{dc} = 50 A/cm²) 116

4.6 Knee Frequency as a Function of Current Density for BARITTs 1 and 6. 120

4.7 Diode Conductance G and the Capacitance Ratio C_{eff}/C_{cold} as a Function of Dc Current Density for BARITTs 1 and 6. 121

4.8 BARITT Diode Video Detector Circuit. [$V_{gT} = V_g/(a + cR_g)$ and $Z_{gT} = (b + dR_g)/(a + cR_g)$] 123

4.9 Voltage Detection Sensitivity and Noise Equivalent Power Factor as a Function of Frequency for BARITT 6. (J_{dc} = 500 A/cm², Video Frequency = 30 MHz and Δf = 1) 127

4.10 Voltage Detection Sensitivity and Noise Equivalent Power Factor as a Function of Frequency for BARITT 12. (J_{dc} = 500 A/cm², Video Frequency = 30 MHz and Δf = 1) 128

4.11 Voltage Detection Sensitivity and Noise Equivalent Power Factor as a Function of Current Density for BARITTs 1, 6 and 12 at 35 GHz. (Video Frequency = 30 MHz and Δf = 1) 129

4.12 Voltage Detection Sensitivity and Noise Equivalent Power Factor as a Function of Dc Current Density for BARITTs 1, 6 and 12 at 94 GHz. (Video Frequency = 30 MHz and Δf = 1) 130

4.13 NEPF for BARITT 1 at 35 and 94 GHz as a Function of Dc Current Density. 131

4.14 NEP, Resistance and Reactance for BARITT 1 as Functions of Diode Diameter. (Dc Current Density Is 4 A/cm² and Frequency Is 35 GHz) 135

Figure		Page

4.15	NEP, Resistance and Reactance of BARITT 1 as Functions of Diode Diameter. (Dc Current Density Is 10 A/cm^2 and Frequency Is 94 GHz)	136
5.1	Basic Formulation of a Mixer Analysis.	142
5.2	Experimental Schottky-Barrier Mixer Conversion Loss as a Function of LO Power Level. (Weinreb and Kerr[100])	146
5.3	Theoretical Conversion Loss as a Function of Absorbed LO Power for the Schottky Diode of Fig. 5.2.	147
5.4	Injection Region Driving Voltage as a Function of Absorbed LO Power. The Parameter Is LO Frequency in GHz.	148
5.5	Mixer Noise Figure as a Function of Injection Region Drive (Normalized with Respect to the Thermal Voltage). The Circles Are the 94-GHz Schottky-Barrier Result While the Triangles Are the 35-GHz Schottky-Barrier Result. (J_{dc} = 10,000 A/cm^2 and the IF Is 300 MHz)	149
5.6	Mixer Noise Figure for Schottky-Barrier Mixer as a Function of Dc Current Density for a LO Drive of $4V_T$. The IF Is 300 MHz. The Circles Are the 94-GHz Result While the Triangles Are the 35-GHz Result.	150
5.7	Mixer Noise Figure for Schottky Barrier as a Function of Intermediate Frequency. The Dc Current Density was 10,000 A/cm^2 and the LO Drive Is $4V_T$. The Circles are the 94-GHz Results While the Triangles are the 35-GHz Results.	151
5.8	Conversion Loss for the Schottky Barrier as a Function of LO Drive. J_{dc} = 10,000 A/cm^2 and the IF Is 300 MHz. The Circles Are the 94-GHz Results While the Triangles Are the 35-GHz Results.	152
5.9	Mixer IF Output Impedance for the Schottky Barrier as a Function of Dc Current Density. The IF Is 300 MHz and the LO Drive Is $4V_T$. The Circles Are the 94-GHz Results While the Triangles Are the 35-GHz Results. —— Is Resistance and --- Is Reactance.	154
5.10	The Signal Frequency Embedding Circle Impedance as a Function of Dc Current Density. All Parameters and Descriptions Are Identical with Those of Fig. 5.9.	155

Figure | Page

5.11 The Signal Frequency Embedding Circuit Impedance as a Function of IF. The LO Drive Is $4V_T$ and the Dc Current Density Is 10,000 A/cm². The Circles Are the 94-GHz Data and the Triangles Are the 35-GHz Data. —— Is Resistance and --- Is Reactance. 156

5.12 LO Injection Region Drive as a Function of LO Absorbed Power for BARITTs 1, 6, and 12. The LO Frequency Is 35 GHz and J_{dc} = 500 A/cm². 158

5.13 LO Injection Region Drive as a Function of Absorbed LO Power for BARITTs 1, 6, and 12 at 94 GHz. 159

5.14 The Conversion Loss as a Function of IF for BARITT 6. The LO Drive Is $4V_T$ and J_{dc} = 25 A/cm². The Triangles Are the 94-GHz LO Data and the Circles Are the 35-GHz Data. 165

5.15 Stability Analysis Factors as a Function of IF for BARITT 6. The LO Drive and J_{dc} Are Identical with those of Fig. 5.16. The Circles Are the 35-GHz Data while the Triangles Are the 94-GHz Data. —— Is g'_{oo}, --- Is g'_{11} and – – – Is Linvill Stability Factor. 166

5.16 Conversion Loss as a Function of LO Frequency for BARITTs 1, 6, and 12. The LO Drive Level Is $4V_T$ in all Cases and the IF Is 4 GHz. BARITT 12 Is Biased at 175 A/cm² While 25 A/cm² Is the Bias Current for the Other Devices. The Circles Designate BARITT 1 While the Triangles Designate BARITT 6 and the Pluses Designate BARITT 12. 167

5.17 Signal Frequency Embedding Impedance as a Function of LO Frequency for BARITTs 1, 6, and 12. All Other Parameters and Descriptions Are Identical with those of Fig. 5.16. 168

5.18 Absorbed LO Power as a Function of Dc Current Density for BARITT 12 when Operated as a Self-Oscillating Mixer at 35 GHz. The LO Drive Is 0.02 V. 169

5.19 Mixer Noise Figure for the Self-Oscillating Mixer (BARITT 12 at 35 GHz) as a Function of Dc Current Density. 170

5.20 Conversion Loss of the Self-Oscillating BARITT Mixer as a Function of Dc Current Density. 171

Figure		Page
5.21	Mixer IF Output Impedance as a Function of Dc Current Density for the Self-Oscillating BARITT Mixer. —— Is Resistance and --- Is Reactance.	172
5.22	Conversion Loss as a Function of Dc Current Density for BARITT 12. Driving Voltage Is $4V_T$ and IF Is 300 MHz. Optimal Conversion Loss Termination Was Used. Circles Are the 35-GHz Result While Triangles Are the 94-GHz Result.	174
5.23	Conversion Loss for BARITT 12 as a Function of Dc Current Density. All Parameters Are Identical with those of Fig. 5.22 Except that Here the Optimal Noise Figure Termination Was Used.	175
5.24	The Signal Frequency Termination Used as a Function of Dc Current Density in Fig. 5.23.	176
5.25	The Signal Frequency Embedding Circuit Termination Used in Fig. 5.22 Plotted as a Function of Dc Current Density.	177
5.26	Conversion Loss of BARITTs 1, 6 and 12 Plotted as a Function of LO Frequency. This Plot Is Identical with Fig. 5.16 Except that Here the Minimal Noise Figure Termination Is Used.	178
5.27	Mixer IF Output Impedance for BARITTs 1, 6, and 12 Plotted as Functions of Dc Current Density. BARITT 12 Was Biased at 175 A/cm^2 While the Other Two Devices Were Biased at 25 A/cm^2. The IF Frequency Is 4 GHz and the LO Drive Is $4V_T$. Circles Designate BARITT 1 While Triangles Designate BARITT 6 and the Pluses Designate BARITT 12.	179
5.28	The Signal Frequency Embedding Impedance (Optimizes Noise Figure) which Corresponds to Fig. 5.27.	180
5.29	The Mixer Noise Figure for the Case of Figs. 5.26 Through 5.28.	181
5.30	Mixer Noise Figure in BARITT 1 as a Function of LO Drive Level. The Bias and IF Conditions Are Identical with those of Figs. 5.26 Through 5.29. The Circles Designate BARITT 1 While the Triangles Designate BARITT 6 and the Pluses Designate BARITT 12.	182
5.31	Noise Figure as a Function of LO Frequency for BARITT 1 with Dc Current Density as a Parameter. The LO Drive Is $4V_T$ and the IF Is 4 GHz. The Circles Designate 50 A/cm^2; the Triangles, 75 and the Pluses, 100.	183

Figure		Page

Figure	Title	Page
5.32	Noise Figure for BARITT 6 as a Function of LO Frequency with Current Density as a Parameter. All Other Parameters and Symbols Are Identical with those of Fig. 5.31.	184
5.33	Noise Figure for BARITT 1 as a Function of LO Frequency with Current Density as a Parameter. The Circles Designate 150 A/cm^2; the Triangles, 200 and the Pluses, 250.	185
5.34	Imaginary Part of Γ_D for BARITT 1 as a Function of Frequency with Current Density as a Parameter.	187
5.35	Imaginary Part of Γ_D for BARITT 6 as a Function of Frequency with Current Density as a Parameter.	188
5.36	Imaginary Part of Γ_D for BARITT 12 as a Function of Frequency with Current Density as a Parameter.	189
5.37	Optimum Excess Noise Figure for McCleer's Dc Maximum Power Structure No. 2. This corresponds to Fig. 7.21 of McCleer.[30]	190
5.38	The Same Calculation as Is Shown in Fig. 5.37 Obtained Using the Analysis Presented Here. (VLO = 10 V_T)	191
6.1	The Basic Accelerate-Scatter Iteration of the Monte Carlo Method.	196
6.2	Scattering Rates for the Central Valley. (AP_{a+e} = Acoustic Phonon Absorption Plus Emission; $POP_{a,e}$ = Polar Optic Phonon Absorption and Emission, Respectively; $IV_{a,e}$ = Intervalley Absorption and Emission, Respectively)	198
6.3	Scattering Rates for the Satellite Valley. (AP_{A+e} = Acoustic Phonon Absorption Plus Emission; $POP_{a,e}$ = Polar Optic Phonon Absorption and Emission, Respectively; $IV_{a,e}$ = Intervalley Absorption and Emission, Respectively)	199
6.4	A Velocity Overshoot Study. The Parameter Is the Final Electric Field in kV/cm.	204
6.5	The Velocity Overshoot of Fig. 6.4 Plotted as a Function of Mean Distance Traveled.	205
6.6	The Velocity Collapse Following an Instantaneous Switch of the Field to Zero. The Parameter Is the Initial Field in kV/cm.	206

Figure		Page

6.7	The Mean Distance Traveled as a Function of Time After the Field Is Shut Off. The Parameter Is the Initial Field in kV/cm.	207
6.8	The Jones-Rees Central Valley Behavior. (a) Momentum Space Behavior and (b) Velocity as a Function of Time for a Ballistic Flight Across the Central Valley.	208
6.9	Central Valley Energy Transients Following a Sudden Application of an Electric Field. The Parameter Is the Final or Applied Field in kV/cm.	210
6.10	Central Valley Energy Transient of Fig. 6.9 as a Function of Mean Distance Traveled.	211
6.11	Satellite Valley Energy Transient Corresponding to the Case of Fig. 6.9 as a Function of Mean Distance Traveled.	212
6.12	Central Valley Energy Transients Following a Field Shut Off. The Parameter Is the Initial Field in kV/cm.	213
6.13	Upper Valley Energy Transients Following the Field Shut Off. The Parameter Is the Initial Field in kV/cm.	214
6.14	Velocity Transient for the Case of a Switch from 10 kV/cm to 6 kV/cm.	216
6.15	Velocity Transient for the Case of a Switch from a Field of 6 kV/cm to 10 kV/cm.	217
6.16	Induced Current Waveform Tailoring by Velocity Transients which Could Enhance the Oscillation Efficiency. The Terminal Voltage Waveform Is Shown for Reference. The Induced Current Dip Following the 180-Degree Phase Point Is a Result of a Velocity Undershoot While the Peak in the Last Quarter Cycle Is a Result of a Velocity Overshoot.	219
6.17	Velocity Transients for a Step Down in Field. The Initial Field Is 6 kV/cm and the Parameter Is the Final Field in kV/cm.	221
6.18	Ratio of Satellite Valley Population (N2) to Central Valley Population (N1) as a Function of Time for the Field Steps of Fig. 6.17.	222
6.19	In-Phase and Quadrature-Phase Velocity Components at 250 GHz as Functions of RF Driving Field Level. The Dc Field Was Zero.	225
6.20	Three Lag Windows.	235

Figure		Page

6.21	Three Spectral Windows.	237
6.22	Window Closing Experiment for Room Temperature Undoped GaAs at a Field of 10 kV/cm. A Dc Normalized Spectral Component of One Corresponds to a Diffusion Coefficient of 62 cm^2/s.	243
6.23	Comparison of Smoothed and Unsmoothed Periodograms. [S(0) = 2D Where D = 62 cm^2/s]	244
6.24	Total and Individual Valley Velocity Fluctuation Noise Spectra. [S(0) = 2D Where D = 62 cm^2/s]	245
6.25	Overall Velocity Autocovariance or Velocity Fluctuation Autocorrelation.	248
6.26	Individual Valley Velocity Autocovariance Functions.	249
6.27	Valley Random Process Autocovariance Function Estimate.	250
B.1	Flow Chart of Mixer Analysis Program.	267
B.2	Flow Chart of Subroutine SMSIG.	268
B.3	Flow Chart of Subroutine NOISE.	270
B.4	Flow Chart of Subroutine TTDEV.	272
C.1	Representation of a Linear Two-Port Network with all Internal Noise Sources Expressed as Equivalent Input Noise Sources $\hat{V}_n$ and $\hat{I}_n$.	274

LIST OF TABLES

Table		Page
1.1	Transit-Time Device Parameters in the Sharp Pulse (θ_w = 0) Approximation.	16
1.2	State of the Art of Schottky-Barrier Millimeter-Wave Mixers.	32
1.3	State of the Art of Mott Barrier Millimeter-Wave Mixers.	34
1.4	A Typical 100-GHz Schottky-Barrier Mixer Diode.	36
4.1	Parameters for Schottky and Mott Diodes.	99
4.2	Definition of BARITT Structures.	101
4.3	Peak Field in kV/cm for BARITTs at 500 A/cm^2.	102
4.4	VBDMAR for BARITTs.	104
4.5	Diameter in Microns for 50-Ω Real Part of Impedance at 300 MHz for BARITTs Biased at 500 A/cm^2.	108
4.6	Ratio of Area for 50-Ω Real Part of Impedance at 300 MHz to Areas for 1-Ω Real Part of Impedance at 35 GHz (Top) and 94 GHz (Bottom) for BARITTs Biased at 500 A/cm^2.	109
4.7	Thermal Resistance of Mesa for Diameters of Table 4.5.	112
4.8	Thermal Spreading Resistance into a Gold Heat Sink for Diameters of Table 4.5.	113
4.9	Negative-Resistance Bands for BARITT Structures (GHz).	114
4.10	Ratio of C_{eff} to C_{cold} for BARITTs at J_{dc} = 500 A/cm^2.	117
4.11	Knee Frequency in GHz for BARITTs at J_{dc} = 500 A/cm^2.	118
4.12	NEPF Values for BARITTs. (J_{dc} = 50 A/cm^2, 30 MHz Video Frequency, 35 GHz RF, Values in dB with Respect to W/cm)	133
4.13	NEPF Values for BARITTs. (J_{dc} = 50 A/cm^2, 30 MHz Video Frequency, 94 GHz RF, Values in dB with Respect to W/cm)	134

Table		Page
5.1	Tests Against the Original NASA Data.	145
5.2	Dc Current Density Survey at 35 GHz.	160
5.3	Dc Current Density Survey at 94 GHz.	161
5.4	IF Sweep at 35 GHz.	162
5.5	IF Sweep at 94 GHz.	163
6.1	Lag and Spectral Window Functions.	234
6.2	Properties of Spectral Window Estimates.	238

LIST OF SYMBOLS

A	Device cross-sectional area (cm^2).
C_B	Capacitance of injection region (F or $F \cdot cm^{-2}$).
C_{eff}	Effective low-frequency capacitance of transit-time device (F or $F \cdot cm^{-2}$).
C_j	Junction capacitance (F or $F \cdot cm^{-2}$).
C_{jo}	Zero bias capacitance (F or $F \cdot cm^{-2}$).
$\overline{COR}$	Injection region noise correlation matrix (A^2).
$\overline{COR}_{ID}$	Intrinsic diode noise correlation matrix (A^2).
C_s	Specific heat ($W \cdot s \cdot g^{-1} \cdot {}^{o}K^{-1}$).
D_n	Electron diffusion coefficient ($cm^2 \cdot s^{-1}$).
D_p	Hole diffusion coefficient ($cm^2 \cdot s^{-1}$).
d	Diode diameter (μm).
E	Electric field ($V \cdot cm^{-1}$).
E_c	Critical field for avalanche breakdown ($V \cdot cm^{-1}$).
$E(g)$	Statistical expectation of quantity g.
F	Noise factor.
F_e	Excess noise factor.
F_{SSB}	Single-sideband noise factor.
f_{high}	Highest frequency of negative conductance (Hz).
f_{low}	Lowest frequency of negative conductance (Hz).
f_{opt}	Frequency of maximum negative conductance (Hz).
G_{DEV}	Device conductance (mho or $mho \cdot cm^{-2}$).
G_{max}	G_{DEV} at f_{opt} (mho or $mho \cdot cm^{-2}$).
g	Electron-hole pair generation rate ($cm^{-3} \cdot s^{-1}$).
$h(t - \tau_n)$	Linear time-invariant filter impulse response function.

I	Electrical current (A).
I_{dc}	Dc current (A).
I_{ind}	Induced current (A).
I_{inj}	Injected current (A).
I_{max}	Maximum induced current (A).
I_s	Saturation current (A).
J_{dc}	Dc current density ($A \cdot cm^{-2}$).
J_n, J_p	Electron and hole current densities, respectively ($A \cdot cm^{-2}$).
J_T	Total current density ($A \cdot cm^{-2}$).
K_X	Autocovariance of random process X(t).
k	Boltzmann's constant (1.380×10^{-23} J/°K).
L_B	Avalanche inductance (H or $H \cdot cm^2$).
L_c	Conversion loss.
ℓ	Layer width (μm).
$N(t)$	Counting random variable.
N_B	Background doping density (cm^{-3}).
N_D	Donor doping density (cm^{-3}).
NEPF	Noise equivalent power factor (W/cm).
n	Electron density (cm^{-3}).
P_{dc}	Dc power (W).
P_{RF}	RF power (W).
p	Hole density (cm^{-3}).
q	Magnitude of electronic charge (1.602×10^{-19} C).
R_j	Junction resistance.
R_s	Parasitic or series resistance (Ω or $\Omega \cdot cm^2$).
R_{TH}	Thermal resistance (°K/W).

R_X	Autocorrelation of random process X(t).
S_X	Power spectral density of random process X(t).
T	Temperature (^oK).
T_M	Equivalent mixer input noise temperature (^oK).
t	Time (s).
V_a	Applied voltage (V).
V_{BD}	Avalanche breakdown voltage (V).
VBDMAR	Margin against avalanche breakdown (V).
V_{bi}	Built-in potential voltage (V).
V_{dc}	Dc voltage (V).
V_{PT}	Punch-through voltage (V).
V_{RF}	Peak RF voltage amplitude (V).
V_{TH}	Thermal voltage (0.0259 V at room temperature).
v_n, v_p	Electron and hole velocities, respectively (cm/s).
x	Spatial coordinate.
x_B	Injection region width (cm).
x_D	Drift region width (cm).
$\overline{Y}_{aug}$	Augmented network conversion admittance matrix (mhos or mhos$\cdot$cm^{-2}).
$\overline{Y}_B$	Injection region conversion admittance matrix (mhos or mhos$\cdot$cm^{-2}).
$\overline{Y}_D$	Drift region equivalent circuit parameter (mhos$\cdot$cm^{-2}).
$\overline{Y}_{ID}$	Intrinsic diode conversion admittance matrix (mhos or mhos$\cdot$cm^{-2}).
$\overline{Y}_{TD}$	Total diode conversion admittance matrix (mhos or mhos$\cdot$cm^{-2}).
$\overline{Z}_{aug}$	Augmented network conversion impedance matrix (Ω or $\Omega\cdot$cm^2).
$\overline{Z}_B$	Injection region conversion impedance matrix (Ω or $\Omega\cdot$cm^2).

Z_e Embedding circuit impedance (Ω).

$\overline{Z}_{ID}$ Intrinsic diode conversion impedance matrix (Ω or $\Omega \cdot cm^2$).

Z_{in_m} Mixer input impedance at the mth sideband frequency (Ω or $\Omega \cdot cm^2$).

Z_{par} Parasitic impedance (Ω or $\Omega \cdot cm^2$).

$\overline{Z}_{TD}$ Total diode conversion impedance matrix (Ω or $\Omega \cdot cm^2$).

Γ Drift region equivalent circuit parameter.

γ_m Voltage detection sensitivity ($\Omega \cdot cm^2/V$).

$\delta\overline{I}_{aug}$ Vector of small-signal currents at augmented network ports (A).

$\delta\overline{I}_B$ Vector of small-signal currents at injection region terminals (A).

$\delta\overline{I}_D$ Vector of small-signal currents through the drift region (A).

$\delta\overline{I}_{ID}$ Vector of small-signal currents at intrinsic diode terminals (A).

$\delta\overline{I}_s$ Vector of injection region shot noise currents (A).

$\delta\overline{V}_{aug}$ Vector of small-signal voltages at augmented network terminals (V).

$\delta\overline{V}_B$ Vector of small-signal voltages at injection region terminals (V).

$\delta\overline{V}_D$ Vector of small-signal voltages across the drift region (V).

$\delta\overline{V}_{ID}$ Vector of small-signal voltages at intrinsic diode terminals (V).

ε Material electrical permittivity (F/cm).

η_{max} Oscillator efficiency at f_{max}.

θ_D Drift transit angle (rad).

θ_m Width of peak value of I_{inj} (rad).

θ_w Angular width of injected current pulse (rad).

κ_s Thermal conductivity ($W \cdot {}^oK^{-1} \cdot cm^{-1}$).

ρ_m Mass density ($g \cdot cm^{-3}$).

τ_{TH} Thermal time constant (s).

ω_o Intermediate frequency ($rad \cdot s^{-1}$).

ω_1 Signal frequency ($rad \cdot s^{-1}$).

ω_a Avalanche frequency ($rad \cdot s^{-1}$).

ω_k Knee frequency of device impedance ($rad \cdot s^{-1}$).

ω_{LO} Radian frequency of local oscillator or pump ($rad \cdot s^{-1}$).

ω_m Mth sideband frequency in Saleh's notation ($rad \cdot s^{-1}$).

CHAPTER I. INTRODUCTION

1.1 Historical Background

Frequency conversion utilizing the nonlinear resistance of a metal-semiconductor barrier has been employed in microwave receivers for decades with the first systematic studies occurring in the second world war radar development effort. A text summarizing these studies was issued in 1948 as a part of the MIT Radiation Laboratory series.[1] Point contact mixer diodes were used in conjunction with vacuum tube local oscillators throughout the 1950s since no solid-state local oscillators were available. Advancing fabrication and materials technology changed both the choice of mixer diode and local oscillator in the 1960s. The first change came with the advent of Schottky-barrier diodes which proved superior to point contact mixer diodes in most performance criteria.[2,3] The same advances in fabrication technology also permitted fabrication of several solid-state microwave sources. Physically, these sources either use a broadband negative resistance (tunnel diodes), a negative differential conductivity associated with III-V semiconductors such as GaAs (Gunn diodes), or a band-limited transit-time produced negative resistance. One of these transit-time devices is evaluated as a frequency converter in this study.

The concept of a transit-time negative resistance in a solid-state device was introduced by Shockley.[4] He demonstrated in 1954 that transit-time effects could produce a negative resistance in pnp structures. This particular transit-time device is now called the barrier injection transit-time (BARITT) diode. It was not

achieved experimentally[5] until 1971. In the meantime Read[6] proposed a structure in which the doping profile localized and separated a high-field ionization or avalanche region from a lower field drift region. The combination of avalanche multiplication with transit-time effects allowed much higher powers and efficiencies than the BARITT device. Due to fabrication difficulties, the structure Read proposed in 1958 was not experimentally successful as an oscillator until 1965.[7] Around that time it was realized that simple uniformly doped structures[8,9] could also be used as avalanche transit-time devices. All of these avalanche devices are now called impact ionization avalanche transit-time (IMPATT) diodes. The term Read diode now identifies structures where the doping profile creates the spatially localized high field region as originally proposed by Read.

Throughout the late 1960s and early 1970s a great deal of effort was exerted in the fabrication, testing, and modeling of these solid-state microwave sources. By the late 1970s it was generally accepted that tunnel diodes were rarely the device of choice in any application. The BARITT device was securely established as a low-power, low-noise device. Gunn diodes were commercially successful as medium-power, medium-noise sources of frequencies as high as 75 GHz with laboratory results near 100 GHz. (This was in agreement with theory.) The IMPATT was well-established as a high-power, high-noise device.

The upper frequency limits to IMPATT operation were and still are inadequately understood. Although GaAs IMPATTs exhibit excellent performance at microwave frequencies, superior in fact to Si devices, their performance rapidly decreases with increasing frequency.

Essentially no experimental results at frequencies higher than 90 GHz and few past 60 GHz have been reported for GaAs devices while Si devices have been operated well into the low submillimeter-wave region.

Elta and Haddad[10] suggested that this problem is the result of a yet unknown physical mechanism which slows the avalanche process in GaAs much more than in Si. Supporting evidence for this hypothesis is provided by IMPATT noise measurements.[11] Elta and Haddad suggested that in this case superior millimeter-wave GaAs transit-time devices could be built by using a tunnelling or mixed tunnel-avalanche breakdown process. Read[6] considered a tunnel transit-time (TUNNETT) device but it had attracted little attention as he demonstrated that it would be an inefficient microwave oscillator. Recently, interest has revived and GaAs TUNNETT oscillation has been reported at high millimeter-wave frequencies.[12,13] Elta et al.[14] obtained CW oscillations at 150 GHz from a GaAs mixed tunnel-avalanche transit-time (MITATT) device.

Early in the development of these solid-state sources it was discovered that they could function as frequency converters. Studies of tunnel diodes showed that self-oscillating mixer performance using either fundamental or second-harmonic pumping[15] was possible. Alternatively, the device could function as a passive or externally pumped mixer. It was also found that the tunnel diode could function simultaneously as a video detector (the autodyne or unpumped receiver) and as a negative-resistance reflection amplifier.[16] Stability and other considerations prevented the tunnel diode from being commercially useful in these applications.

The performance of BARITT, IMPATT, and Gunn devices in these frequency conversion applications was also evaluated. The Gunn device was found to be a poor downconverter in self-oscillating mixer operation.[17-19] The IMPATT, on the other hand, functions well as a parametric frequency converter.*[20-23] However, its noise was found to prevent it from being useful in these applications. The associated parametric instabilities were found to be an important complication of IMPATT oscillator and amplifier design.[24-26]

BARITT devices have proved to be particularly well suited for some frequency conversion applications. They are consistently found to be superior in short-range, self-oscillating doppler systems.[18,19,27-30] Both experimental and theoretical studies demonstrated that BARITTs function well as both active (video detection and reflection amplification) and passive (video detection alone) mode video detectors.[31,32]

In this study, further investigations of BARITT device frequency converters are made. The frequency range of interest is 30 to 110 GHz. Schottky-barrier mixer diodes, particularly at the upper portion of this range, tend to have adequate electrical performance while being both thermally and mechanically fragile. Therefore the durability of BARITTs will be considered in some detail.

---

* Throughout this study conventional usage is followed in which frequency conversion in a nonlinear resistance is called mixing while conversion in a nonlinear reactance is called parametric conversion.

1.2 Fundamental Principles of Transit-Time Devices

The basic principles of transit-time device operation are illustrated by the simple waveforms shown in Fig. 1.1. The device is driven by the voltage waveform (a sinusoidal RF voltage and a constant dc voltage) shown in Fig. 1.1a. The device response to this waveform is illustrated in Figs. 1.1b and 1.1c. This response is conceptually divided into two portions. In the first portion, a current or carrier pulse forms and is injected across a plane near one end of the device. This end of the device is referred to as the injection region (Fig. 1.2). The conduction current pulse crossing the injection plane is called the injected current. (In some structures, an a priori injection plane cannot easily be specified. However, the conceptual division of the response into the steps given here is still useful.) In the second portion of the device response to the applied voltage, the injected carrier pulse moves through the drift region and is collected at the far end. The movement of these charge carriers creates an induced current at the device terminals (Fig. 1.1c) as a consequence of the induced current or Ramo-Shockley[33,34] theorem. In all transit-time devices the goal of the device design is to adjust the phasing of these steps properly and attain a large current during the second half of the RF cycle when the voltage is low. The resulting 180-degree phase shift between the voltage and the fundamental component of the current is characterized by a negative resistance.

The waveforms shown can be analyzed to yield simple analytic guidelines for transit-time device performance.[10] The dc current is

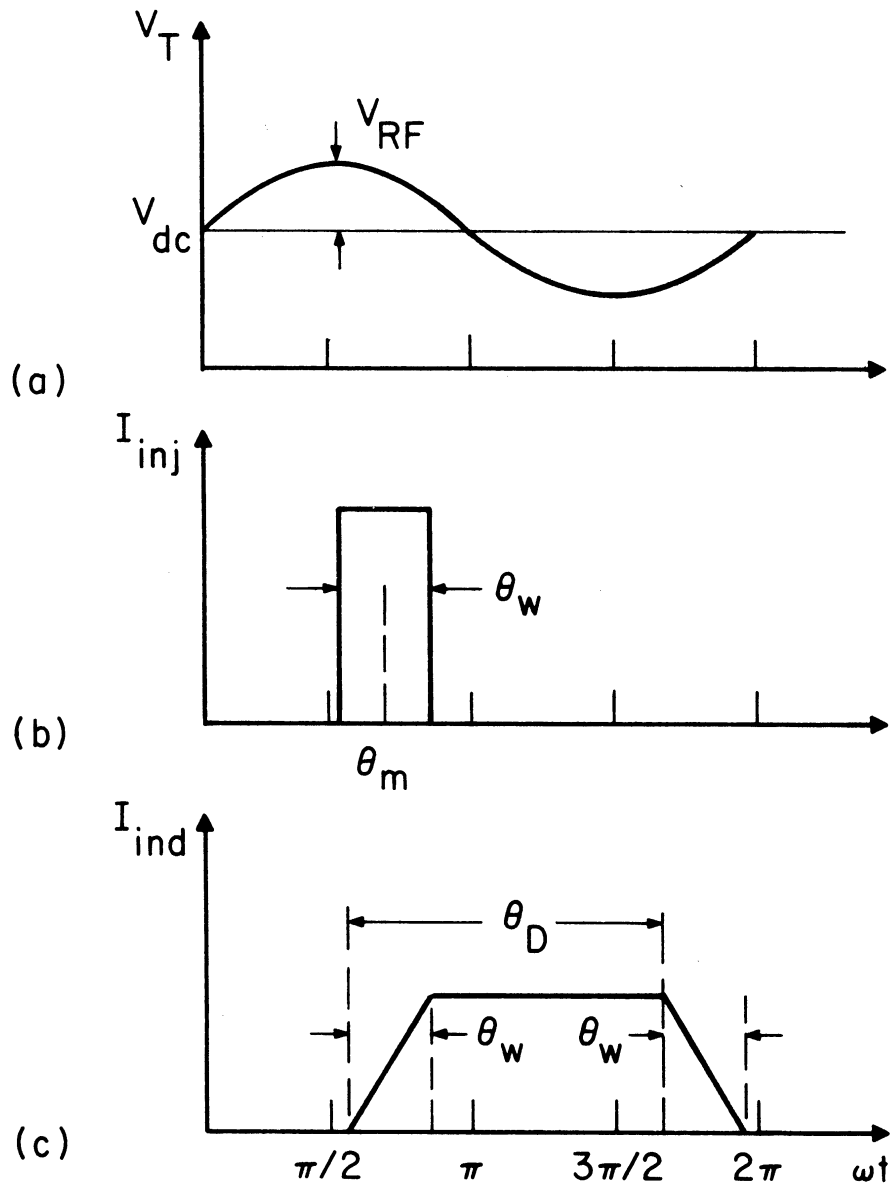

FIG. 1.1 SIMPLE WAVEFORMS FOR TRANSIT-TIME DEVICE MODELING. (a) TERMINAL VOLTAGE WAVEFORM, (b) INJECTED CURRENT WAVEFORM AND (c) INDUCED CURRENT CONTRIBUTION TO THE TERMINAL CURRENT. (ELTA AND HADDAD[10])

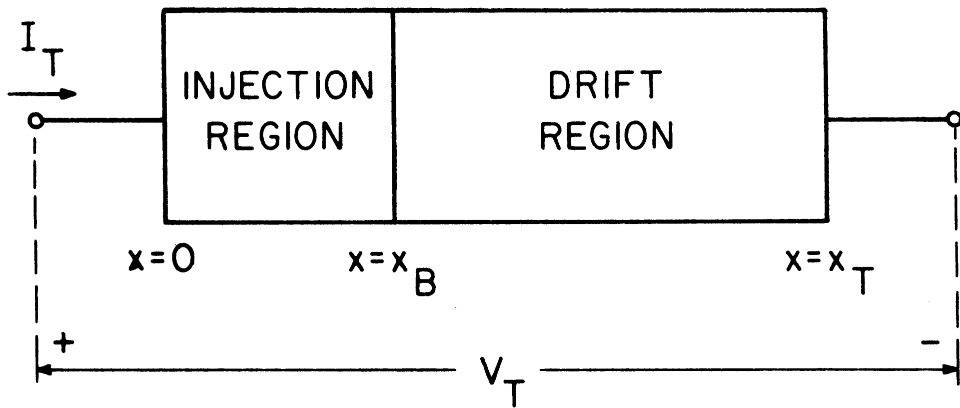

FIG. 1.2 SEPARATION OF A TRANSIT-TIME DEVICE INTO INJECTION AND DRIFT REGIONS.

$$I_{dc} = \frac{1}{2\pi}\int_0^{2\pi} I_{inj}(\omega t)\, d(\omega t) = \frac{1}{2\pi}\int_0^{2\pi} I_{ind}(\omega t)\, d(\omega t) \quad , \tag{1.1}$$

where I_{inj} and I_{ind} are the injected and induced currents, respectively. A consequence of Eq. 1.1 is

$$I_{max} = (2\pi/\theta_D)I_{dc} \quad . \tag{1.2}$$

The dc and RF powers are

$$P_{dc} = V_{dc}I_{dc} \tag{1.3}$$

and

$$P_{RF} = \frac{1}{2\pi}\int_0^{2\pi} I_{ind}(\omega t)V_{RF} \sin(\omega t)\, d(\omega t) \tag{1.4}$$

$$= V_{RF}I_{dc} \frac{\sin(\theta_w/2)}{\theta_w/2} \frac{\cos\theta_m - \cos(\theta_m + \theta_D)}{\theta_D} \quad . \tag{1.5}$$

The device efficiency is

$$\eta = \frac{P_{RF}}{P_{dc}} = \frac{V_{RF}}{V_{dc}} \frac{\sin(\theta_w/2)}{\theta_w/2} \frac{\cos\theta_m - \cos(\theta_m + \theta_D)}{\theta_D} \quad . \tag{1.6}$$

From Eq. 1.6, the following conclusions are readily obtained:

1. The oscillator efficiency decreases with increasing injected pulse width.

2. The maximum possible efficiency corresponds to an induced current waveform consisting of a delta function at $3\pi/2$.

3. The efficiency is proportional to the voltage modulation depth V_{RF}/V_{dc}.

Although the waveforms shown in Fig. 1.1 are often called ideal, the induced current waveform shown does not correspond well with waveforms seen in real high-efficiency transit-time devices. In these devices, a variety of physical mechanisms interact to tailor the induced current waveform into more of a delta-function-like form. The various transit-time devices differ in the mechanisms which produce the injected current, tailor the induced current, and limit the voltage modulation depth. These mechanisms are reviewed for each device in the next several sections.

1.2.1 IMPATT Diode. Although the IMPATT device will not be studied in this investigation, it is the most widely used and best understood transit-time device. It is reviewed here in some detail as many of the concepts and ideas first developed in IMPATT theory also apply to other transit-time devices. More comprehensive discussions can be found in a variety of review articles,[35-37] a book,[38] and other sources collected in Reference 39.

In the IMPATT device, the injected current is produced by avalanche multiplication in the injection region (the injection region is usually called the avalanche region in IMPATT literature). During the first half of the RF cycle, the field in the injection or avalanche region is high enough to support an impact ionization avalanche process. Since the electron-hole pair generation rate in such a process is roughly proportional to the carrier density, the carrier density grows roughly exponentially during the entire first half-cycle. The resulting injected current pulse peaks near $\theta_m = \pi$. This 90-degree

phase shift is often modeled by a nonlinear inductance in IMPATT equivalent circuits.

During the 1960s and early 1970s, it was commonly believed that efficient IMPATT operation required maintenance of a drift region field large enough to saturate the carrier velocity at all times. Since any undepleted regions contributed losses, it was felt that the drift region field should punch or reach through to the collecting contact. With these assumptions, both simple analytic[40,41] and more exact numerical[36] models predicted a maximum efficiency of 25 to 30 percent in GaAs IMPATTs. In this model, the induced current waveforms would ideally match those of Fig. 1.1 and no attention was paid to induced current waveform tailoring.

The situation changed dramatically with the first successful fabrication of GaAs Read IMPATTs. These devices had efficiencies of approximately 35 percent and were not punched through.[42] In the following several years a variety of induced current tailoring mechanisms were described in an effort to theoretically understand the experimental results. The most important are described here. The resulting device physics is sufficiently complex that large-signal models of the time-evolving carrier and field profiles in the device[43,44] are needed to understand the details of the device behavior.

The most obvious induced current tailoring mechanism in a nonpunch-through device is depletion-layer width modulation.[45] The simplest description of depletion-layer width modulation argues that the Ramo-Shockley theorem states that

$$I_{ind}(t) = \frac{Qv}{w(t)} ,$$

where Q is the drifting charge, v is the drift velocity, and w(t) is the time-varying depletion-layer width. Since w(t) has a minima at $3\pi/2$, a peak is expected in I_{ind} at $3\pi/2$. The actual physical mechanism is more complicated as the device terminals at which the induced current is measured do not move and the undepleted portion of the drift region is not a perfect conductor. Therefore, the details of the carrier transport in the undepleted region must be considered. This transport not only affects the induced current but also controls the response of the depletion-layer edge to the applied voltage.

If the carrier velocity in the low field or undepleted regions can exceed the high field saturated velocity, the depletion-layer edge can intercept the drifting carrier pulse somewhere inside the drift region. This is referred to as premature collection[46] and is a very important mechanism in GaAs devices. (The velocity-electric field characteristic in Si does not have the necessary low field peak.) Premature collection is experimentally observed by a sudden increase in efficiency accompanied by a small mode jump in frequency. The result is a device negative conductance-RF voltage characteristic[46-48] similar to that shown in Fig. 1.3

Another important induced current tailoring mechanism can occur in GaAs IMPATTs as a consequence of their velocity-electric field characteristics. The space charge of the drifting carrier pulse tends to raise the field in front of the pulse and depress the field behind the pulse as is shown in Fig. 1.4a. When the drifting carrier pulse

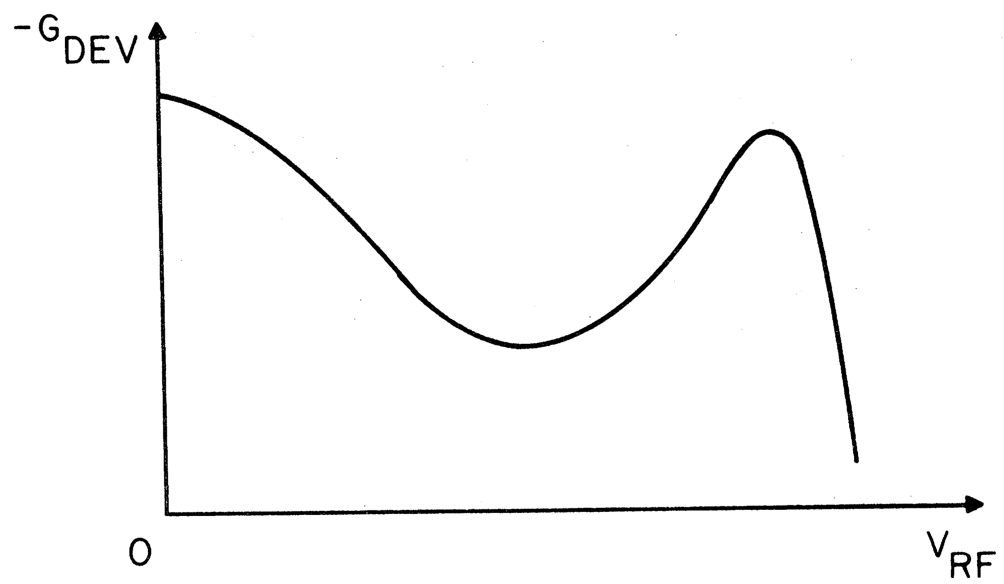

FIG. 1.3 THE NEGATIVE CONDUCTANCE-RF VOLTAGE AMPLITUDE CHARACTERISTIC OF A GaAs IMPATT DRIVEN INTO PREMATURE COLLECTION MODE OPERATION.

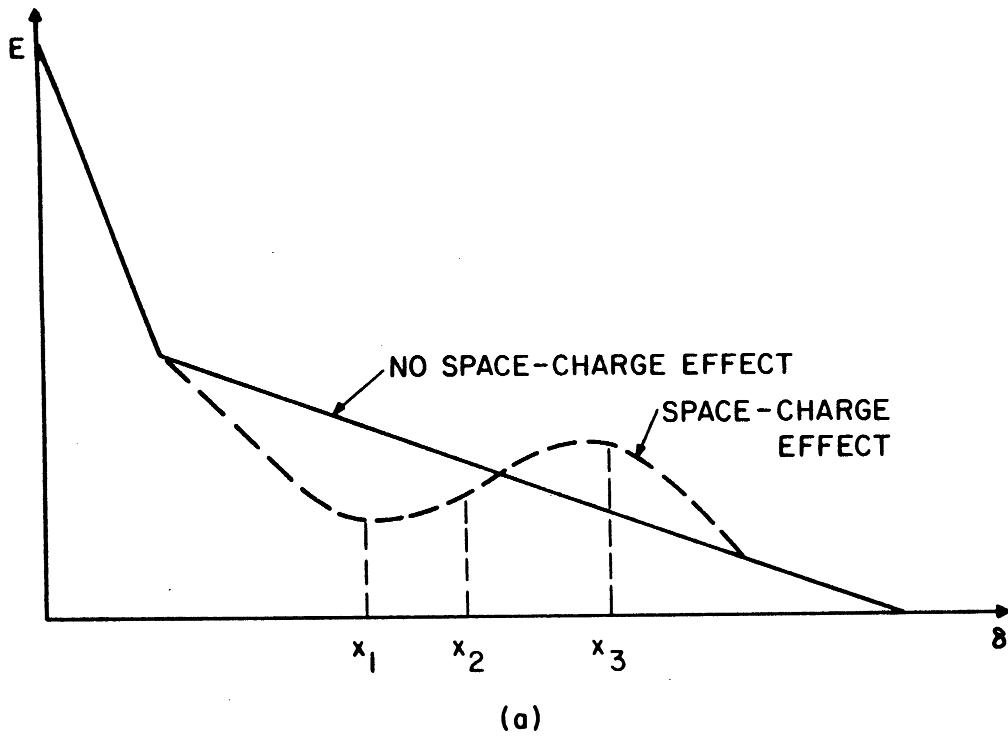

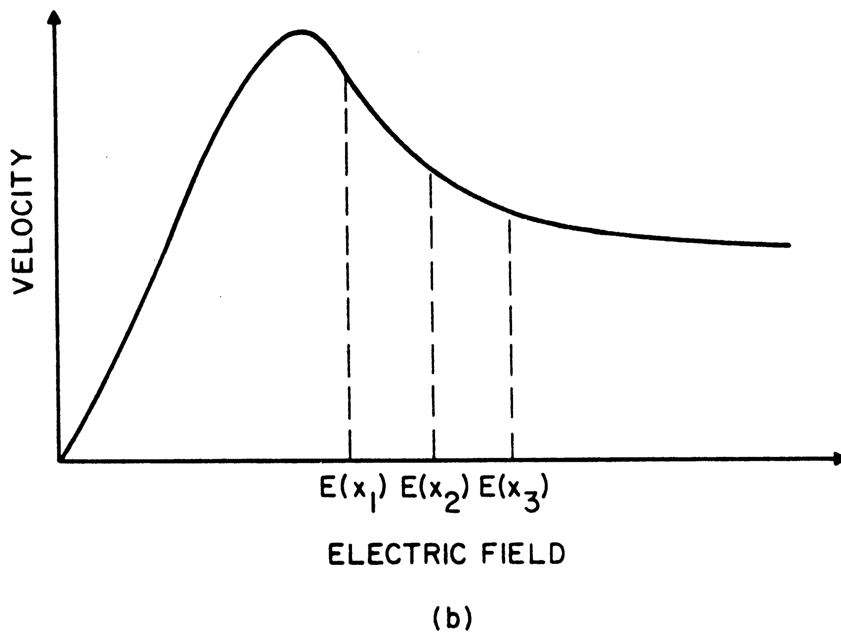

FIG. 1.4 PHYSICAL BASIS FOR CHARGE-LIMITED DOMAIN OR SURFING MODE OPERATION. (a) EFFECT OF THE DRIFTING CARRIER PULSE SPACE-CHARGE ON THE ELECTRIC FIELD PROFILE AND (b) RESULTING VELOCITY MODULATION.

enters a region where the field lies in the negative differential mobility portion of the velocity-electric field characteristic, the velocity modulation shown in Fig. 1.4b can occur. Carriers behind the pulse speed up while carriers in front of the pulse show down with respect to the carriers in the pulse. This velocity modulation improves the efficiency by keeping the pulse spatially sharp. For this reason, this tailoring mechanism is sometimes called a charge-limited domain.[49] The induced current also increases because the pulse velocity tends to be larger than the saturated velocity. For this reason the tailoring mechanism is sometimes called the surfing mode.[50]

There are several mechanisms which limit the voltage modulation depth in IMPATTs. These include:

1. If either the depletion-layer edge velocity of the RF conduction current in the undepleted region exceed the limit imposed by the peak velocity, the losses of the undepleted region rapidly increase.[48,51]

2. At sufficiently large RF drives, the injected current space charge can prematurely depress the avalanche field and terminate the avalanche.

3. At large RF drives, the device back bias or rectification can either represent an increased loss or create bias circuit instabilities.[52]

4. The nonlinear inductive behavior of the avalanche region can create parametric instabilities.[24]

All of these mechanisms and others, such as drift region ionization, correspond to a limit on the field modulation at some point in the device. A very important point is that different doping profiles will create different voltage modulations for the same

limiting field modulation. In general, Read structures are superior to uniformly doped structures and nonpunch-through structures are superior to punch-through structures in that the same field modulation produces a larger voltage modulation.[53] It has been suggested[43] that part of the reason for the failure of X-band Si IMPATTs to experimentally achieve the predicted efficiencies is that they are sensitive to parametric instabilities since the large losses of undepleted Si[54] require that they be punch-through devices.

A summary of important device criteria for IMPATT, TUNNETT, and BARITT devices is provided in Table 1.1. Here, η_{max} is the maximum efficiency; f_{low} and f_{high} are the lower and upper threshold frequencies, respectively, for the band-limited negative conductance, and f_{opt} is the frequency at which the maximum negative conductance $-G_{max}$ is found. All of these parameters for the IMPATT are obtained from the waveforms of Fig. 1.1 except for f_{low}. f_{low} is generally known as the avalanche frequency[55] (ω_a) and is determined by the injection region as opposed to the drift region. It is commonly defined by

$$\omega_a = \left(\frac{2\alpha'(E_c)v_s J_{dc}}{\varepsilon}\right)^{1/2} , \qquad (1.7)$$

where $\alpha'(E_c)$ is the derivative of the ionization rate α with respect to the electric field evaluated at the critical field for avalanche breakdown E_c, J_{dc} is the dc current density, ε is the material electrical permittivity, and v_s is the saturated carrier velocity. ω_a is related to f_{low} by

$$f_{low} = \frac{\omega_a}{2\pi} . \qquad (1.8)$$

Table 1.1

Transit-Time Device Parameters in the Sharp Pulse ($\theta_w = 0$) Approximation

Device	θ_m	η_{max}	$-G_{max}$	f_{opt}	f_{low}	f_{high}
IMPATT	π	$-\frac{2}{\pi}\frac{V_{RF}}{V_{dc}}$	$\frac{4}{\pi}\frac{I_{dc}}{V_{RF}}$	$\frac{1}{2}\frac{v_s}{x_T - x_B}$	$\frac{1}{2}\left[\frac{2\alpha'(E_c)v_s J_{dc}}{\varepsilon}\right]^{1/2}$	$\frac{v_s}{x_T - x_B}$
TUNNETT	$\frac{\pi}{2}$	$-\frac{2}{3\pi}\frac{V_{RF}}{V_{dc}}$	$\frac{4}{3\pi}\frac{I_{dc}}{V_{RF}}$	$\frac{3}{4}\frac{v_s}{x_T - x_B}$	$\frac{1}{2}\frac{v_s}{x_T - x_B}$	$\frac{v_s}{x_T - x_B}$
BARITT	$\frac{\pi}{2}$	$-\frac{2}{3\pi}\frac{V_{RF}}{V_{dc}}$	$\frac{4}{3\pi}\frac{I_{dc}}{V_{RF}}$	$\frac{3}{4}\frac{v_s}{x_T - x_B}$	$\frac{1}{2}\frac{v_s}{x_T - x_B}$	$\frac{v_s}{x_T - x_B}$

1.2.2 TUNNETT Diode. In the TUNNETT device the injected current pulse is generated by quantum mechanical tunneling through the potential barrier of a reverse-biased p-n junction or Schottky barrier. The tunneling current is determined solely by the barrier height or electric field. Therefore, the current peaks $\theta_m = \pi/2$, and there is no inductive phase shift associated with the injection region.

Successful TUNNETT operation requires that very high peak fields (> 10^6 V/cm) be achieved in a sufficiently narrow region that little or no impact ionization occurs. To do this the peak field must be reduced by an order of magnitude in several hundred angstroms. This can be accomplished in either a narrow highly doped structure or a Read structure. The "HI" doping in a HI-LO structure or the doping in a uniformly doped structure must be near[56] 10^{18} atoms/cm^3. The clump or "HI" doping in a LO-HI-LO structure must be near[57] 5×10^{18} atoms/cm^3. Since the dc current will determine the peak field, TUNNETT device drift region field levels are very sensitive to variations in the HI doping.

The induced current tailoring mechanisms in a GaAs TUNNETT are identical in principle to those of a GaAs IMPATT, although they have not been studied in detail. The only reported large-signal simulations[57,58] clearly show depletion-width modulation effects.

The voltage modulation depth in the TUNNETT will be limited by either space-charge effects, drift region ionization, or by a switch of the undepleted epitaxial material into a lossy state. The voltage modulation properties of the TUNNETT differ from those of the IMPATT in that they are expected to improve with frequency. In the

TUNNETT, the drift region length reduces with frequency while the injection region length remains essentially constant. Numerical studies[57] show the oscillator efficiency of a TUNNETT as increasing throughout the low millimeter-wave region and peaking near 100 GHz. TUNNETT properties are summarized in Table 1.1. The waveforms of Fig. 1.1 are used to determine all of the tabulated parameters.

It is also possible to operate a device in a mixed tunnel-avalanche breakdown or MITATT mode. In such a device the relative contributions of tunneling and avalanche are a complicated function of device structure, dc current density, RF drive, temperature and frequency.[57-59] In general, long injection regions increase the avalanche contribution. If high-frequency or low-noise operation is required the tunneling contribution is beneficial. MITATT properties will lie somewhere between the TUNNETT and IMPATT properties summarized in Table 1.1

1.2.3 BARITT Diode. The injection mechanism of the BARITT device is illustrated in Fig. 1.5. Although a metal-semiconductor-metal (MSM) device is shown (Fig. 1.5a) the mechanism also applies to pnp structures. At zero bias the electric field arises from the built-in potentials of the junctions. As the device voltage increases almost all of the voltage increase appears across the reverse-biased junction (Fig. 1.5b). Reversing the polarity only interchanges the locations of the forward- and reverse-biased junctions. At a sufficiently large voltage the electric field punches or reaches through the device. For transit-time or BARITT operation the device is biased near the punch-through voltage. The upward voltage swing during the first half of the RF cycle in Fig. 1.1 then reduces the forward

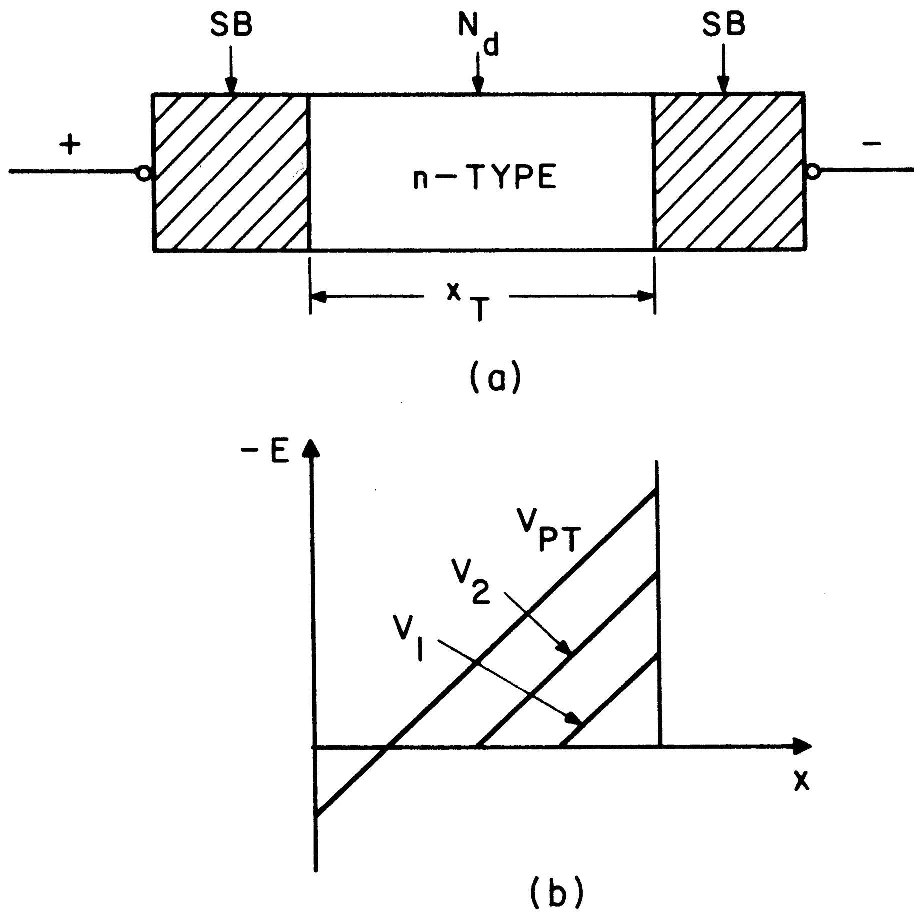

FIG. 1.5 BARITT DEVICE STRUCTURE AND OPERATION. (a) MSM BARITT STRUCTURE AND (b) ELECTRIC FIELD PROFILE AS A FUNCTION OF TERMINAL VOLTAGE.

barrier height and increases the injected hole current. Therefore, as was the case for the TUNNETT, the injected current peaks at $\theta_m = \pi/2$ and there is no injection region inductance.

The induced current tailoring mechanisms in the BARITT differ from those of the IMPATT and TUNNETT devices. The most important tailoring mechanism in the BARITT is the low field region (Fig. 1.5b) into which the carriers are injected.[60,61] In this region the carrier transport occurs at low velocities and is diffusion dominated. The resulting induced current waveform is shown in Fig. 1.6. The depression during the second quarter of the RF cycle improves the oscillator efficiency.

Due to the low efficiencies, it has been suggested[62] that the BARITT structure be designed in a fashion that optimizes this low-field retardation effect. This is particularly important at higher frequencies[63,64] and in GaAs.[64,65] The best experimental results[66,67] have been obtained in n^+ipnn^+ Si devices in which this optimization occurs. Another approach to induced current tailoring in BARITTs is to use a heterostructure (<u>do</u>uble <u>ve</u>locity <u>t</u>ransit-<u>t</u>ime or DOVETT) device.[68-70]

Very few of the IMPATT induced current tailoring mechanisms apply to the BARITT. Depletion-width modulation and premature collection are not seen as the device remains punched through during the entire RF cycle.[64,64,71] (The premature collection referred to by Kwok and Haddad[71] is a result of a spatially broad carrier pulse.) Charge-limited-domain formation has been reported in GaAs BARITT simulations[64] but has not been reported experimentally.

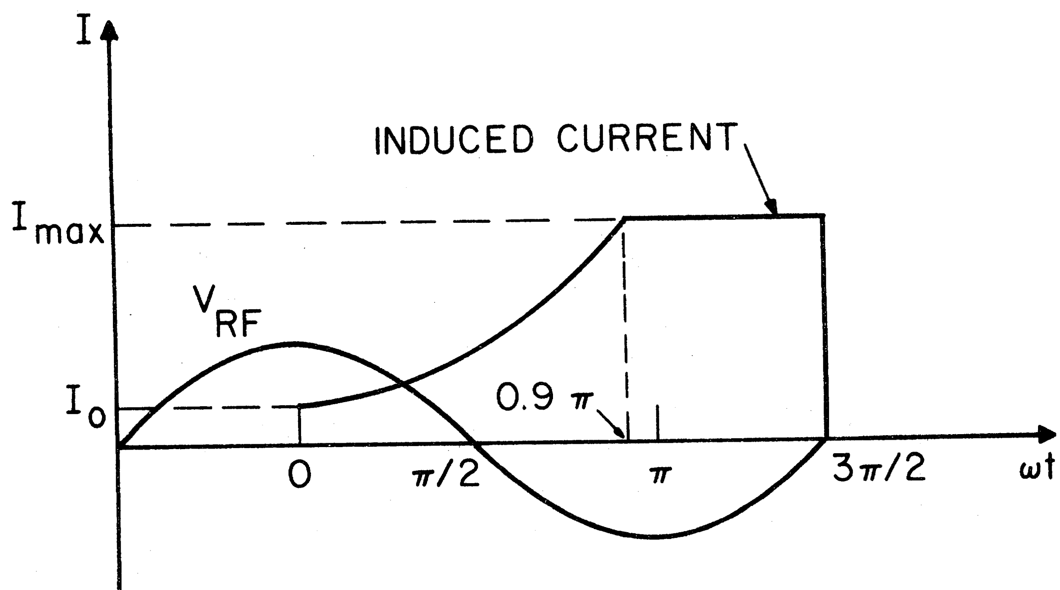

FIG. 1.6 EFFECT OF INJECTION INTO A LOW-FIELD REGION ON THE INDUCED CURRENT IN A BARITT DEVICE. (NGUYEN-BA AND HADDAD[65])

The voltage modulation depth in a BARITT is severely limited by several effects. These are: (1) the necessity of avoiding avalanche breakdown, (2) the necessity of maintaining the fields needed for reasonable carrier drift velocities, and (3) space-charge limits on the injection process. These effects are sufficiently restrictive that the voltage modulation depth of the BARITT is much lower than that of the other devices discussed. The properties of BARITTS are summarized in Table 1.1 using the waveforms of Fig. 1.1.

1.2.4 Schottky and Mott Barriers. The oldest of the devices considered in this study is the Schottky barrier (discovered by Braun[72] in 1874) and its derivative the Mott barrier.[73] A brief discussion is offered here largely to introduce some notation and terminology. For details, a variety of textbook discussions[1,74-77] are available.

Simple electric field and doping profiles for these devices are shown in Figs. 1.7 and 1.8. The essential difference between the two devices is that the Mott barrier punches through at zero bias while the Schottky does not. As a result, Mott barriers can be obtained by either reducing the epitaxial doping or epitaxial width of a typical Schottky-barrier diode.

The current-voltage characteristic (I-V) and capacitance-voltage characteristic (C-V) of a Schottky-barrier diode are shown in Fig. 1.9. There are a variety of theories for the I-V characteristic including thermionic emission, diffusion, thermionic diffusion, field emission (tunneling), and thermionic-field emission. Although the details differ from theory to theory, the results usually have the form of the experimentally observed exponential diode law

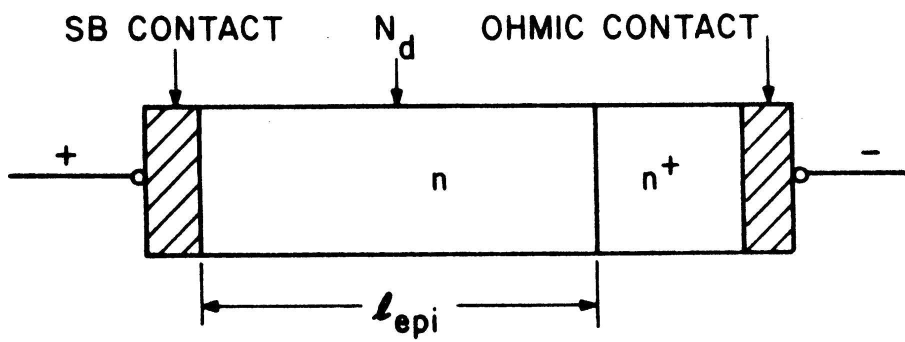

FIG. 1.7 DEVICE STRUCTURE FOR SCHOTTKY (N_d HIGH) AND MOTT (N_d LOW) DEVICES.

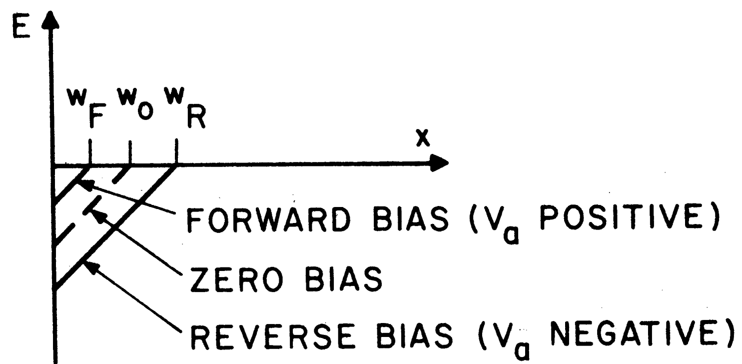

(a)

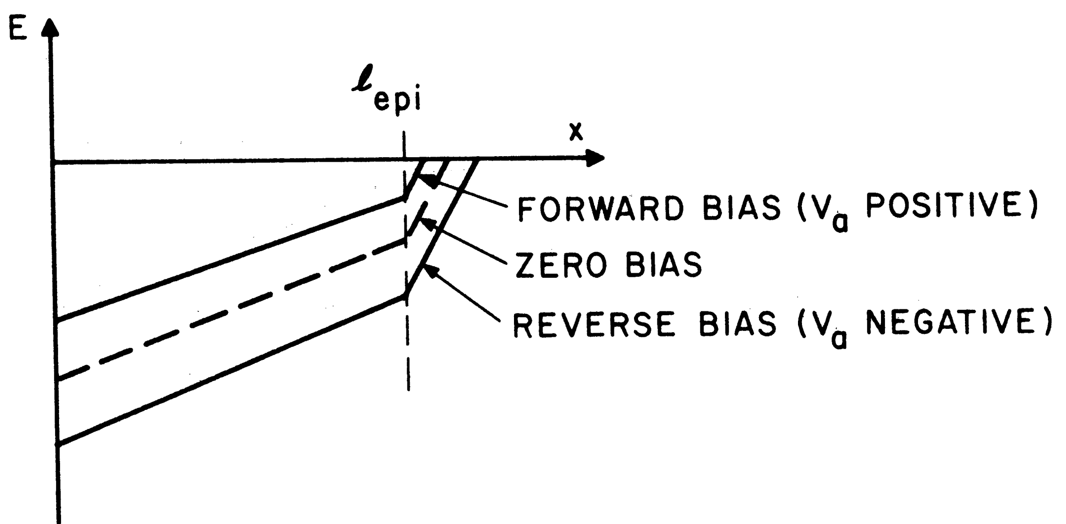

(b)

FIG. 1.8 ELECTRIC FIELD PROFILES IN (a) SCHOTTKY AND (b) MOTT DEVICES AS A FUNCTION OF TERMINAL VOLTAGE.

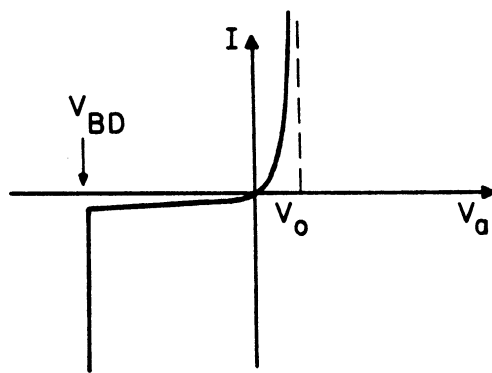

(a)

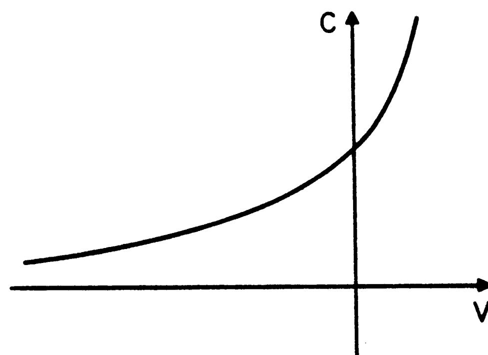

(b)

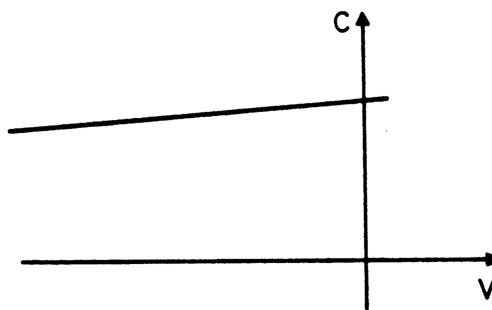

(c)

FIG. 1.9 (a) CURRENT-VOLTAGE AND (b) CAPACITANCE-VOLTAGE CHARACTERISTICS OF A SCHOTTKY DIODE.
(c) CAPACITANCE-VOLTAGE CHARACTERISTIC OF A MOTT DEVICE.

$$I = I_s[\exp(qV/\eta_i kT) - 1] \quad , \qquad (1.9)$$

where I_s is a saturation current (which may be voltage dependent), q is the electronic charge magnitude, T is the device temperature, k is Boltzmann's constant, and η_i is a temperature and voltage dependent ideality factor. The C-V characteristic is determined by the depletion-layer capacitance which, for a uniformly doped diode (doping N_B), is

$$C(V) = C_{jo}\left(1 - \frac{V}{V_{bi}}\right)^{-1/2} \quad , \qquad (1.10)$$

where the zero-bias capacitance is

$$C_{jo} = A\left(\frac{q\varepsilon N_B}{2V_{bi}}\right)^{1/2} \qquad (1.11)$$

and V_{bi} is the built-in potential.

The equivalent circuits of the various devices are qualitatively compared in Fig. 1.10. The equivalent circuit of the Schottky-barrier device (Fig. 1.10a) consists of an injection region followed by two series resistances. The injection region is modeled by a resistance connected in parallel with the depletion capacitance. The first series resistance is the parasitic resistance of the undepleted epitaxial material while the second represents the unavoidable losses associated with the electrical contacts. The Mott device equivalent circuit (Fig. 1.10b) differs from the Schottky device circuit in only two respects. First, the depletion capacitance is not a function of voltage in the punch-through Mott device. Second, there is not parasitic loss from the undepleted epitaxial material as there is no undepleted

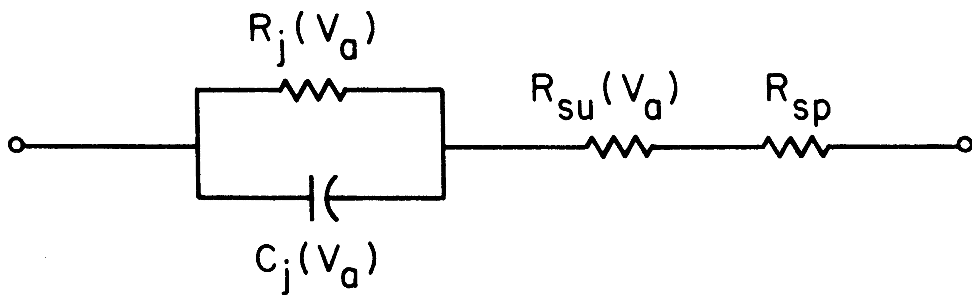

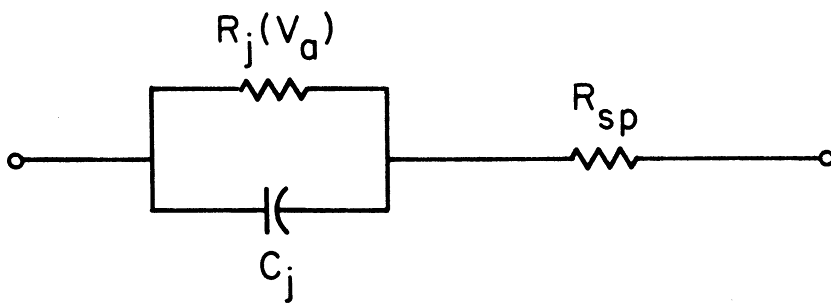

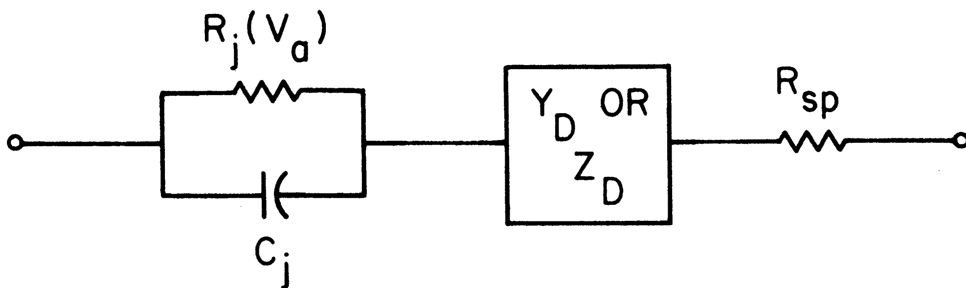

FIG. 1.10 EQUIVALENT CIRCUITS OF VARIOUS SEMICONDUCTOR DIODES. (a) SCHOTTKY DIODE, (b) MOTT BARRIER DIODE AND (c) BARITT DEVICE.

epitaxial material. A general equivalent circuit for BARITT devices is shown in Fig. 1.10c. The injection region in both devices consists of a conductance connected in parallel with a depletion-layer capacitance. The voltage dependency of this capacitance depends on the doping profile and on the assumptions made in the device modeling effort. It will generally be ignored here. Instead of a parasitic resistance representing the undepleted epitaxial material, there is a complex valued drift region impedance. This drift region impedance may or may not have a negative resistance component.

1.3 State of the Art for Transit-Time Device Oscillators

The state of the art[78-96] for IMPATT, MITATT and TUNNETT sources is shown in Figs. 1.11 and 1.12. For BARITTs, powers of over 100 mW are reported for microwave frequencies with the highest reported CW operating frequency being 31 GHz.

The state of the art for Si devices is shown in Fig. 1.11. Throughout the 30- to 110-GHz range of interest to this study, the output powers are thermally limited in CW operation although at higher frequencies electronic considerations limit the output power.[97] The higher frequency results often require harmonic output[87] or cryogenic operation.[90] However good performance is seen in fundamental mode operation at room temperature for frequencies in excess of 200 GHz. Relatively undramatic progress has been reported since Bauhahn's[98] state-of-the-art survey in 1977.

The state of the art for GaAs transit-time devices is shown in Fig. 1.12. Here dramatic progress has been made since Bauhahn's survey. The pulsed TUNNETT results of Nishizawa et al.,[12,13] the CW MITATT result of Elta et al.,[14] and the anomalous bucket or tub structure

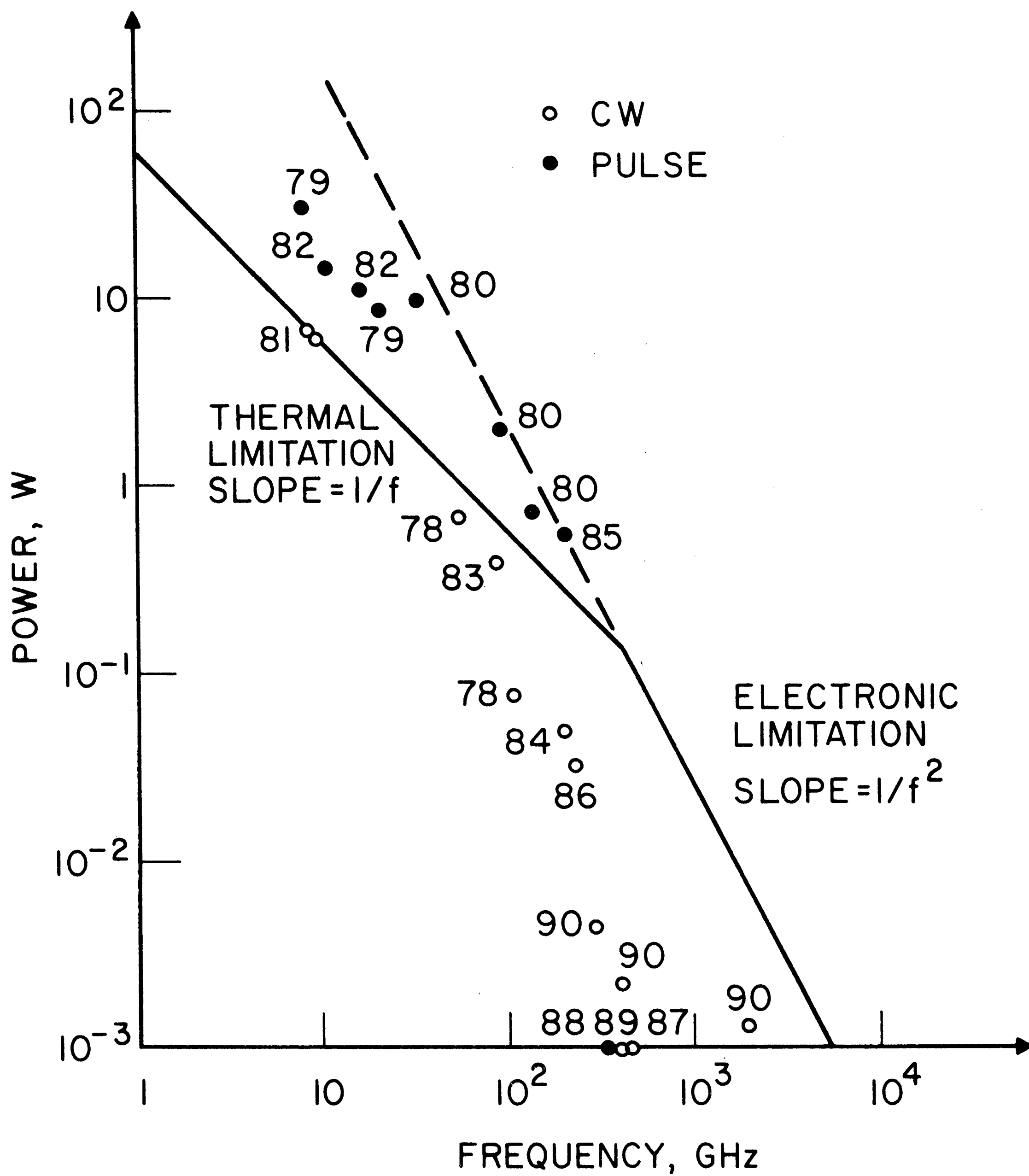

FIG. 1.11 STATE OF THE ART FOR Si TRANSIT-TIME DEVICE OSCILLATORS.

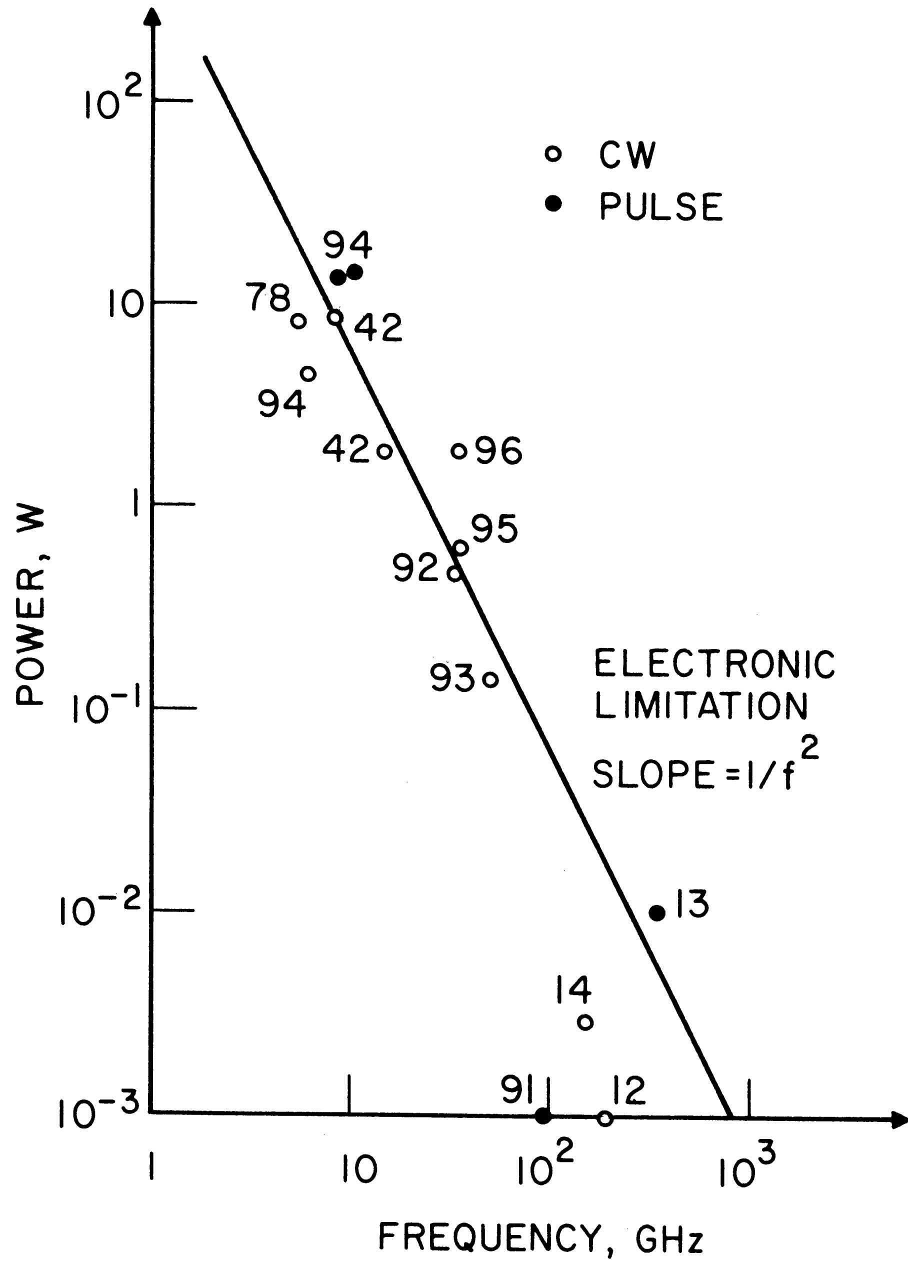

FIG. 1.12 STATE OF THE ART FOR GaAs TRANSIT-TIME DEVICE OSCILLATORS.

result of Masse et al.[96] had not been reported in 1977. Standard GaAs IMPATTs still have not worked well at frequencies in the millimeter-wave region and not at all for frequencies higher than 100 GHz.

The potential of the various solid-state sources as local oscillators for heterodyne receivers operating in the 30- to 110-GHz range can now be assessed. For frequencies below 75 GHz the Gunn device is presently commercially competitive. Above 75 GHz it may be useful if recent laboratory results[99] are successfully transferred to commercial production. Above 75 GHz, commercial Si IMPATTs provide sufficient power but are too noisy for many applications.

1.4 State of the Art for 30- to 110-GHz Mixers

The state of the art for Schottky-barrier mixers is illustrated by the results[100-106] shown in Table 1.2. These results do not constitute a complete literature survey but are representative. Generally, the GaAs Schottky-barrier mixer diode is commercially available for frequencies below 75 GHz. Most results for higher frequencies represent either experimental laboratory results or devices intended for use in radio telescopes. As can be seen, the electrical performance of these devices is quite satisfactory. T_M is the mixer equivalent input noise temperature in degrees Kelvin, L_c is the mixer conversion loss in dB, and NF is the mixer noise figure in dB. One interesting result is that of Bernues et al.[105] They found that, contrary to common belief, Si mixer diodes at high frequencies perform as well as GaAs devices.

Table 1.2

State of the Art of Schottky-Barrier Millimeter-Wave Mixers

Reference	Pump Frequency (GHz)	Performance
Weinreb and Kerr[100]	33	T_M = 623, L_c = 5.9
	85	T_M = 800, L_c = 6.8
Held and Kerr[101]	87	T_M = 500 to 1000
		L_c = 5 to 8
Anand and Christou[102]	36	NF = 6 to 7
Christou et al.[103]	36	NF = 6.5, L_c = 5 to 6
Anand et al.[104]	36	NF $\geq$ 6.5, L_c = 5
Bernues et al.[105]	107	L_c = 7 to 8.5 GaAs Diode
		L_c = 6 to 8 Si Diode
Keen[106]	111	T_M = 740
		L_c = 6.5

The state of the art for Mott devices is surveyed[107-111] in Table 1.3. Here, all the devices are experimental devices operated at high frequencies and generally cooled to cryogenic temperatures. These Mott devices have achieved the lowest noise performance yet reported for high millimeter-wave mixers.

Recently, subharmonically pumped mixers have received a great deal of attention.[112-115] Such mixers have matched conventional mixer performance in the 30- to 110-GHz range. Subharmonically pumped mixers have the following advantages:

1. A lower frequency oscillator can be used as the local oscillator.

2. The local oscillator AM noise sidebands are suppressed allowing noisier devices (e.g., IMPATTs) to be used.

3. There is inherent protection against large peak inverse voltages in the antiparallel diode configuration used.

4. The increased separation between the local oscillator and signal frequencies simplifies the mixer circuit design. The pump-to-signal port isolation is improved while the filter losses are reduced.

5. If a self-biasing arrangement is used, no dc return is needed.

The electrical performance of these devices is quite adequate to meet most system needs. However, there are basic problems posed by the device structure. A typical Schottky-barrier diode designed for use as a 100-GHz mixer is described in Table 1.4. The device has a high doping, micron diameter, and submicron epitaxial layer thickness. The fabrication and bonding of this device is not easy.

Table 1.3

State of the Art of Mott Barrier Millimeter-Wave Mixers

Reference	Pump Frequency (GHz)	Performance
Schneider et al.[107]	100	T_m = 55, Physical Temperature = 15°K
Vizard et al.[108]	111	T_m = 700 to 1000 at Room Temperature
		T_m = 280 to 1000, Physical Temperature = 16°K
Keen et al.[109]	111	T_m = 800, Physical Temperature = 295°K
		T_m = 200, Physical Temperature = 20°K
McColl and Millea[110]	110	NF = 6.3
Linke et al.[111]	81	T_m = 312, Physical Temperature = 18°K

The small size also makes the device fragile. The small area leads to high current and power densities. For example, an incident power of 1 mW would create a power density of 20,000 W/cm^2 in the structure of Table 1.4. Such high current and power densities can create significant thermal problems.

The thermal problems are worsened by the high thermal resistance and short thermal time constant. The thermal resistance of Table 1.4 was calculated using

$$R_{TH} = \frac{1}{\pi r^2} \frac{\ell_{epi}}{\kappa_s} , \qquad (1.12)$$

where r is the device radius, ℓ_{epi} is the epitaxial layer thickness, and κ_s is the thermal conductivity of the semiconductor. Equation 1.12 ignores the contribution of spreading resistance and therefore underestimates the total thermal resistance. The thermal time constant is calculated using

$$\tau_{TH} = \frac{\ell^2_{epi} \rho_m C_s}{\kappa_s} , \qquad (1.13)$$

where ρ_m is the material mass density and C_s is the material specific heat. The time constant also ignores the spreading resistance contribution but does show that the "active" portion of the device can respond thermally to a sudden incident power pulse more rapidly than an external protective power limiter may respond.

An additional problem is posed by the high doping. High dopings result in steep electrical field gradients. These steep gradients, in turn, reduce the avalanche breakdown voltage and

Table 1.4

A Typical 100-GHz Schottky-Barrier Mixer Diode

Doping	10^{17} atoms/cm^3
Diameter	2.5 μm
Epitaxial Layer Thickness	0.2 μm
C_{jo}	10 fF
η_i	1.1
R_s	8 Ω
Dc Current	1 mA
Dc Current Density	20,000 A/cm^2
Breakdown Voltage	15 V
Peak Field at -1 V	≈ 50 kV/cm
Thermal Resistance of Mesa Alone	800°K/W
Thermal Time Constant of Mesa Alone	1.7 ns

create high electric fields internally for relatively small applied terminal voltages. As a result, these devices are susceptible to avalanche and microplasma burnout.

1.5 Outline of Present Study

BARITT devices may not be competitive in local oscillator applications at millimeter-wave frequencies. However, they are excellent frequency converters at microwave frequencies and there is no reason to suppose that they will cease to be good converters in the low millimeter-wave region. In Section 1.4 it was shown that Schottky and Mott devices provide good electrical performance in the frequency range of interest but are small, fragile devices. Their small device size and high doping are the result of an attempt to simultaneously have low losses in the undepleted epitaxial layer and an acceptable device capacitance. The BARITT device however has a depleted drift region instead of an undepleted series resistance. For frequencies above the negative-resistance band, the impedance of the drift region is essentially capacitive[30] and can therefore be tuned out by the circuit. Therefore, the device length and area can be made substantially larger in a BARITT while the doping can be kept substantially smaller. The BARITT is expected to be a more rugged and durable device that is easier to fabricate and bond.

In Chapter II standard mixer theory is extended to include the case of a fundamentally pumped transit-time device. Subharmonically pumped mixers will not be considered in this study as they complicate mixer analysis without changing the relative merits of Schottky, Mott and BARITT devices as mixing elements. In Chapter III the

large-signal noise correlation effects generally seen in junction devices are described along with methods for their modeling. The device modeling techniques are presented in Chapter IV. In Chapter V BARITT, Mott and Schottky devices are compared as mixer diodes. In Chapter VI Monte Carlo methods are used to check some of the assumptions made at various points in the study. The general results and conclusions are summarized in Chapter VII along with some suggestions for future investigations.

CHAPTER II. FREQUENCY CONVERSION IN TWO-TERMINAL JUNCTION DEVICES

2.1 Introduction

Two-terminal devices presently dominate millimeter-wave systems. Furthermore, it is not expected that conventional three-terminal devices will provide significant performance advantages past the low millimeter-wave region. With the exception of Gunn devices all these two-terminal devices are junction diodes. This allows some aspects of their performance to be treated in a unified manner. A unified small-signal model of frequency conversion in two-terminal junction devices at millimeter-wave frequencies is presented here.

Frequency conversion occurs in all the devices because of the nonlinear response of the junction to electrical signals. In some devices the nonlinearity is the conductance associated with the junction current-voltage characteristic. This characteristic is controlled by the mechanisms by which charge is transported through the junction. This mechanism is classical (e.g., diffusion or thermionic emission) in some devices (Schottky or Mott barriers and BARITT devices) and quantum mechanical (tunneling) in other devices (tunnel diodes).

In other cases the nonlinearity is a nonlinear reactance. In varactors the nonlinear reactance is created by the junction depletion capacitance. In IMPATT and MITATT devices avalanche effects introduce a nonlinear inductance. In some situations both a nonlinear conductance and a nonlinear reactance are present.

The frequency conversion properties of these two types of nonlinearity differ in general. This difference is reflected by a distinction in terminology. Frequency conversion in a nonlinear conductance is called mixing while frequency conversion in a nonlinear reactance is called parametric conversion. Both can be either desirable or undesirable depending upon the device and application. For purposes of low-noise amplification and upconversion parametric frequency converters are used. In downconversion applications parametric converters can be unstable and a mixer is preferred.

There are several main methods in which either effect degrades device performance. Rectification can lead to bias circuit instabilities in IMPATT oscillators[116] while parametric instabilities produced by the avalanche inductance can create spurious oscillations.[24-26] The nonlinear capacitance in Schottky-barrier mixer diodes can result in a mixer which is active[101,117] and unstable.[118] Lastly, frequency conversion in combination with correlation effects plays an important role in determining the noise performance of most junction devices.[15,24,30,101,119-128] Noise modeling techniques are discussed elsewhere.

The unified treatment of frequency conversion in junction devices presented here is developed by extending conventional Schottky-barrier mixer theory.[101] The extension either involves new junction models or the addition of a transit-time device drift region or both. The treatment of frequency conversion in the devices presented here differs from the conventional treatment in that first a general model is developed and then specific devices are discussed. The existence of an explicitly defined general mathematical framework allows for easy

direct comparison of different devices in frequency conversion applications. Such comparisons are made later.

The discussion starts by breaking the general frequency conversion problem down into manageable pieces. The modeling of these pieces (junction or injection region, drift region and the diode parasitics and embedding circuit impedance) is then described. As the specific problem of interest is downconversion the model will be applied to mixers. Procedures by which the general N frequency mixer is reduced to a two-frequency mixer (signal plus intermediate or IF) are presented. The stability of a linear two-port representation of this two-frequency mixer is discussed. Since the reduction technique can also be used to reduce a general mixer to a three-frequency mixer (signal, image, and IF), the embedding circuit impedance at the signal frequency which minimizes the conversion loss for an arbitrary image frequency impedance in the three-frequency mixer is derived.

2.2 Frequency Conversion in Two-Terminal Junction Devices

2.2.1 General Frequency Converter. The general frequency converter is illustrated in Fig. 2.1. The two-terminal device is addressed through an embedding network that presents an impedance $Z_e(\omega)$ to the diode. Two sources, a bias source and a pump source or local oscillator (LO), are applied. Determining the device response to these sources is the large-signal problem. This problem has been addressed by a variety of workers for all the devices considered and it is not treated here. However, the voltage and current waveforms associated with the nonlinearity, which are determined by the large-signal analysis, are the starting points of the small-signal analysis

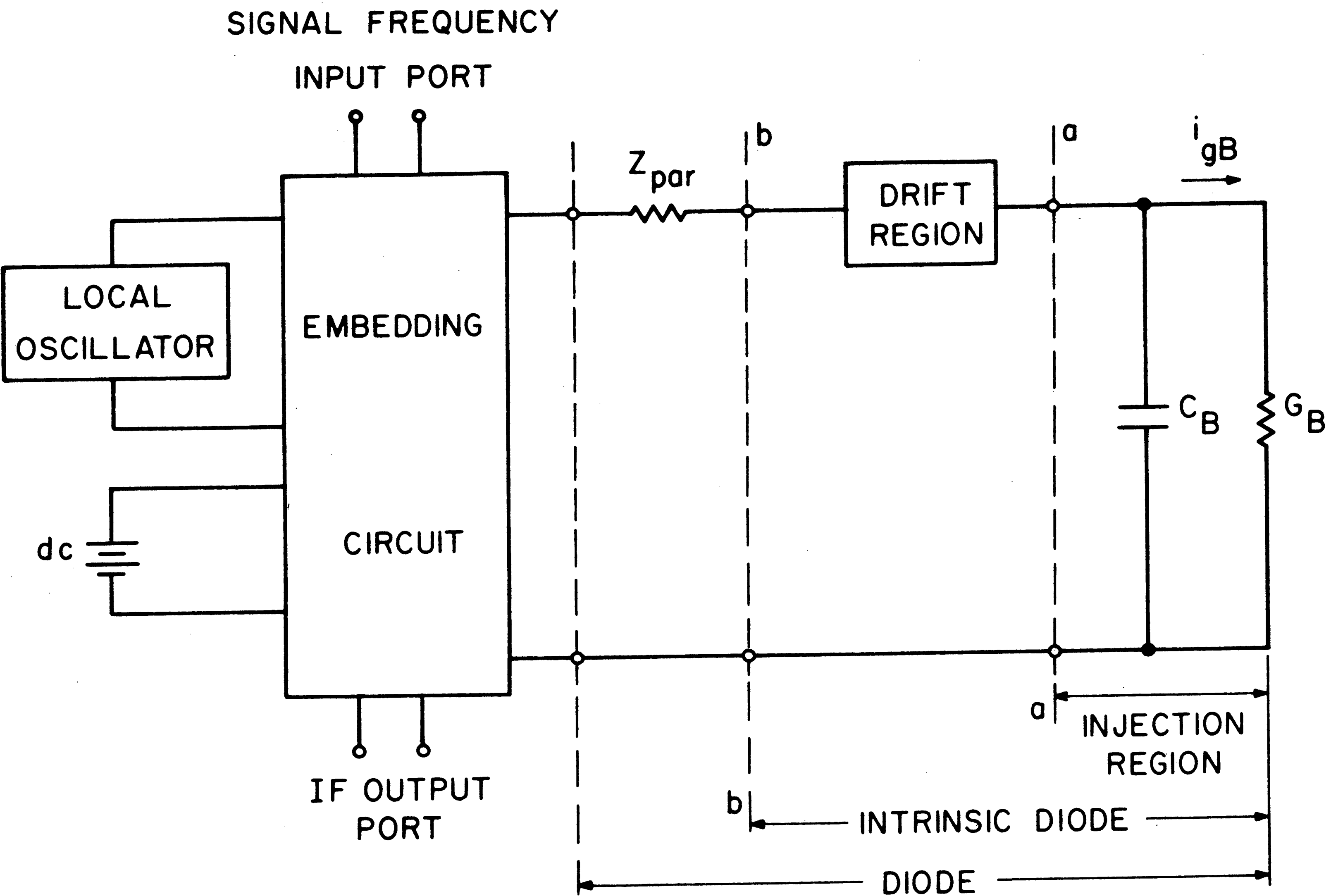

FIG. 2.1 GENERAL FREQUENCY CONVERTER.

presented. This small-signal analysis determines how power delivered at the signal port is transferred to the IF port.

In some situations the local oscillator (LO) source shown here is actually provided by the junction device itself. For devices with a negative resistance (i.e., transit-time devices and the tunnel diode) the device can be operated simultaneously as a frequency converter and as its own local oscillator. In a noise analysis the signal source is the noise generated by the diode itself.

The basic small-signal analysis is based on a division of the semiconductor device into the three regions shown in Fig. 2.1. The injection region is the junction or barrier region present in all the devices. All the devices also have some parasitics that always have a resistive component and sometimes have reactive components (either through leads, carrier inertial effects,[129,130] or skin effects*). The drift region however is present only in transit-time devices.

The small-signal analysis developed here describes how small-signal voltages at any sideband frequency are related to currents at any sideband frequency. The sideband frequencies are expressed in the notation of Saleh[131] where the mth radian sideband frequency is

$$\omega_m = \omega_o + m\omega_{LO} ,$$

where ω_o is the radian IF and ω_{LO} is the radian local oscillator frequency. When ω_m is negative the impedance used in the equations presented here is the complex conjugate of the impedance at $|\omega_m|$.

---

* Commonly the skin effect is modeled by a frequency- dependent resistance. However without a frequency-dependent reactance this is a noncausal filter as well as a simplification of electromagnetic theory.

The analysis proceeds from right to left through the circuit of Fig. 2.1. There are three major steps which are divided by the planes aa and bb. These steps correspond to the subdivision of the device. First, the vector of small-signal currents at plane aa,

$$\overline{\delta I_B} = [\ldots, \delta I_{B_1}, \delta I_{B_0}, \delta I_{B_{-1}} \ldots]^t \quad , \tag{2.1}$$

where t denotes vector transpose and subscript i denotes that the current is associated with ω_i, is related to the vector of small-signal voltages at plane aa,

$$\overline{\delta V_B} = [\ldots, \delta V_{B_1}, \delta V_{B_0}, \delta V_{B_{-1}} \ldots]^t \quad . \tag{2.2}$$

This relationship defines the injection region conversion admittance matrix $\overline{Y}_B$, i.e.,

$$\overline{\delta I_B} = \overline{Y}_B \overline{\delta V_B} \quad . \tag{2.3}$$

The inverse of $\overline{Y}_B$ is the injection region conversion impedance matrix $\overline{Z}_B$.

The next step is to describe the interrelationship of the small-signal voltages and currents at the intrinsic diode terminal plane which is plane bb. The small-signal voltage vector at the intrinsic diode terminal plane is $\overline{\delta V_{ID}}$ and the small-signal current vector is $\overline{\delta I_{ID}}$. The relationship between these two vectors is described by the intrinsic diode conversion admittance matrix $\overline{Y}_{ID}$ and its inverse, the intrinsic diode conversion impedance matrix $\overline{Z}_{ID}$. The terminology of "injection region" and "drift region" is borrowed from transit-time device analysis. For other devices the injection region terminal plane aa and the intrinsic diode terminal plane bb are coincident and $\overline{Y}_{ID} = \overline{Y}_B$.

The last step in the analysis describes the effects of the device parasitics and embedding circuit. This is done by forming the augmented network conversion impedance matrix $\bar{Z}_{aug}$. The use of this matrix, introduced by Held and Kerr,[101] is illustrated later.

In principle, the matrices and vectors defined here have an infinite number of elements. In computational practice they must be truncated, usually rather severely. For millimeter-wave devices this truncation has a physical justification. For all the devices, the injection region contains a shunt capacitance which effectively short circuits the injection region at sufficiently high frequencies.

One of the more important assumptions that is made here is that the drift region is linear and introduces no frequency conversion effects. This prevents the model from being applied to transit-time devices that exhibit either depletion-layer width modulation[45] or premature collection.[46] Although these effects are important in high-efficiency GaAs IMPATTs at microwave frequencies, they have not been reported in millimeter-wave devices. Furthermore they may take on different forms in millimeter-wave devices.[132]

<u>2.2.2 Injection Region</u>. The injection region models are shown in Fig. 2.2. For devices without injection region resonances, the circuit of Fig. 2.2a is used to model the injection region. For devices with injection region resonances, a circuit such as that of Fig. 2.2b is used. The inductance L_B is a result of the dependence of the avalanche generation rate on both the field and the carrier density.[35]

In both circuits, C_B is the injection region depletion-layer capacitance

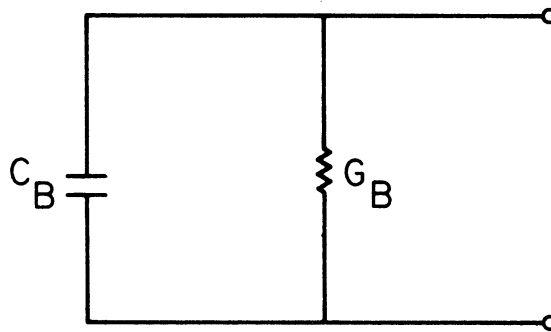

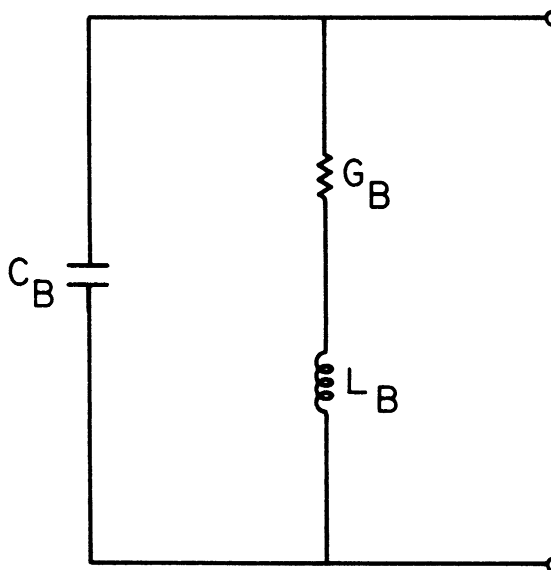

FIG. 2.2 (a) EQUIVALENT CIRCUIT FOR THE INJECTION REGION OF BARITT, TUNNETT, TUNNEL, SCHOTTKY AND MOTT DIODES (ANY DEVICE WITH NEGLIGIBLE AVALANCHING) AND (b) EQUIVALENT CIRCUIT FOR IMPATT AND MITATT DEVICE INJECTION REGIONS.

$$C_B = \frac{\varepsilon A}{x_B} , \qquad (2.4)$$

where ε is the material electrical permittivity, A is the device area, and x_B is the injection region width. In Fig. 2.2a, G_B is the differential conductivity

$$G_B = \frac{\partial I}{\partial V} , \qquad (2.5)$$

where I is the dc current and V is the dc injection region voltage. For devices with avalanche effects the parameters are developed by solving the Read equation.[24]

There is an important assumption made in Eq. 2.5. It assumes that carrier transport in the injection region is not a function of frequency. For tunneling devices this is an excellent approximation at millimeter-wave frequencies. For barrier devices it is a much poorer approximation. There has been some investigation of this problem[133,134] but to date no easily usable small-signal model and no large-signal model of any sort has been developed. There is some experimental evidence that Eq. 2.5 requires modification at high millimeter-wave frequencies in Mott barriers[110] and at infrared frequencies in Schottky devices.[135] As yet, however, neither effective models nor systematic experimental investigations are available. Therefore, Eq. 2.5 is used here.

The construction of the injection region conversion admittance matrix is based directly on the large-signal waveforms representing the time-varying capacitance $C_B(t)$ and the time-varying particle current flow. For barrier devices the particle current flows

through G_B. The mnth element of the injection region conversion admittance matrix then is[1,101,117]

$$[Y_B]_{mn} = G_{B_{m-n}} + j\omega_m C_{B_{m-n}} , \qquad (2.6)$$

where $G_{B_{m-n}}$ and $C_{B_{m-n}}$ are the mnth complex Fourier coefficients of $G_B(t)$ and $C_B(t)$.

For avalanche devices the particle current flow through the junction is modeled by the Read equation.[21,24,127,136] This equation, however, fails to accurately model GaAs IMPATTs at microwave frequencies and is qualitative at best for millimeter-wave frequencies. Numerical techniques[43,44] can be used to obtain good results at microwave frequencies in most situations. At millimeter-wave frequencies that are some problems in the basic physical model.[137,138] For any model, however, once the large-signal particle current flow through the injection region is determined, the analysis of Hines[24] (with appropriate adjustment of the sideband frequency notation) can be used to construct the injection region conversion admittance matrix.

In Read-type transit-time device structures as well as in Mott barrier devices C_B is fixed by the doping profile. Under these conditions C_B is not a function of voltage and therefore is not a function of time. The resulting conversion admittance matrix of the injection region has off-diagonal elements that are determined solely by the particle current flow. C_B is also assumed to be constant in other structures as well.

2.2.3 Drift Region. For transit-time devices the transition through the drift region to the intrinsic diode terminal plane must now be considered. This problem has been previously addressed by

Hines[24] and by McCleer.[30] The approach presented here is essentially that of McCleer[30] and differs from that of Hines mainly in the use of a more general drift region model. This drift region model is shown in Fig. 2.3. The parameters Y_D and Γ_D can be determined either by following the analysis of McCleer et al.[139] or by experimental measurements. J_p^o is the injected particle current density and J_t is the total current density.

Although the drift region model is linear it modifies the frequency conversion properties of the device. The reason for this is illustrated in Fig. 2.4. It is noted that the frequency conversion in the injection region produces additional particle currents which, in turn, control the response of the drift region. In the notation used here, the basic problem is illustrated in Fig. 2.5. The controlling equations are

$$\delta I_{B_m} = \delta I_{ID_m} = \Gamma_{D_m}(\delta I_{B_m} - j\omega_m C_B \delta V_{B_m}) + Y_{D_m}\delta V_{D_m} \tag{2.7}$$

and

$$\delta V_{ID_m} = \delta V_{D_m} + \delta V_{B_m} \quad , \tag{2.8}$$

where subscript m denotes evaluation at a sideband frequency ω_m. Combining these two equations yields

$$Y_{D_m}\delta V_{ID_m} = \delta I_{ID_m}(1 - \Gamma_{D_m}) + (Y_{D_m} + j\omega_m C_B \Gamma_{D_m})\delta V_{B_m} \quad . \tag{2.9}$$

Since the injection region is a frequency converter δV_{B_m} is related to every element of $\overline{\delta I_B}$ (or $\overline{\delta I_{ID}}$). This relationship is described by the mth row of the injection region conversion impedance matrix, i.e.,

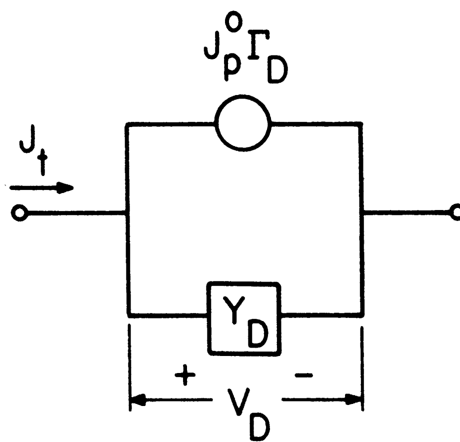

FIG. 2.3 GENERAL TRANSIT-TIME DEVICE DRIFT REGION EQUIVALENT CIRCUIT.

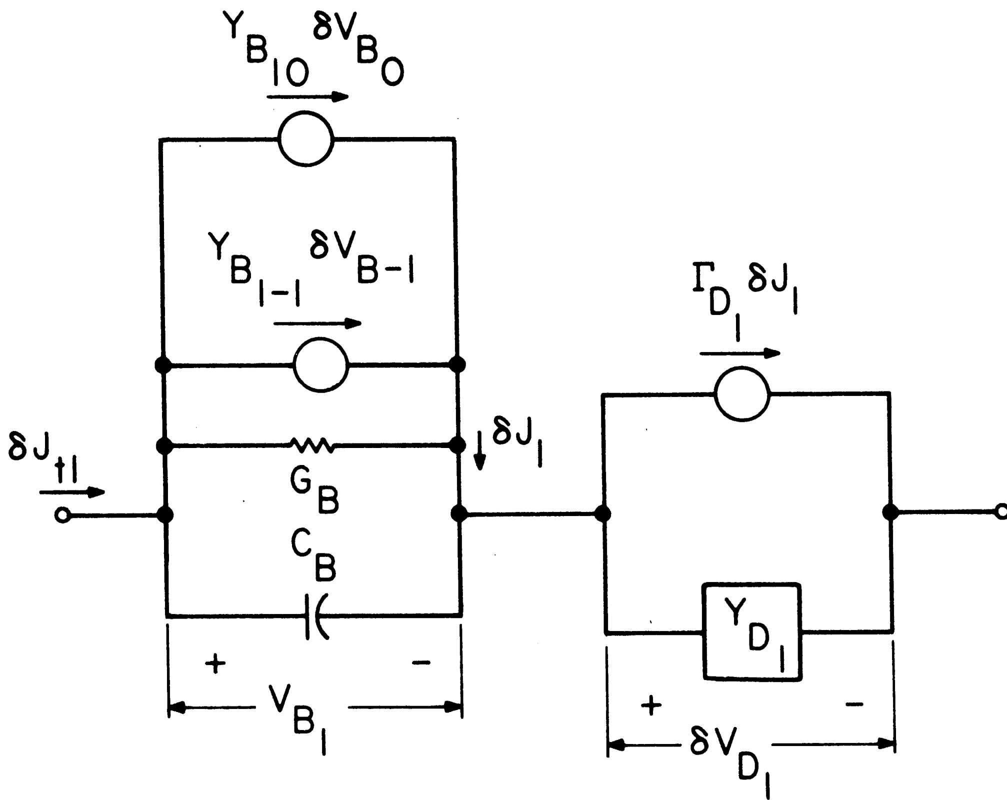

FIG. 2.4 A COMPLICATION IN TRANSIT-TIME DEVICE FREQUENCY CONVERTERS. FREQUENCY CONVERSION IN THE INJECTION REGION PRODUCES ADDITIONAL PARTICLE CURRENT AT ANY FREQUENCY OF INTEREST, FOR EXAMPLE, THE SOURCES $Y_{B_{10}} \delta V_o$ AND $Y_{B_{1-1}} \delta V_{-1}$. THIS MODIFIES THE DRIFT REGION RESPONSE EVEN THOUGH THE DRIFT REGION IS LINEAR.

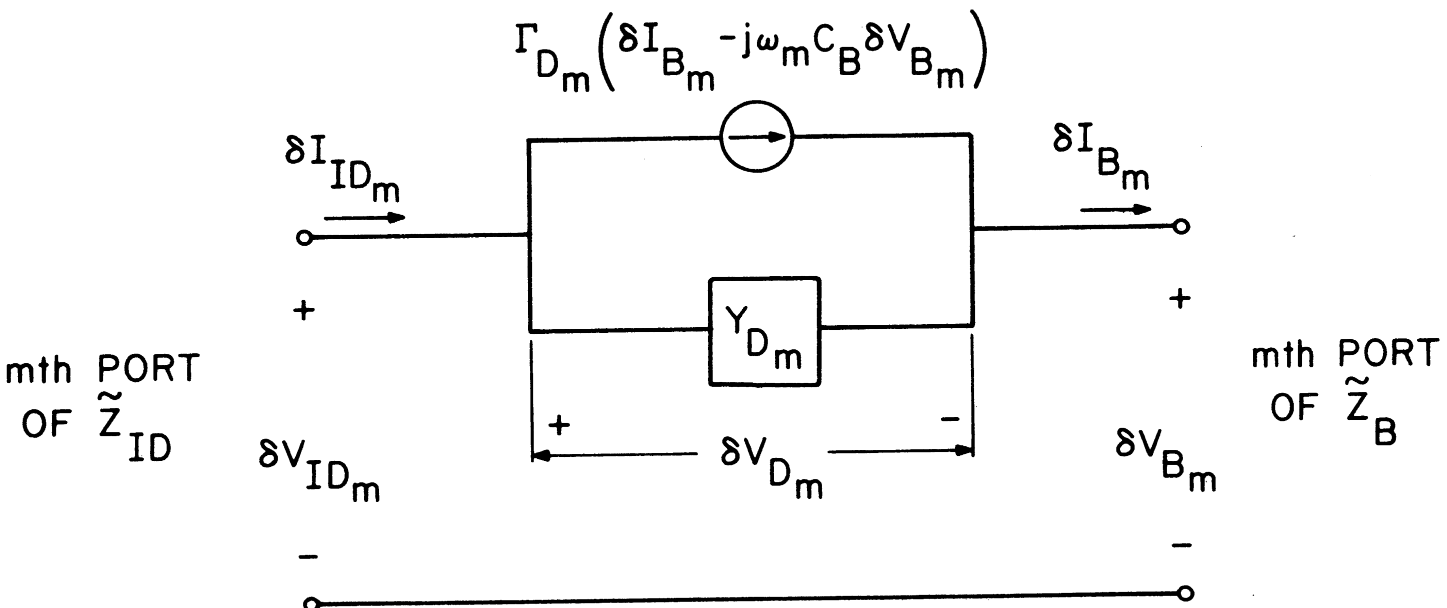

FIG. 2.5 THE EQUIVALENT CIRCUIT DESCRIBING THE TRANSFORMATION FROM THE INJECTION REGION TO THE INTRINSIC DIODE TERMINALS AT THE mth SIDEBAND FREQUENCY.

$$\delta V_{B_m} = (\text{mth row of } \overline{Z}_B)\overline{\delta I}_{ID} = \overline{Z}_{B_m} \overline{\delta I}_{ID} \quad , \tag{2.10}$$

where $\overline{Z}_{B_m}$ denotes the mth row of $\overline{Z}_B$.

Together, Eqs. 2.9 and 2.10 define the intrinsic diode conversion impedance matrix elements. These elements are

$$[\overline{Z}_{ID}]_{m,n} = (j\omega_m C_B \Gamma_{D_m} + Y_{D_m})[\overline{Z}_B]_{m,n}/Y_{D_m} \quad m \neq n \tag{2.11}$$

and

$$[\overline{Z}_{ID}]_{m,n} = \frac{1 - \Gamma_{D_m} + (j\omega_m C_B \Gamma_{D_m} + Y_{D_m})[\overline{Z}_B]_{m,n}}{Y_{D_m}} \quad . \tag{2.12}$$

Equation 2.11 shows that the presence of a drift region alters the frequency conversion properties (i.e., the off-diagonal elements of the intrinsic diode conversion impedance matrix) even in the absence of any negative-resistance effects.

2.3 Complete Frequency Converter

2.3.1 Augmented Network.

$\overline{Y}_{ID}$ and $\overline{Z}_{ID}$ describe the frequency conversion properties of the intrinsic diode. To describe the complete frequency converter the effects of the diode parasitics and the embedding circuit must also be included. This is done by forming the augmented network. The augmented network was introduced by Held and Kerr[101] and the discussion presented here follows their development, found in several sources,[101,117,140] quite closely.

The augmented network is formed by connecting the various ports of the intrinsic diode multiport in parallel with the series

combination of the diode parasitic impedance $\overline{Z}_{par}$ and the embedding circuit impedance $\overline{Z}_e$. This is illustrated in Fig. 2.6. The result is the augmented network multiport whose conversion admittance matrix is

$$\overline{Y}_{aug} = \overline{Y}_{ID} + \overline{Y}_{diag} , \qquad (2.13)$$

where $\overline{Y}_{diag}$ is a diagonal matrix whose mmth element is $[Z_{par}(\omega_m) + Z_e(\omega_m)]^{-1}$. Then $\overline{\delta I}_{aug} = \overline{Y}_{aug}\overline{\delta V}_{aug}$. The augmented network describes how the parasitics and embedding circuit affect the response of the converter to sources connected across the intrinsic diode terminal plane and, therefore, its ports are not physically accessible. However, it is simple to use the augmented network to describe both the overall frequency conversion and the noise properties of the converter. This requires describing how signals (either deterministic or noise) are transformed to the intrinsic diode terminal plane. This is a straightforward exercise.

2.3.2 Calculating Port Impedances. The augmented network is now used to produce expressions for several important mixer performance parameters. The first of these is mixer input impedance. This is the impedance presented by the total diode (intrinsic diode plus parasitics) to the embedding circuit. At sideband frequency ω_m this is[101]

$$Z_{in_m} = [\overline{Z}_{aug}; Z_{e_m} = \infty]_{mm} + Z_{par}(\omega_m) , \qquad (2.14)$$

where $[\overline{Z}_{aug}; Z_{e_m} = \infty]_{mm}$ denotes the mmth element of the augmented network formed with $Z_e(\omega_m)$ replaced by an open circuit.

It is usually possible to alter the embedding circuit impedance at the IF without altering the impedance at other frequencies. This is

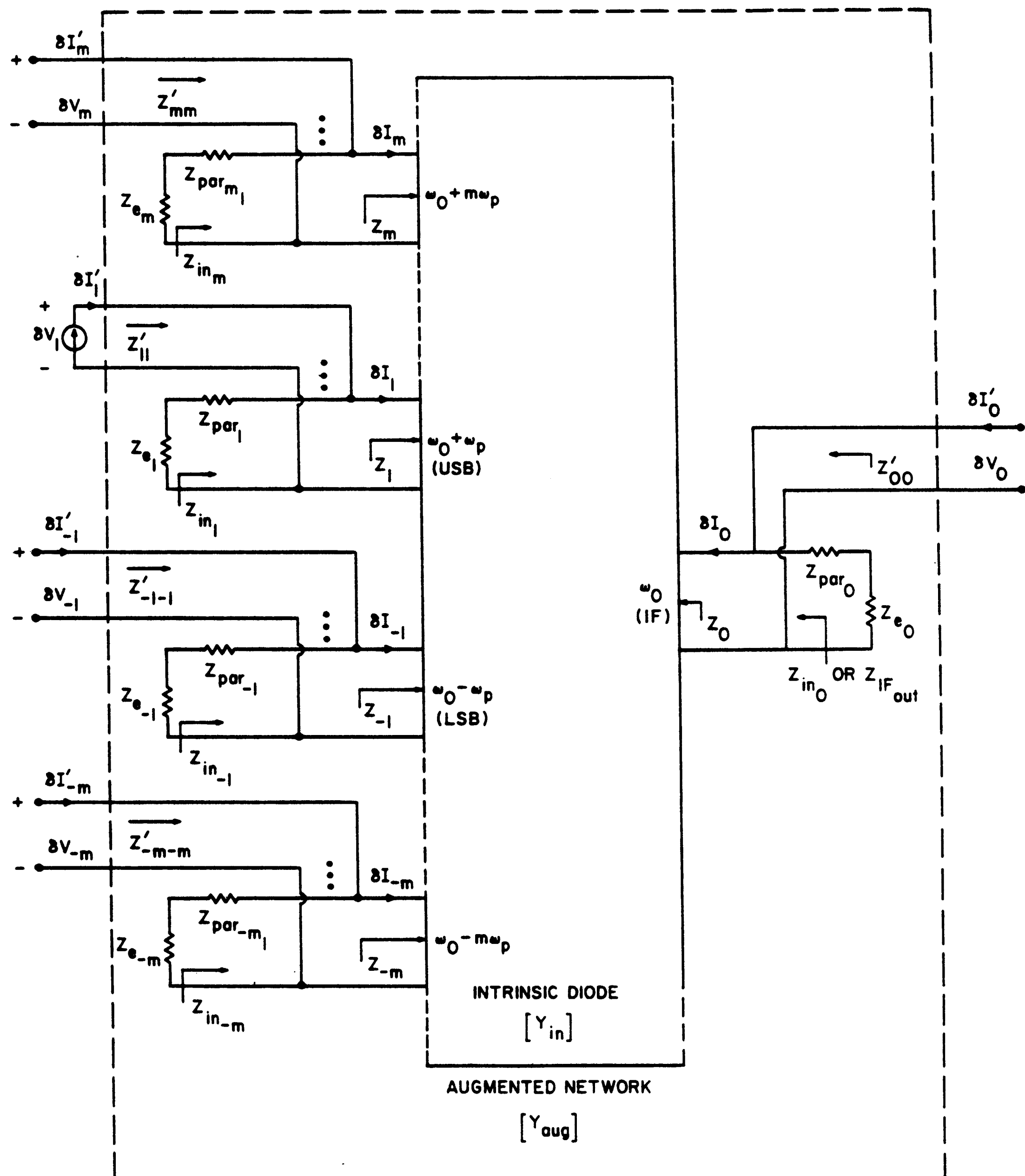

FIG. 2.6 FORMATION OF THE AUGMENTED NETWORK. HERE THE INTRINSIC DIODE CONVERSION ADMITTANCE MATRIX IS REPRESENTED AS A MULTIPORT. (SIEGEL AND KERR[117])

a result of the usually large frequency separation between the IF and the other frequencies of interest and the necessity of a physically separate IF port in a real mixer. As conversion loss is defined in terms of power transfer to the IF load (this is discussed in the next section), it is minimized by providing a conjugate match of the IF load to the mixer IF output port impedance. Such a conjugate match is sometimes assumed here. However, there are circumstances where the mixer IF output port impedance has a negative real part. Under these conditions a conjugate match is physically impossible. In Section 2.4.2 it is shown that such an output port impedance is not expected in an unconditionally stable mixer.

2.3.3 Calculating Conversion Loss. The augmented network conversion impedance can also be used to calculate the conversion loss from a signal source at sideband frequency ω_n to a load at sideband frequency ω_m. The total conversion loss is the product of the inherent conversion loss associated with the intrinsic diode (and calculated using $\overline{Z}_{aug}$) and the losses in the diode parasitics at the two sideband frequencies. These parasitic losses are

$$K_n = \frac{\text{power available from } Z_e(\omega_n)}{\text{power available from } Z_e(\omega_n) + Z_{par}(\omega_n)}$$

$$= \frac{\mathrm{Re}[Z_e(\omega_n) + Z_{par}(\omega_n)]}{\mathrm{Re}[Z_e(\omega_n)]} \quad (2.15)$$

and

$$K_m = \frac{\text{power delivered to } Z_e(\omega_m) + Z_{par}(\omega_m)}{\text{power delivered to } Z_e(\omega_m)}$$

$$= \frac{\mathrm{Re}[Z_e(\omega_m) + Z_{par}(\omega_m)]}{\mathrm{Re}[Z_e(\omega_m)]} \quad . \tag{2.16}$$

The inherent conversion loss of the intrinsic diode is

$$L_{mn}^{inh} = \frac{\text{power available from } Z_e(\omega_n) + Z_{par}(\omega_n)}{\text{power delivered to } Z_e(\omega_m) + Z_{par}(\omega_m)} \quad . \tag{2.17}$$

The power available from a current source δI_{aug_n} associated with source impedance $Z_e(\omega_n) + Z_{par}(\omega_n)$ is

$$P_{avail} = |\delta I_{aug_n}|^2 |Z_e(\omega_n) + Z_{par}(\omega_n)|^2 / \mathrm{Re}[Z_e(\omega_n) + Z_{par}(\omega_n)] \quad . \tag{2.18}$$

The power delivered to the load $Z_e(\omega_m) + Z_{par}(\omega_m)$ is

$$P_{deliv} = \frac{|[\overline{Z}_{aug}]_{mn}|^2 |\delta I_{aug_n}|^2 \mathrm{Re}[Z_e(\omega_m) + Z_{par}(\omega_m)]}{|Z_e(\omega_m) + Z_{par}(\omega_m)|^2} \quad . \tag{2.19}$$

Therefore,

$$L_{mn}^{inh} = \frac{|Z_e(\omega_m) + Z_{par}(\omega_m)|^2 |Z_e(\omega_n) + Z_{par}(\omega_n)|^2}{4|[\overline{Z}_{aug}]_{mn}|^2 \mathrm{Re}[Z_e(\omega_m) + Z_{par}(\omega_m)] \mathrm{Re}[Z_e(\omega_n) + Z_{par}(\omega_n)]} \tag{2.20}$$

and the total conversion loss is[101]

$$L_{mn} = L_{mn}^{inh} K_m K_n = \frac{|Z_e(\omega_m) + Z_{par}(\omega_m)|^2 |Z_e(\omega_n) + Z_{par}(\omega_n)|^2}{4|[\overline{Z}_{aug}]_{mn}|^2 \text{Re}[Z_e(\omega_m)]\text{Re}[Z_e(\omega_n)]} . \quad (2.21)$$

There are several reasons for defining L_{mn} for sidebands other than those associated with the actual input signal and IF. These include the possibility of modeling subharmonically pumped mixers.[115] More important for the cases considered here is the evaluation of the importance of higher-order sideband frequencies. For example, it is possible to have nearly as much power delivered to the sum sideband frequency ω_2 as there is to the image sideband frequency ω_{-1}.[101] Under these conditions it is doubtful that a simple three-frequency mixer model would accurately predict the real mixer performance. Lastly, having all the conversion losses allows a check of the mixer passivity. If

$$\sum_{m,m\neq n} L_{mn}^{-1} > 1 , \quad (2.22)$$

then the mixer delivers more small-signal power to the various loads than enters through the signal port ω_n. The mixer then is an active device. Activity can be achieved either through negative-resistance effects associated with a transit-time device or through parametric effects. This active nature can be a source of instabilities.

2.4 Upper-Sideband Downconverter

2.4.1 Reduction to a Two-Port.

In this section the basic theory for conversion loss and stability of an upper-sideband downconverter are reviewed. The first step in the analysis is to

represent the mixer as a two-frequency (signal plus IF) mixer. This is done by applying a general reduction technique described here. The most important reason for this reduction is that the two-frequency mixer is the simplest algebraic mixer model. Also this is not a bad approximation in realistic mixers. In a real mixer the physical circuit layout often fixes the higher-order sidebands while allowing some independent control of the signal and IF impedances as these two ports must be physically accessible.

The starting point in the reduction is the total diode conversion impedance matrix equation for the 2N + 1 frequency mixer

$$\overline{\delta V}_{TD} = \overline{\overline{Z}}_{TD}\overline{\delta I}_{TD} \quad . \tag{2.23}$$

The total conversion impedance matrix is then formed by adding the diode parasitic impedance to the diagonal elements of $\overline{\overline{Z}}_{ID}$:

$$[Z_{TD}]_{mn} = [Z_{ID}]_{mn} + \delta(m - n)Z_{par}(\omega_m) \quad . \tag{2.24}$$

The total diode conversion admittance matrix $\overline{\overline{Y}}_{TD}$ is then $\overline{\overline{Z}}_{TD}^{-1}$. Equation 2.23 can be rewritten for the upper-sideband downconverter as

$$\overline{\delta I}_R = \begin{bmatrix} Y_{TD_{11}} & Y_{TD_{10}} \\ Y_{TD_{01}} & Y_{TD_{00}} \end{bmatrix} \overline{\delta V}_R + \overline{A\delta V}_{ex} \quad , \tag{2.25}$$

where $\overline{\delta V}_R$ and $\overline{\delta I}_R$ are the reduced voltage and current vectors

$$\overline{\delta V}_R = [\delta V_{TD_1}, \delta V_{TD_0}]^t \tag{2.26}$$

and

$$\overline{\delta I}_R = [\delta I_{TD_1}, \delta I_{TD_o}]^t \quad , \tag{2.27}$$

and the extraneous small-signal voltage vector is

$$\overline{\delta V}_{ex} = [\delta V_{TD_N}, \ldots, \delta V_{TD_3}, \delta V_{TD_2}, \delta V_{TD_{-1}}, \delta V_{TD_{-2}}, \ldots, \delta V_{TD_{-N}}]^t \quad . \tag{2.28}$$

Matrix $\overline{A}$ is the 2 x (2N - 1) matrix

$$\overline{A} = \left[\begin{array}{cc|cc} Y_{TD_{1N}} & \ldots Y_{TD_{12}} & Y_{TD_{1-1}} & \ldots Y_{TD_{1-N}} \\ Y_{TN_{oN}} & \ldots Y_{TD_{o2}} & Y_{TD_{o-1}} & \ldots Y_{TD_{o-N}} \end{array}\right] = [\overline{A}_L \mid \overline{A}_R] \quad , \tag{2.29}$$

where the dotted line denotes the partition defining submatrices $\overline{A}_L$ and $\overline{A}_R$. The reduction is completed by the matrix equation

$$\overline{\delta I}_{ex} = \overline{B}\overline{\delta V}_R + \overline{C}\overline{\delta V}_{ex} = - \overline{Y}_e \overline{\delta V}_{ex} \quad , \tag{2.30}$$

where $\overline{B}$ is the (2N - 1) x 2 matrix

$$\overline{B} = \left[\begin{array}{cc} Y_{TD_{N1}} & Y_{TD_{No}} \\ \vdots & \vdots \\ Y_{TD_{21}} & Y_{TD_{20}} \\ \hline Y_{TD_{-11}} & Y_{TD_{-10}} \\ \vdots & \vdots \\ Y_{TD_{-N1}} & Y_{TD_{-No}} \end{array}\right] = \left[\begin{array}{c} \overline{B}_U \\ \hline \overline{B}_L \end{array}\right] \quad , \tag{2.31}$$

$\overline{C}$ is the (2N - 1) x (2N - 1) matrix

$$\overline{C} = \left[\begin{array}{ccc|ccc} Y_{TD_{NN}} & \cdots & Y_{TD_{N1}} & Y_{TD_{N-1}} & \cdots & Y_{TD_{N-N}} \\ \vdots & & \vdots & \vdots & & \vdots \\ Y_{TD_{2N}} & \cdots & Y_{TD_{22}} & Y_{TD_{2-1}} & \cdots & Y_{TD_{2-N}} \\ \hline Y_{TD_{-1N}} & \cdots & Y_{TD_{-12}} & Y_{TD_{-1-1}} & \cdots & Y_{TD_{-1-N}} \\ \vdots & & \vdots & \vdots & & \vdots \\ Y_{TD_{-NN}} & \cdots & Y_{TD_{-N2}} & Y_{TD_{-N-1}} & \cdots & Y_{TD_{-N-N}} \end{array}\right]$$

$$= \left[\begin{array}{c|c} C_{UL} & C_{UR} \\ \hline C_{LL} & C_{LR} \end{array}\right], \tag{2.32}$$

and $\overline{Y}_e$ is the diagonal embedding circuit admittance matrix at the extraneous sideband frequencies

$$\overline{Y}_e = \left[\begin{array}{ccccc|ccccc} 1/Z_e(\omega_N) & & & & & & & & & \\ & 1 & & & & & & & 0 & \\ & & \ddots & & & & & & & \\ & & & 1 & & & & & & \\ & & & & 1/Z_e(\omega_2) & & & & & \\ \hline & & & & & 1/Z_e(\omega_{-1}) & & & & \\ & & & & & & 1 & & & \\ & 0 & & & & & & \ddots & & \\ & & & & & & & & 1 & \\ & & & & & & & & & 1/Z_e(\omega_{-N}) \end{array}\right]. \tag{2.33}$$

The partitions shown correspond to the following partition of the total diode conversion admittance matrix

$$\overline{Y}_{TD} = \left[\begin{array}{c|cc|c} \overline{C}_{UR} & \multicolumn{2}{c|}{\overline{B}_U} & \overline{C}_{UR} \\ \hline & Y_{TD_{11}} & Y_{TD_{10}} & \\ \overline{A}_L & & & \overline{A}_R \\ & Y_{TD_{01}} & Y_{TD_{00}} & \\ \hline \overline{C}_{LL} & \multicolumn{2}{c|}{\overline{B}_L} & \overline{C}_{LR} \end{array}\right] . \qquad (2.34)$$

The formal solution to Eq. 2.30 is

$$\overline{\delta V}_{ex} = -(\overline{C} + \overline{Y}_e)^{-1}\overline{B}\overline{\delta V}_R \quad , \qquad (2.35)$$

where $-(\overline{C} + \overline{Y}_e)^{-1}\overline{B}$ is a (2N - 1) x 2 matrix. The solution to Eq. 2.25 is then

$$\overline{\delta I}_R = \overline{Y}_R\overline{\delta V}_R \quad , \qquad (2.36)$$

where the reduced 2 x 2 matrix is

$$\overline{Y}_R = \begin{bmatrix} Y_{TD_{11}} & Y_{TD_{10}} \\ Y_{TD_{01}} & Y_{TD_{00}} \end{bmatrix} - \overline{A}(\overline{C} + \overline{Y}_e)^{-1}\overline{B} \quad . \qquad (2.37)$$

This technique can be used to reduce any 2N + 1 frequency mixer to a two-frequency upper-sideband downconverter. It obviously can be generalized to lower-sideband downconverters and to reductions to any M frequency mixer. The method could also be applied to the intrinsic diode conversion admittance matrix alone. Here it was applied to the total diode conversion admittance to facilitate the specification

of an optimum embedding circuit impedance. This specification is the subject of the next section.

2.4.2 Optimum Three-Frequency Mixer. In this section a three-frequency mixer is discussed. The goal is the specification of the signal frequency embedding circuit impedance that minimizes the mixer conversion loss. This may not actually represent the optimal mixer design (an arbitrary image termination is assumed, for example) and will not, in general, minimize the mixer noise figure. However, it does provide a nonarbitrary method of selecting sideband impedances in a systematic comparison of various devices as mixers. For each device the results developed here can be used to choose the embedding circuit terminations that are fair in the sense that they optimize one important mixer performance measure, the conversion loss. The analysis is based on a Schottky-barrier mixer analysis provided by Peterson.[141]

The starting point is the three-frequency mixer conversion admittance equation

$$\begin{bmatrix} \delta I_1 \\ \delta I_0 \\ \delta I_{-1} \end{bmatrix} = \begin{bmatrix} Y_{11} & Y_{10} & Y_{1-1} \\ Y_{01} & Y_{00} & Y_{0-1} \\ Y_{-11} & Y_{-10} & Y_{-1-1} \end{bmatrix} \begin{bmatrix} \delta V_1 \\ \delta V_0 \\ \delta V_{-1} \end{bmatrix} , \qquad (2.38)$$

where the Y matrix can be either the result of the reduction process described in Section 2.4.1 or the total diode conversion admittance matrix. The image frequency termination Y_{L-1} is retained in the analysis although it will not be optimized. Applying the reduction technique here yields

$$\begin{bmatrix} \delta I_1 \\ \delta I_o \end{bmatrix} = \begin{bmatrix} Y'_{11} & Y'_{1o} \\ Y'_{o1} & Y'_{oo} \end{bmatrix} \begin{bmatrix} \delta V_1 \\ \delta V_o \end{bmatrix} , \qquad (2.39)$$

where

$$Y'_{11} = Y_{11} + Y_{1-1}Y_{-11}/(Y_{-1-1} + Y_{L-1}) , \qquad (2.40)$$

$$Y'_{1o} = Y_{1o} + Y_{1-1}Y_{-1o}/(Y_{-1-1} + Y_{L-1}) , \qquad (2.41)$$

$$Y'_{o1} = Y_{o1} + Y_{o-1}Y_{-11} / (Y_{-1-1} + Y_{L-1}) , \qquad (2.42)$$

and

$$Y'_{oo} = Y_{oo} + Y_{o-1}Y_{-1o}/(Y_{-1-1} + Y_{L-1}) \qquad (2.43)$$

and

$$Y_{L-1} = 1/Z_e(\omega_{-1}) \qquad (2.44)$$

is the image frequency termination.

The next step is to specify the conversion loss in terms of Eq. 2.39. The power available from the signal source shown in Fig. 2.6 is

$$P_{avail} = \frac{|I_s|^2}{4G_{L1}} , \qquad (2.45)$$

where

$$G_{L1} = \mathrm{Re}[Y_{L1}] = \mathrm{Re}[1/Z_e(\omega_1)] . \qquad (2.46)$$

The voltage δV_1 produced by I_s is

$$\delta V_1 = (\delta I_s - Y'_{1o}\delta V_o)/(Y'_{11} + Y_{L1}) \qquad (2.47)$$

and the IF load current is

$$\delta I_o = \frac{Y'_{o1}\delta I_s}{Y'_{11} + Y_{L1}} + \left(Y'_{oo} - \frac{Y'_{o1}Y'_{1o}}{Y'_{11} + Y_{L1}}\right)\delta V_o \quad . \tag{2.48}$$

The power available to the IF load is

$$P_{load} = \frac{\left|\dfrac{Y'_{o1}}{Y'_{11} + Y_{L1}}\right|^2 |I_s|^2}{4\mathrm{Re}\left(Y'_{oo} - \dfrac{Y'_{1o}Y'_{o1}}{Y'_{11} + Y_{L1}}\right)} \tag{2.49}$$

and the conversion loss is

$$L = \Big(g'_{oo}[(g_{11} + G_{L1})^2 + (b'_{11} + B_{L1})^2] - \mathrm{Re}(Y'_{1o}Y'_{o1})(g'_{11} + G_{L1})$$

$$- \mathrm{Im}(Y'_{1o}Y'_{o1})(b_{11} + B_{L1})\Big)/(G_{L1}|Y'_{o1}|^2) \quad , \tag{2.50}$$

where $Y'_{mn} = g'_{mn} + jb'_{mn}$ and $Y_{L1} = G_{L1} + jB_{L1}$.

The signal frequency embedding circuit termination that minimizes the conversion loss is defined by the solution to

$$\frac{\partial L}{\partial G_{L1}} = \frac{\partial L}{\partial B_{L1}} = 0 \quad . \tag{2.51}$$

The resulting admittance is

$$B_{L1} = \mathrm{Im}(Y'_{1o}Y'_{o1})/(2g'_{oo}) - b'_{11} \tag{2.52}$$

and

$$G_{L1} = g'_{11}\left\{1 - \frac{\mathrm{Re}(Y'_{10}Y'_{01})}{g'_{11}g'_{00}} - \frac{[\mathrm{Im}(Y'_{10}Y'_{01})]^2}{4(g'_{00}g'_{11})^2}\right\}^{1/2} \quad . \tag{2.53}$$

The minimum conversion loss is then

$$L_{min} = \frac{\mathrm{Re}(Y'_{10}Y'_{01})}{|Y'_{01}|^2}\ \frac{1+\sqrt{\ }}{1-\sqrt{\ }} + \frac{\mathrm{Im}(Y'_{10}Y'_{01})}{2g'_{00}g'_{11}}\ \frac{1}{1+\sqrt{\ }} \quad , \tag{2.54}$$

where the radical sign denotes the radical quantity in Eq. 2.53. The first term in Eq. 2.54 is analogous to the standard resistive mixer result while the second term represents a "parametric" contribution.

2.4.3 Stability of the Upper-Sideband Downconverter. The upper-sideband downconverter described by Eqs. 2.36 and 2.37 has the simple two-port equivalent circuit representation shown in Fig. 2.7. Here

$$Y_{R_{11}} = G_{11} + jB_{11} \tag{2.55}$$

and

$$Y_{R_{00}} = G_{00} + jB_{00} \quad . \tag{2.56}$$

Assessing the stability of a linear two-port is a standard exercise.[142,143] The linear two-port shown in Fig. 2.7 is unconditionally stable if all three of the following conditions are satisfied: (1) $G_{11} > 0$, (2) $G_{00} > 0$ and (3) $0 \leq C < 1$ where C is the Linvill stability factor[142]

$$C = \frac{|Y_{R_{01}}Y_{R_{10}}|}{2G_{11}G_{00} - \mathrm{Re}(Y_{R_{01}}Y_{R_{10}})} \quad . \tag{2.57}$$

The significance of condition (3) is that when it is not satisfied there exists a set of passive terminations that provide either

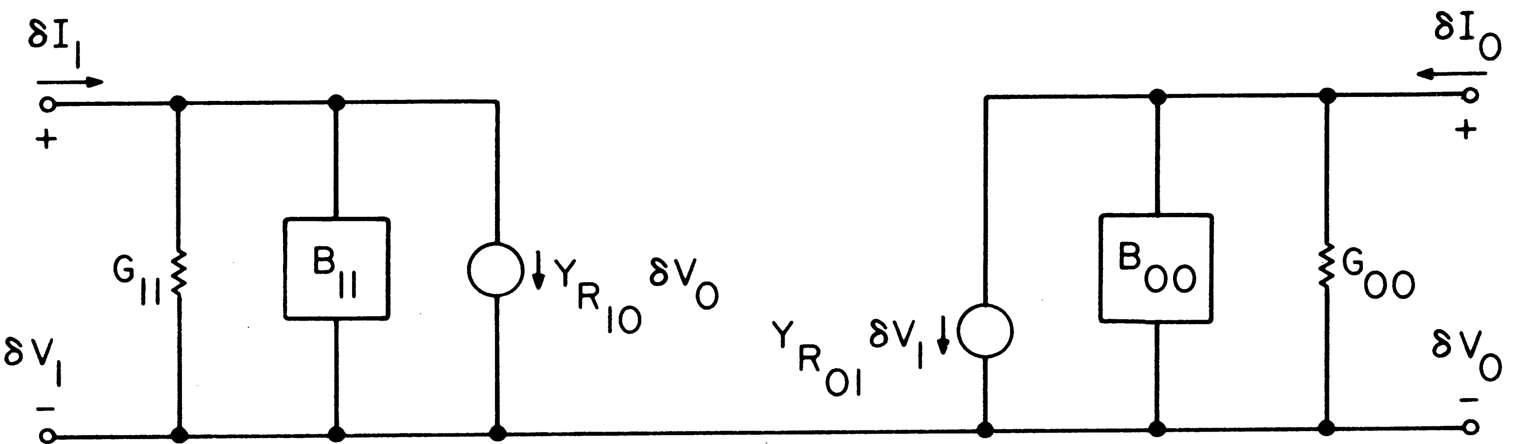

FIG. 2.7 Y PARAMETERS FOR A REDUCED FREQUENCY CONVERTER NETWORK FOR A KNOWN IMAGE TERMINATION.

a negative input conductance, a negative output conductance, or both. It should be noted that such negative conductances do not prevent frequency conversion. They can, in fact, provide conversion gain. In a passive mixer they do present worrisome instabilities.

Another situation of interest is the analysis of parametric instabilities in IMPATT diodes. A parametric instability results in a spurious amplification of noise signals. The stability analysis presented here can also be applied to this problem and is equivalent to the stability analysis of Hines.[24]

2.5 Summary

A general theory of frequency conversion in two-terminal junction semiconductor devices was presented. The analysis is applicable to Schottky, Mott, varactor, tunnel, p-n junction, BARITT, TUNNETT, MITATT and IMPATT devices. The effects of the embedding circuit and device parasitics are included.

A procedure for reducing a general N frequency mixer to an M frequency mixer was presented. This allows a standard linear two-port to be used to check the stability of the frequency converter. General criteria controlling both the real and imaginary parts of the signal frequency embedding circuit admittance for a three-frequency upper-sideband downconverter with arbitrary image termination and parametric effects were developed. These criteria minimize the conversion loss and can be easily generalized to the lower-sideband downconverter as well. In the context of the general mixer reduction procedure they should prove to be useful in practical mixer design.

CHAPTER III. NOISE CORRELATION IN TWO-TERMINAL JUNCTION DEVICES

3.1 Introduction

3.1.1 Introduction. A common element in the noise theory for two-terminal junction devices is noise correlation. The presence of correlation effects in mixers was first noted by Strutt[119] in 1946. Simple analyses were presented later for mixer tubes by van der Ziel and Watters[121] and for tunnel diode mixers by Kim.[15] In 1958 Uhlir[120] presented a general analysis of correlated shot noise in p-n junction frequency converters which was extended by Dragone[122] in 1968 to include thermal noise. Correlation effects were recently included in the BARITT diode mixer analysis by McCleer[30] and in the theory of Josephson junction mixers by Taur.[144] Standard Schottky-barrier mixer analyses, e.g., Held and Kerr,[101] include such effects as they are both experimentally observable[123] and contradict several common misconceptions concerning the interrelationship of conversion loss and noise figure.[145]

The existence of similar correlation effects in IMPATT oscillators was first noted by Sjolund.[146] The prominent role played by these effects in IMPATT oscillators was clearly demonstrated by Kuvas.[127] In a recent analysis of IMPATT oscillators and amplifiers[126] these correlation effects are modeled by a correlation matrix. Such correlation matrices were first introduced into mixer noise analysis by Dragone[122] and substantially ease the analytic formulation of the noise problem. To date, however, the basic identity of noise correlation in mixers and noise correlation in oscillators has escaped notice.

Here a unified theory of noise correlation in two-terminal junction devices is developed. First a random process, applicable to all devices, is used to demonstrate that noise correlation is expected in any junction device when it is driven by a periodic signal or pump. The correlation matrix for the injection region is then formulated. The effects of the transformation through the drift region in transit-time devices are described mathematically. It is shown that, although correlation effects in velocity fluctuation noise are conventionally neglected, such correlations are in fact expected. Expressions for mixer noise performance incorporating the resulting correlation matrices are presented. These expressions clearly show that correlation effects alter the device noise performance. Connections with the general IMPATT oscillator-amplifier noise theory of Goedbloed and Vlaardingerbroek[126] are discussed.

3.1.2 Mathematical Introduction. In this section the mathematical notation and operations used in this chapter are introduced. The statistical average, mean or expectation of a function g is denoted by the expectation operator $E[g]$. The autocovariance function of a random process $x(t)$ is defined as

$$K_X(t_1,t_2) = E\Big\{\{X(t_1) - E[X(t_1)]\}\{X(t_2) - E[X(t_2)]\}\Big\} \quad . \quad (3.1)$$

When the process is wide sense stationary (WSS) then $K_X(t_1,t_2)$ depends only on $t_2 - t_1 = \tau$:

$$K_X(t_1,t_2) = K_X(\tau) \quad . \quad (3.2)$$

For such WSS processes the spectral density of the process is defined by

$$S_X(f) = \frac{1}{2\pi} \int_{-\infty}^{\infty} K_X(\tau)\, e^{-j2\pi f\tau}\, d\tau \quad . \tag{3.3}$$

This Fourier transform exists whenever $|K_X(\tau)|$ is integrable. Unfortunately, this integral does not exist if $K_X(\tau)$ is purely periodic.

3.1.3 Origin of the Noise Correlation. In this section a brief discussion of how the periodic pumping of a mixer leads to statistical correlation between sidebands connected by harmonics at the pump frequency. Similar discussions by Kuvas[127] and Sjolund[146] fail to accurately take into account the question of integrability discussed in Section 3.1.2. However, their answer is fundamentally correct. Here the correct approach is outlined.

The starting point is a periodic noisy current

$$I(t) = A(t) \exp\,[j(\omega t + \phi(t))] \quad , \tag{3.4}$$

where $\phi(t)$ is a random phase uniformly distributed from $-\pi$ to π. $A(t)$ is a wide sense stationary process with autocovariance $K_A(\tau)$. The autocovariance of $I(t)$ is then related to $K_A(\tau)$ multiplied by some periodic function of τ. Since $K_A(\tau)$ is integrable, the spectral density of $I(t)$ will be integrable as well. The rest of the argument would proceed along lines similar to those of Kuvas[127] and Sjolund.[146] The answer will be similar to that of Kuvas which is

$$E[I(\omega_1)I(\omega_2)] = \sum_{m=-\infty}^{\infty} \delta(\omega_1 + \omega_2 - M\omega_{LO}) S_M\left(\frac{\omega_2 - \omega_1}{2}\right) \quad , \tag{3.5}$$

where S_M is the mth harmonic coefficient of the spectrum at the periodic component of $K_I(t)$.

3.2 Poisson Point Process Model of Injection Region Noise

3.2.1 Poisson Point Process. The current in the injection region of the devices of interest is a summation of the contributions of each individual charge carrier as the carrier transits the injection region. The noise results from statistical variations in the rate at which carriers transit the injection region. An appropriate model of this process is the filtered Poisson point process[147]

$$I(t) = \sum_{n=1}^{N(t)} h(t - \tau_n) . \tag{3.6}$$

In Eq. 3.6 $I(t)$ is the current and $N(t)$ is the total number of carriers that have been injected into or transited the injection region since t_o, the point in time at which the diode was turned on. $N(t)$ is a random variable called the counting variable. For a Poisson point process $N(t)$ satisfies

1. $$\Pr[N(t_o) = 0] = 1 . \tag{3.7}$$
2. $$\Pr[N(t) - N(s) = n] = \frac{1}{n!}[\Lambda(t) - \Lambda(s)]^n \exp\{-[\Lambda(t) - \Lambda(s)]\} . \tag{3.8}$$

3. $N(t)$ has independent increments, i.e., the number of points in any set of nonoverlapping intervals are statistically independent. The points counted by the counting variable $N(t)$ are carriers crossing the injection region. Property (2) states that the number of points in any interval is Poisson distributed and therefore is responsible for the nomenclature "Poisson point process." The parameter function $\Lambda(t)$ in Eq. 3.8 need only be nonnegative and nondecreasing. It does not need to be either continuous or differentiable. Here, however, it is useful to assume that

$$\Lambda(t) = \int_{t_o}^{t} \lambda(s)\, ds , \tag{3.9}$$

where $\lambda(s)$ is a nonnegative function of time called the intensity function. The intensity function is the instantaneous average rate at which points occur, i.e., carriers enter the injection region.

The only parameter not yet defined in Eq. 3.6 is $h(t - \tau_n)$. τ_n is the time at which the nth carrier transited the injection region. $h(t - \tau_n)$ is the filter impulse response function. It satisfies all the properties of a causal linear time invariant filter response function. In particular,

$$h(t - \tau_n) = 0 \quad , \quad t < \tau_n \tag{3.10}$$

and

$$\int_0^\infty h(s)\, ds = q \quad , \tag{3.11}$$

where q is the charge of the carrier. Although here $h(t - \tau_n)$ is assumed to be a delta function, the effects of a nonzero injection region transit-time can be included by using a nondelta function form for h(s).

Snyder[147] shows that the autocovariance of I(t) is

$$K_I(t_1,t_2) = \int_{t_o}^{\min(t_1,t_2)} \lambda(\tau)\, E[h(t_1 - \tau)h(t_2 - \tau)]\, d\tau \quad . \tag{3.12}$$

For the deterministic delta type-h functions used here

$$K_I(t_1,t_2) = \int_{t_o}^{\min(t_1,t_2)} \lambda(\tau)q^2 \delta(t_1 - \tau)\delta(t_2 - \tau)\, d\tau = q^2\lambda[\min(t_1,t_2)] \quad . \tag{3.13}$$

If $t_2 = t_1 + \tau$, then

$$K_I(t_1,t_1 + \tau) = \begin{cases} q^2\lambda(t_1) \quad , & \tau \geqq 0 \\ q^2\lambda(t_1 + \tau) \quad , & \tau < 0 \end{cases} \quad . \tag{3.14}$$

If $\lambda(s)$ is periodic then $K_I(t_1,t_1 + \tau)$ will also be periodic. Therefore, if the instantaneous rate at which carriers transit the injection region is periodic, i.e., the current is periodic, $K_I(t_1,t_1 + \tau)$ is also periodic in the absolute time t_1 and noise correlation is expected.

3.2.2 Connection with Deterministic Injection Region Models. The expected value of I(t) is[147]

$$E[I(t)] = \int_{t_o}^{t} \lambda(s)E[h(t - s)]\, ds \quad . \tag{3.15}$$

For deterministic delta h functions

$$E[I(t)] = q\lambda(t) \quad . \tag{3.16}$$

Since the deterministic models of I(t) typically used to determine the injection region behavior actually predict E[I(t)], they can be used in conjunction with Eq. 3.16 to determine $\lambda(t)$.

When the cases of periodic $\lambda(t)$ are considered, Eqs. 3.13 and 3.16 lead to the result

$$K_I(t_1,t_1 + \tau) = \begin{cases} qI(t_1) \quad , & \tau \geq 0 \\ qI(t_1 + \tau) \quad , & \tau < 0 \end{cases} \tag{3.17}$$

and, therefore, the Fourier expansion of K_I with respect to t_1 is q times the Fourier expansion of I(t). Equation 3.5 becomes

$$E[I(\omega_1)I(\omega_2)] = q \sum_m \delta(\omega_1 + \omega_2 - m\omega_{LO})I_m[(1/2)(\omega_2 - \omega_1)] \quad , \tag{3.18}$$

where I_m is the mth Fourier coefficient of I(t).

3.3 Correlation Matrix

3.3.1 Injection Region Correlation Matrix. In Eq. 3.18 it was found that the correlation between two frequencies ω_1 and $\omega_1 + m\omega_{LO}$ in an injection region pumped by a periodic current I(t) with radian frequency ω_{LO} is proportional to the mth Fourier coefficient of I(t). A useful tool developed in mixer theory[101] for the analysis of this situation is the correlation matrix. The mnth element of the correlation matrix is

$$[COR]_{mn} = E[I(\omega_m)I(\omega_n)] = 2qI_{m-n} , \quad (3.19)$$

where I_{m-n} is the mnth Fourier coefficient of the injection region particle current. The remainder of the discussion here illustrates how the drift region of a transit-time device is incorporated into the correlation matrix and how the correlation matrix is used in calculations.

3.3.2 Drift Region and Noise Correlation Matrix. The equivalent circuit of Fig. 2.3 is used to study the effect of the transit-time device drift region on the noise correlation matrix. Γ_d and Y_d can still be produced using either the calculation of McCleer et al.[139] or by experiment. J_p^o is replaced by δI_{Bp}, the particle current injected into the drift region from the injection region. It is assumed to be related to the total current δI_B, the noise current δI_s, and the voltage δV_B across the injection region by

$$\overline{\delta I}_{Bp} = \overline{\delta I}_B - \overline{\delta I}_s - j\omega C_B \overline{\delta V}_B , \quad (3.20)$$

where the bars indicate vectors of small-signal quantities defined at each sideband of interest. C_B is the depletion-layer capacitance

of the injection region. At the kth sideband

$$\delta I_{Bp_K} = \delta I_{B_K} - \delta I_{s_K} - j\omega_K C_B \delta V_{B_K} \quad . \tag{3.21}$$

The problem of interest is illustrated in Fig. 3.1. The equations describing Fig. 3.1 under short-circuit noise analysis conditions are

$$\delta I_{ID_K} + \delta I_{s_K} = \delta I_{B_K} \quad , \tag{3.22}$$

$$\delta V_{ID_K} = \delta V_{D_K} + \delta V_{B_K} \quad , \tag{3.23}$$

and

$$\delta I_{ID_K} = \Gamma_{D_K}(\delta I_{B_K} - \delta I_{s_K} - j\omega_K C_B \delta V_{B_K}) + Y_{D_K} \delta V_{D_K} \quad . \tag{3.24}$$

Combining Eqs. 3.23 and 3.24 gives

$$\delta I_{ID_K} = \Gamma_{D_K} \delta I_{B_K} - \Gamma_{D_K} \delta I_{s_K} + j\omega_K C_B \Gamma_{D_K} \delta V_{D_K} + Y_{D_K} \delta V_{D_K} \quad , \tag{3.25}$$

$$\delta V_{D_K} = \frac{\delta I_{ID_K} - \Gamma_{D_K}(\delta I_{B_K} - \delta I_{s_K})}{Y_{D_K} + j\omega_K C_B \Gamma_{D_K}} \tag{3.26}$$

or, in vector form,

$$\overline{\delta V}_D = \overline{Z}_{D1} \overline{\delta I}_{ID} + \overline{Z}_{D2}(\overline{\delta I}_B - \overline{\delta I}_s) \quad , \tag{3.27}$$

where $\overline{Z}_{D1}$ and $\overline{Z}_{D2}$ are diagonal matrices. Their elements are

$$[\overline{Z}_{D1}]_{KK} = \frac{1}{Y_{D_K} + j\omega_K C_B \Gamma_{D_K}} \tag{3.28}$$

and

$$[\overline{Z}_{D2}]_{KK} = -\Gamma_{D_K}[Z_{D1}]_{KK} \quad . \tag{3.29}$$

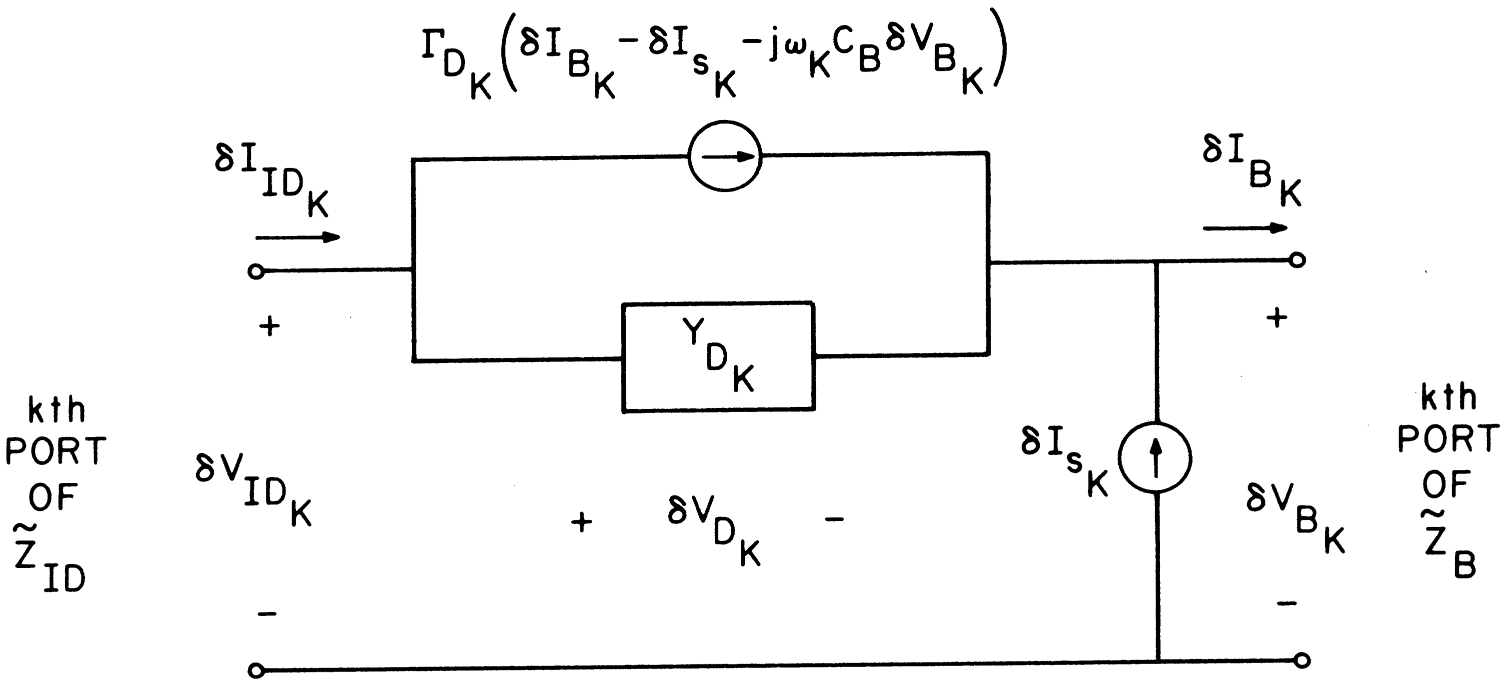

FIG. 3.1 EQUIVALENT CIRCUIT FOR THE TRANSFORMATION OF THE INJECTION REGION NOISE CURRENT SOURCE TO THE INTRINSIC DIODE TERMINAL PLANE AT THE kth SIDEBAND FREQUENCY.

Equation 3.27 is the last tool needed to solve the fundamental problem of this section which is to find the intrinsic diode noise current due to injection region noise currents and to describe the correlation matrix for this intrinsic diode noise current. In equivalent circuit form the problem is to transform the circuit of Fig. 3.2 to the circuit of Fig. 3.3. The defining equations are

$$\overline{\delta I}_{ID} + \overline{\delta I}_{s} = \overline{\delta I}_{B} \quad , \tag{3.30}$$

$$\overline{\delta V}_{B} = \overline{Z}_{B}\overline{\delta I}_{B} \quad , \tag{3.31}$$

$$\overline{\delta V}_{ID} = \overline{Z}_{ID}\overline{\delta I}_{ID} \quad , \tag{3.32}$$

$$\overline{\delta V}_{ID} = 0 = \overline{\delta V}_{D} + \overline{\delta V}_{B} \tag{3.33}$$

and Eq. 3.27. Here $\overline{Z}_B$ is the injection region conversion impedance and $\overline{Z}_{ID}$ is the intrinsic diode conversion impedance matrix. Both $\overline{Z}_B$ and $\overline{Z}_{ID}$ are defined in Chapter II.

Combining Eqs. 3.27, 3.30 and 3.31 yields

$$\overline{Z}_{ID}\overline{\delta I}_{ID} = \overline{Z}_{B}\overline{\delta I}_{B} + \overline{Z}_{D1}\overline{\delta I}_{ID} + \overline{Z}_{D2}\overline{\delta I}_{B} - \overline{Z}_{D2}\overline{\delta I}_{s} \tag{3.34}$$

or

$$(\overline{Z}_{ID} - \overline{Z}_{D1})\overline{\delta I}_{ID} = (\overline{Z}_{B} + \overline{Z}_{D2})\overline{\delta I}_{B} - \overline{Z}_{D2}\delta\overline{I}_{s} \quad . \tag{3.35}$$

The $\overline{\delta I}_B$ can be eliminated using Eq. 3.30 to obtain

$$(\overline{Z}_{ID} - \overline{Z}_{D1} - \overline{Z}_{B} - \overline{Z}_{D2})\overline{\delta I}_{ID} = \overline{Z}_{B}\overline{\delta I}_{s} \quad . \tag{3.36}$$

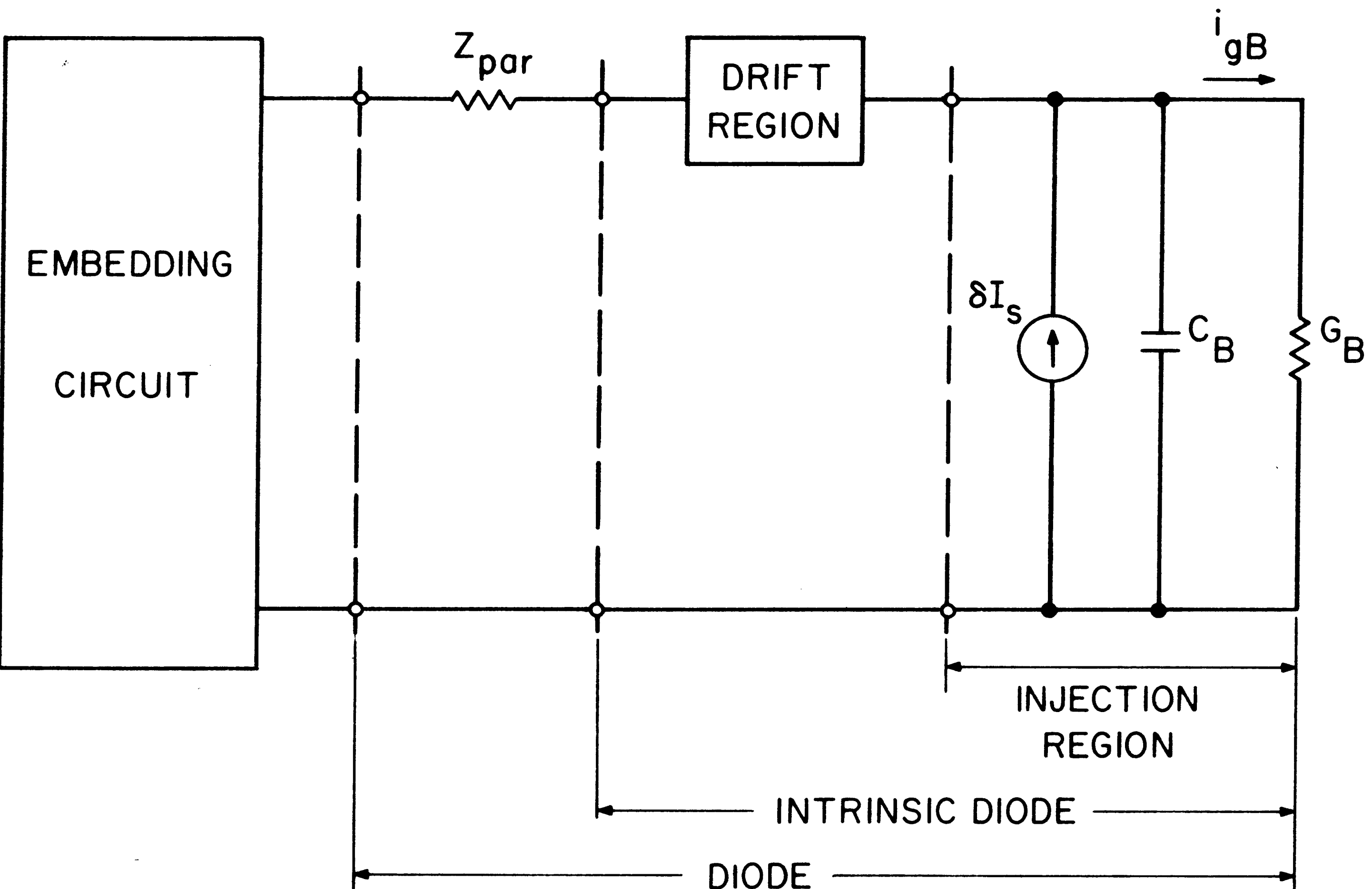

FIG. 3.2 INJECTION REGION NOISE IN THE MIXER PRIOR TO ITS TRANSFORMATION TO THE INTRINSIC DIODE TERMINAL PLANE.

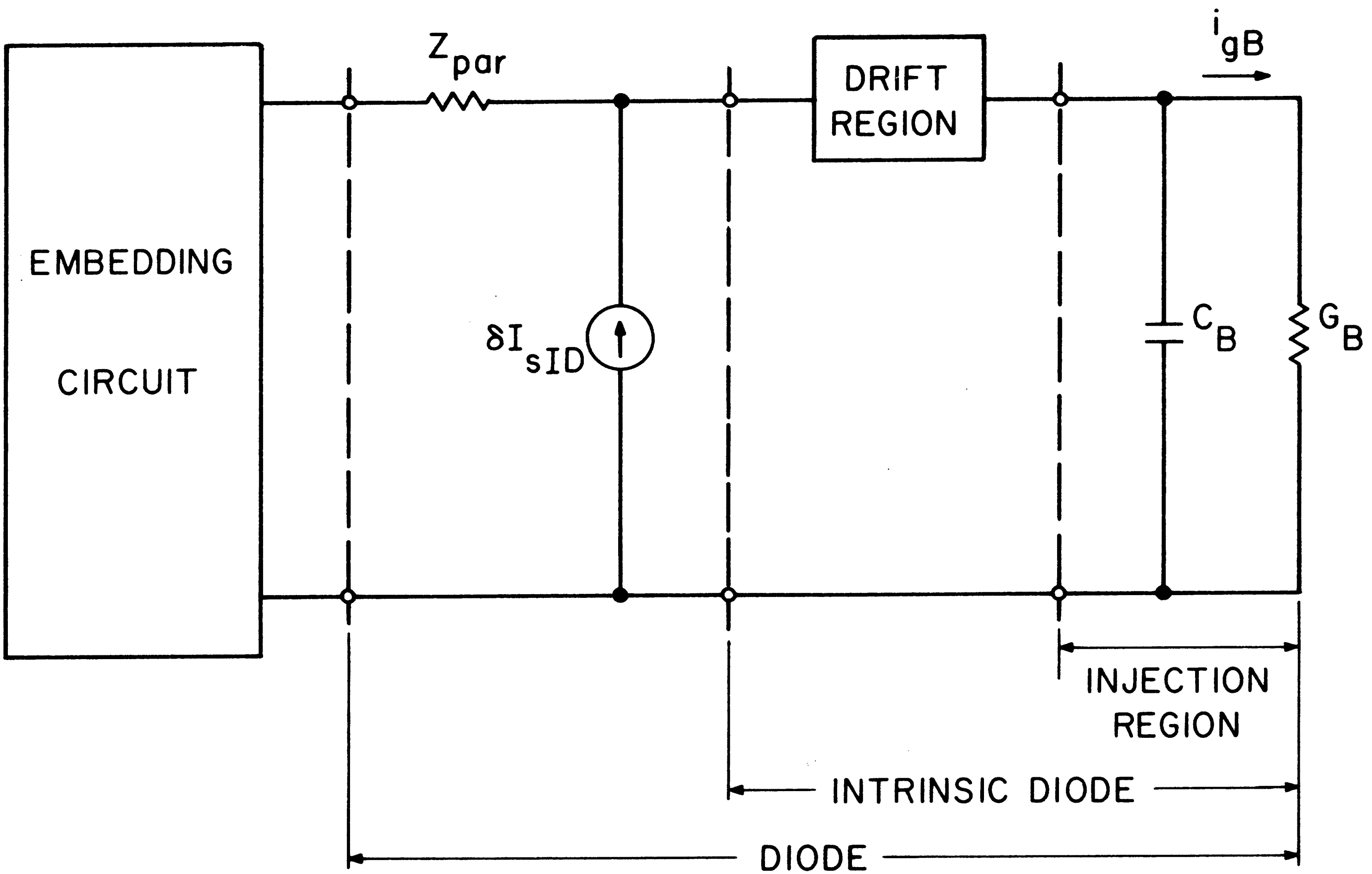

FIG. 3.3 INJECTION REGION NOISE CURRENT IN THE MIXER AFTER ITS TRANSFORMATION TO THE INTRINSIC DIODE TERMINAL PLANE.

The intermediate intrinsic diode noise matrix is defined as

$$\overline{H}_{sID} = (\overline{Z}_{ID} - \overline{Z}_{D1} - \overline{Z}_{B} - \overline{Z}_{D2})^{-1}\overline{Z}_{B} \quad . \qquad (3.37)$$

The intrinsic diode noise current shown in Fig. 3.4 is

$$\overline{\delta I}_{ID} = \overline{H}_{sID}\overline{\delta I}_{s} = \overline{\delta I}_{sID} \quad . \qquad (3.38)$$

Having found the intrinsic diode noise current, the last step is to describe its correlation. The matrix element needed is

$$[\overline{COR}_{ID}]_{KJ} = E[\delta I_{sID_K} \delta I^*_{sID_J}] \quad , \qquad (3.39)$$

where $\overline{COR}_{ID}$ is the intrinsic diode noise correlation matrix. When Eq. 3.38 is used the intrinsic diode noise current can be related to the injection region noise currents by

$$\delta I_{sID_K} \delta I^*_{sID_J} = \overline{H}_{sID_K}\overline{\delta I}_{s}(\overline{H}_{sID_J}\overline{\delta I}_{s})^* = \overline{H}_{sID_K}(\overline{\delta I}_{s}\overline{\delta I}^{\psi}_{s})\overline{H}^{\psi}_{sID_J} \quad , \qquad (3.40)$$

where $\overline{H}_{sID_J}$ denotes the Jth row of $\overline{H}_{sID}$ and ψ denotes conjugate transpose. The interior portion of Eq. 3.40 is the injection region noise correlation matrix. Therefore, the intrinsic diode noise correlation matrix is

$$[COR_{ID}]_{K,J} = \overline{H}_{sID_K}[\overline{COR}]_{KJ}\overline{H}^{\psi}_{sID_J} \quad . \qquad (3.41)$$

3.3.3 Velocity Fluctuation and Thermal Noise. There are additional sources of noise in these devices. Two of them, thermal noise and velocity fluctuation noise, are considered here.

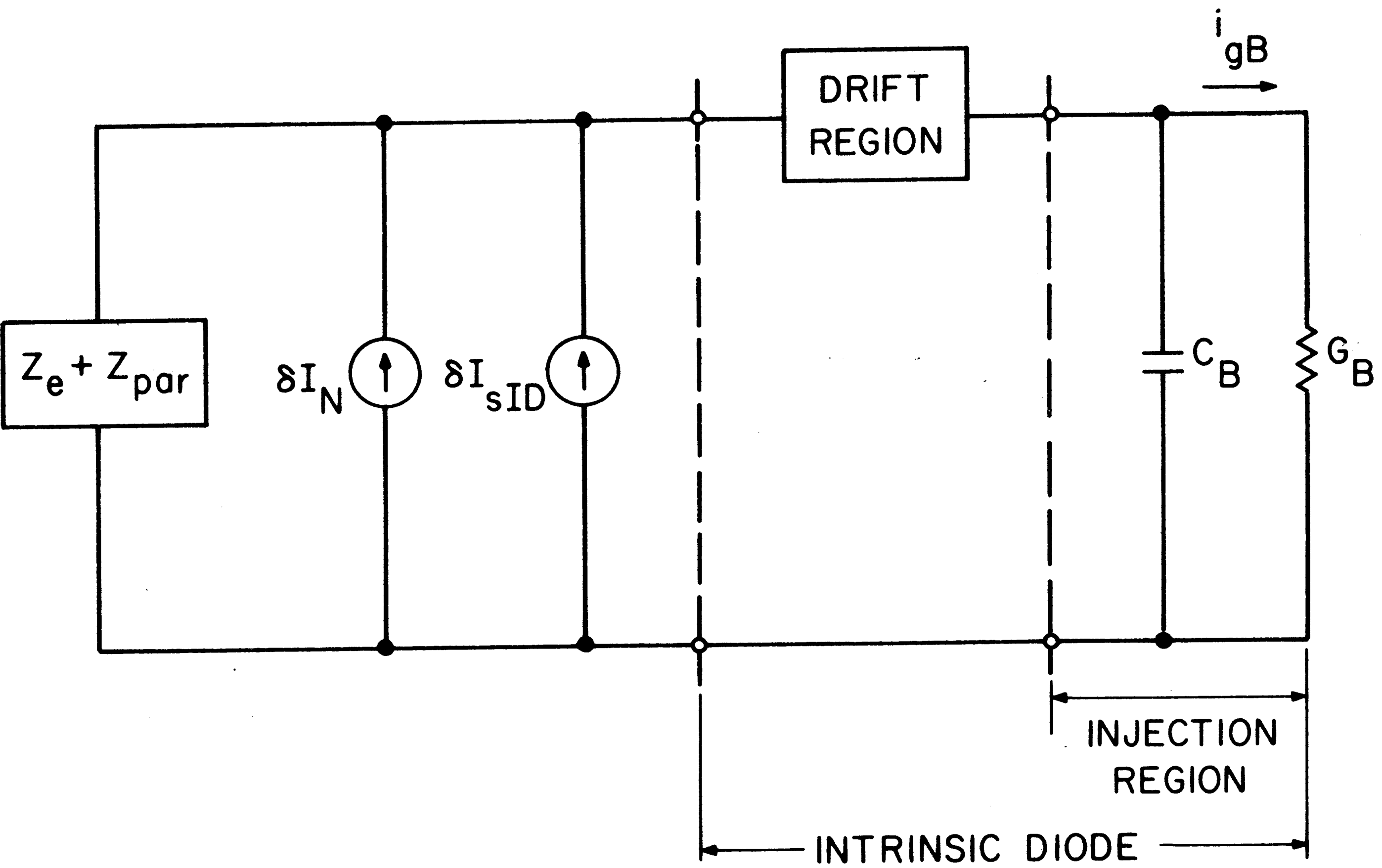

FIG. 3.4 THERMAL AND VELOCITY FLUCTUATION NOISE CURRENT SOURCES COMBINED INTO THE NOISE CURRENT SOURCE δI_N. THE PROBLEM IS NOW READY FOR SOLUTION USING THE CORRELATION MATRICES AND THE AUGMENTED NETWORK CONVERSION IMPEDANCE MATRIX.

Thermal noise is the noise from the real part of an impedance in thermal equilibrium with its surroundings. The words "thermal equilibrium" are underlined because the devices considered here are rarely in equilibrium with their surroundings. As a result some of the parasitic impedances may also be in a state of thermal inequilibrium and the actual noise power delivered by such a parasitic impedance to the intrinsic diode may differ from the thermal noise level. Some evidence for this was reported in millimeter-wave mixers.[101,106] Here, however, it is always assumed that the parasitics are in equilibrium and can be modeled by thermal noise. The embedding circuit is also assumed to be in equilibrium, and it is further assumed that the parasitic impedance is not pumped. For example, the effects of depletion-layer width modulation and velocity saturation are neglected in calculating the series resistance of a Schottky barrier. Under this unpumped condition the thermal noise contains no correlated sideband structure (provided the temperature is constant) and is modeled as an addition to the main diagonal of the correlation matrix.

One example of nonequilibrium noise is velocity fluctuation noise. This is the noise due to scattering induced random fluctuations in the carrier velocity. Since the same velocity fluctuations are also the physical source of diffusion currents, velocity fluctuation noise is closely related to diffusion and its dc spectral power density is proportional to the diffusion coefficient.[148,149] This proportionality, when used in conjunction with the Einstein relation, leads to the equivalence of velocity fluctuation noise and thermal noise in the limit of thermal equilibrium. It also allows noise measurements to be used to determine diffusion coefficients[149] and underlies a common

nomenclature in which velocity fluctuation noise is called diffusion noise. (It should be noted, however, that velocity fluctuation noise is present in the absence of diffusion current.[150]) Velocity fluctuation noise is also sometimes called hot carrier noise. This name reflects the role played by the heating of the carriers with respect to the crystal lattice.

In a previous analysis of transit-time device mixers McCleer[30] treated velocity fluctuation noise as being uncorrelated. Under these conditions it, like thermal noise, contributes only to the main diagonal of the correlation matrix. This assumption is also made here for two reasons. First, it corresponds to the small-signal model of the drift region being used in the frequency conversion and injection region noise calculations. Second, and more importantly, there are no expressions available for the off-diagonal elements of a velocity fluctuation noise matrix.

It is not difficult, however, to show that in a pumped drift region, i.e., a periodic field, velocity fluctuation noise is expected to have correlation structure. The following random flight process is considered:

$$v(t) = v_o + \sum_{i=0}^{N(t)} \Delta v_i \quad . \tag{3.42}$$

Here v_o is the initial carrier velocity at time t_o, $N(t)$ is some counting random variable, and Δv_i is the total change in velocity as a result of the ith flight. Δv_i has two components. One is the random change due to scattering at the end of the flight. Since the scattering rates are determined by the instantaneous velocity the scattering

component of Δv_i will be periodic when the instantaneous average velocity is periodic. This happens when the field is periodic.[98,130] The second component of Δv_i is the field acceleration during the flight. When the field is periodic this component will be periodic also.

If Δv_i is periodic and if N(t) is a Poisson process with a constant rate parameter, Eq. 3.12 clearly shows that the autocovariance of v(t) is periodic and therefore correlation structure will be present. In fact, in all Monte Carlo programs the model actually implemented is an expanded version of Eq. 3.42 (v_o and Δv_i become vectors with additional components representing energy and valley) with a Poisson distributed N(t) that has a constant rate parameter. This results from the use of the self-scattering mechanism of Rees.[151] Self-scattering is a fictitious scattering mechanism in which the carrier state is left totally unchanged. It, therefore, has no effect on carrier transport. However, by properly specifying its rate as a function of electronic wave vector the "total" scattering rate (real scattering plus self-scattering) becomes constant over wave vector. When the total scattering rate is constant the flight duration between scatterings is an exponentially distributed random variable. Self-scattering is used in Monte Carlo programs because it is less expensive to compute this exponentially distributed flight duration than the real flight duration between real scattering events. In spite of this great simplification self-scattering is rarely used in analytical transport models. Here, since any point process in which the distance between points (the interarrival time) is exponentially distributed is a Poisson process, employing self-scattering in the analytic model allows a well-understood random process to be used as the basic model. One obvious conclusion of such an analysis is

that velocity fluctuation noise in the presence of a periodically varying field is expected to have correlated sideband structure.

3.4 Applications of Correlation Matrices

3.4.1 Applications in Mixers. In Chapter II it was shown that, for the devices of interest here, the basic mixer problem could be characterized by the augmented network conversion impedance matrix $\overline{Z}_{aug}$. This matrix described how small-signal voltages and currents at the intrinsic diode terminals are controlled by the intrinsic diode, its parasitics, and the embedding circuit. To use it in a noise analysis the noise currents at the intrinsic diode terminals and their correlation properties must be described. These properties are already described by $\overline{COR}_{ID}$ for the noise produced in the injection region. Additional contributions from thermal and velocity fluctuation noise must also be considered.

The starting point is the circuit shown in Fig. 3.5. Both the thermal noise and velocity fluctuation noise are characterized by equivalent noise voltage sources. These sources are transformed into current sources (Fig. 3.4) by a Thevenin-to-Norton transformation where the source impedance is assumed to be the diode parasitic impedance connected in series with the embedding circuit impedance. The equivalent noise source then is

$$\delta I_N^2 = \delta I_{ID}^2 + \frac{\overline{\delta V_T^2} + \overline{\delta V_{VF}^2}}{|Z_{e_m} + R_{s_m}|^2} \quad , \quad m \neq 0 \tag{3.43}$$

and

$$\delta I_N^2 = \delta I_{ID}^2 + (\overline{\delta V_T^2} + \overline{\delta V_{IF}^2})/|Z_{e_o} - R_{s_o}|^2 \quad , \tag{3.44}$$

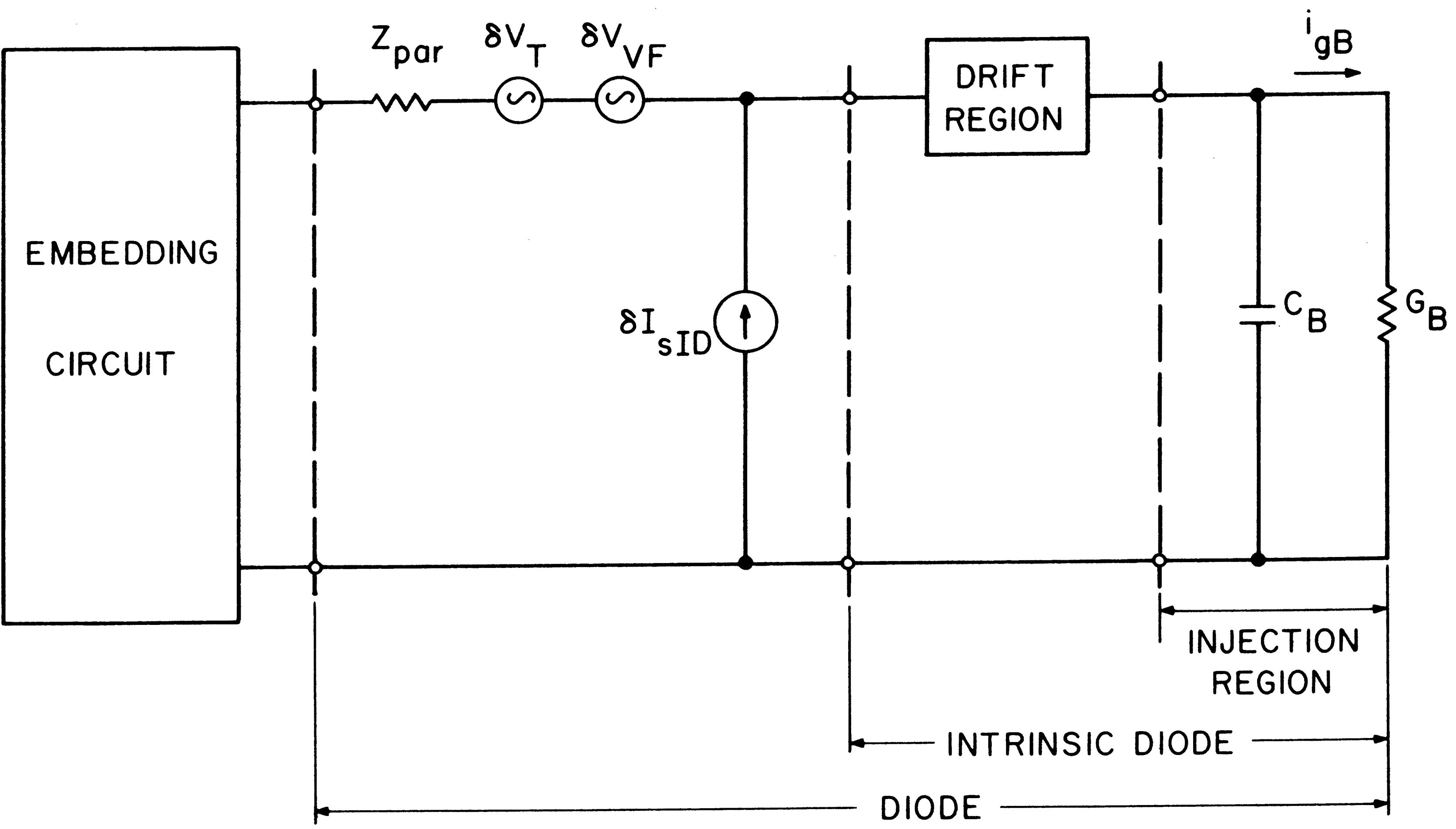

FIG. 3.5 THERMAL AND VELOCITY FLUCTUATION EQUIVALENT NOISE VOLTAGE SOURCES IN THE MIXER.

where the mean square noise voltage for the thermal noise is

$$\overline{\delta V_T^2} = 4kTR_{s_m} \Delta f \quad , \tag{3.45}$$

$R_{s_m} = \mathrm{Re}[Z_{par}(\omega_m)]$ and $Z_{e_m} = Z_e(\omega_m)$. Δf is the measurement bandwidth and k is Boltzmann's constant. The mean square noise voltage for velocity fluctuation noise is described in Chapter IV. It is noted that the expression for the noise voltage at the IF differs from the other sidebands. This is because the noise properties of a mixer are determined by the noise power delivered to the IF load.[101,117] It is also assumed that the injection region noise source, the thermal noise source, and the velocity fluctuation noise source are all mutually uncorrelated.

The output noise voltage at the IF port is

$$\delta V_{N_o} = \overline{Z}_{aug_o} \overline{\delta I_N} \quad , \tag{3.46}$$

where $\overline{Z}_{aug_o}$ is the zeroth row of $\overline{Z}_{aug}$. The mean square noise voltage at the IF port is

$$\overline{\delta V_{N_o}^2} = E[\delta V_N \delta V_N^*] = E[(\overline{Z}_{aug_o} \overline{\delta I_N})(\overline{Z}_{aug_o} \delta I_N)^*] = \overline{Z}_{aug_o} \overline{COR}_{ID} \overline{Z}^{\psi}_{aug_o} \quad , \tag{3.47}$$

where $\overline{COR}_{ID}$ contains the contributions of thermal and velocity fluctuation noise on its main diagonal. The correlated sideband structure produces nondiagonal elements in $\overline{COR}_{ID}$. Equation 3.47 shows that such correlation effects change $\overline{\delta V_{N_o}^2}$.

Both the equivalent mixer input noise temperature and the noise factor can be defined using Eq. 3.47. The mixer equivalent input noise temperature is (for an upper-sideband downconverter)[101,117]

$$T_M = \frac{\overline{\delta V^2_{N_o}} \, |Z_{e_1} + R_{s_1}|^2}{4k\Delta f |Z_{aug_{o1}}|^2 \mathrm{Re}[Z_{e_1}]} \quad . \tag{3.48}$$

The single-sideband noise factor is defined by

$$F_{SSB} = 1 + \frac{T_M}{290} \quad . \tag{3.49}$$

3.4.2 Applications to Oscillators and Amplifiers. The existence and importance of noise correlation effects in IMPATT oscillators was discussed by Kuvas.[127] In this section the noise analysis of Goedbloed and Vlaardingerbroek[126] is briefly reviewed as it explicitly contains noise correlation matrices. Kuvas included noise correlation effects but used a cumbersome summation representation. Goedbloed and Vlaardingerbroek have a correlation matrix in their main analytical result but they ignored the correlation (i.e., used a diagonal correlation matrix) in their calculations.

The formal solution to the IMPATT oscillator-amplifier noise problem obtained by Goedbloed and Vlaardingerbroek is

$$\langle \overline{i}_t \overline{i}_t^{\psi} \rangle = \overline{S}^{-1}\overline{M}\langle \overline{gg^{\psi}} \rangle \overline{M}^{\psi}(\overline{S}^{-1})^{\psi} + \overline{S}^{-1}\overline{F}\langle \overline{V}_e \overline{V}_e^{\psi} \rangle \overline{F}^{\psi}(\overline{S}^{-1})^{\psi} \quad , \tag{3.50}$$

where $\overline{i}_t$ is the total noise current, $\overline{M}$ is a multiplication matrix associated with the avalanche or injection region (a Read model is used), $\overline{S}$ and $\overline{F}$ are matrices determined by the amplifier (oscillator) loop impedance equation which includes the drift region impedance, and $\overline{V}_e$ is the noise or modulation present in the amplifier input noise signal. $\langle \overline{gg^{\psi}} \rangle$ and $\langle \overline{V}_e \overline{V}_e^{\psi} \rangle$ are correlation matrices. Goedbloed

and Vlaardingerbroek ignore the off-diagonal terms and show how Eq. 3.50 can be used to solve a wide range of problems. The techniques developed here can be directly incorporated into their model resulting in a general and elegant theory. Since the main conclusion of any IMPATT noise theory is that an IMPATT is always noisy this problem is not treated here.

3.5 Summary

The theory of noise correlation in two-terminal junction devices was reviewed in detail. It was demonstrated that all these devices will have noise correlation structures under large-signal periodic drive. A general mathematical theory for this correlation was presented. Applications to mixers were discussed and the techniques developed here were shown to easily fit into the formal structure of the IMPATT oscillator-amplifier noise theory of Goedbloed and Vlaardingerbroek.[126] These correlation effects are retained in later calculations.

CHAPTER IV. VIDEO DETECTOR STUDIES

4.1 Introduction

In this chapter the video detector performance of transit-time devices is studied and compared with those of Schottky- and Mott-barrier devices. The chapter starts in Section 4.2 with a review of the transit-time device models. In Section 4.3 the intrinsic properties, i.e., no frequency conversion, of the devices are studied. The video detector properties are then described in Section 4.4. Silicon pnp BARITT and Schottky- and Mott-barrier devices are considered.

4.1.1 The Basic Semiconductor Equations. Although the problem of charge transport in a solid is basically a quantum mechanical problem, the approach universally used in the modeling of a realistic semiconductor device is much simpler. The quantum nature of the charge transport is lumped into an energy band structure and effective masses. The charge transport is then modeled by modeling the transport of two species of charged classical bodies or quasi-free particles: electrons and holes. Since these particles are classical, their dynamics are controlled by Maxwell's equations. For a one-dimensional device with negligible magnetic fields, the results are:

Poisson's equation,

$$\varepsilon \frac{\partial E}{\partial x} = q(p - n + N_D) \quad ; \qquad (4.1)$$

carrier continuity equations,

$$\frac{1}{q} \frac{\partial J_n}{\partial x} = \frac{\partial n}{\partial t} - g \qquad (4.2)$$

and

$$\frac{1}{q}\frac{\partial J_p}{\partial x} = -\frac{\partial p}{\partial t} + g \quad ; \tag{4.3}$$

and the current continuity equation,

$$\frac{\partial}{\partial x}(J_T) = \frac{\partial}{\partial x}\left(J_n + J_p + \varepsilon\frac{\partial E}{\partial t}\right) = 0 \quad . \tag{4.4}$$

In Eqs. 4.1 through 4.4, ε is the material electrical permittivity; q is the electronic charge magnitude; g is the electron-hole pair generation rate; x is the spatial variable; t is time; J_n and n are the electron conduction current density and the electron density, respectively; J_p and p are the hole conduction current density and the hole density, respectively; E is the electric field; and J_T is the total current density.

The primary value of Eqs. 4.1 through 4.4 is that their validity depends primarily on the assumption that the charge is transported by quasi-free particles. Limitations of this assumption are discussed elsewhere.[137,152,153] In practice, better first-principles models of semiconductor devices do not exist. A more important limitation therefore is that Eqs. 4.1 through 4.4 constitute a set of three independent equations in six unknowns. Additional constitutive relations are needed which in turn introduce additional approximations. A survey of the various possible approximations and the resulting modeling techniques is found in Reference 137.

The constitutive relations used here are

$$g = 0 \quad , \tag{4.5}$$

and drift-diffusion transport equations

$$J_p = qv_p p - q \frac{\partial}{\partial x}(D_p p) \qquad (4.6)$$

and

$$J_n = - qv_n n + q \frac{\partial}{\partial x}(D_n n) \quad , \qquad (4.7)$$

where $v_{n,p}$ and $D_{n,p}$ are field-dependent velocity and diffusion coefficients for electrons (subscript n) and holes (subscript p). The sign conventions are described in Fig. 4.1. All material parameters used are tabulated in Appendix A. Equation 4.5 means that optical effects and avalanche effects will not be included here. Equations 4.6 and 4.7 introduce an assumption that the carrier distribution in momentum phase space instantaneously relaxes to the steady-state value appropriate to the instantaneous local field E(x,t). Limitations of this quasi-static pseudo-local approximation are also reviewed elsewhere.[137,154,155] A general conclusion is that drift-diffusion approaches are valid in Si throughout the low millimeter-wave region. For GaAs, however, energy and momentum relaxation can take several picoseconds. Since several picoseconds constitute 30 or more degrees of RF phase angle at 40 GHz, Eqs. 4.6 and 4.7 are qualitative when applied to GaAs millimeter-wave transit-time devices.

4.1.2 Modeling Methods. No substantially new device models were developed in this investigation. Instead, earlier models substantially developed by McCleer[30] were employed. Some modifications were made to increase computational efficiency. These modifications and models will be briefly described here.

The dc drift region model is a single carrier model (holes for the pnp BARITTs). The basic equations are obtained by removing the time derivatives in Eqs. 4.1 through 4.7. A double-mesh scheme

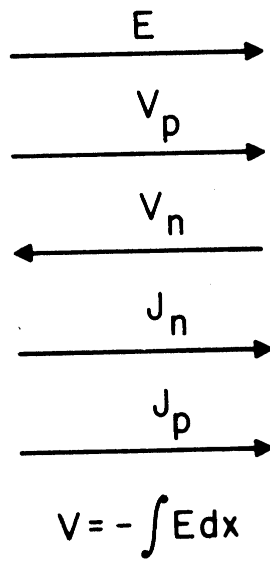

FIG. 4.1 SIGN CONVENTIONS.

is used in which carrier concentration and doping are described on a space-charge mesh while fields and currents are described on an interweaved mesh. The equations are set up in the fashion of McCleer.[30] The result is a Jacobian matrix equation in which the current error vector is used to determine a carrier concentration update vector for any specified initial carrier concentration. The Jacobian matrix is upper bidiagonal and is solved by back substitution. A drift-only outflow boundary condition is imposed at the collecting contact.

For BARITTs the injection region model of McCleer[30] is used with the exception of the specification of the injection point location. McCleer used a depletion approximation to relate the injection region width to the injection region voltage. Here a first-order correction for the hole space charge in the injection region is included.[156]

The small-signal drift region model used here is that of McCleer et al.[139] It is a single carrier model in which complete field dependence of both diffusion and velocity is allowed. The resulting equivalent circuit is that used in the mixer analysis presented in Chapters II and III. When applied in a noise model, this drift region model has the disconcerting property that it does not converge to the correct solution when the grid spacing is made very small.[157] Therefore, a simple approximation is used here.

This simple approximation for the mean square noise voltage appearing across the drift region due to velocity fluctuations is now described. The expression is motivated by the transfer impedance formalism of Gummel and Blue,[158] where the noise voltage is

$$V_{VF} = \int Z_{trans}(x) J_{VF}(x)\, dx \quad , \tag{4.8}$$

where $Z_{trans}(x)$ is the transfer impedance which relates the noise voltage at the terminals to a unit current source in an otherwise open-circuited region. $J_{VF}(x)$ is the noise current source.

In the approximation used here the device is divided into two regions, a high-field region and a low-field region, in the same way as in the small-signal model. The noise voltage in each of these regions is assumed to be uncorrelated with the other voltage. The voltage in the high-field region is calculated using a modification of the expression of Statz et al.[150] Their expression is an analytical result applicable to a region in which a constant carrier concentration p_o is transported at a constant velocity. Diffusion current is neglected, but a constant diffusion coefficient is included as part of the velocity-fluctuation noise-source formulation. Here the product $p_o Dl$ in the Statz expression is replaced by the integral of the product of the dc carrier concentration and diffusion coefficient over the high-field region.

In the low-field region it is assumed that the transfer impedance is constant. Since the integral of the transfer impedance is equal to the small-signal impedance, the assumed constant value used here is a multiple of the spatial average of the small-signal impedance of the low-field region. The noise current source is set to the value appropriate to the injection point. This value is

$$4q^2 DKp_{sat} \Delta f \quad ,$$

where p_{sat} is the carrier concentration needed to transport J_{dc} at

v_{sat} and K is a boundary condition parameter as defined by McCleer and Haddad.[159] After some experimentation, it was found that setting the low-field transfer impedance to three times the spatial average yielded a reasonable approximation to the small-signal BARITT noise data of Bjorkman and Snapp.[160]

The small-signal injection region model used is a conductance connected in parallel with the capacitance. This model has been previously used by Weller[161] and McCleer.[30] It is identical with the Schottky-barrier small-signal model described in Chapter I.

For large-signal calculations a modification of the large-signal BARITT model of McCleer is used.[30] While McCleer divides the drift region into a low-field portion in which only diffusion occurs and a high-field portion in which only drift occurs, here the small-signal drift region model is applied without modification. The modified Bessel function representation of the Fourier coefficients of a sinusoidally pumped exponential used by McCleer is used here.

These models were extensively tested against the experimental BARITT data of Snapp and Weissglas[162] as well as Bjorkman and Snapp.[160] The performance of the model was found to be satisfactory. The most significant limitation probably is the neglect of drift-region space charge in the large-signal model. The large-signal model was found to predict more rectification for a given RF voltage than the experimental data showed. This suggests that the large-signal model overestimates the ratio of the injection-region RF voltage to the total RF voltage in the BARITT. Another factor which is related to this is the assumption that the injection point does not move during the RF cycle.

4.1.3 Device Design and Specification. The Schottky-barrier and Mott-barrier device parameters are presented in Table 4.1. The data in this table are generally based on the data used by Held and Kerr[101] for the Schottky device, while the Mott data are an amalgam of the structures of Keen,[106] McColl and Millea,[110] and Linke et al.[111] The BARITT structures considered are described in Table 4.2. Uniformly doped pnp Si devices are assumed. Throughout the chapter the entry ABPT in any Baritt data table indicates that the structure avalanches before it punches through.

4.2 Intrinsic Diode Properties

4.2.1 Introduction. In this section the intrinsic diode properties are compared. Here "intrinsic" means that no frequency conversion effects are included. However, the field and impedance levels and areas can be considered along with the thermal properties to provide useful background information concerning device design, reliability and stability.

4.2.2 Dc Studies. The basic dc studies are the determination of the peak electric field level seen in the device along with the margin possessed against avalanche breakdown. The peak field for various BARITT devices biased at a current density of 500 A/cm^2 is given in Table 4.3. In a relatively short lightly doped structure, the fields are much lower than the peak fields in either the Shottky- or Mott-barrier devices. The peak fields are also much lower than the critical field needed for avalanche breakdown, E_c. Since the average field is lower and the dc current density is lower also, the BARITT device should be less susceptible to localized microplasmas.

Table 4.1

Parameters for Schottky and Mott Diodes

Parameter	Schottky Value	Mott Value
Doping	2.5×10^{17} cm^{-3}	2.5×10^{16} cm^{-3}
Epitaxial layer length	0.2 μm	0.1 μm
C_{jo}	1.4×10^{-7} F/cm^2	2.0×10^{-7} F/cm^2
V_{bi}	0.95	1.0
Saturated current density	1.9×10^{-9} A/cm^2	--
Series resistance	5×10^{-7} Ω-cm^2	5×10^{-8} Ω-cm^2
I-V ideality factor	1.05	1.05
Peak field at zero bias	200 to 300 kV/cm	100 kV/cm
Breakdown voltage	10 V	10 V
Dc current density	10,000 A/cm^2	10,000 A/cm^2
τ_{TH}	1.7 ns	0.4 ns
Diameter for 50-Ω resistance at 300 MHz	2.64 μm	2.64 μm
Diameter for 50-Ω resistance at 35 GHz	2.64 μm	2.64 μm
Diameter for 50-Ω resistance at 94 GHz	2.57 μm	2.64 μm
Thermal resistance of mesa	812°K/W	406°K/W
Thermal speading resistance into gold heat sink	600°K/W	600°K/W
C_{eff}	1.5×10^{-18} F/cm^2	1.5×10^{-18} F/cm^2
Knee frequency	600 GHz	400 GHz

(Cont.)

Table 4.1 (Cont.)

Parameter	Schottky Value	Mott Value
f_c	2300 GHz	16,000 GHz
α	0.22	0.019
γ_m at 35 GHz	3.98×10^{-4} V-cm^2-W^{-1}	4.62×10^{-4} V-cm^2-W^{-1}
γ_m at 94 GHz	3.96×10^{-4} V-cm^2-W^{-1}	4.61×10^{-4} V-cm^2-W^{-1}
NEPF at 35 GHz	-94.1 dB with respect to W-cm^{-1}	-94.8 dB with respect to W-cm^{-1}
NEPF at 94 GHz	-94.1 dB with respect to W-cm^{-1}	-94.8 dB with respect to W-cm^{-1}

Table 4.2

Definition of BARITT Structures

Length (μm)	Doping (cm^{-3})			
	2×10^{15}	4×10^{15}	6×10^{15}	8×10^{15}
2	1	7	10	12
3	2	8	11	ABPT
4	3	9	ABPT	ABPT
5	4	ABPT	ABPT	ABPT
6	5	ABPT	ABPT	ABPT
7	6	ABPT	ABPT	ABPT

Table 4.3

Peak Field in kV/cm for BARITTs at 500 A/cm^2

Length (μm)	Doping (cm^{-3})			
	2×10^{15}	4×10^{15}	6×10^{15}	8×10^{15}
2	69.6	122.7	178.2	235.1
3	105.7	189.5	276.0	ABPT
4	141.9	256.7	ABPT	ABPT
5	178.1	ABPT	ABPT	ABPT
6	214.6	ABPT	ABPT	ABPT
7	251.0	ABPT	ABPT	ABPT

The margin against avalanche breakdown in a BARITT structure is calculated using

$$\text{VBDMAR} = E_c \ell - q\frac{N_D \ell^2}{\varepsilon} , \tag{4.9}$$

where ℓ is the total device length. The results are shown in Table 4.4. It should be noted that for a fixed N_D there is an optimum length which maximizes the margin against avalanche breakdown. This optimum length is

$$\ell_{opt} = \frac{\varepsilon E_c}{2qN_D} , \tag{4.10}$$

and it is plotted in Fig. 4.2 along with the corresponding margin. In comparison, the avalanche breakdown voltage of the Schottky- and Mott-barrier devices is approximately 10 V (see Table 4.1). Also, the margin would be higher in a GaAs BARITT structure than in a Schottky- or Mott-barrier device.

The thermal time constant of the active region (assuming that the device is a mesa structure with mesa height equal to the active region length) is

$$\tau_{TH} = \frac{\ell^2 \rho_m C_s}{K_s} , \tag{4.11}$$

where the semiconductor material parameters are the mass density ρ_m, the specific heat C_s, and the thermal conductivity K_s. τ_{TH} is not a function of either doping or area. It is plotted as a function of length for both Si and GaAs mesas in Fig. 4.3 at an ambient temperature of 300°K. The GaAs devices have a longer thermal time constant than Si mesas. The significance of τ_{TH} is that it represents the fastest thermal response possible. It does not include any heat

Table 4.4

VBDMAR for BARITTs

Length (μm)	Doping (cm^{-3})			
	2×10^{15}	4×10^{15}	6×10^{15}	8×10^{15}
2	47.7	35.4	23.2	10.9
3	62.4	34.8	7.2	ABPT
4	70.9	21.9	ABPT	ABPT
5	73.3	ABPT	ABPT	ABPT
6	69.6	ABPT	ABPT	ABPT
7	59.7	ABPT	ABPT	ABPT

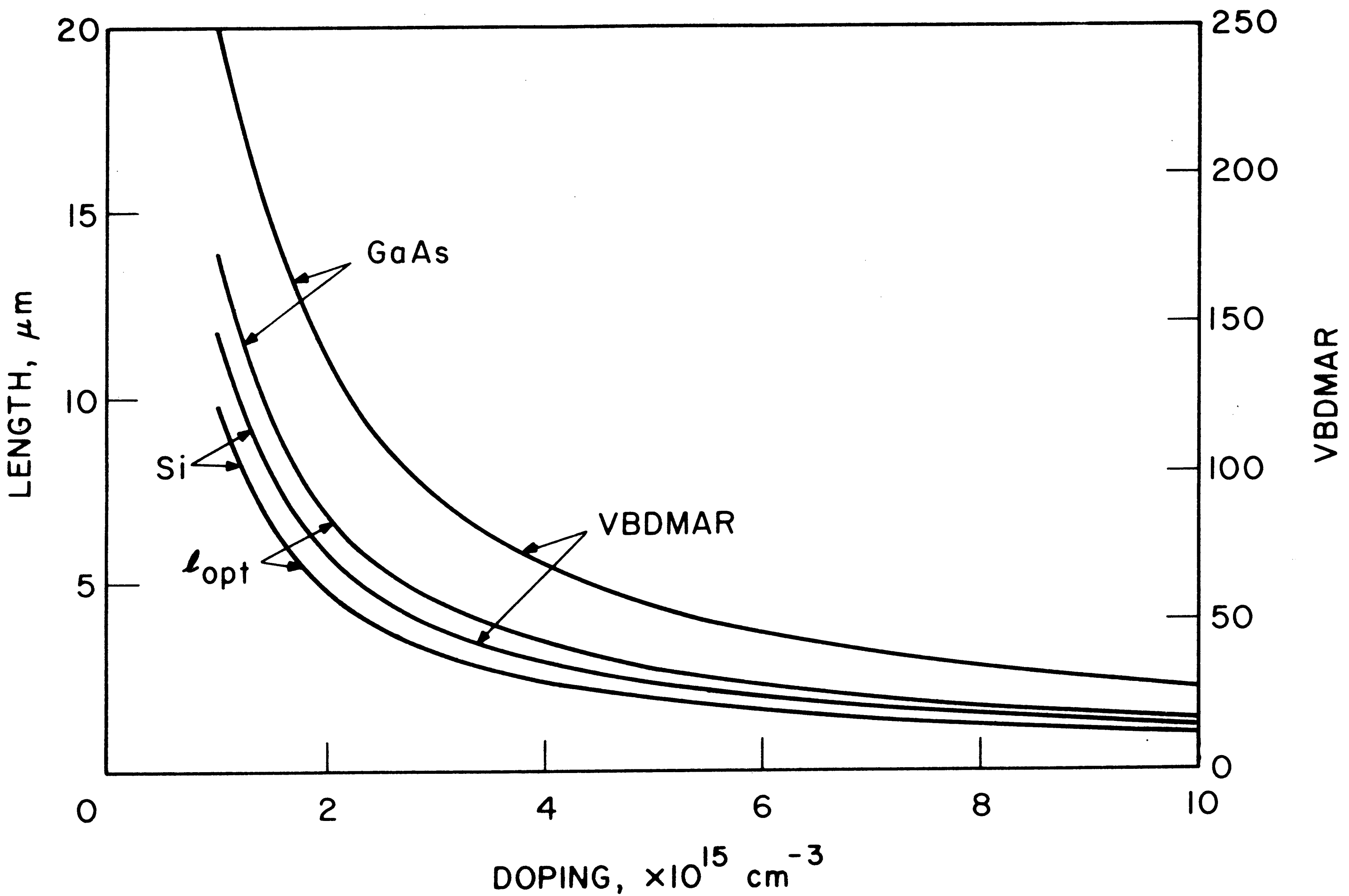

FIG. 4.2 OPTIMUM DEVICE LENGTH AND VBDMAR AS A FUNCTION OF DOPING FOR Si AND GaAs BARITTS.

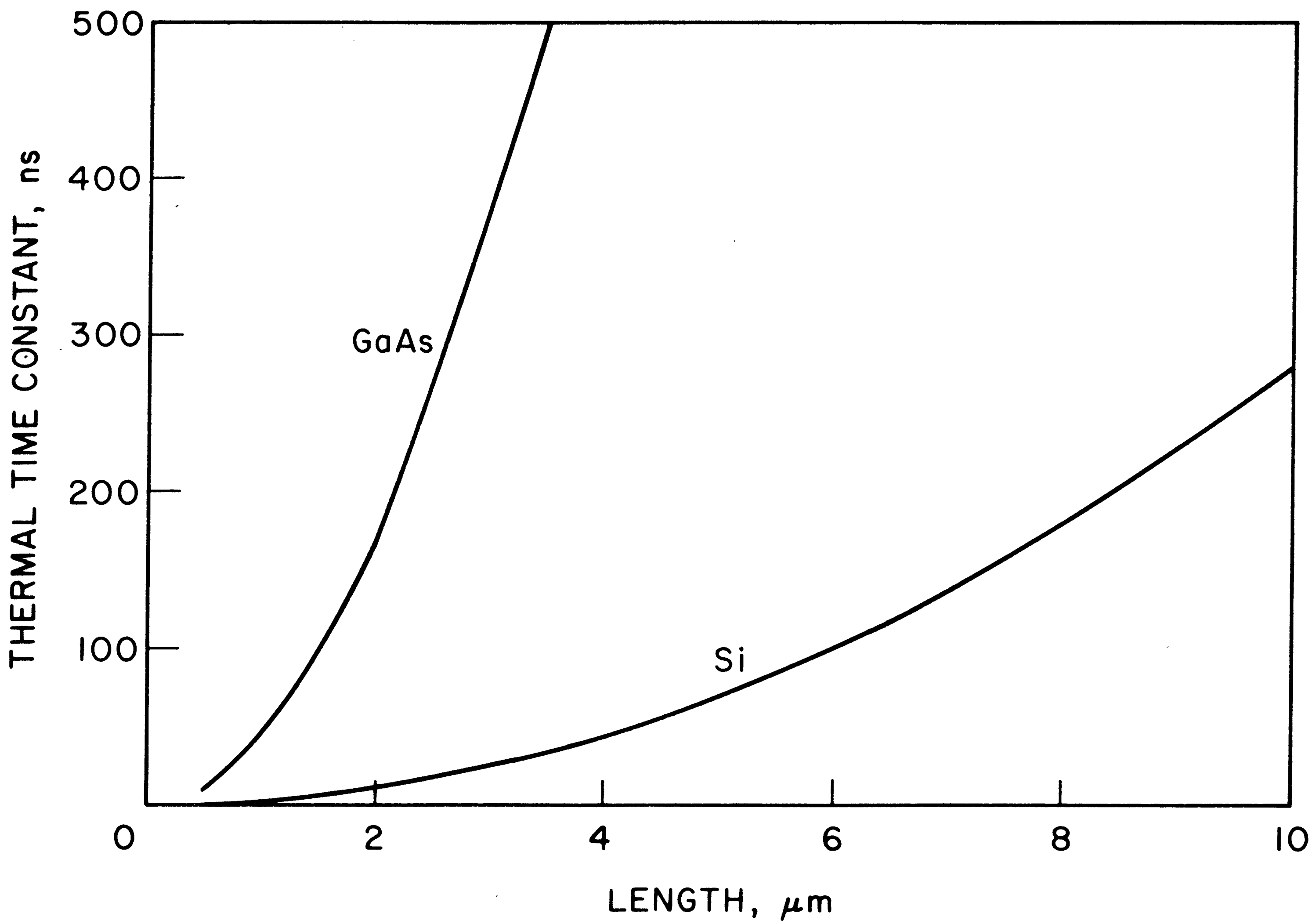

FIG. 4.3 THERMAL TIME CONSTANT AS A FUNCTION OF LENGTH OR MESA HEIGHT FOR MESA STRUCTURES.

sink thermal response effects, and therefore the actual response can be slower. τ_{TH} for typical Schottky and Mott devices is given in Table 4.1. From a system point of view, a long thermal time constant is advantageous in that it allows sufficient time for a power limiting device to be activated and to protect the device if that is found to be necessary. It can be disadvantageous if long thermally induced transients are important.

4.2.3 Small-Signal Impedance Studies. In this section the small-signal impedances of the various devices are calculated. These impedances provide some guidelines on device areas, matching circuit design, and negative resistance bands. The studies are carried out for a range of video or intermediate frequencies (1 MHz to 10 GHz) and for a range of pump or signal frequencies (1 to 120 GHz).

The diode diameter d, which provides a 50-Ω real part of impedance at a frequency of 300 MHz is shown in Table 4.5 for BARITTs biased at 500 A/cm^2. The areas needed for a 1-Ω real part of impedance at 35 and 94 GHz were also calculated. The ratio of the 300 MHz area to these areas is shown in Table 4.6. Similar data for the Schottky and Mott devices is provided in Table 4.1. The BARITT devices can be made much larger than the Schottky and Mott devices. Also, as the device length increases, it becomes more and more difficult to specify an area which provides a good impedance for matching purposes at both low IF or video frequencies and at millimeter-wave frequencies. In Fig. 4.4 the diameter is shown as a function of current density for BARITTs 6 and 12. It is a function of current density.

Table 4.5

Diameter in Microns for 50-Ω Real Part of Impedance at 300 MHz for BARITTs Biased at 500 A/cm²

Length (μm)	Doping (cm^{-3})			
	2×10^{15}	4×10^{15}	6×10^{15}	8×10^{15}
2	93.7	90.5	88.65	87.5
3	134.4	129.3	126.4	ABPT
4	173.6	166.8	ABPT	ABPT
5	211.7	ABPT	ABPT	ABPT
6	249.0	ABPT	ABPT	ABPT
7	285.9	ABPT	ABPT	ABPT

Table 4.6

Ratio of Area for 50-Ω Real Part of Impedance at 300 MHz to Areas for 1-Ω Real Part of Impedance at 35 GHz (Top) and 94 GHz (Bottom) for BARITTs Biased at 500 A/cm²

Length (μm)	Doping (cm^{-3})			
	2×10^{15}	4×10^{15}	6×10^{15}	8×10^{15}
2	0.8473 2.57	2.465 2.81	6.510 3.26	8.79 3.81
3	1.039 5.242	0.8742 5.734	0.8745 6.59	ABPT
4	3.349 8.710	2.719 9.568	ABPT	ABPT
5	3.202 12.90	ABPT	ABPT	ABPT
6	4.648 17.82	ABPT	ABPT	ABPT
7	7.592 23.43	ABPT	ABPT	ABPT

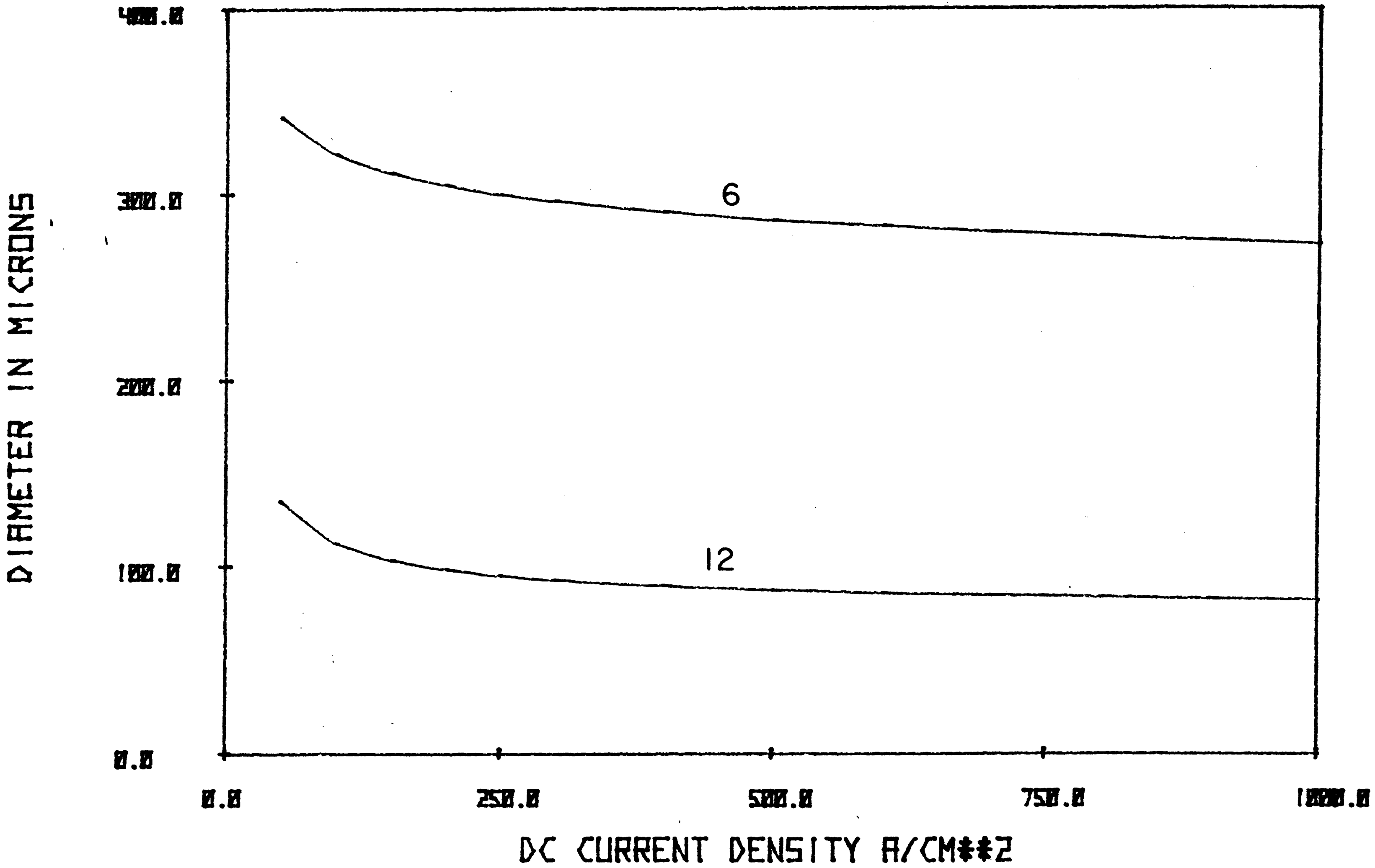

FIG. 4.4 DIAMETER FOR 50-Ω MATCH OF REAL PART OF IMPEDANCE AT 300 MHz FOR BARITTS 6 AND 12 AS A FUNCTION OF CURRENT DENSITY.

The mesa thermal resistances which correspond to these IF diameters were also calculated. The thermal resistance of the mesa is

$$R_{TH_{mesa}} = \frac{4}{\pi d^2} \frac{\ell}{K_s} . \tag{4.12}$$

This represents the minimum thermal resistance as any contributions due to the heat sink are neglected. The heat sink contribution is calculated using the spreading resistance formula

$$R_{TH_{sp}} = \frac{1}{2K_{HS}d} , \tag{4.13}$$

where K_{HS} is the thermal conductivity of the heat sink material. $R_{TH_{mesa}}$ and $R_{TH_{sp}}$ are provided for the BARITT devices in Tables 4.7 and 4.8, and for the Schottky and Mott devices in Table 4.1. The data show that the transit-time devices have a significantly lower thermal resistance as a result of their significantly larger areas. These larger areas also mean that for the same incident pulse of RF energy the power density flowing through the transit-time device is much lower than the power density flowing through the Schottky or Mott device.

Another concern is the possibility of negative resistances in the transit-time devices. The BARITTs were examined at dc current densities of 50, 250 and 500 A/cm^2. The resulting negative-resistance bands are shown in Table 4.9. No negative resistances are expected from the Schottky or Mott devices unless the effects of the parametric variation in the capacitance of the Schottky device are included. Such effects are neglected here.

Table 4.7

Thermal Resistance of Mesa for Diameters of Table 4.5

Length (μm)	Doping (cm^{-3})			
	2×10^{15}	4×10^{15}	6×10^{15}	8×10^{15}
2	2.354	2.523	2.63	2.696
3	1.715	1.854	1.940	ABPT
4	1.372	1.485	ABPT	ABPT
5	1.153	ABPT	ABPT	ABPT
6	1.00	ABPT	ABPT	ABPT
7	0.885	ABPT	ABPT	ABPT

Table 4.8

Thermal Spreading Resistance into a Gold Heat Sink

for Diameters of Table 4.5

Length (μm)	Doping (cm^{-3})			
	2×10^{15}	4×10^{15}	6×10^{15}	8×10^{15}
2	16.94	17.54	17.91	18.13
3	11.81	12.28	12.56	ABPT
4	9.145	9.515	ABPT	ABPT
5	7.499	ABPT	ABPT	ABPT
6	6.373	ABPT	ABPT	ABPT
7	5.551	ABPT	ABPT	ABPT

Table 4.9

Negative-Resistance Bands for BARITT Structures (GHz)

Length (μm)	Doping (cm^{-3}) 2×10^{15}	4×10^{15}	6×10^{15}	8×10^{15}
2	None	None	25 to 33	25 to 37
3	14 to 15	16 to 26	17 to 28	ABPT
4	12 to 19	13 to 21	ABPT	ABPT
5	10 to 16	ABPT	ABPT	ABPT
6	9 to 14	ABPT	ABPT	ABPT
7	8 to 12	ABPT	ABPT	ABPT

The small-signal admittance data were also calculated. A typical plot of the diode admittance vs. frequency is shown in Fig. 4.5 for the IF range. It is shown that the susceptance is nearly linearly related to frequency. However, there is a definite electronic contribution to this susceptance in addition to the cold or depletion capacitance.

The conductance is nearly constant. Since B can be used to define an effective capacitance

$$C_{eff} = \frac{B}{\omega} , \tag{4.14}$$

an interesting result is obtained when the admittance is transformed into an impedance. The resulting impedance is

$$Z = \frac{1}{G^2} \frac{1}{1 + (\omega/\omega_K)^2} (G - j\omega C_{eff}) , \tag{4.15}$$

where the knee frequency is

$$\omega_K = \frac{G}{C_{eff}} . \tag{4.16}$$

Below the knee frequency, the device resistance is constant. The reactance is negative and linearly proportional to frequency, that is, a reactance which is capacitive in sign but inductive in its frequency dependence. Therefore, a constant series inductance could provide an effective broadband match. C_{eff} and ω_K are provided for the BARITT devices in Tables 4.10 and 4.11, and for the Schottky and Mott devices in Table 4.1. For both the Schottky and Mott devices, the large dc current densities assumed provide a conductance which dominates the device admittance at most of the frequencies of interest

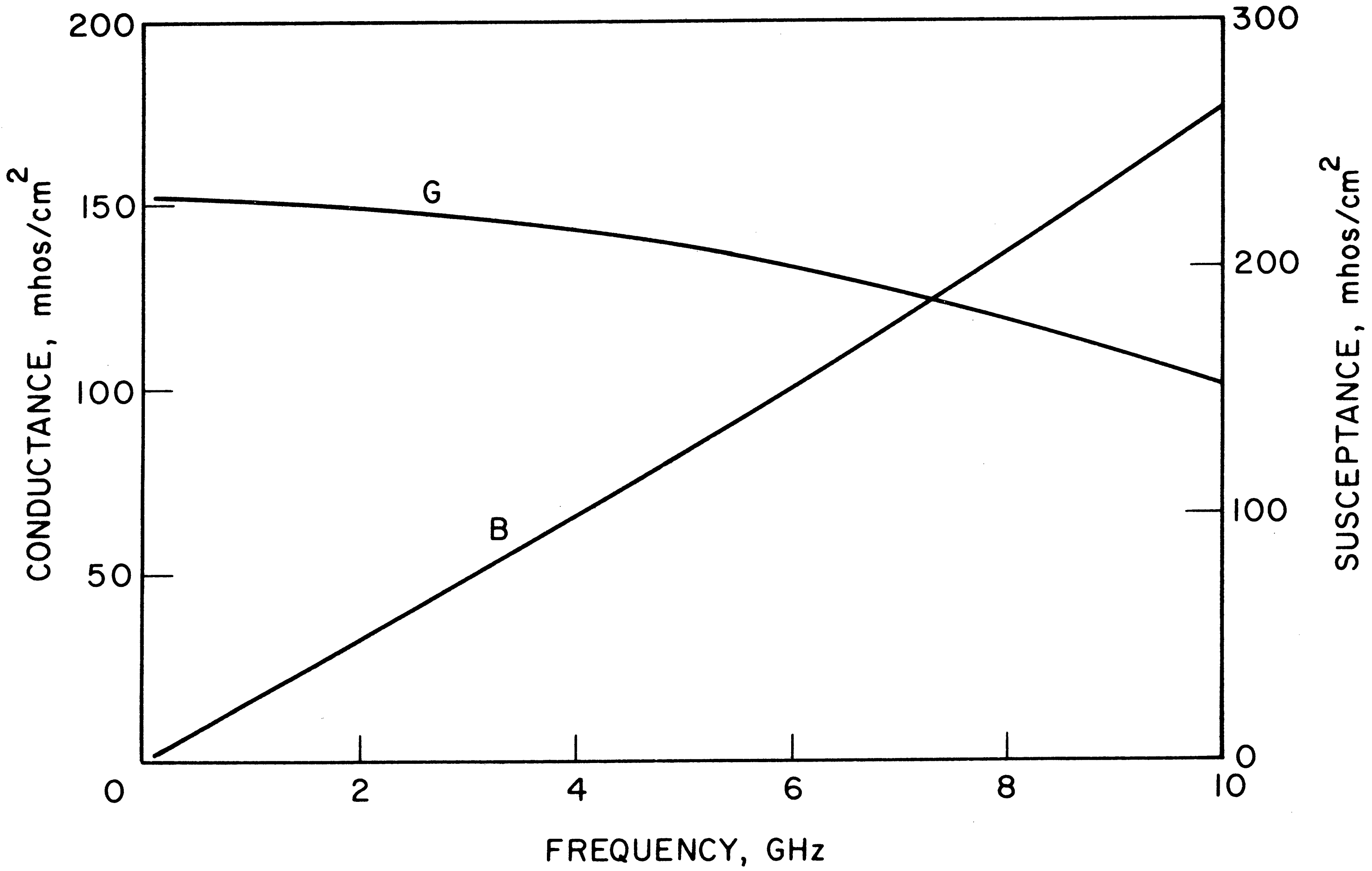

FIG. 4.5 DIODE CONDUCTANCE G AND SUSCEPTANCE B AS A FUNCTION OF FREQUENCY FOR BARITT 1. (J_{dc} = 50 A/cm²)

Table 4.10

Ratio of C_{eff} to C_{cold} for BARITTs at J_{dc} = 500 A/cm^2

Length (μm)	Doping (cm^{-3})			
	2×10^{15}	4×10^{15}	6×10^{15}	8×10^{15}
2	0.7354	0.701	0.6844	0.6748
3	0.6923	0.670	0.6611	ABPT
4	0.6732	0.6582	ABPT	ABPT
5	0.6634	ABPT	ABPT	ABPT
6	0.6581	ABPT	ABPT	ABPT
7	0.6551	ABPT	ABPT	ABPT

Table 4.11

Knee Frequency in GHz for BARITTs at J_{dc} = 500 A/cm^2

Length (μm)	Doping (cm^{-3})			
	2 x 10^{15}	4 x 10^{15}	6 x 10^{15}	8 x 10^{15}
2	12.01	13.52	14.42	15.00
3	9.29	10.38	11.01	ABPT
4	7.64	8.46	ABPT	ABPT
5	6.51	ABPT	ABPT	ABPT
6	5.69	ABPT	ABPT	ABPT
7	5.06	ABPT	ABPT	ABPT

here. This is reflected by the high knee frequencies and the low effective capacitance values.

For frequencies above the knee frequency, Eq. 4.15 should no longer be used since transit-time effects become important and begin to dominate the frequency dependence of the device admittance and impedance. In this range both the effective capacitance and the knee frequency become strong functions of frequency themselves. The device conductance is also frequency dependent in this range.

These quantities are also functions of the dc current density. The knee frequency is plotted as a function of dc current density for several BARITT devices in Fig. 4.6. Similar plots for the effective capacitance and the conductance are provided in Fig. 4.7. As the dc current density is reduced, the importance of the particle current path is also reduced. The conductance decreases and the knee frequency is reduced.

4.3 Video Detectors

4.3.1 Introduction.

In this section the relative performance of BARITT, Schottky and Mott devices as video detectors is discussed. The performance of BARITTs as video detectors has already been studied, both experimentally and theoretically, by McCleer and Haddad.[31] They demonstrated that the device can simultaneously function as a reflection amplifier and video detector (in an active mode) or as a video detector alone (in a passive mode). In the active mode, extremely sensitive detectors can be obtained in a very narrow band and the performance is limited by circuit tuning considerations, i.e., the onset of negative-resistance oscillations. Here the voltage

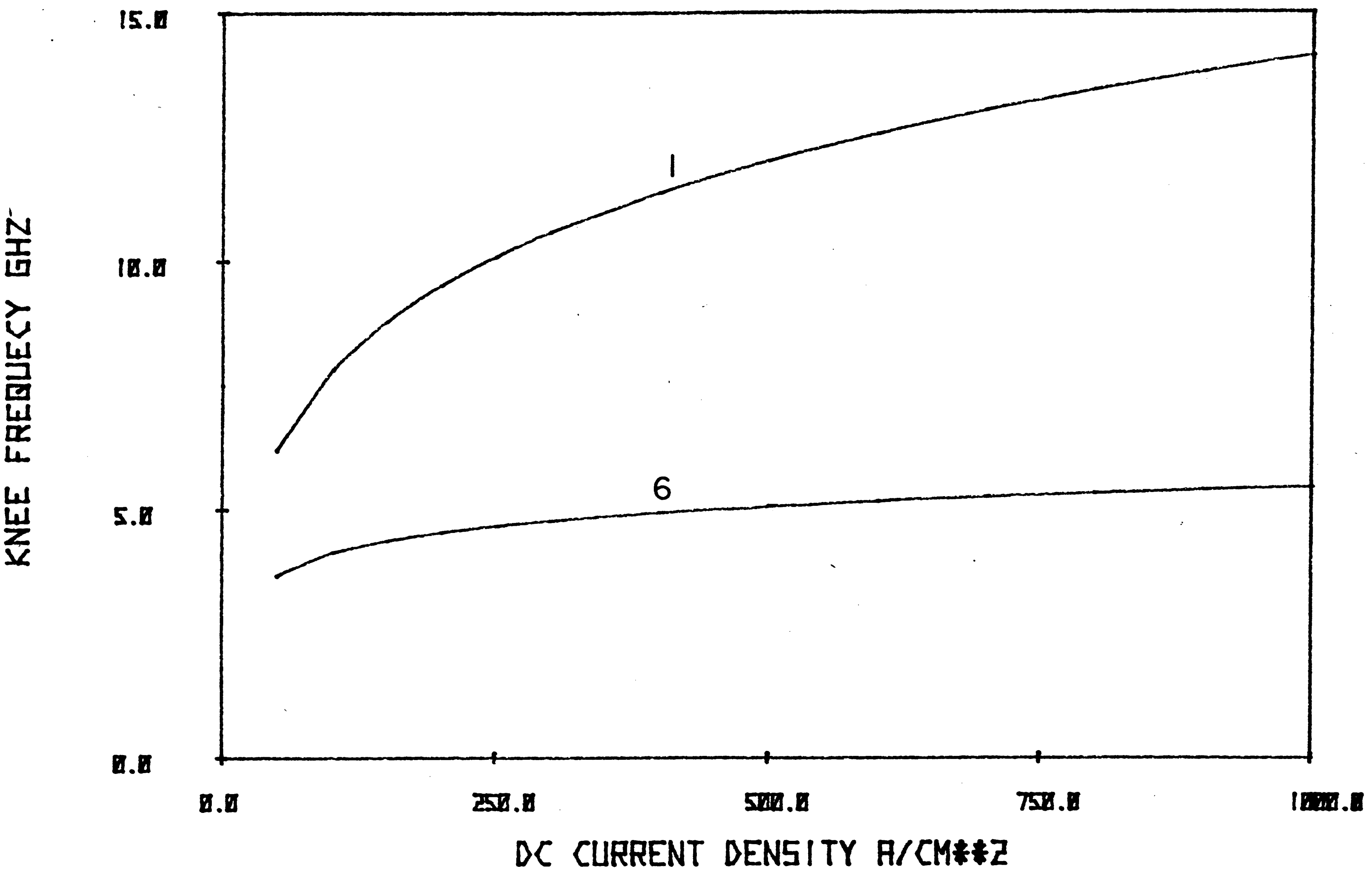

FIG. 4.6 KNEE FREQUENCY AS A FUNCTION OF CURRENT DENSITY FOR BARITTS 1 AND 6.

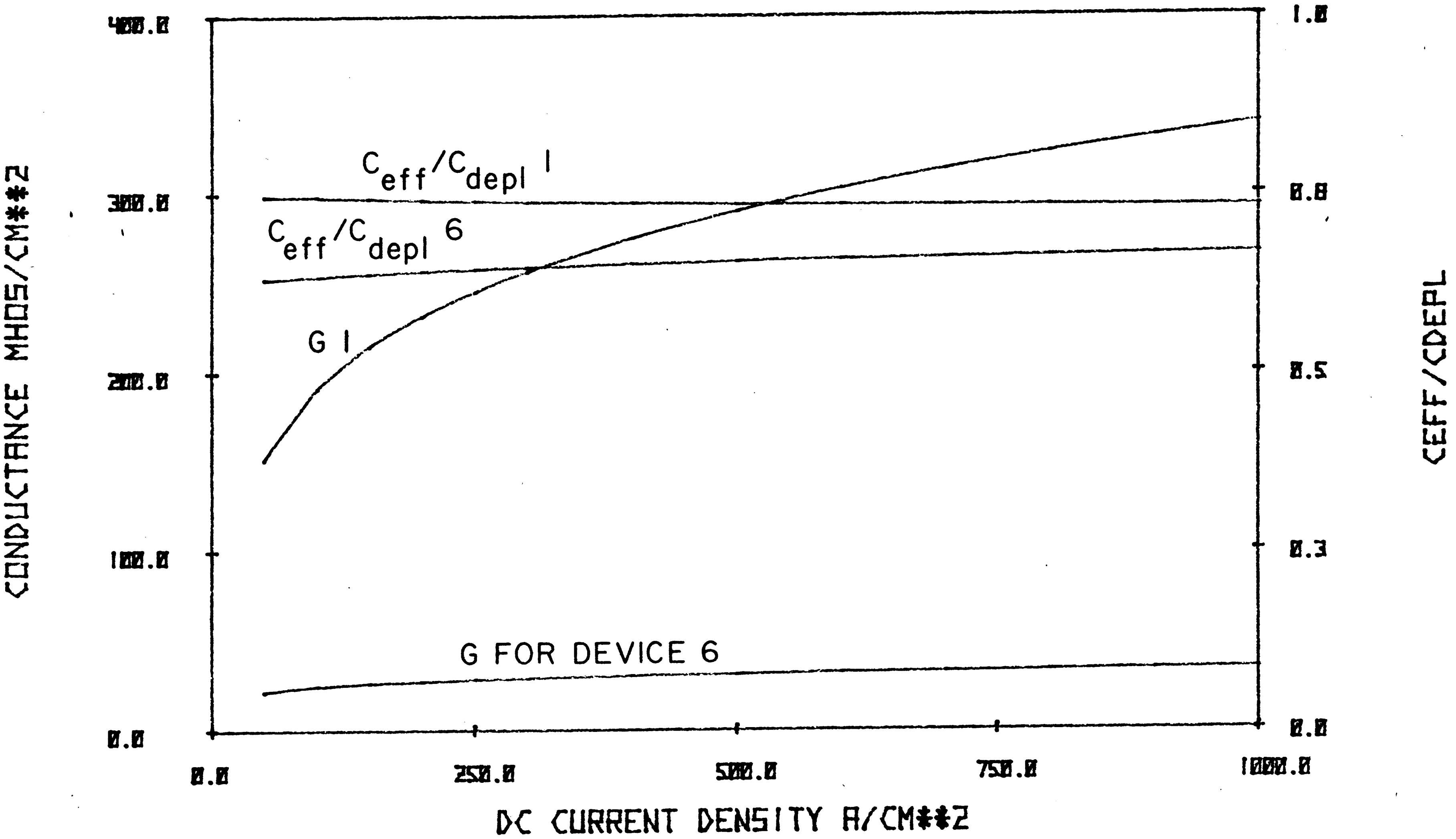

FIG. 4.7 DIODE CONDUCTANCE G AND THE CAPACITANCE RATIO C_{eff}/C_{cold} AS A FUNCTION OF DC CURRENT DENSITY FOR BARRITS 1 AND 6.

detection analysis developed by McCleer and Haddad is combined with the noise analysis to estimate the noise equivalent power (NEP) of a passive mode video detector.

4.3.2 Analysis. The voltage detection sensitivity is calculated by analyzing the circuit shown in Fig. 4.8. Here Z_B is the impedance of the injection region, Z_D is the impedance of the drift region, and R_s is a parasitic series resistance. The incoming signal is represented by a signal generator with voltage V_g and impedance Z_g. V_g and Z_g are transformed by the diode embedding circuit into V_{gT} and Z_{gT} at the diode terminal plane. This transformation is described by the ABCD parameters a, b, c, and d.

The voltage detection sensitivity can then be expressed as[31]

$$\gamma = \eta_c \gamma_m \quad , \tag{4.17}$$

where the circuit transforming efficiency is

$$\eta_c = \frac{4R_g |R_s + R_{DEV}|}{|a + cR_g|^2 (R_{gT} + R_s + R_{DEV})^2} \tag{4.18}$$

and the inherent diode voltage detection sensitivity is

$$\gamma_m = \frac{|Z_B|^2}{2V_x |R_s + R_{DEV}|} \quad . \tag{4.19}$$

In Eqs. 4.18 and 4.19, R_{DEV}, R_g and R_{gT} are the real parts of the total intrinsic device impedance $Z_B + Z_D$, Z_g and Z_{gT}, respectively. V_x is the voltage defined by

$$V_x = f'(V_{BO})/f''(V_{BO}) \quad , \tag{4.20}$$

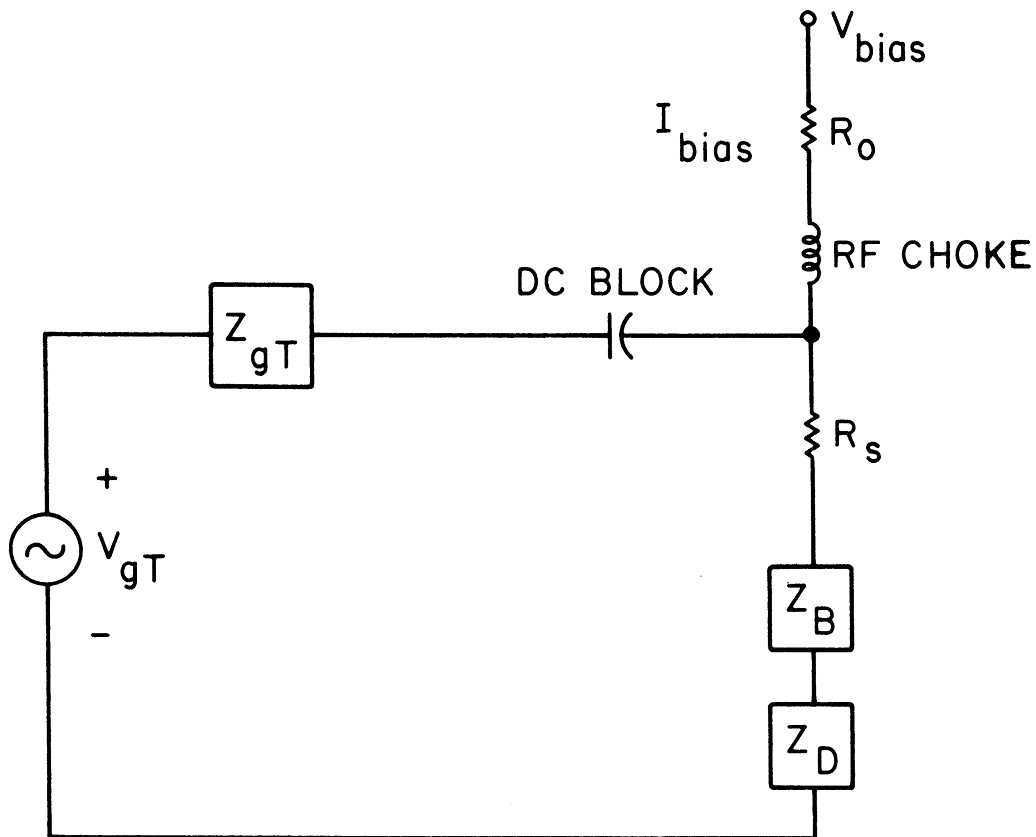

FIG. 4.8 BARITT DIODE VIDEO DETECTOR CIRCUIT.

[$V_{gT} = V_g/(a + cR_g)$ AND $Z_{gT} = (b + dR_g)/ \cdot (a + cR_g)$]

where the injection-region dc current-voltage characteristic is defined by the function $I_B = f(V_B)$, and V_{BO} is the dc injection-region voltage. The primes denote differentiation with respect to V_B.

The two different modes of video detection operation can be expressed by slightly different formulations. In the active mode the voltage detection sensitivity can be expressed as[30]

$$\gamma = \eta_c \Gamma \gamma_m \quad , \tag{4.21}$$

where

$$\Gamma = \left| \frac{R_{gT} - R_{DEV}}{R_{gT} + R_{DEV}} \right|^2 \tag{4.22}$$

is the reflection amplifier power gain. In the passive mode, the inherent voltage detection sensitivity is

$$\gamma_m = \frac{R_s + R_D}{2V_x[\alpha + (f/f_c)^2]} \quad , \tag{4.23}$$

where $R_D = \mathrm{Re}(Z_d)$,

$$\alpha = G_B(R_s + R_D)[1 + G_B(R_s + R_D)] \tag{4.24}$$

and

$$f_c = \frac{1}{2\pi C_B |R_s + R_D|} \quad . \tag{4.25}$$

Equations 4.23 through 4.25 are analogous to the conventional Schottky- or Mott-barrier expressions

$$\gamma_m = \frac{R_s}{2V_x[\alpha + (f/f_c)^2]} \quad , \tag{4.26}$$

$$\alpha = G_B R_s (1 + G_B R_s) \tag{4.27}$$

and

$$f_c = \frac{1}{2\pi C_B R_s} \quad . \tag{4.28}$$

For all devices, V_x equals kT/q.

Several interesting observations can be made concerning Eqs. 4.23 through 4.25. These observations are based on the realization that R_D can be negative even when R_{DEV} is not. Therefore, γ_m can be negative valued. The cutoff frequency is often used as a figure of merit for video detectors. For a transit-time device, however, it can be misleading as f_c becomes infinite for finite γ_m when $R_s + R_D$ is zero.

Another commonly used video detector performance measure is the noise equivalent power or NEP. The NEP in dBW is

$$\text{NEP} = 10 \log (\text{NEPF}) + 5 \log (\text{area in cm}^2) \quad , \tag{4.29}$$

where the noise equivalent power factor (NEPF) is defined along lines similar to those used by Cowley and Sorensen[2] as

$$\text{NEPF} = \frac{\overline{V^2_{oc}}}{\gamma_m} \quad ,$$

where $\overline{V^2_{oc}}$ is the mean square terminal noise voltage at the video frequency. The other term in Eq. 4.29 arises from the area factors in γ_m and $\overline{V^2_{oc}}$. γ_m measures the detected voltage-per-unit incident power density. It has an area dependence because in a smaller device less incident power is needed to maintain the same power density. The area scaling of $\overline{V^2_{oc}}$ arises from a $J_{dc}A$ dependence of the mean square noise current source and a 1/A dependence of impedances.

4.3.3 Results. In this section a variety of numerical studies will be presented. In all cases the video frequency is 30 MHz and the measurement bandwidth is 1 Hz. The first study is focused on the dependency of BARITT video detector performance on RF frequency. The dependency of γ_m and NEPF on RF frequency is illustrated by the examples shown in Figs. 4.9 and 4.10. In Fig. 4.9 the behavior of BARITT 6 is illustrated. It has a nearly constant video detector performance over the low millimeter-wave band. The performance of BARITT 12, as is illustrated in Fig. 4.10, however, exhibits some obvious frequency dependence. The enhanced performance at approximately 35 and 75 GHz is related to the transit-time effects which allow this structure to sometimes have a negative resistance at approximately 35 GHz as is noted in Table 4.9.

Examples of the role of dc current density are provided in Figs. 4.11 and 4.12. In Fig. 4.11, γ_m and NEPF are plotted as functions of dc current density for BARITTs 1, 6 and 12. The RF frequency is 35 GHz. Similar data is provided for 94 GHz in Fig. 4.12. At 35 GHz, transit-time effects and possible negative resistances are evident for the short, highly doped BARITT 12. At 94 GHz, however, no such effects are present. From these two figures it would appear that in the passive mode of operation the video detector performance improves as J_{dc} is reduced. In Fig. 4.13 the performance at lower current densities for BARITT 1 at both 35 and 94 GHz is plotted. As can be seen, there is an optimum dc current density. This optimum occurs because of a tradeoff in the shot noise. While the mean square shot noise current source is proportional to J_{dc}, the mean square terminal noise voltage due to shot noise is a transformation of this current

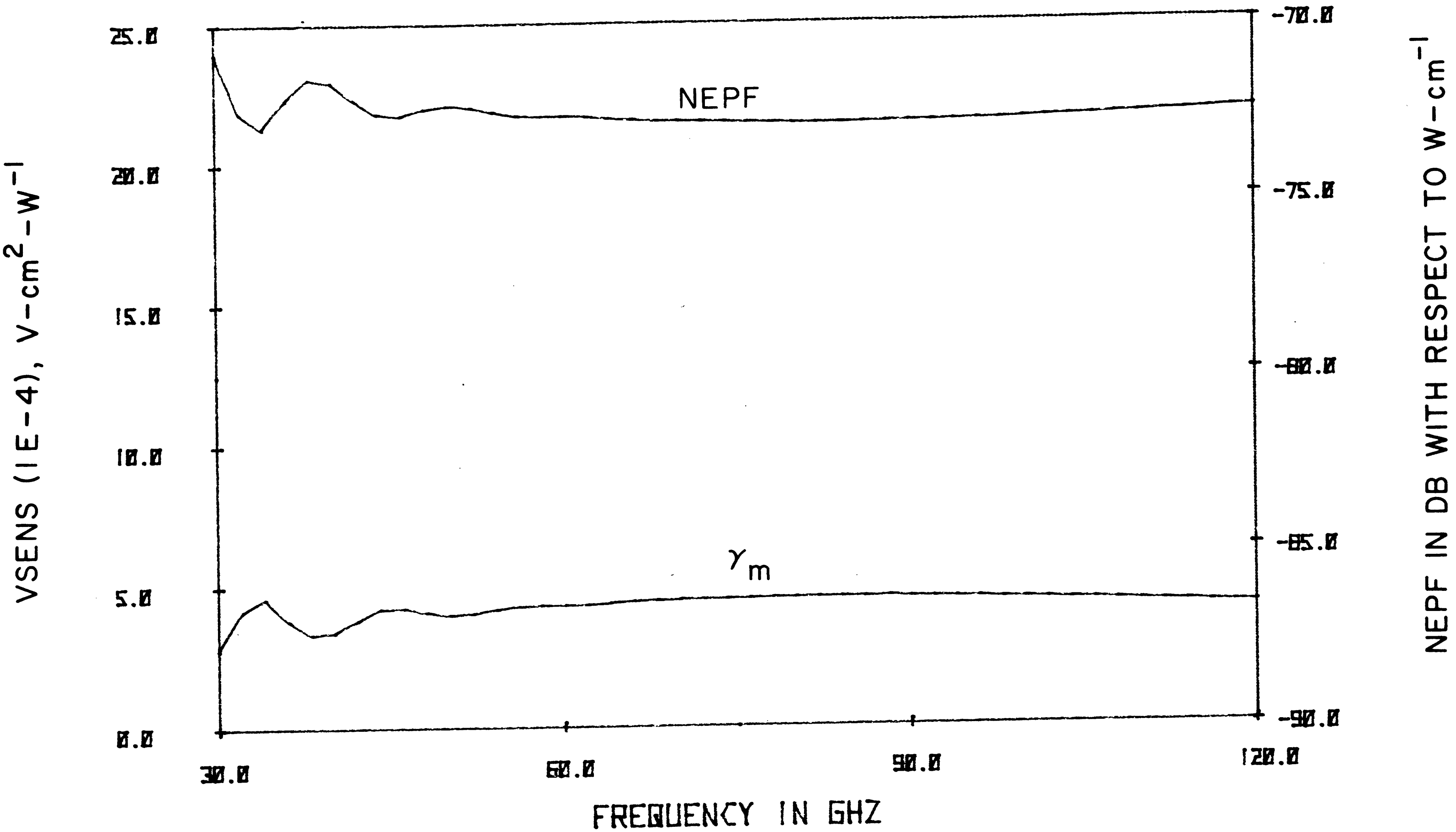

FIG. 4.9 VOLTAGE DETECTION SENSITIVITY AND NOISE EQUIVALENT POWER FACTOR AS A FUNCTION OF FREQUENCY FOR BARITT 6. (J_{dc} = 500 A/cm^2, VIDEO FREQUENCY = 30 MHz AND Δf = 1)

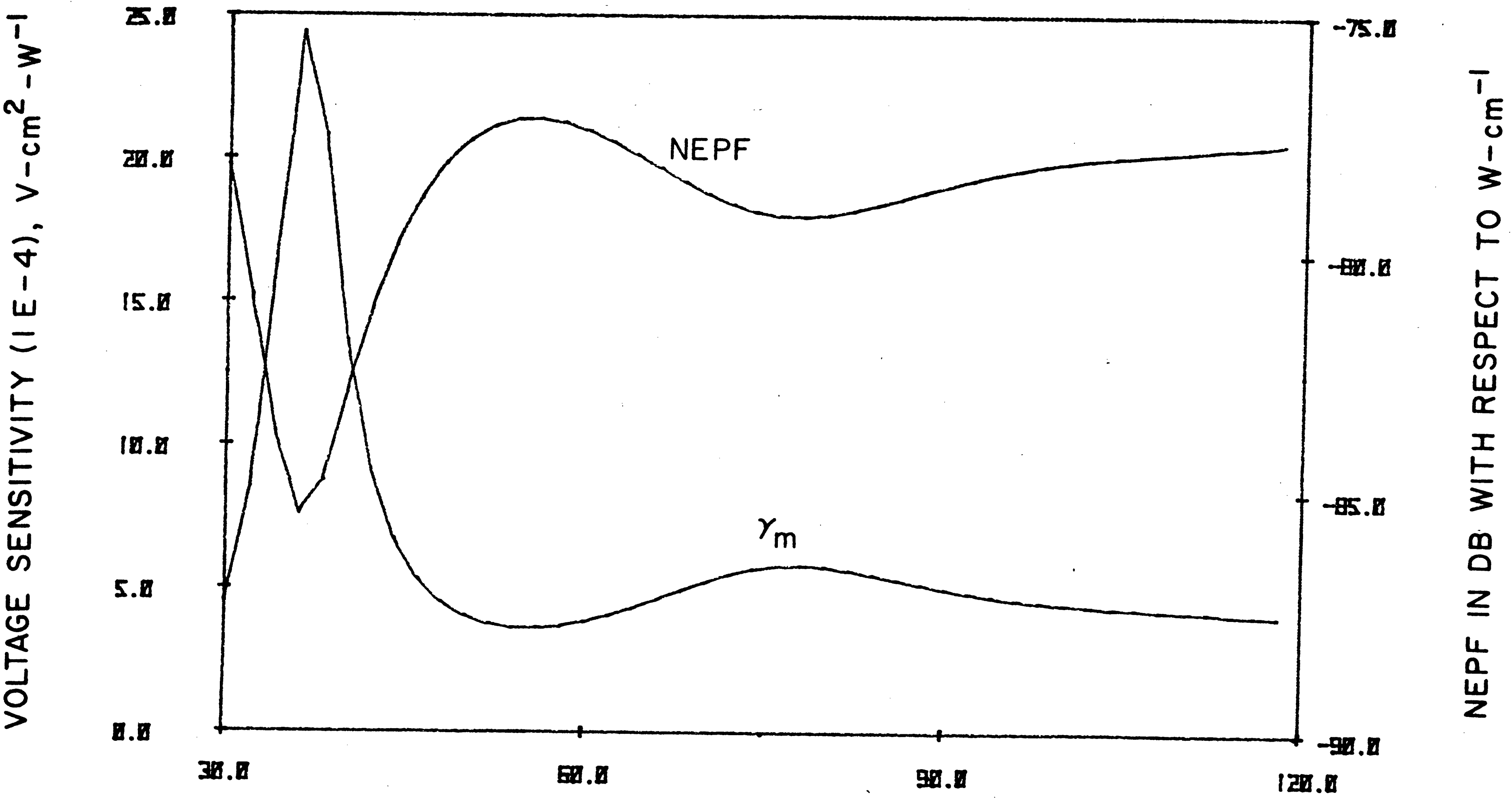

FIG. 4.10 VOLTAGE DETECTION SENSITIVITY AND NOISE EQUIVALENT POWER FACTOR AS A FUNCTION OF FREQUENCY FOR BARITT 12. (J_{dc} = 500 A/cm^2, VIDEO FREQUENCY = 30 MHz AND Δf = 1)

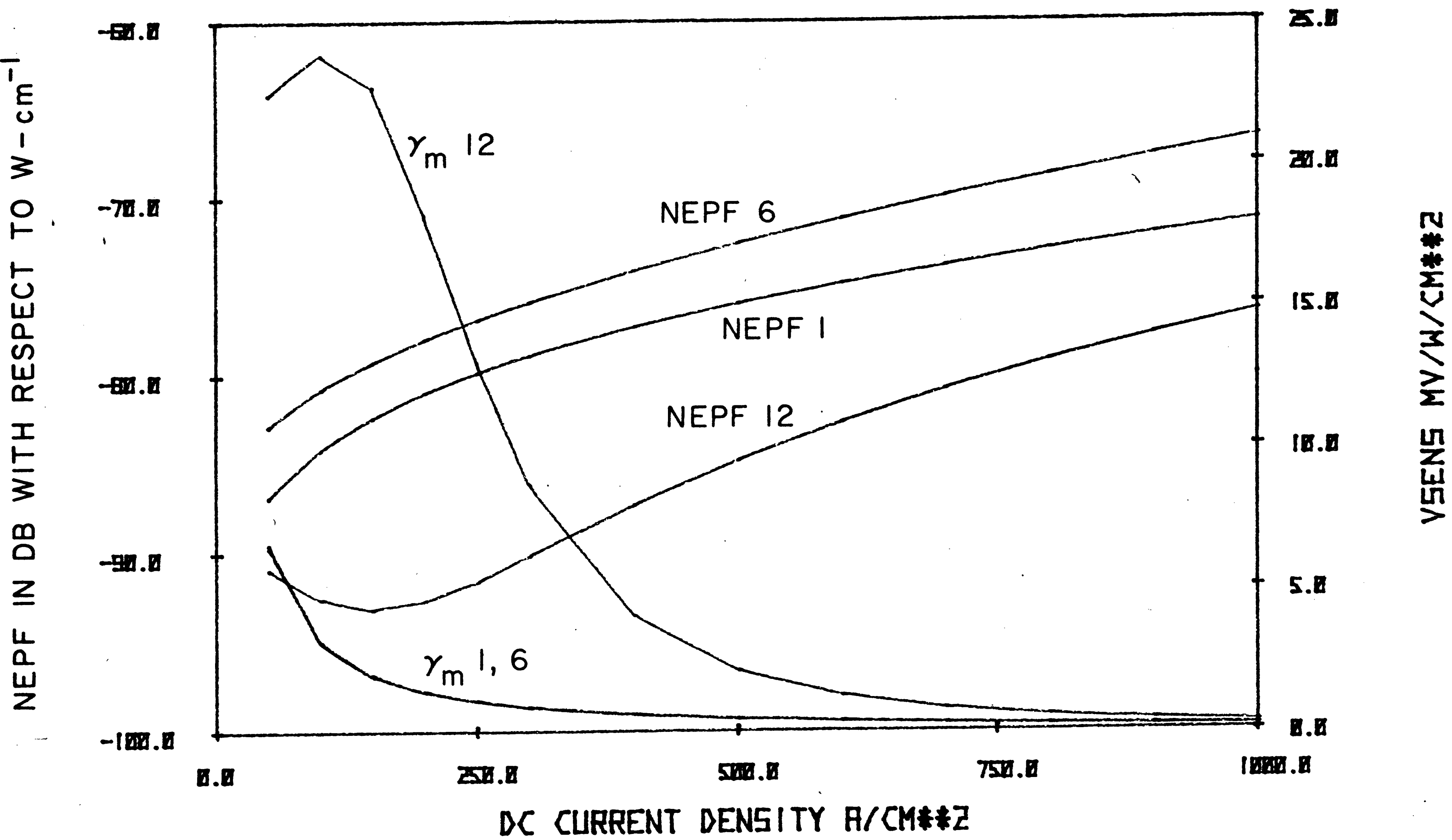

FIG. 4.11 VOLTAGE DETECTION SENSITIVITY AND NOISE EQUIVALENT POWER FACTOR AS A FUNCTION OF CURRENT DENSITY FOR BARITTS 1, 6 AND 12 AT 35 GHz. (VIDEO FREQUENCY = 30 MHz AND Δf = 1)

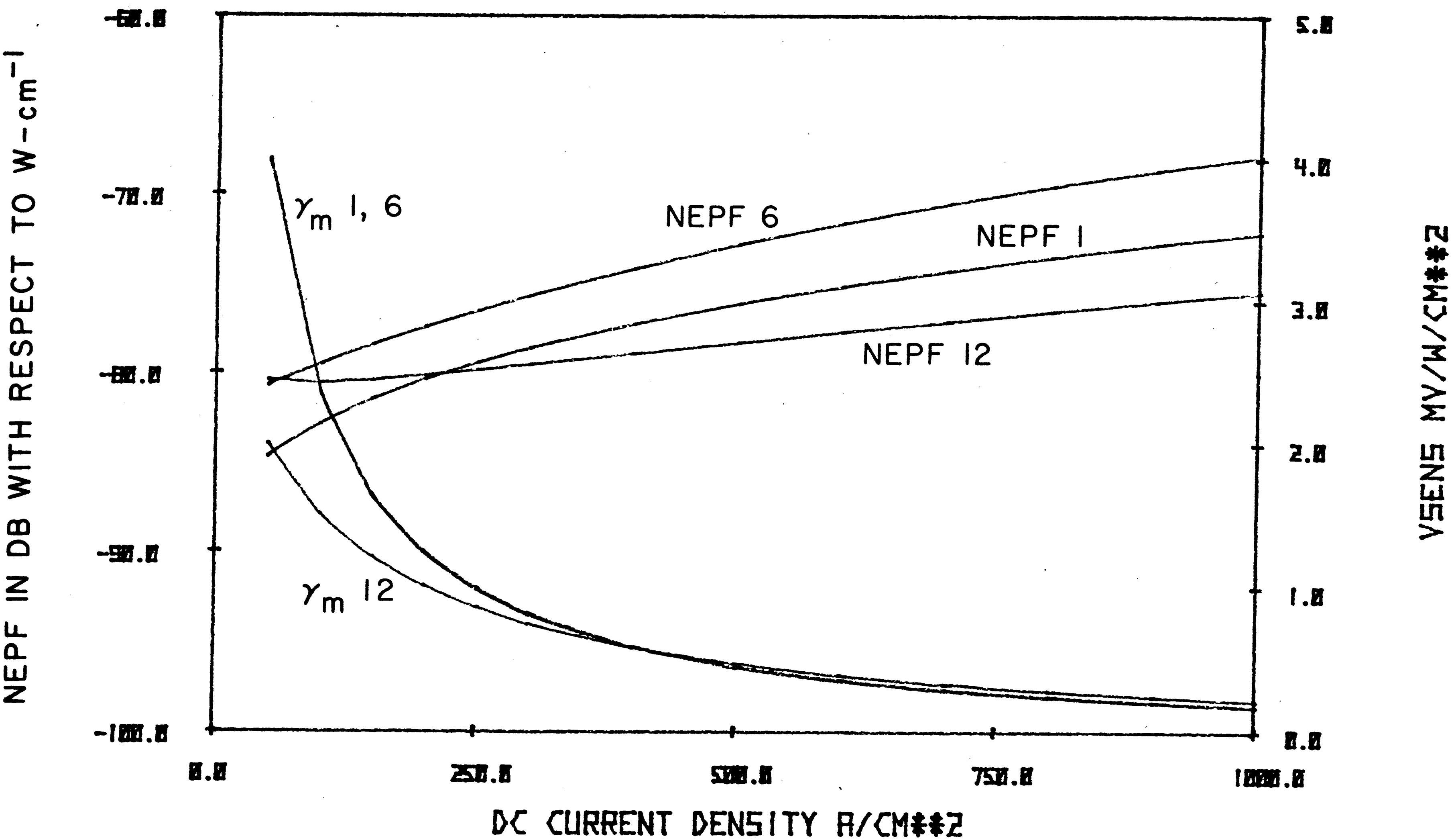

FIG. 4.12 VOLTAGE DETECTION SENSITIVITY AND NOISE EQUIVALENT POWER FACTOR AS A FUNCTION OF DC CURRENT DENSITY FOR BARITTS 1, 6 AND 12 AT 94 GHz. (VIDEO FREQUENCY = 30 MHz AND Δf = 1)

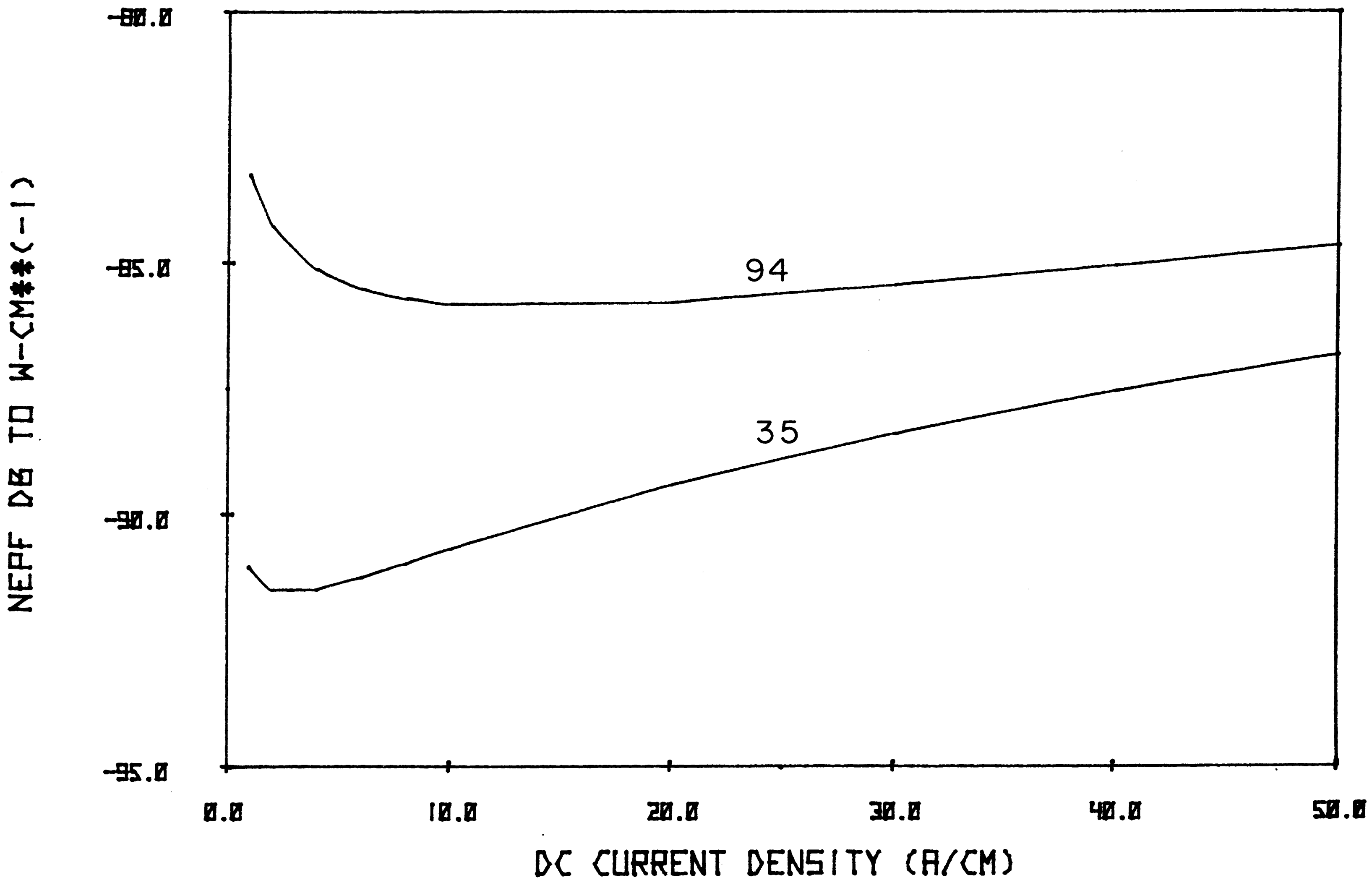

FIG. 4.13 NEPF FOR BARITT 1 AT 35 AND 94 GHz AS A FUNCTION OF DC CURRENT DENSITY.

source through the device drift region to the terminals. The transforming factor at first is not strongly dependent upon J_{dc} but then tends to decrease with increasing J_{dc}. The optimum bias point results from a tradeoff between this decrease and the increasing noise current source magnitude.

In Tables 4.12 and 4.13 the basic video detector parameters and the associated microwave impedance levels are shown for the various BARITT structures. All of the structures are biased at 50 A/cm^2. In Table 4.12 the frequency is 35 GHz, while in Table 4.13 the frequency is 94 GHz. When compared to the Schottky device data in Table 4.1, several differences are obvious. First the BARITT, as measured by γ_m, is a more sensitive detector. However, it has lower NEPFs which indicate that it is a noisier device at video frequencies. The extra noise present in the BARITT comes from both velocity fluctuation noise and from the transformation of the shot noise through the drift region. This transformation is roughly proportional to the square of the ratio of the total device length to the injection-region length. The other major difference is that while the Q of the Schottky device is near 1, the Q of the BARITT is typically of the order of 100. This will lead to some differences in impedance-matching considerations.

The tradeoff between NEP and impedance matching is illustrated in Figs. 4.14 and 4.15. In Fig. 4.14 the NEP and impedance parameters for BARITT 1 at 35 GHz with a dc current density of 4 A/cm^2 are plotted as functions of device diameter. Similar data is plotted in Fig. 4.15 for the RF frequency, 94 GHz, and current density, 10 A/cm^2. The dc current densities are the optimum values obtained from Fig. 4.13. As can be seen, while extremely sensitive detectors can be obtained by

Table 4.12

NEPF Values for BARITTs. (J_{dc} = 50 A/cm^2, 30 MHz Video Frequency, 35 GHz RF, Values in dB with Respect to W/cm)

BARITT	f_c (GHz)	γ_m [10^{-4} (V·cm^2/W)]	NEPF (dB per W·cm^{-1})	RDEV (Ω·cm^2)	XDEV (Ω·cm^2)
1	226.7	65.76	- 86.84	6.670E-5	- 8.560E-4
2	298.7	71.67	- 85.23	6.037E-5	- 1.302E-3
3	284.8	70.69	- 85.28	6.134E-5	- 1.724E-3
4	215.5	64.60	- 84.11	6.806E-5	- 2.168E-3
5	309.4	72.38	- 83.91	5.968E-5	- 2.600E-3
6	214.0	64.45	- 82.80	6.825E-5	- 3.034E-3
7	903.4	86.13	- 87.89	2.712E-5	- 8.590E-4
8	192.0	56.90	- 84.56	4.620E-5	- 1.316E-3
9	781.3	122.9	- 86.74	1.602E-5	- 1.750E-3
10	667.9	134.0	- 89.19	7.219E-6	- 8.677E-4
11	147.0	46.43	- 82.94	3.971E-5	- 1.315E-3
12	344.8	224.0	- 90.89	- 1.941E-6	- 8.747E-4

Table 4.13

NEPF Values for BARITTs. (J_{dc} = 50 A/cm^2, 30 MHz Video Frequency, 94 GHz RF, Values in dB with Respect to W/cm)

BARITT	f_c (GHz)	γ_m[10^{-4} (V·cm^2/W)]	NEPF (dB per W·cm^{-1})	RDEV (Ω·cm^2)	XDEV (Ω·cm^2)
1	518.4	39.92	- 84.67	9.117E-6	- 3.239E-4
2	516.5	39.83	- 83.68	9.159E-6	- 4.860E-4
3	516.1	39.81	- 82.79	9.169E-6	- 6.480E-4
4	515.4	39.78	- 82.00	9.184E-6	- 8.101E-4
5	515.4	39.78	- 81.31	9.185E-6	- 9.722E-4
6	515.0	39.76	- 80.70	9.194E-6	- 1.134E-3
7	426.2	30.03	- 83.32	5.592E-6	- 3.243E-4
8	426.6	30.04	- 81.79	5.583E-6	- 4.863E-4
9	426.0	30.02	- 80.62	5.597E-6	- 6.484E-4
10	370.6	23.95	- 81.71	3.891E-6	- 3.243E-4
11	370.7	23.96	- 80.06	3.888E-6	- 4.864E-4
12	334.4	20.00	- 80.41	2.880E-6	- 3.243E-4

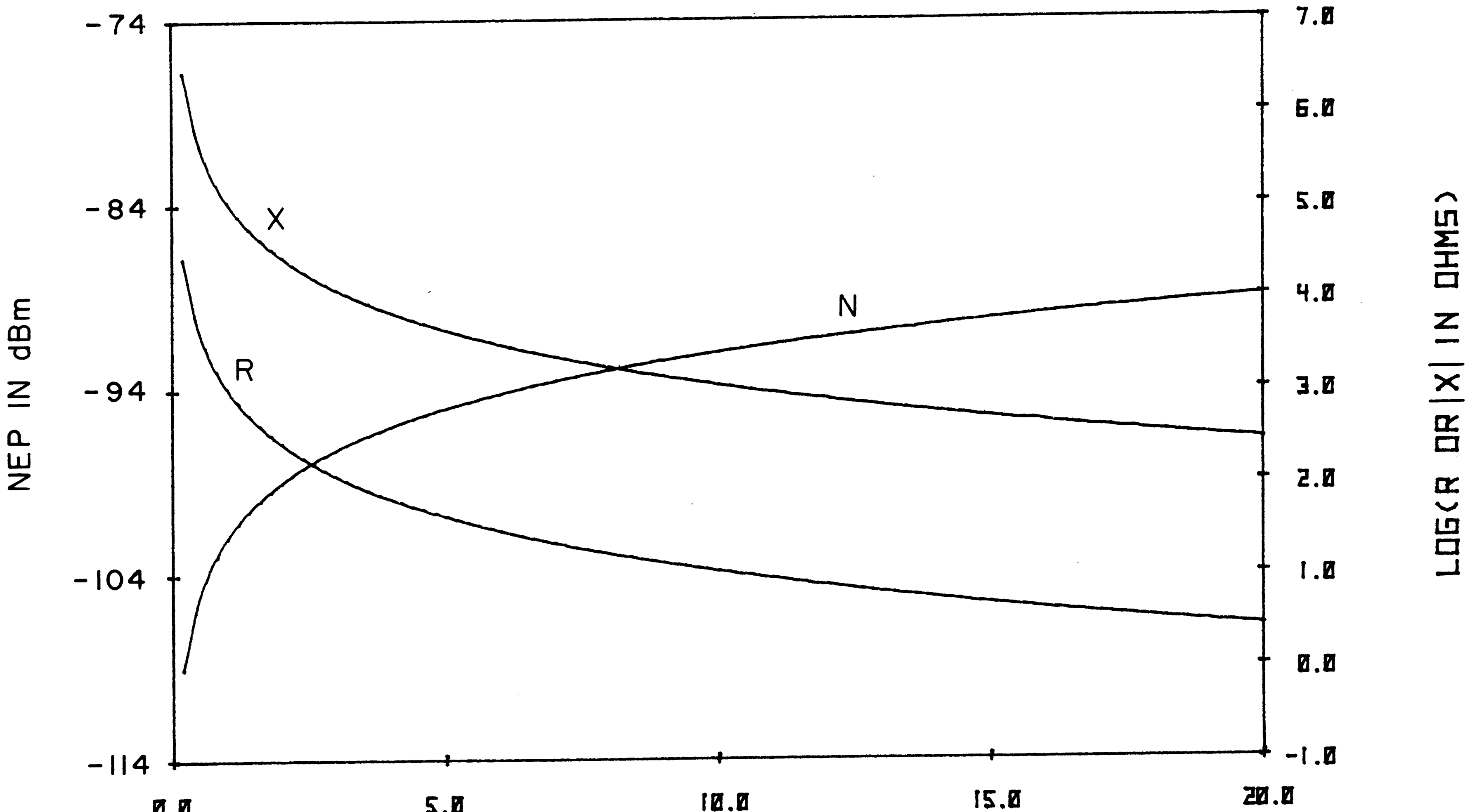

FIG. 4.14 NEP, RESISTANCE AND REACTANCE FOR BARITT 1 AS FUNCTIONS OF DIODE DIAMETER. (DC CURRENT DENSITY IS 4 A/cm^2 AND FREQUENCY IS 35 GHz)

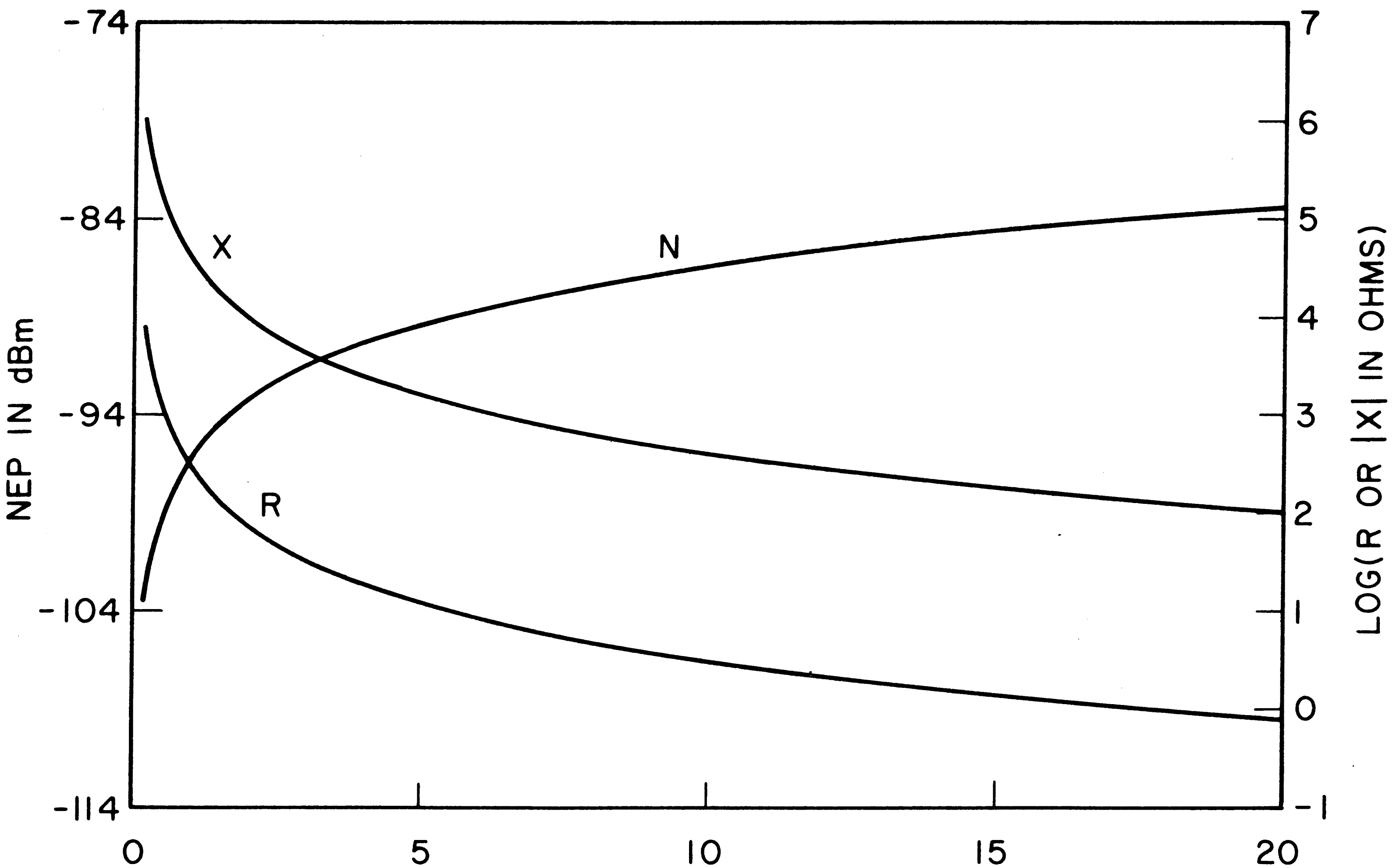

FIG. 4.15 NEP, RESISTANCE AND REACTANCE OF BARITT 1 AS FUNCTIONS OF DIODE DIAMETER. (DC CURRENT DENSITY IS 10 A/cm^2 AND FREQUENCY IS 94 GHz)

making the device very small, the impedance levels become too large to be matched. However, diameters in the 20-μm range yield NEPs of -80 to -90 dBm and acceptable impedances. These NEPs would be competitive with Schottky devices in this range.

Figure 4.15 can be used as an example of how a BARITT video detector might be designed. First, it is required that the real part of the device impedance be more than 1 Ω. If it is smaller, the various parasitic losses in the system would often begin to mask it from the matching circuit. Second, it is required that the imaginary part of the impedance be less than 500 Ω. If the reactance becomes much larger than this, it would be difficult to design efficient impedance transformers. Since the reactance and resistance of the BARITT differ so dramatically, such impedance transformers will probably be more important in BARITT detectors than they are in Schottky-barrier detectors. In Fig. 4.15 these two impedance criteria correspond to a diameter range of 9 to 17 μm. In this range the NEP values are -85 to -90 dBm. Such NEPs are comparable to some of the best Schottky results at 100 GHz. Since the diameter is a factor of 4 to 8 times larger, there will also be at least an order of magnitude increase in area when the BARITT is compared to the Schottky.

4.4 Discussion and Summary

4.4.1 Discussion. In the NEPF calculations, 1/f or flicker noise has been neglected. This was done because there is no generally valid physical model for 1/f noise. It is typically described in a totally phenomenological fashion by a noise corner frequency. For frequencies below this corner frequency, flicker noise dominates,

while for frequencies above the corner frequency other noise sources dominate. The noise corner frequency itself is essentially determined by purely technological considerations which are often themselves difficult to quantify. Examples include surface, contact, and material quality. The calculations presented here indicate that BARITT mounts should probably be designed differently from Schottky-barrier mounts as the BARITT is a much higher Q structure. However, it is theoretically possible to choose a low dc current density, device doping, length, and area simultaneously which should allow for an acceptable impedance level and lead to excellent performance as a video detector. This excellent performance arises from the higher voltage detection sensitivities exhibited by the BARITT device which allow it to overcome the higher video frequency noise levels that it exhibits when compared to the Schottky-barrier diode.

A central motivation behind the video detector study is the long BARITT hypothesis of McCleer.[30] McCleer proposed that a long BARITT, i.e., one in which the drift transit angle is many multiples of 2π, would be an excellent video detector. The central idea is that for long BARITTs, R_D becomes small and Eq. 4.25 then predicts large cutoff frequencies. The data presented here indicate that long BARITTs are not necessarily better than short ones. (It should be noted that the short BARITTs here, in fact, had negative-resistance bands which lay below the frequencies used in the video detector analysis.) Part of the reason for the lack of any dramatic improvement with increasing device length is seen by examining Eq. 4.23. Most of the performance gain in γ_m comes when f_c increases from the operating frequency f to several times f. For example, the performance

gain from an increase of $f_c = f$ to $f_c = 3f$ is 90 percent of the performance gain when f_c becomes infinite. For the frequencies considered here, any increase in f_c past several hundred GHz, therefore, will not dramatically improve the detector performance.

A related practical point is the reduction of the parasitic series resistance R_s. The long BARITT hypothesis simultaneously assumes that R_s is much less than R_D and that R_D is small. Once R_D is reduced below R_s, further reductions will not substantially alter the detection performance. As McCleer[30] has suggested, the long BARITT is best realized in a honeycomb structure. The results presented here indicate that the advantages of a long honeycomb BARITT will become more apparent at high millimeter- or submillimeter-wave frequencies.

4.4.2 Summary. In this chapter the device modeling techniques used were briefly reviewed. A collection of BARITT structures was designed.

Dc and small-signal characterizations were performed. A knee frequency was defined below which the device could be well represented as a constant conductance connected in parallel with a constant capacitance. An expression for the device length which maximized the margin against avalanche breakdown in a BARITT was derived. BARITTs were found to have much greater areas, lower thermal resistances, longer thermal time constants, and greater margins against avalanche breakdown than Schottky and Mott devices.

The properties of the BARITT device as a video detector were then studied. BARITTs were found to be both more sensitive and more noisy than the Schottky device. However, the gains in sensitivity can overcome the increased noise at low bias levels and allow the BARITT

to have very good NEPs. There is one important practical issue, however, and that is matching the device to the circuit. The results obtained here show that theoretically it is possible to build a BARITT which simultaneously has large enough resistance and small enough reactance to allow the matching problem to be surmounted.

In the 30- to 100-GHz range increasing the device length was found to have little effect on video detector performance. It must be remembered, however, that for frequencies well into the high millimeter-wave region, the long BARITT hypothesis certainly has not been tested. In this region a honeycomb BARITT structure certainly cannot, as yet, be ruled out as a good general purpose detector.

CHAPTER V. MIXER STUDIES

5.1 Introduction

In this chapter the analysis developed in Chapters II and III is used to study the performance of Schottky-barrier and BARITT devices as upper sideband downconverters. This is done using the computer analysis described in Appendix B. The logic flow is illustrated in Fig. 5.1. The analysis starts by determining the Fourier coefficients of the large-signal time-varying admittance of the nonlinear injection region. The deterministic portions of the analysis proceed to form the various conversion impedance matrices and uses them to calculate the conversion loss and impedances of the downconverter. In the noise portion of the analysis, the noise correlation matrix is formed and used in conjunction with the augmented network conversion impedance matrix to characterize the downconverter noise performance.

The computer program is a substantially modified and extended version of a program developed at NASA Goddard Space Flight Center.[117] The original program used a harmonic-balance procedure to numerically model the large-signal mixer device-circuit interaction. While accurate, this method is expensive, assumes a good knowledge of the embedding circuit, and does not always reliably converge. Since the investigations presented here are of a more exploratory nature, a single-frequency sinusoidal voltage is directly applied across the nonlinear injection region. No large-signal device-circuit interaction is considered. Tests show that this simpler approach provides reasonably accurate results at a substantially reduced cost.

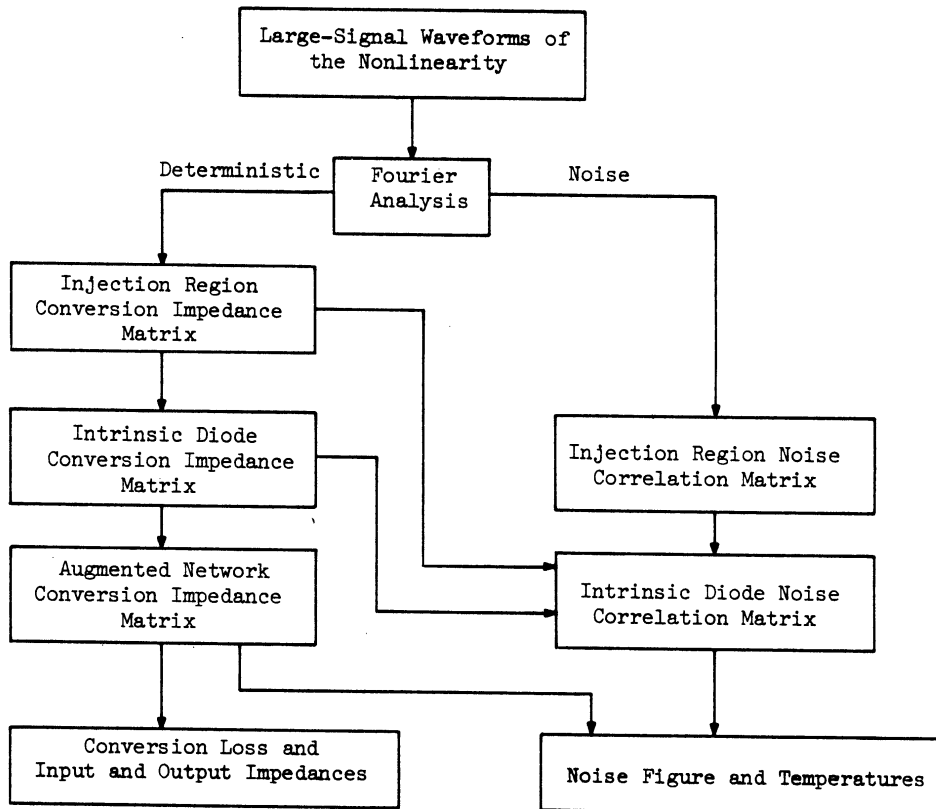

FIG. 5.1 BASIC FORMULATION OF A MIXER ANALYSIS.

Furthermore, there are no numerical convergence difficulties in this simple method.

The small-signal mixer analyses presented here all are for a three-frequency mixer unless otherwise specified. Similarly all assume an open-circuit termination at the image frequency. The embedding circuit termination at the IF is conjugate matched to the mixer IF output impedance unless this requires a negative resistance. Two different procedures are used to select the embedding circuit termination at the signal frequency. One is the minimum conversion loss selection described in Chapter II. The other optimizes the mixer noise performance and is described in Appendix C.

The mixer performance is characterized by its conversion loss, single-sideband noise figure and the impedance levels at the signal and intermediate frequencies. All of these quantities will be calculated as a function of LO drive level and frequency, dc current density, and IF. Additionally, the mixer stability analysis described in Chapter II is performed and the LO power absorbed by the diode is calculated. The main question which is addressed is whether a BARITT device is expected to be a useful downconverter in systems in the 30 to 120 GHz region.

5.2 Schottky-Barrier Mixer Diodes

In this section some Schottky-barrier mixer calculations are presented. These calculations are largely intended to be a standard of comparison for the transit-time device calculations and also as checks on the modeling accuracy as the performance of

Schottky-barrier mixers in this range has been extensively studied experimentally.

The first calculation consisted of rerunning the original sample problem (a 15-GHz Schottky-barrier mixer with an IF of 1.5 GHz) provided by NASA[117] using the various options for sideband termination. As can be seen from the results tabulated in Table 5.1, the effect of the various assumptions made here is to provide approximately 3 to 4 dB of drift in conversion losses and noise figures. Also, even in the original results of Siegel and Kerr, as a result of correlation effects, the noise figure is less than the conversion loss.

Next, the conversion loss of a 35-GHz mixer was calculated as a function of LO power. The diode parameters were chosen to match those of the experimental diode of Weinreb and Kerr.[100] Their experimental result is shown in Fig. 5.2, and the calculated curve is shown in Fig. 5.3. The comparison is satisfactory.

Next two Schottky diodes were studied. One was a 2.5-μm diameter diode operated at 94 GHz, while the other was a 5-μm diode operated at 35 GHz. The remaining parameters are those of Table 4.1. The injection-region RF driving voltage is plotted as a function of the LO power absorbed by the diode in Fig. 5.4. The mixer noise figure is shown in Fig. 5.5 as a function of drive level, in Fig. 5.6 as a function of dc current density, and in Fig. 5.7 as a function of IF. The corresponding conversion loss is shown in Fig. 5.8 as a function of drive level. These results are somewhat optimistic, especially for the 94-GHz diode. This is a result of the assumptions made in the model and also because the series resistance was assumed to be 5 Ω at all frequencies. The results, however, are sufficiently

Table 5.1

Tests Against the Original NASA Data

Option	Conversion Loss (dB)	Noise Figure (dB)	IF Output Impedance
Original NASA results[117]	6.51	4.12	94.14 + j (- 18.36)
Direct reruns with no options	6.47	4.15	93.86 + j (- 18.29)
Three-frequency mixer option	5.30	3.20	92.34 + j (- 19.27)
Three-frequency mixer with minimum L_c	5.19	3.17	86.94 + j (- 5.608)
Three-frequency mixer with open image and minimum L_c	4.61	3.77	105.9 + j (43.45)
Single-frequency injection region drive with no other options	8.74	5.46	334.6 + j (- 160.4)
Single-frequency drive and three-frequency mixer	4.33	1.80	123.8 + j (- 21.81)
Single-frequency drive, three-frequency mixer, minimize L_c	3.30	1.33	152.5 + j (- 51.16)
Single-frequency drive, three-frequency mixer, open image, minimize noise figure	1.98	1.43	166.5 + j (78.74)

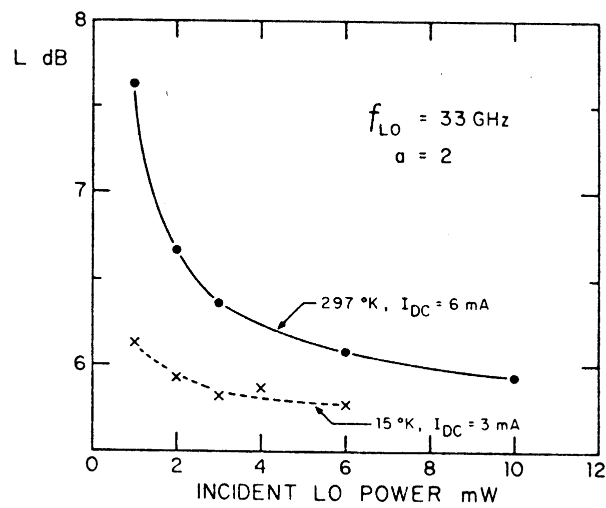

FIG. 5.2 EXPERIMENTAL SCHOTTKY-BARRIER MIXER CONVERSION LOSS AS A FUNCTION OF LO POWER LEVEL. (WEINREB AND KERR[100])

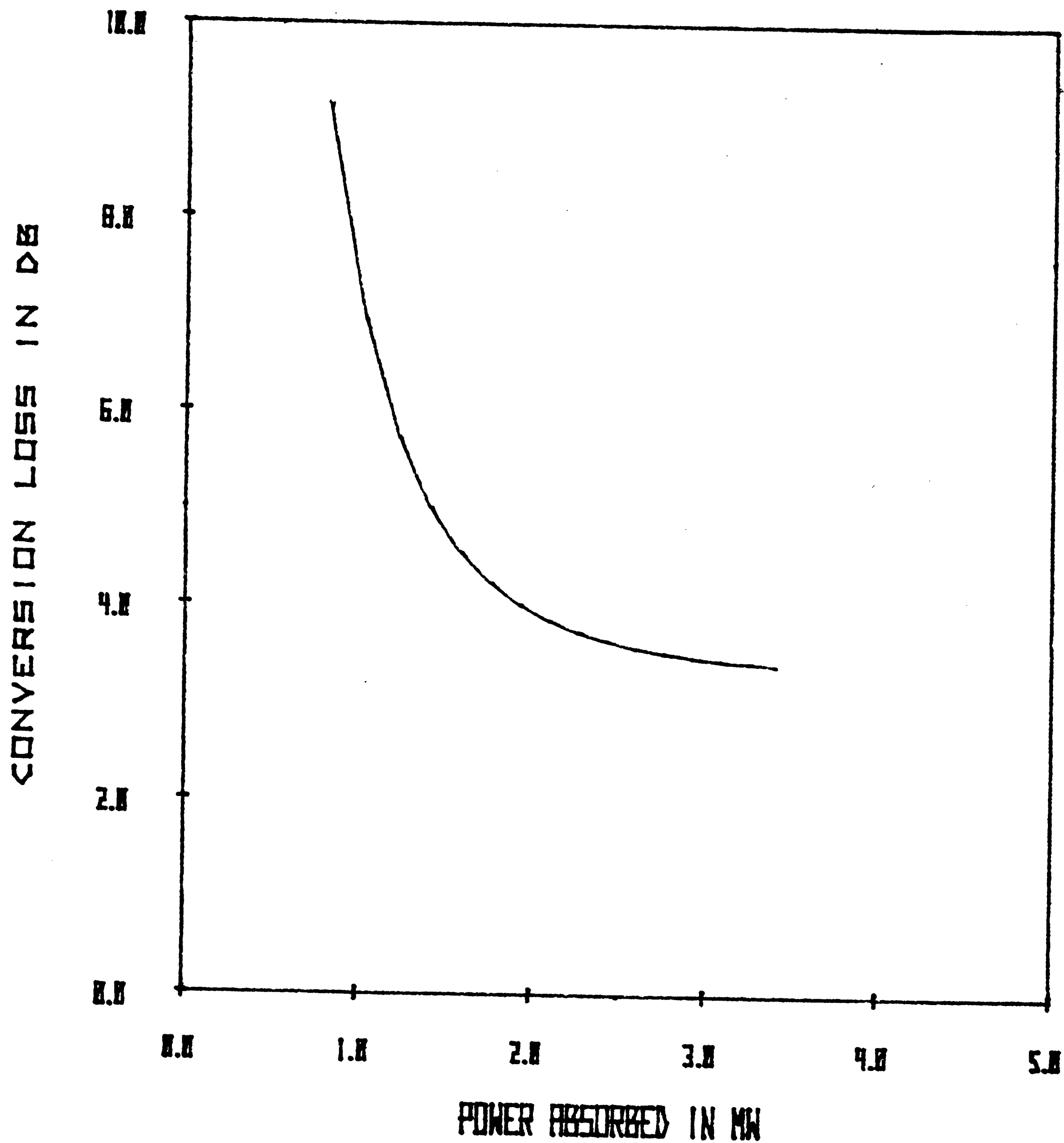

FIG. 5.3 THEORETICAL CONVERSION LOSS AS A FUNCTION OF ABSORBED LO POWER FOR THE SCHOTTKY DIODE OF FIG. 5.2.

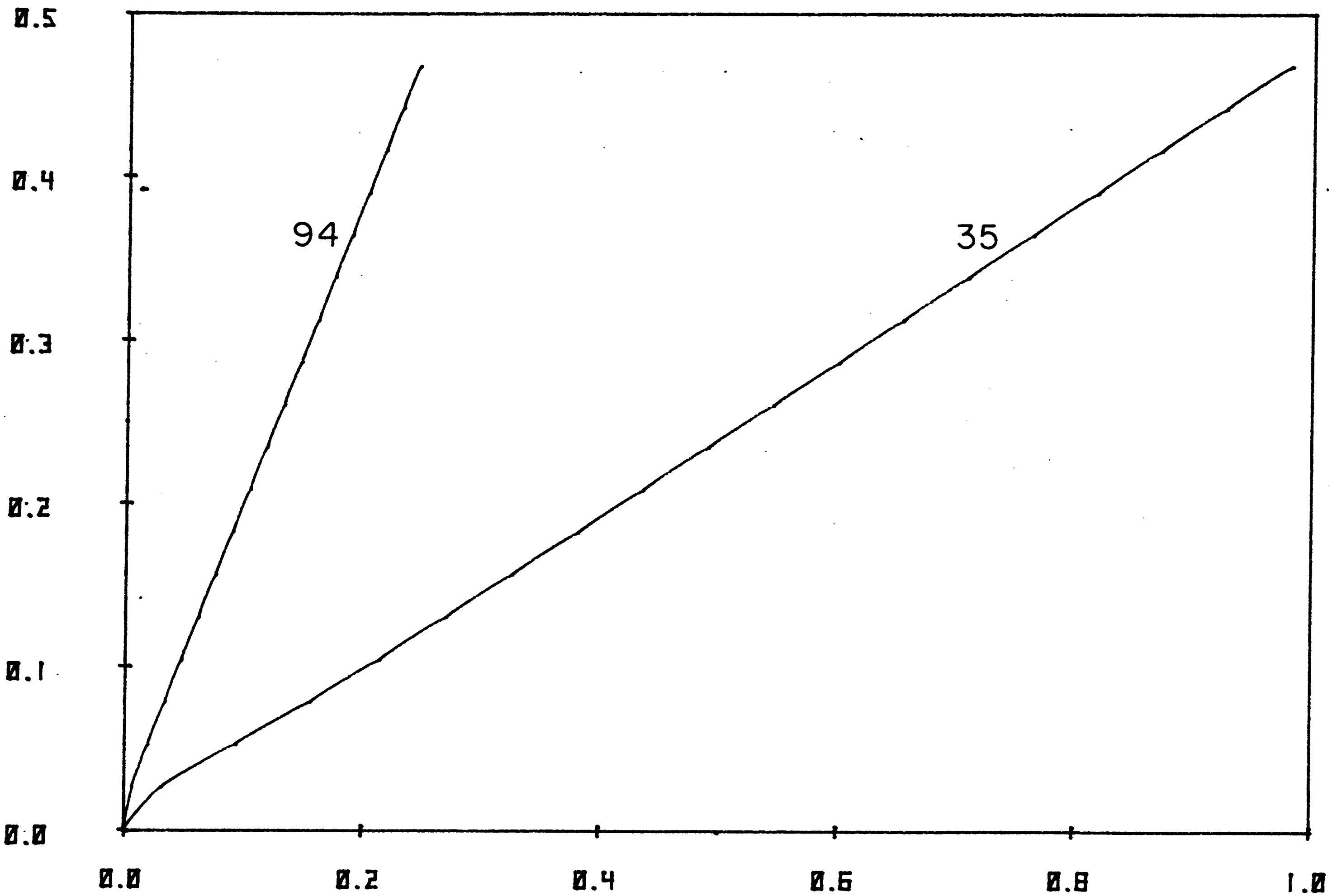

FIG. 5.4 INJECTION REGION DRIVING VOLTAGE AS A FUNCTION OF ABSORBED LO POWER. THE PARAMETER IS LO FREQUENCY IN GHz.

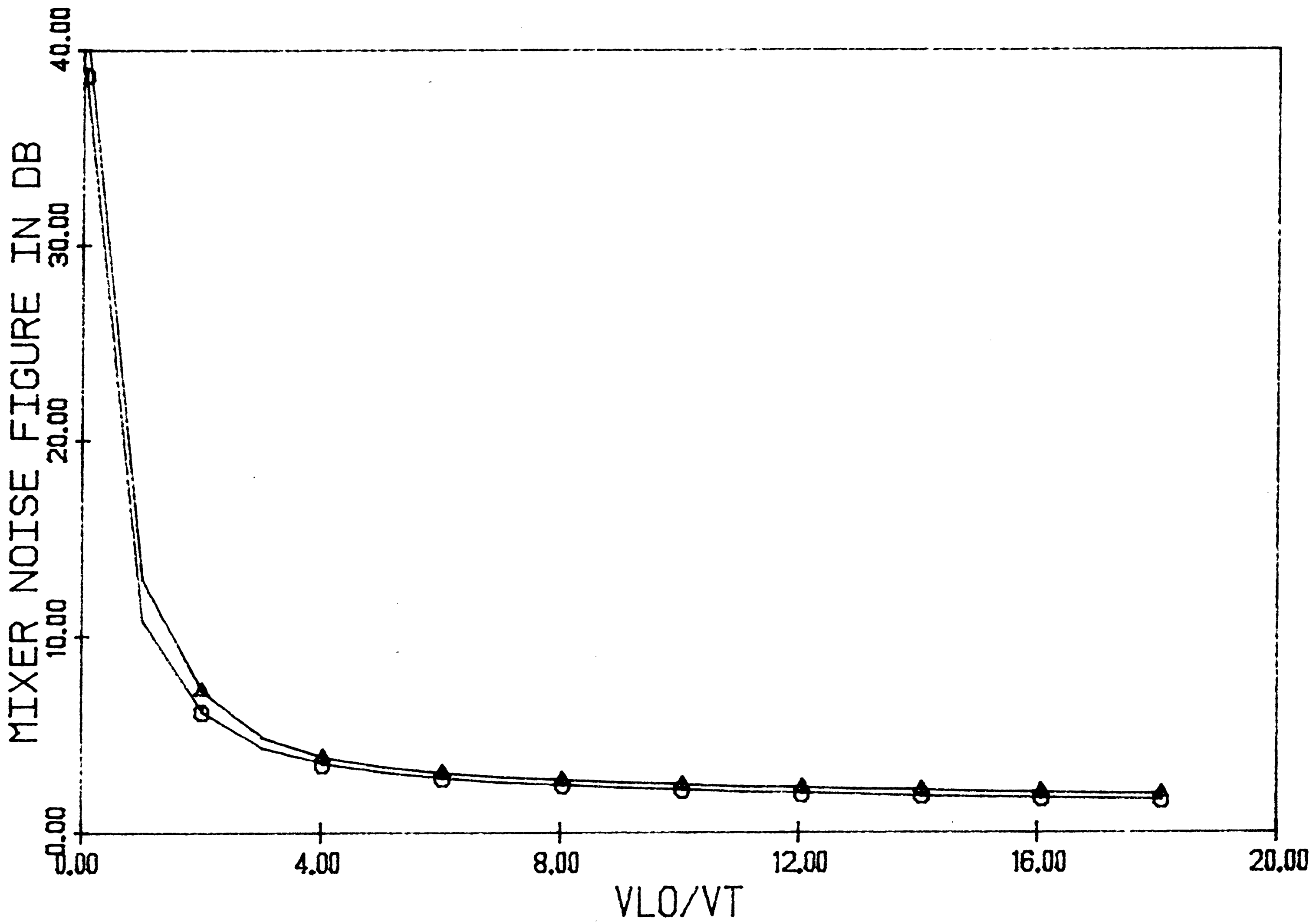

FIG. 5.5 MIXER NOISE FIGURE AS A FUNCTION OF INJECTION REGION DRIVE (NORMALIZED WITH RESPECT TO THE THERMAL VOLTAGE). THE CIRCLES ARE THE 94-GHz SCHOTTKY-BARRIER RESULT WHILE THE TRIANGLES ARE THE 35-GHz SCHOTTKY-BARRIER RESULT. (J_{dc} = 10,000 A/cm^2 AND THE IF IS 300 MHz)

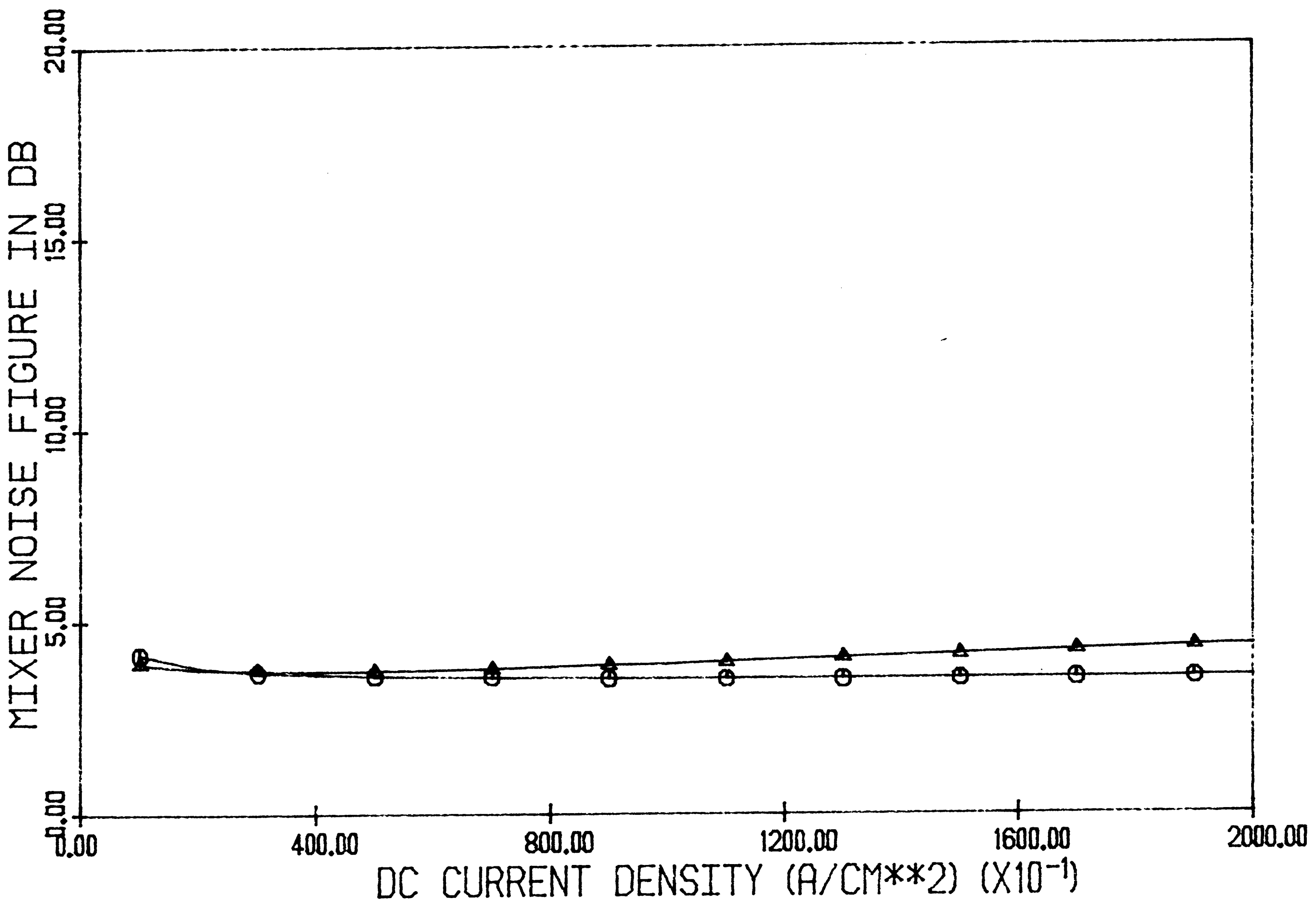

FIG. 5.6 MIXER NOISE FIGURE FOR SCHOTTKY-BARRIER MIXER AS A FUNCTION OF DC CURRENT DENSITY FOR A LO DRIVE OF $4V_T$. THE IF IS 300 MHz. THE CIRCLES ARE THE 94-GHz RESULT WHILE THE TRIANGLES ARE THE 35-GHz RESULT.

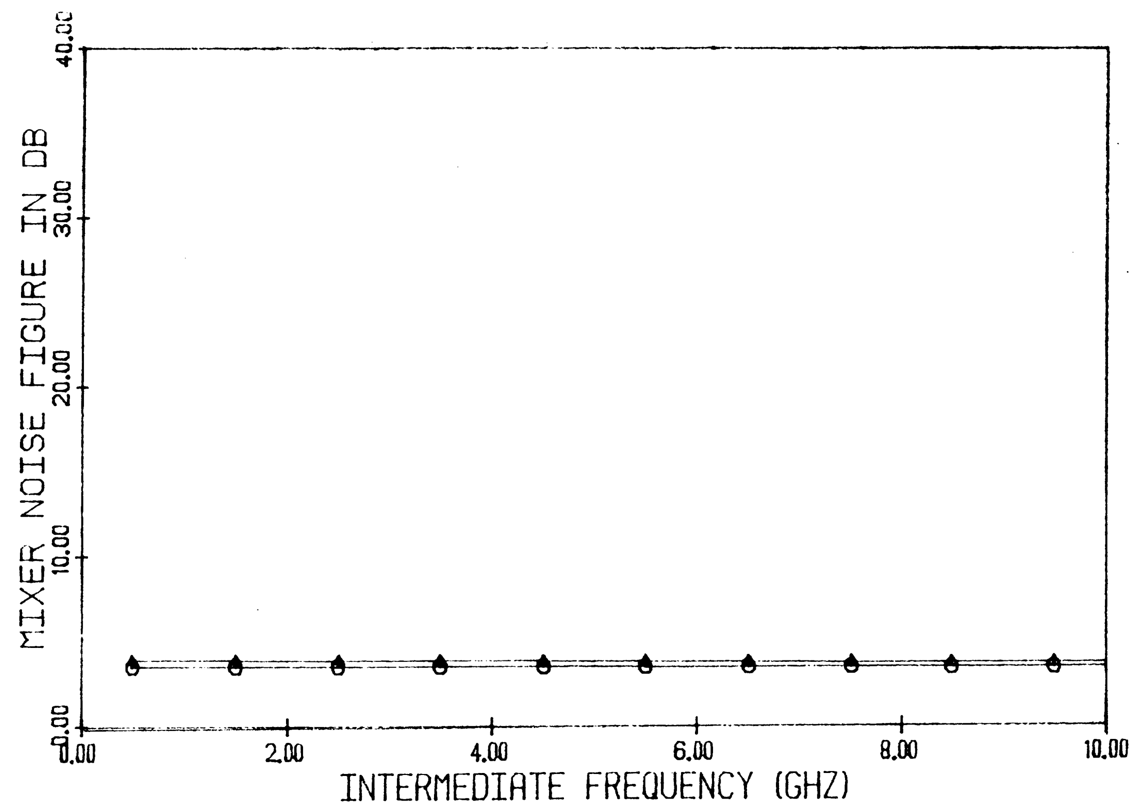

FIG. 5.7 MIXER NOISE FIGURE FOR SCHOTTKY BARRIER AS A FUNCTION OF INTERMEDIATE FREQUENCY. THE DC CURRENT DENSITY WAS 10,000 A/cm^2 AND THE LO DRIVE IS $4V_T$. THE CIRCLES ARE THE 94-GHz RESULTS WHILE THE TRIANGLES ARE THE 35-GHz RESULTS.

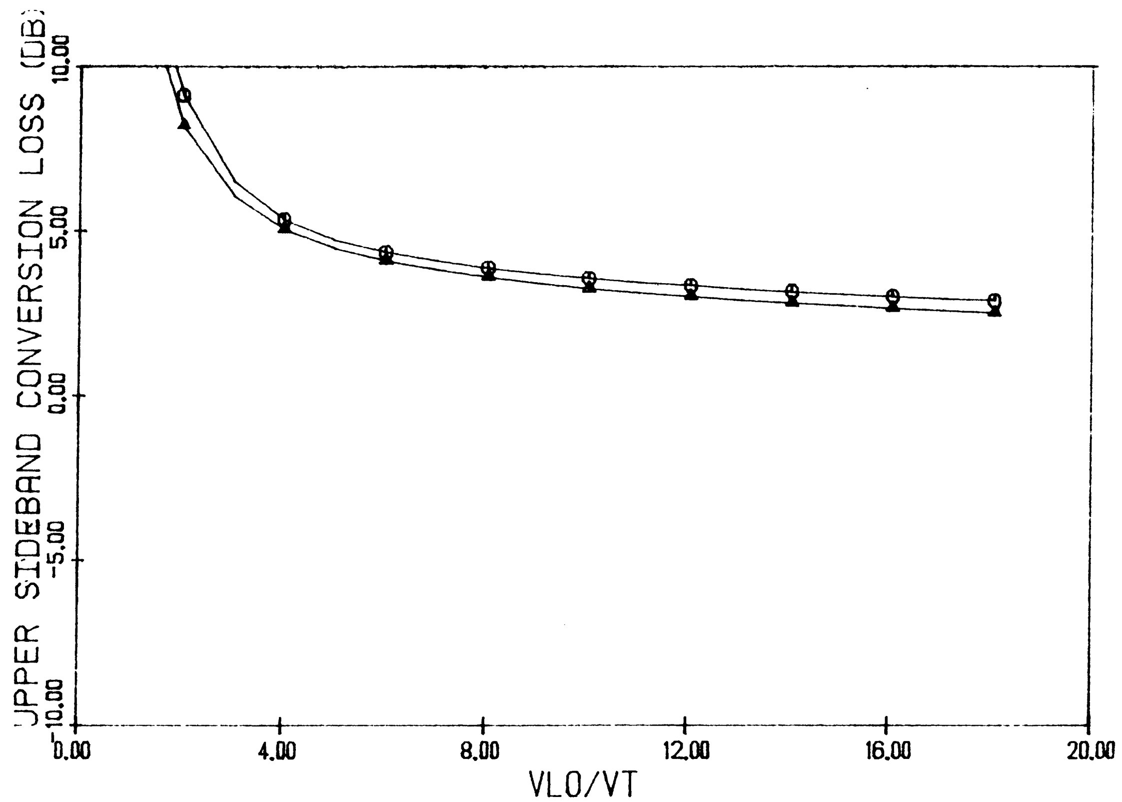

FIG. 5.8 CONVERSION LOSS FOR THE SCHOTTKY BARRIER AS A FUNCTION OF LO DRIVE. J_{dc} = 10,000 A/cm^2 AND THE IF IS 300 MHz. THE CIRCLES ARE THE 94-GHz RESULTS WHILE THE TRIANGLES ARE THE 35-GHz RESULTS.

valid to be used as a basis for comparison with later transit-time device results.

The mixer IF output impedance is shown as a function of dc current density in Fig. 5.9. The general impedance level is several hundred Ω. In Fig. 5.9 it can be seen that as dc current density increases the reactance decreases while the resistance flattens. This is partly a result of the decreasing capacitance of the barrier associated with an increasing level of forward bias.

These calculations were carried out using the signal frequency embedding circuit impedance which minimizes the noise figure. The resulting impedance is shown in Figs. 5.10 and 5.11. These impedance levels could be attained in realistic circuits.

5.3 BARITT Mixers

5.3.1 Introduction. In this section the performance of BARITT devices as mixers is studied. The 12 BARITTs defined in Table 4.2 are surveyed using the optimal conversion loss signal-frequency embedding circuit termination. Then various aspects of BARITT performance as a mixer are studied for devices 1, 6 and 12 in some detail. This second portion of the study will largely use the optimal noise figure termination. A series resistance of 0.1 Ω is used in all calculations, and all the devices will be assumed to have a diameter of 87.5 μm.

5.3.2 The Optimal Conversion Loss Survey. The first step of this survey was to "sweep" each BARITT with a wide range of LO voltages at both 35 and 94 GHz. The results showed that approximately four to five times the thermal voltage (0.0259) was needed to obtain good mixer conversion loss. The dependency of LO voltage on LO power is shown

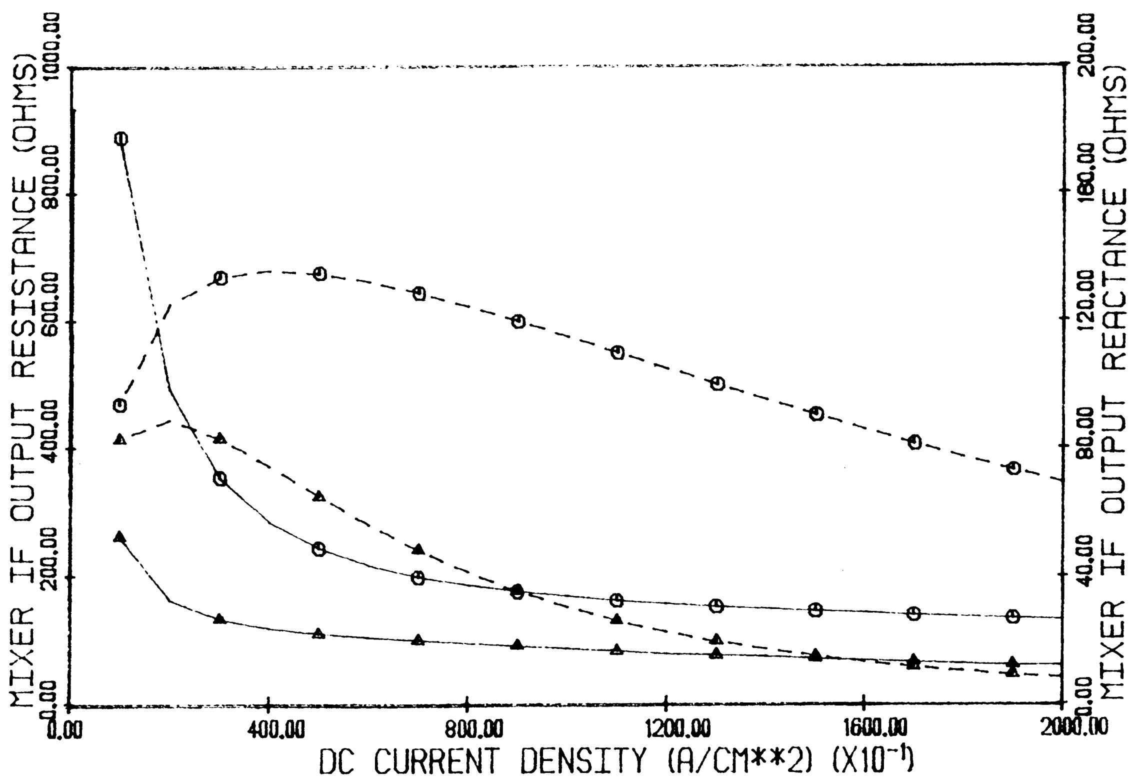

FIG. 5.9 MIXER IF OUTPUT IMPEDANCE FOR THE SCHOTTKY BARRIER AS A FUNCTION OF DC CURRENT DENSITY. THE IF IS 300 MHz AND THE LO DRIVE IS $4V_T$. THE CIRCLES ARE THE 94-GHz RESULTS WHILE THE TRIANGLES ARE THE 35-GHz RESULTS. —— IS RESISTANCE AND --- IS REACTANCE.

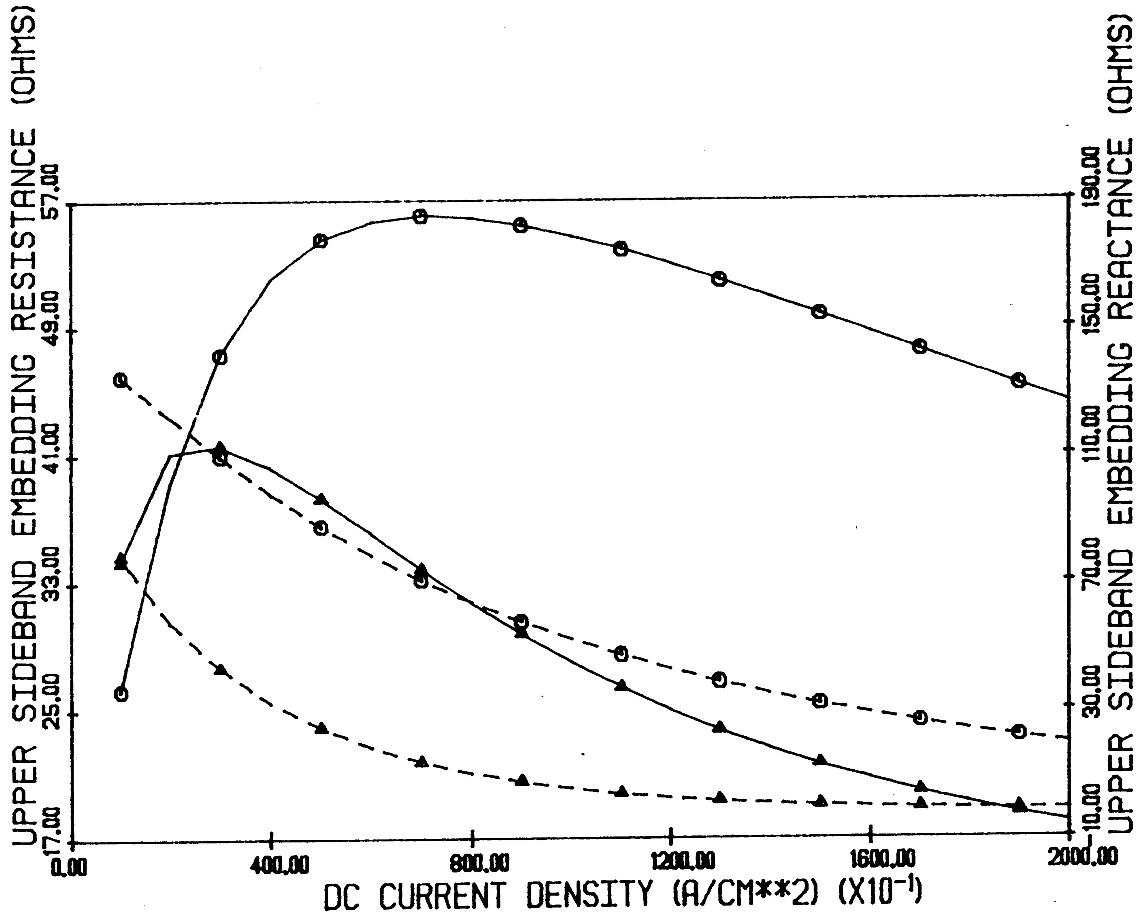

FIG. 5.10 THE SIGNAL FREQUENCY EMBEDDING CIRCUIT IMPEDANCE AS A FUNCTION OF DC CURRENT DENSITY. ALL PARAMETERS AND DESCRIPTIONS ARE IDENTICAL WITH THOSE OF FIG. 5.9.

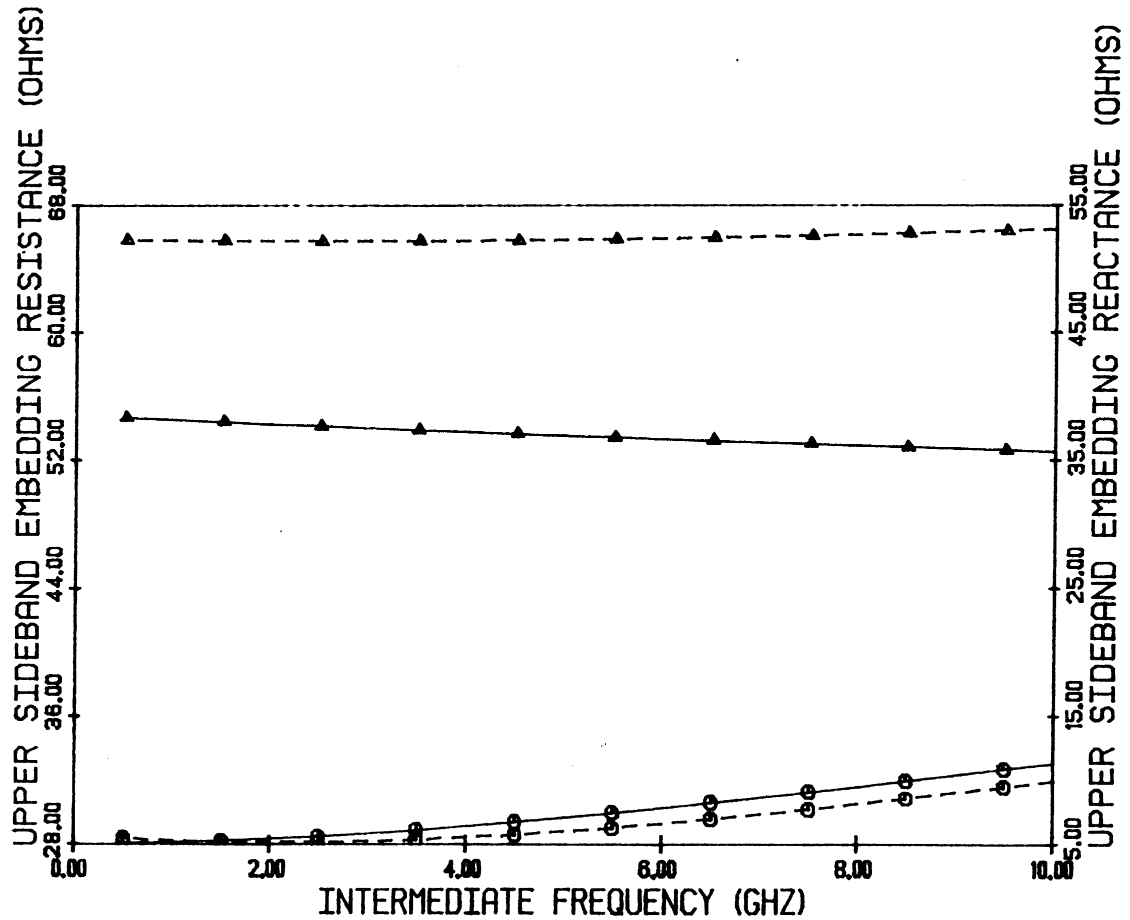

FIG. 5.11 THE SIGNAL FREQUENCY EMBEDDING CIRCUIT IMPEDANCE AS A FUNCTION OF IF. THE LO DRIVE IS $4V_T$ AND THE DC CURRENT DENSITY IS 10,000 A/cm². THE CIRCLES ARE THE 94-GHz DATA AND THE TRIANGLES ARE THE 35-GHz DATA. —— IS RESISTANCE AND --- IS REACTANCE.

in Figs. 5.12 and 5.13. LO powers of 0.5 to 2 mW are absorbed when the injection-region driving voltage is 0.1 V. Length does not greatly affect the absorbed power while doping does. This is a consequence of operation at frequencies higher than the negative-resistance band.

The next survey swept the dc current density in steps of 25 A/cm^2 over the range of 25 to 500 A/cm^2 at both 35 and 94 GHz. The results are summarized in Tables 5.2 and 5.3. Low current density was found to minimize the conversion loss except in short devices. For the BARITTs of 2 μm length, 35 and 94 GHz fall in or near harmonics of the negative-resistance band. For BARITTs 7, 10 and 12, even though at all times the total device resistance was positive in this study, the drift region resistance was negative at 35 GHz. In BARITT 6 conversion gain is obtained at 35 GHz which falls near the third harmonic of the negative-resistance band of this device and in the highly doped short BARITTs as well. It is interesting to note that this conversion gain is not associated with the LO, signal or intermediate frequencies. The optimal signal frequency termination and IF output impedance had achievable values in these devices. All the mixers in both the LO drive sweep and the dc current density sweep were unconditionally stable.

The next survey biased each BARITT at the optimal dc current density found in the dc current density sweep. The IF range of 0.5 to 10 GHz was then swept in 0.5-GHz steps. The results of this IF sweep are reported in Tables 5.4 and 5.5. These results differ from the previous results mainly in the existence of unstable mixers. When the IF frequency fell in a range where the device is expected to have a

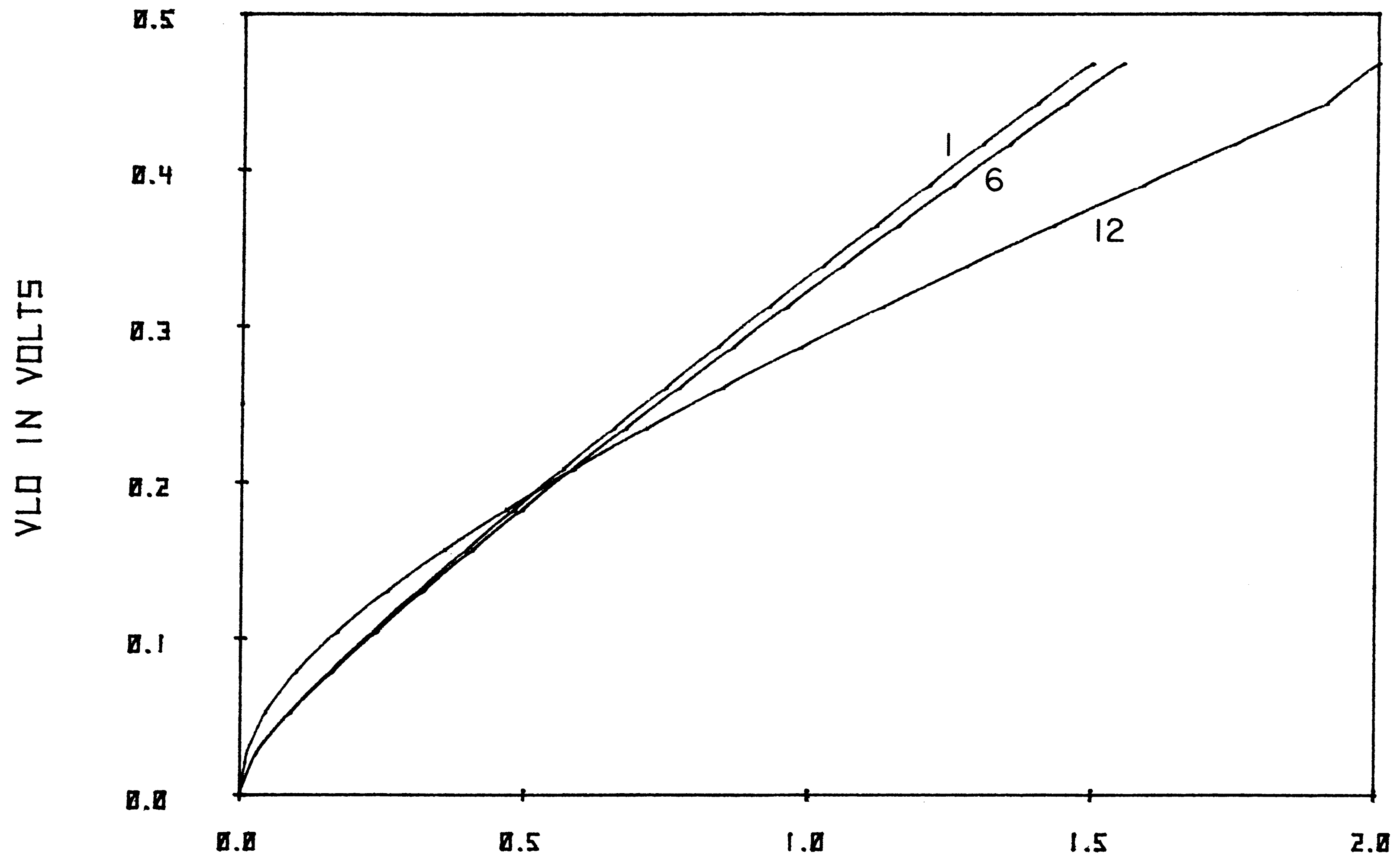

FIG. 5.12 LO INJECTION REGION DRIVE AS A FUNCTION OF LO ABSORBED POWER FOR BARITTS 1, 6, AND 12. THE LO FREQUENCY IS 35 GHz AND $J_{dc} = 500$ A/cm^2.

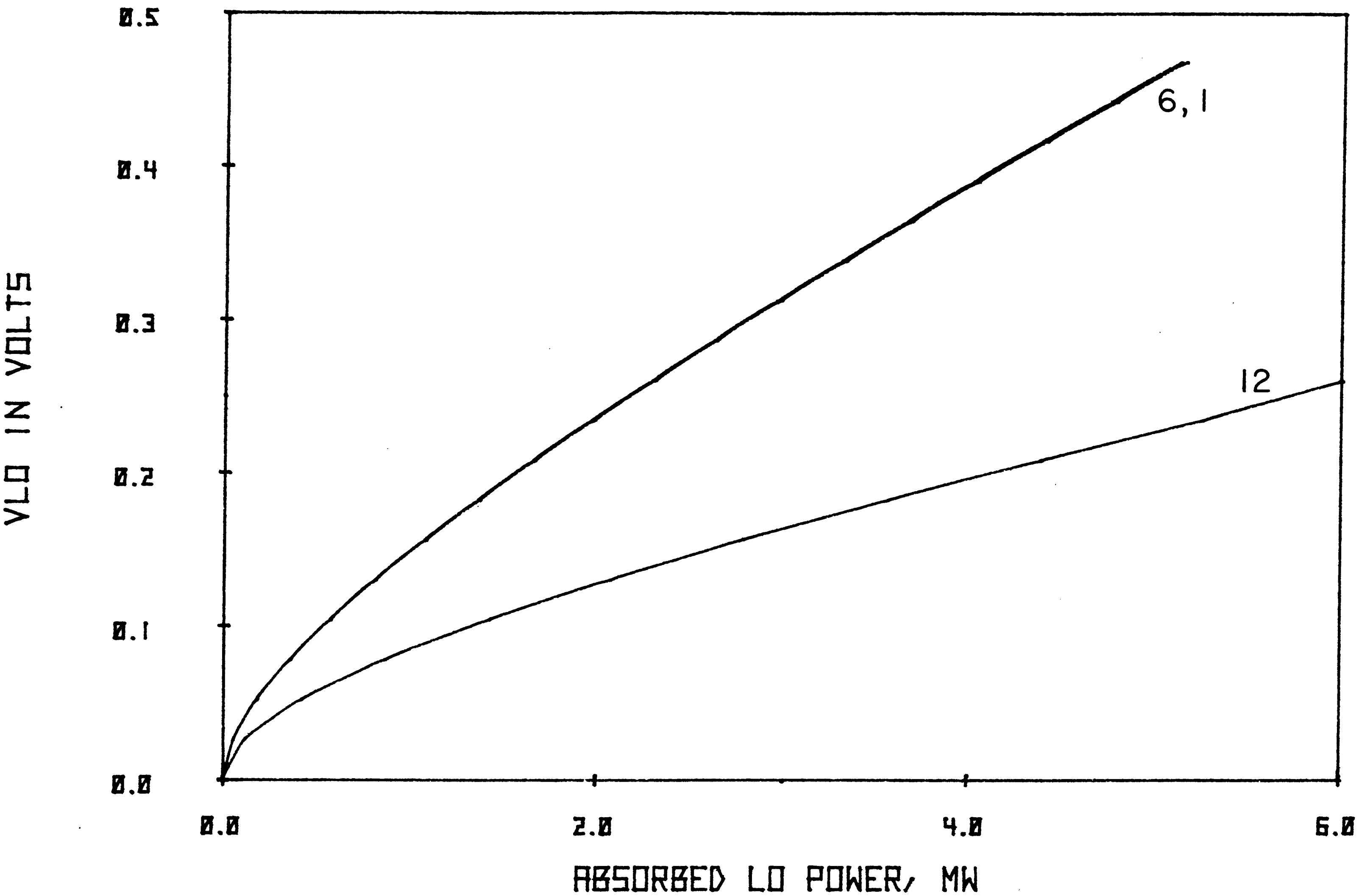

FIG. 5.13 LO INJECTION REGION DRIVE AS A FUNCTION OF ABSORBED LO POWER FOR BARITTS 1, 6, AND 12 AT 94 GHz.

Table 5.2

Dc Current Density Survey at 35 GHz*

Device	$J_{dc,min\ L_c}$	L_c	Z_{e_1}	ZIFOUT	DIA_{IF}	DIA_{SG}
1	25	2.764	0.404 + j14.4	20.2 - j13.9	175.8	7.9
2	25	1.534	0.380 + j21.6	331.1 - j33.94	225	7.6
3	25	0.68	0.364 + j28.7	507.5 - j33.61	279	7.46
4	50	1.67	0.548 + j35.9	529.1 - j35.44	322	7.65
5	25	- 0.37	0.354 + j43.1	870.2 - j82.36	365	7.36
6	25	- 0.49	0.371 + j50.3	1094.8 - j123.3	410	7.53
7	50	0.17	0.305 + j14.3	147.1 + j9.95	150	6.82
8	25	0.29	0.303 + j0.216	366.9 - j67.89	228	6.82
9	25	- 2.72	0.185 + j28.8	454.24 - j59.23	264	5.32
10	100	- 2.853	0.199 + j14.4	98.17 - j11.85	122.5	5.52
11	25	- 0.00856	0.274 + j21.6	366.1 - j82.7	236.9	6.48
12	200	- 7.038	0.0927 + j14.6	61.23 - j9650.6	9.681	3.77

* All devices have an area of 0.601×10^{-4} cm^2 and an injection region low drive of 0.104 V. $J_{dc,min\ L_c}$ is the dc current density (A/cm^2) at which the lowest L_c was found. L_c is that value. Z_{e_1} is the signal frequency termination and ZIFOUT is the mixer IF output impedance. DIA_{IF} and DIA_{SG} are the diameters which yield a 50-Ω match at the IF and signal frequency, respectively.

Table 5.3

Dc Current Density Survey at 94 GHz*

Device	$J_{dc,min\ L_c}$	L_c	Z_{e_1}	ZIFOUT	DIA_{IF}	DIA_{SG}
1	50	6.57	0.167 + j5.38	122.1 - j6.373	136.7	5.06
2	25	5.70	0.141 + j8.07	289.5 - j24.46	210.4	4.6
3	25	5.00	0.140 + j10.80	432.6 - j39.10	257.1	4.6
4	25	4.47	0.139 + j13.4	592.3 - j57.07	301.2	4.6
5	25	4.04	0.138 + j16.1	770.4 - j78.54	343	4.6
6	25	3.70	0.137 + j18.8	965.1 - j103.8	384	4.6
7	75	5.21	0.158 + j5.38	102.2 - j4.393	125	4.9
8	50	4.33	0.142 + j8.07	214.6 - j13.16	181	4.7
9	50	3.65	0.140 + j10.8	324.5 - j21.46	223	4.6
10	100	4.41	0.152 + j5.38	90.85 - j3.196	118	4.8
11	100	3.53	0.150 + j8.07	164.39 - j6.92	159	4.8
12	150	3.82	0.154 + j5.38	77.54 - j2.030	109	4.9

* All devices have an area of 0.601×10^{-4} cm^2 and an injection region low drive of 0.104 V. $J_{dc,min\ L_c}$ is the dc current density (A/cm^2) at which the lowest L_c was found. L_c is that value. Z_{e_1} is the signal frequency termination and ZIFOUT is the mixer IF output impedance. DIA_{IF} and DIA_{SG} are the diameters which yield a 50-Ω match at the IF and signal frequency, respectively.

Table 5.4

IF Sweep at 35 GHz.

Device	J_{dc}	IF^*_{opt}	L_c	DIA_{IF}	DIA_{SG}	Stability Tests
1	25	1	2.774	170	7.7	
2	25	10	- 1.81	18	3.9	
3	25	8	- 4.91	19	2.8	Conditionally unstable 8.5 to 10
4	50	8	- 4.26	57	5.1	Conditionally unstable 8.5 to 10
5	25	6	- 8.19	23	1.7	Conditionally unstable 6.5 to 10
6	25	5	- 4.17	91	5.5	Conditionally unstable 5.5 to 10
7	50	0.5	2.28	151	6.8	
8	25	10	- 2.79	33	4.9	
9	25	8.5	- 6.54	25	3.1	Conditionally unstable 9 to 10
10	100	0.5	- 2.72	123	5.6	
11	25	10	- 2.76	39	4.9	
12	175	0.5	- 6.63	100	3.9	

* IF_{opt} is the IF at which the minimum L_c was found.

Table 5.5

IF Sweep at 94 GHz

Device	J_{dc}	IF^*_{opt}	L_c	DIA_{IF}	DIA_{SG}	Stability Tests
1	25	1	6.69	155	4.7	
2	25	10	4.96	32	4.4	
3	25	9	- 0.20	23	3.6	Conditionally unstable 9.5 to 10
4	25	7.5	- 0.84	36	3.8	Conditionally unstable 8.0 to 10
5	25	6.5	- 0.99	51	3.9	Conditionally unstable 7 to 10
6	25	6	- 2.56	50	3.7	Conditionally unstable 6.5 to 10
7	75	1	5.07	125	4.9	
8	50	10	3.40	57	4.4	
9	50	10	0.63	47	4.2	
10	100	1	4.20	118	4.8	
11	100	10	2.88	76	4.5	
12	175	1	3.58	107	4.9	

* IF_{opt} is the IF at which the minimum L_c was found.

small-signal negative resistance, the mixers were no longer necessarily unconditionally stable, and at times the optimal conversion loss criteria for the embedding circuit signal frequency impedance yielded unrealizable values, i.e., complex valued conductances. The general pattern is illustrated in Figs. 5.14 and 5.15. As the IF frequency increases the conversion gain increases until a point is reached where the mixer is no longer unconditionally stable. This occurs near the lower edge of the small-signal negative-resistance band of the device. The effect is less pronounced at 94 GHz than it is at 35 GHz. The instability is associated with the negative values for g'_{oo}. The accuracy of the device model is such that the difference between the -0.3 and 0 dB figures is insignificant. Therefore even within the limitation imposed by the assumption of a single-frequency LO voltage and three-frequency mixer analysis it cannot be concluded that conversion gain occurs at the lower IF range in Fig. 5.14.

In the final survey, the LO frequency was varied at 5-GHz steps from 35 to 120 GHz. Optimum performance of all devices occurred at the lower end of this range. The conversion loss data and embedding circuit signal frequency impedance data are shown in Figs. 5.16 and 5.17.

5.3.3 Self-Oscillating BARITT Mixers. As BARITT 12 has a small-signal negative resistance at 35 GHz, it could potentially be applied as a self-oscillating BARITT mixer. The dc current density and LO drive were varied in an attempt to find a self-oscillating BARITT mixer in this device. As is seen in Fig. 5.18, where the LO power absorbed is shown as a function of dc current density, such a mixer was found. The noise figure is shown in Fig. 5.19, the conversion loss in Fig. 5.20, and the mixer IF output impedance is shown in Fig. 5.21. The minimum noise

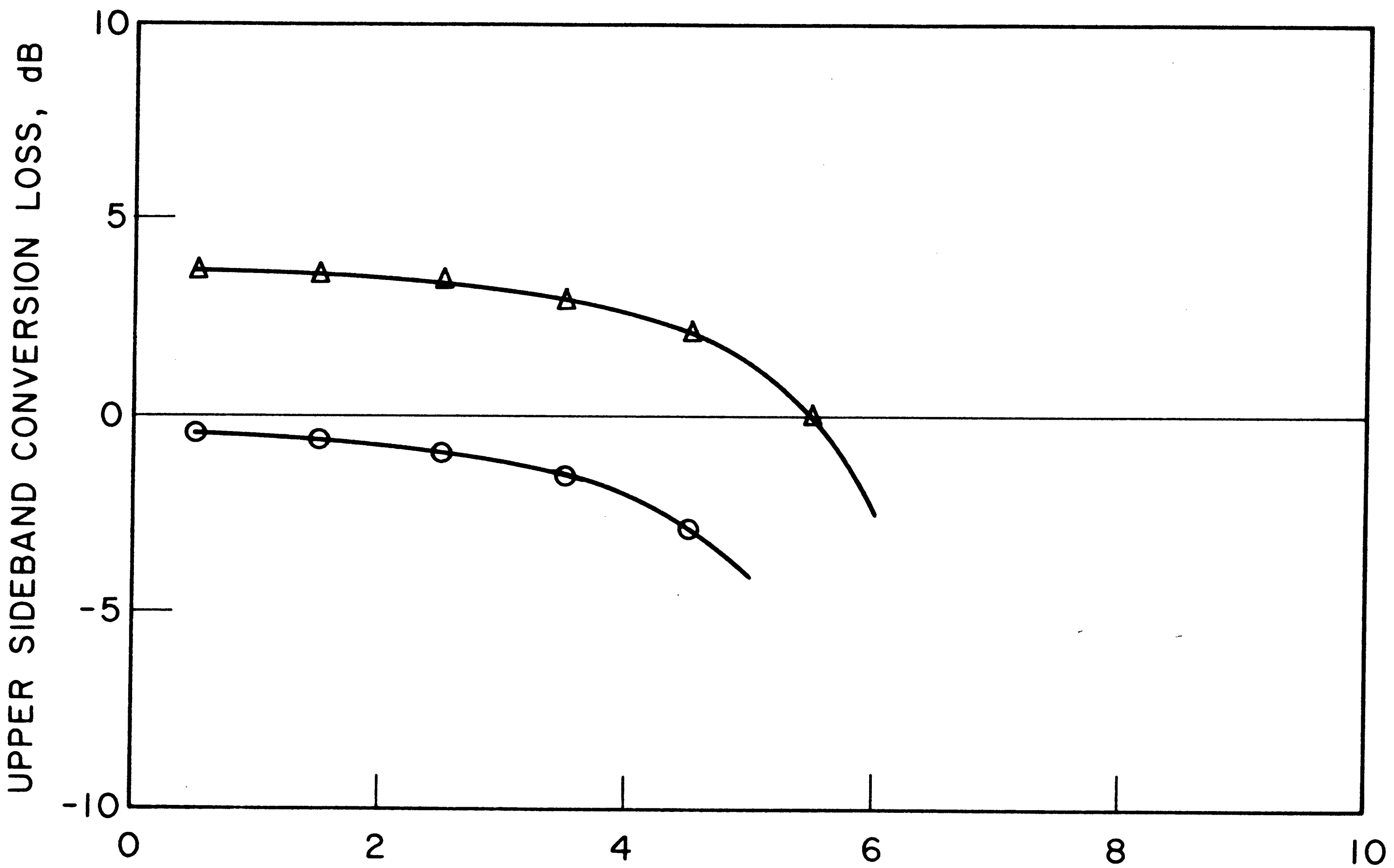

FIG. 5.14 THE CONVERSION LOSS AS A FUNCTION OF IF FOR BARITT 6. THE LO DRIVE IS $4V_T$ AND J_{dc} = 25 A/cm². THE TRIANGLES ARE THE 94-GHz LO DATA AND THE CIRCLES ARE THE 35-GHz DATA.

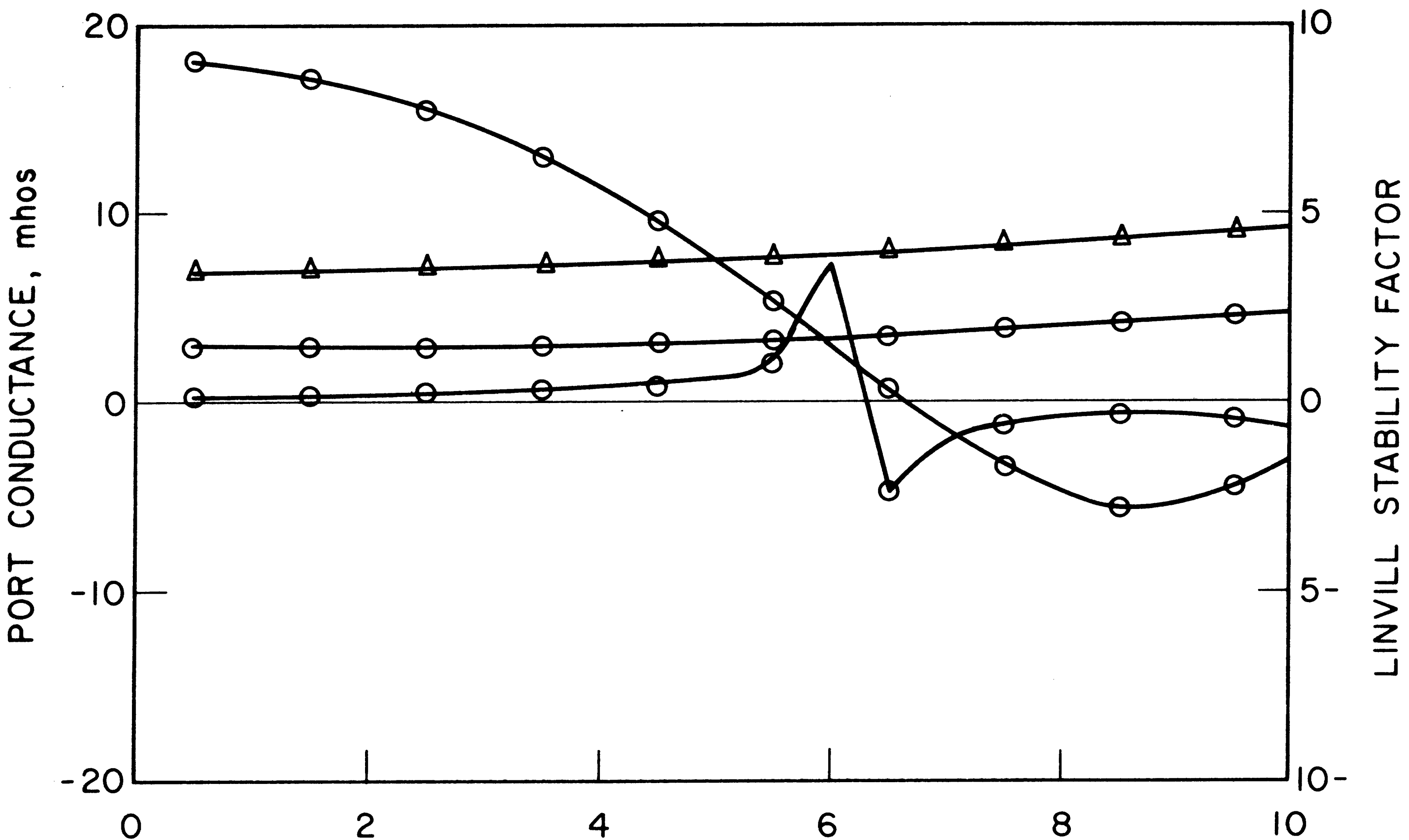

FIG. 5.15 STABILITY ANALYSIS FACTORS AS A FUNCTION OF IF FOR BARITT 6. THE LO DRIVE AND J_{dc} ARE IDENTICAL WITH THOSE OF FIG. 5.16. THE CIRCLES ARE THE 35-GHz DATA WHILE THE TRIANGLES ARE THE 94-GHz DATA. —— IS g'_{oo} , --- IS g'_{11} AND – – – IS LINVILL STABILITY FACTOR.

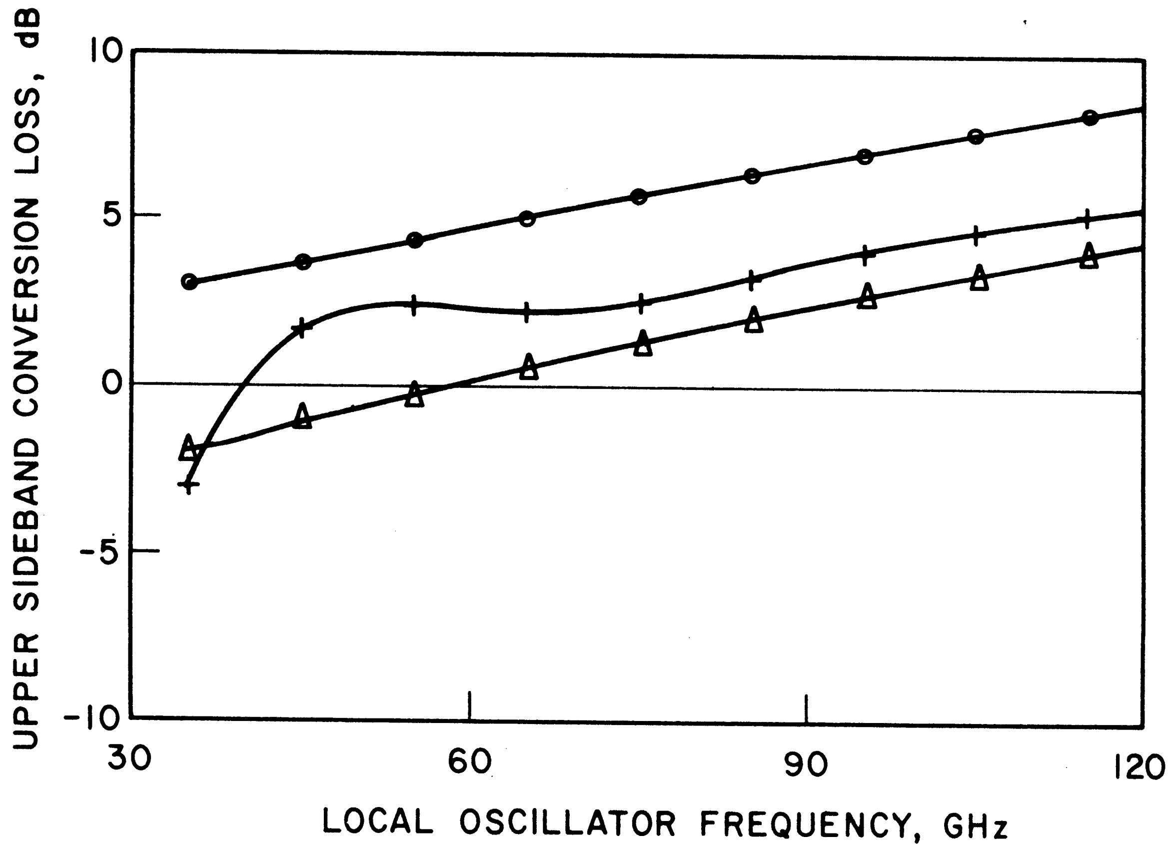

FIG. 5.16 CONVERSION LOSS AS A FUNCTION OF LO FREQUENCY FOR BARITTS 1, 6, AND 12. THE LO DRIVE LEVEL IS $4V_T$ IN ALL CASES AND THE IF IS 4 GHz. BARITT 12 IS BIASED AT 175 A/cm² WHILE 25 A/cm² IS THE BIAS CURRENT FOR THE OTHER DEVICES. THE CIRCLES DESIGNATE BARITT 1 WHILE THE TRIANGLES DESIGNATE BARITT 6 AND THE PLUSES DESIGNATE BARITT 12.

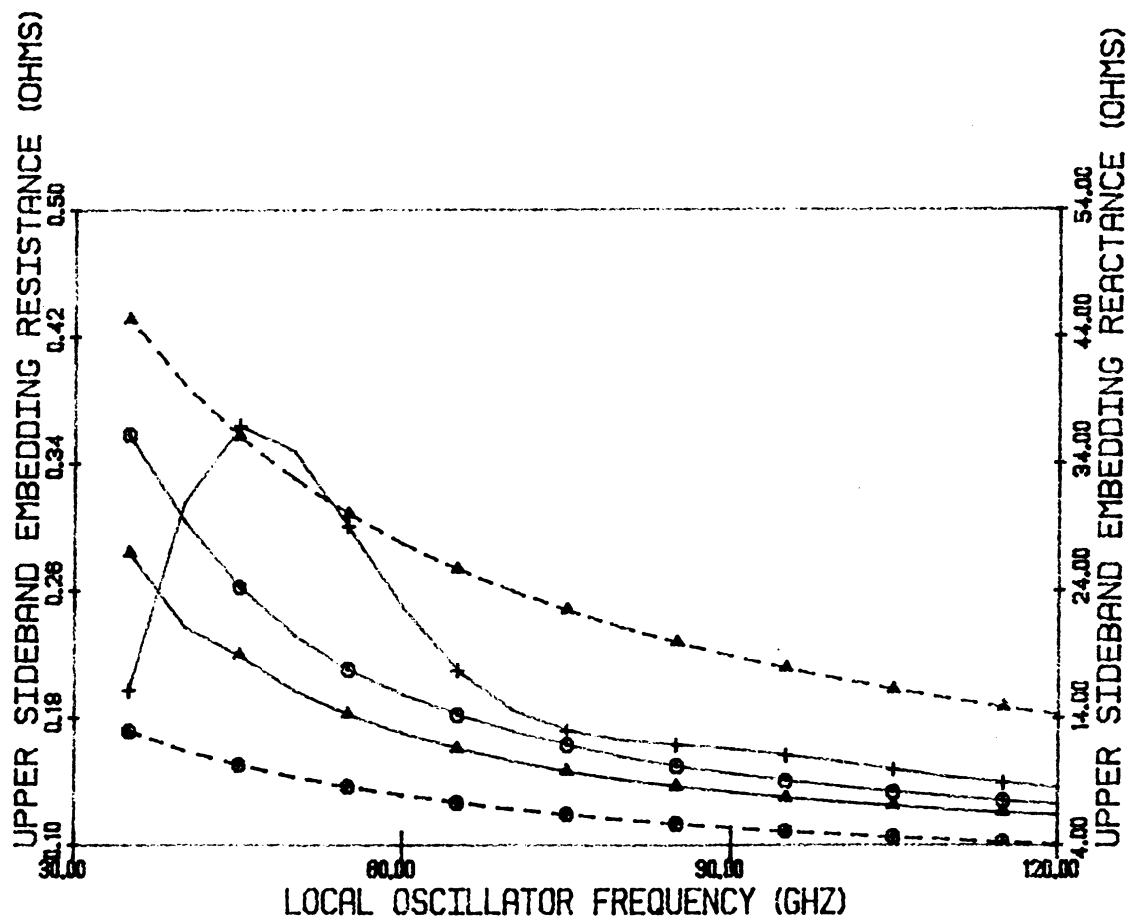

FIG. 5.17 SIGNAL FREQUENCY EMBEDDING IMPEDANCE AS A FUNCTION OF LO FREQUENCY FOR BARITTS 1, 6, AND 12. ALL OTHER PARAMETERS AND DESCRIPTIONS ARE IDENTICAL WITH THOSE OF FIG. 5.16.

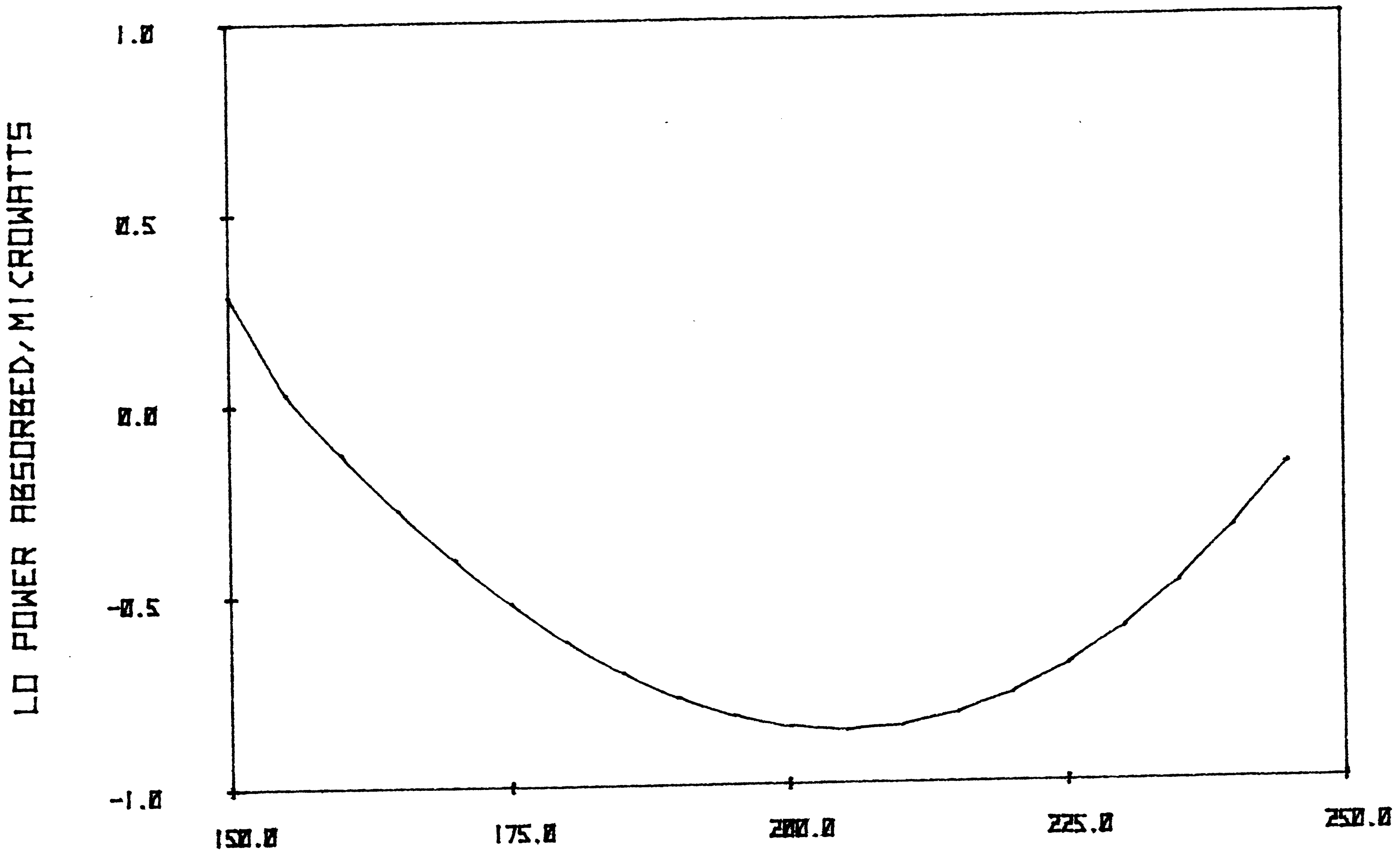

FIG. 5.18 ABSORBED LO POWER AS A FUNCTION OF DC CURRENT DENSITY FOR BARITT 12 WHEN OPERATED AS A SELF-OSCILLATING MIXER AT 35 GHz. THE LO DRIVE IS 0.02 V.

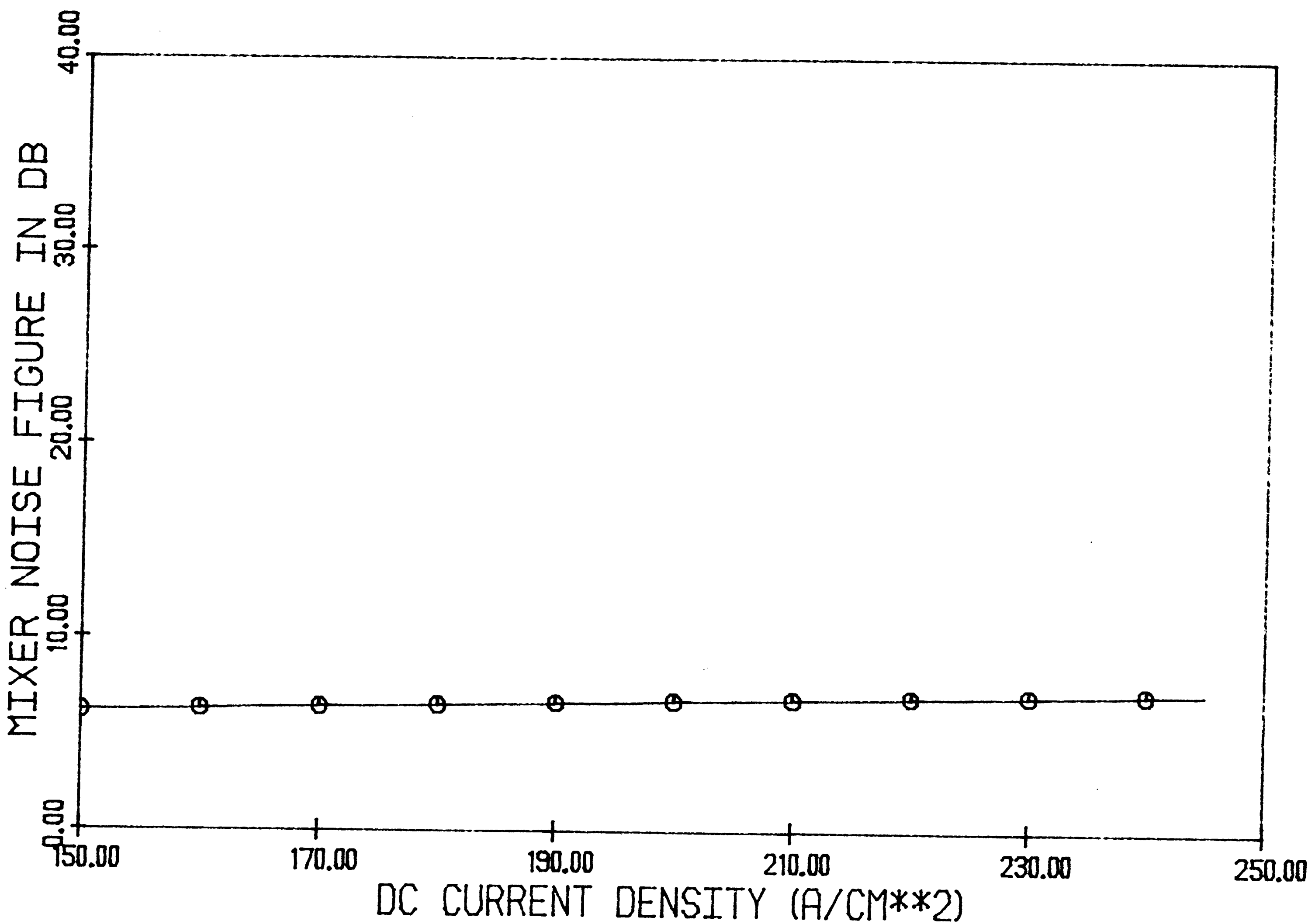

FIG. 5.19 MIXER NOISE FIGURE FOR THE SELF-OSCILLATING MIXER (BARITT 12 AT 35 GHz) AS A FUNCTION OF DC CURRENT DENSITY.

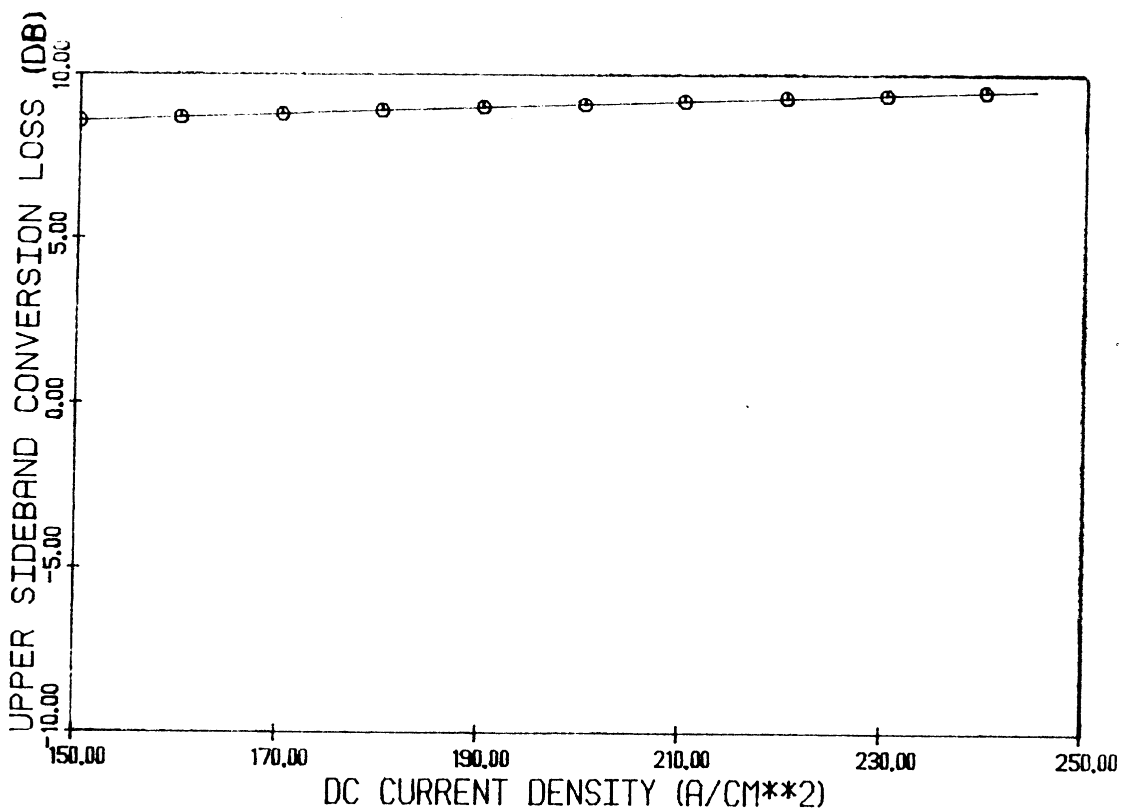

FIG. 5.20 CONVERSION LOSS OF THE SELF-OSCILLATING BARITT MIXER AS A FUNCTION OF DC CURRENT DENSITY.

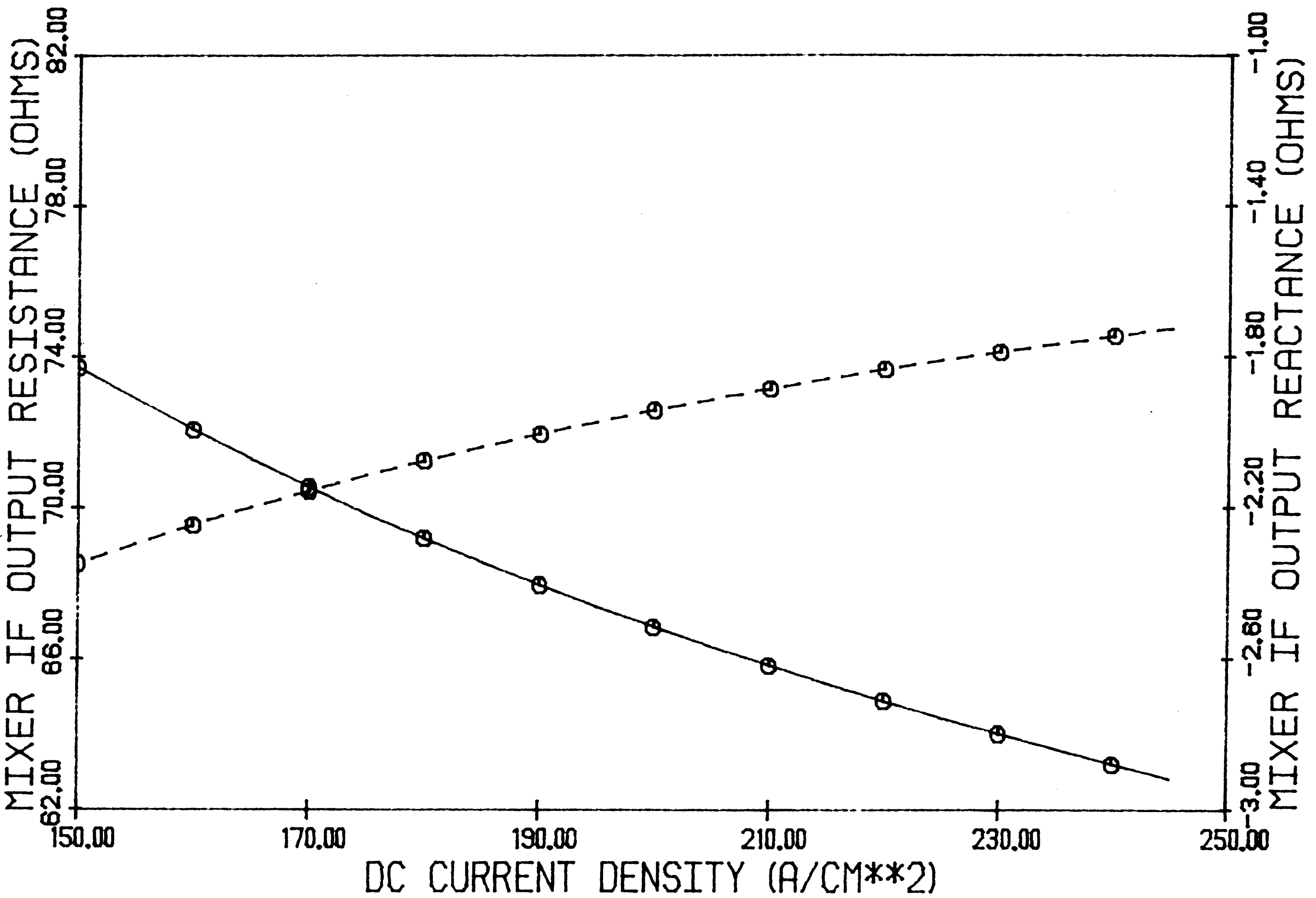

FIG. 5.21 MIXER IF OUTPUT IMPEDANCE AS A FUNCTION OF DC CURRENT DENSITY FOR THE SELF-OSCILLATING BARITT MIXER. —— IS RESISTANCE AND --- IS REACTANCE.

figure optimization procedure was used in this study. As the plots show, although the power level of the oscillation is small, good mixer performance was attained.

5.3.4 Noise Minimization Studies. In structures where conversion gain is possible, it was found that in some instances conversion gain occurred when the minimum conversion loss signal frequency termination was used, while no conversion gain occurred when the minimum noise figure termination was used. An example of this is shown in Figs. 5.22 and 5.23. The actual terminations are shown in Figs. 5.24 and 5.25. As can be seen, almost all the difference between the two optimum criteria lies in the resistive component. For the case of the IF negative-resistance band associated conversion gain, the use of the noise minimization criteria yielded a smaller conversion gain than the minimum noise figure termination.

Figures 5.26 through 5.28 are the basic results of the BARITT mixer study. Figure 5.26 illustrates that low conversion losses and even conversion gains can be achieved in the 30- to 120-GHz band. Figure 5.27 shows that the IF output impedance levels should allow for decent matching in real mixers. Figure 5.28 shows that the noise figure optimizing signal frequency termination also is achievable. Figure 5.29, however, indicates that these performance factors are not necessarily associated with acceptable noise figures.

Figures 5.30 through 5.33 illustrate several attempts at further reducing the noise figures. In Fig. 5.30, the LO drive level was dramatically increased with little effect. In Figs. 5.31 and 5.32, it is shown that increasing the dc current density helps somewhat, but

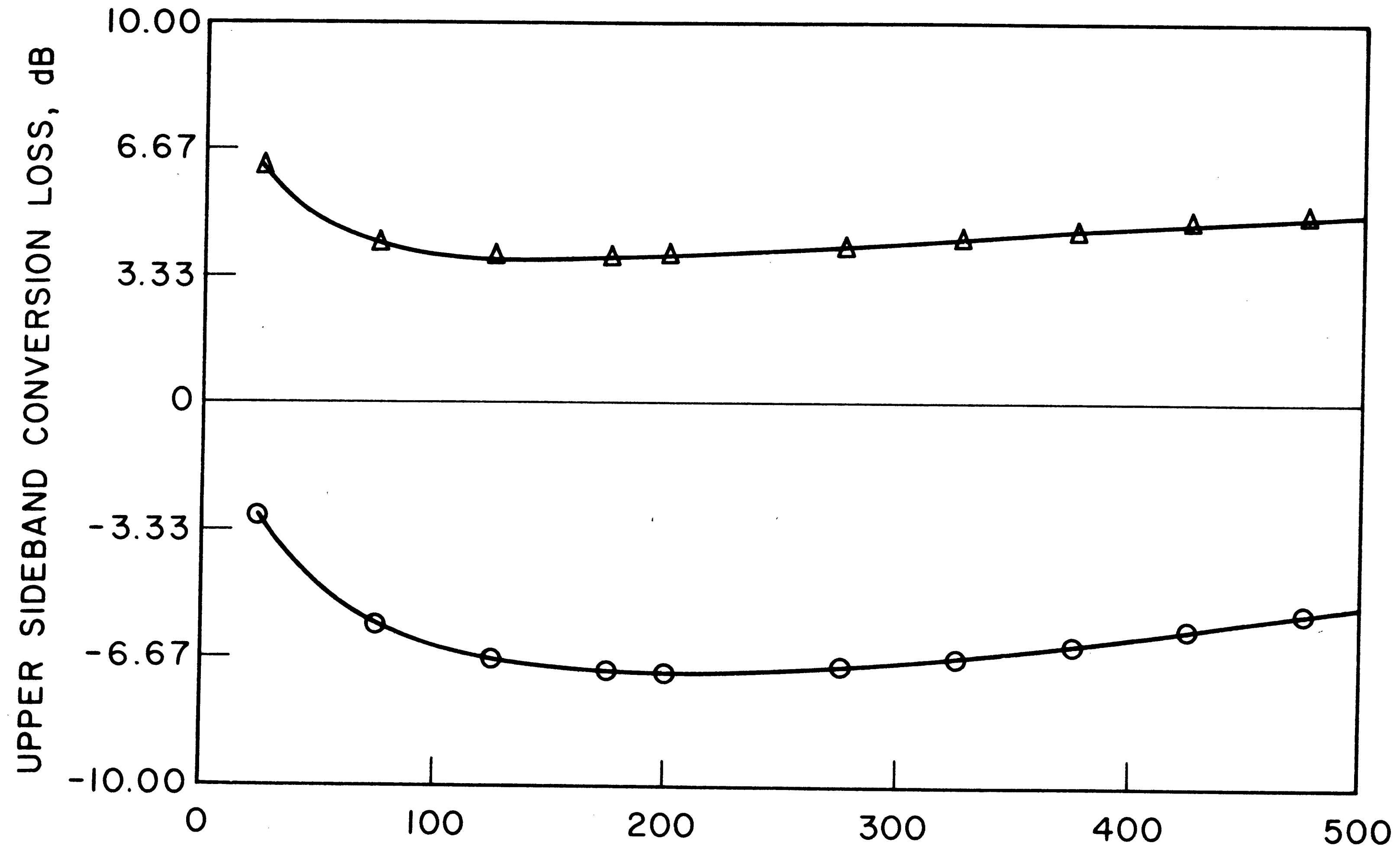

FIG. 5.22 CONVERSION LOSS AS A FUNCTION OF DC CURRENT DENSITY FOR BARITT 12. DRIVING VOLTAGE IS $4V_T$ AND IF IS 300 MHz. OPTIMAL CONVERSION LOSS TERMINATION WAS USED. CIRCLES ARE THE 35-GHz RESULT WHILE TRIANGLES ARE THE 94-GHz RESULT.

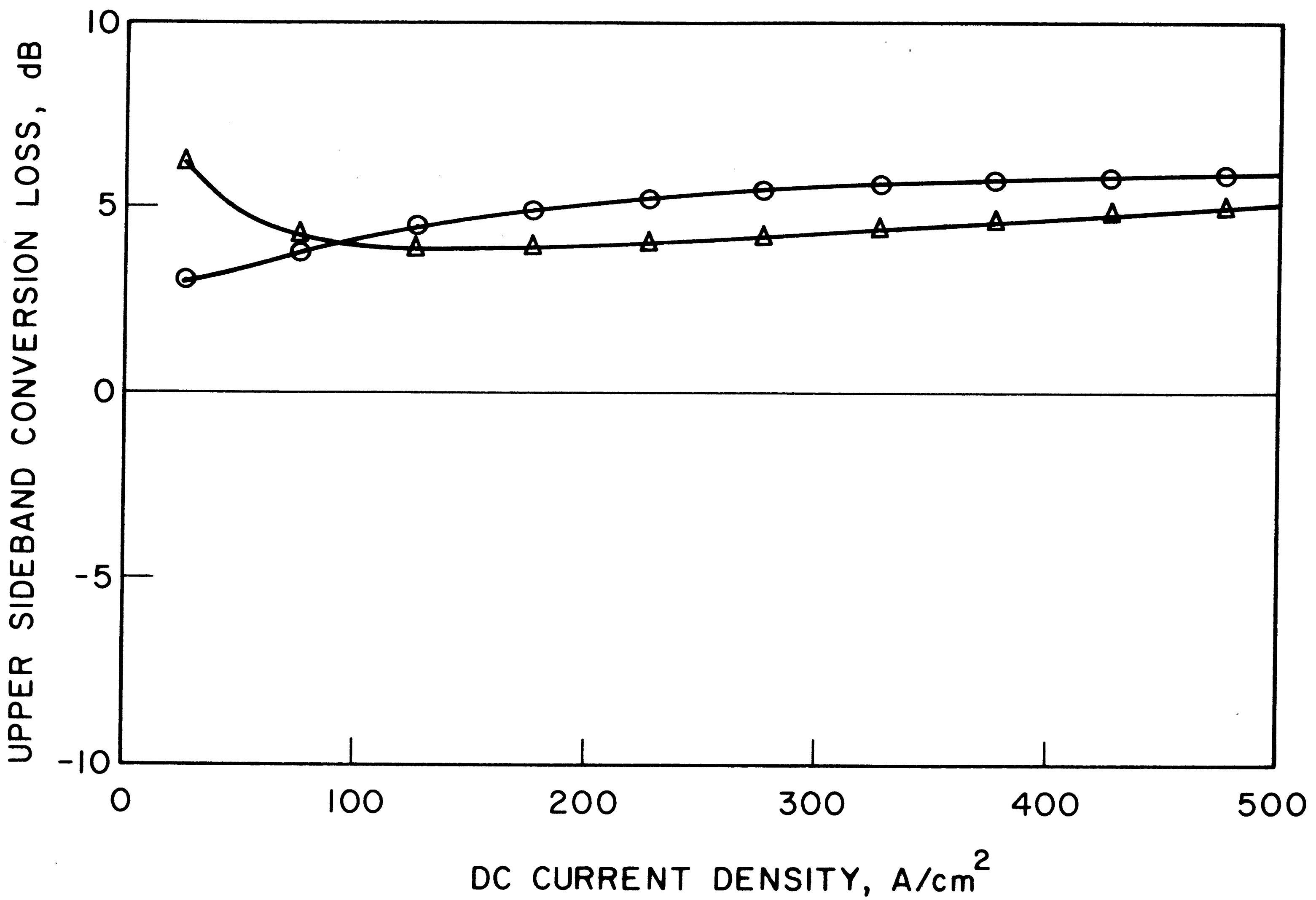

FIG. 5.23 CONVERSION LOSS FOR BARITT 12 AS A FUNCTION OF DC CURRENT DENSITY. ALL PARAMETERS ARE IDENTICAL WITH THOSE OF FIG. 5.22 EXCEPT THAT HERE THE OPTIMAL NOISE FIGURE TERMINATION WAS USED.

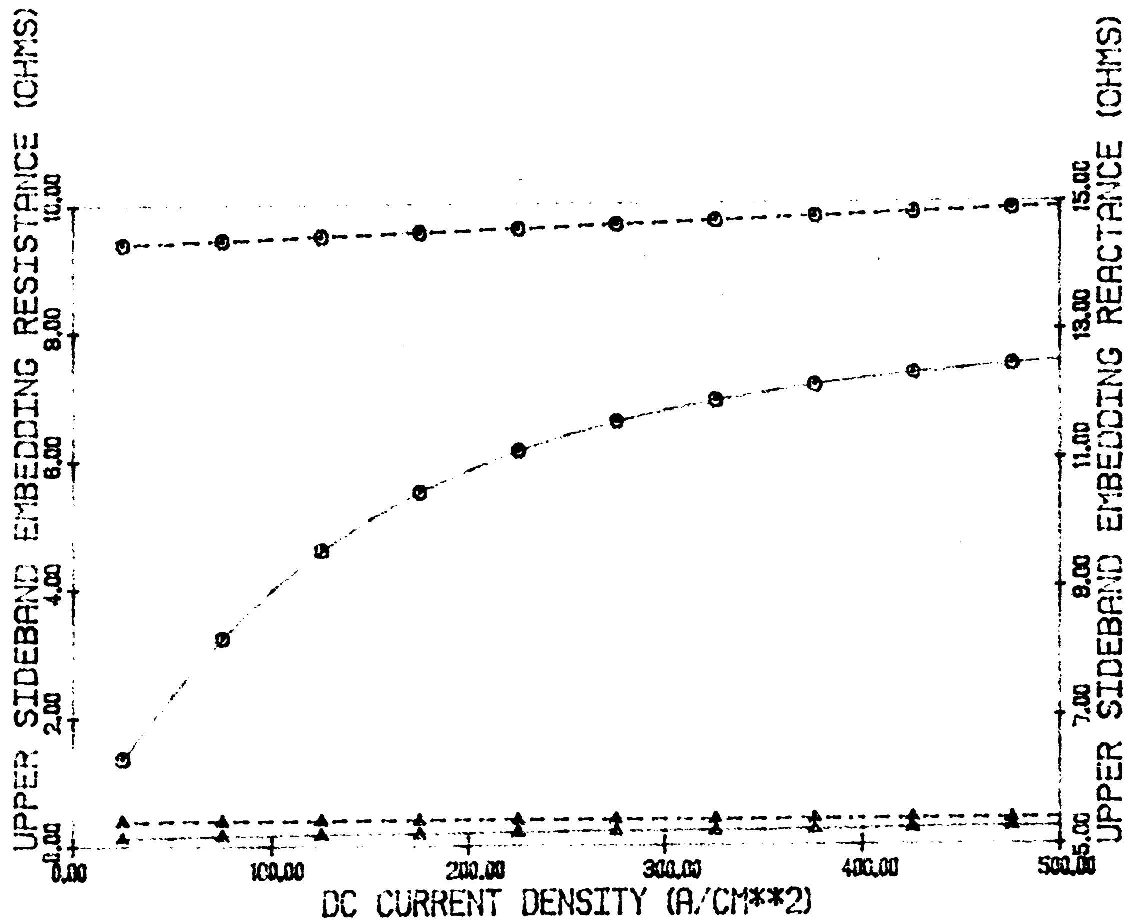

FIG. 5.24 THE SIGNAL FREQUENCY TERMINATION USED AS A FUNCTION OF DC CURRENT DENSITY IN FIG. 5.23.

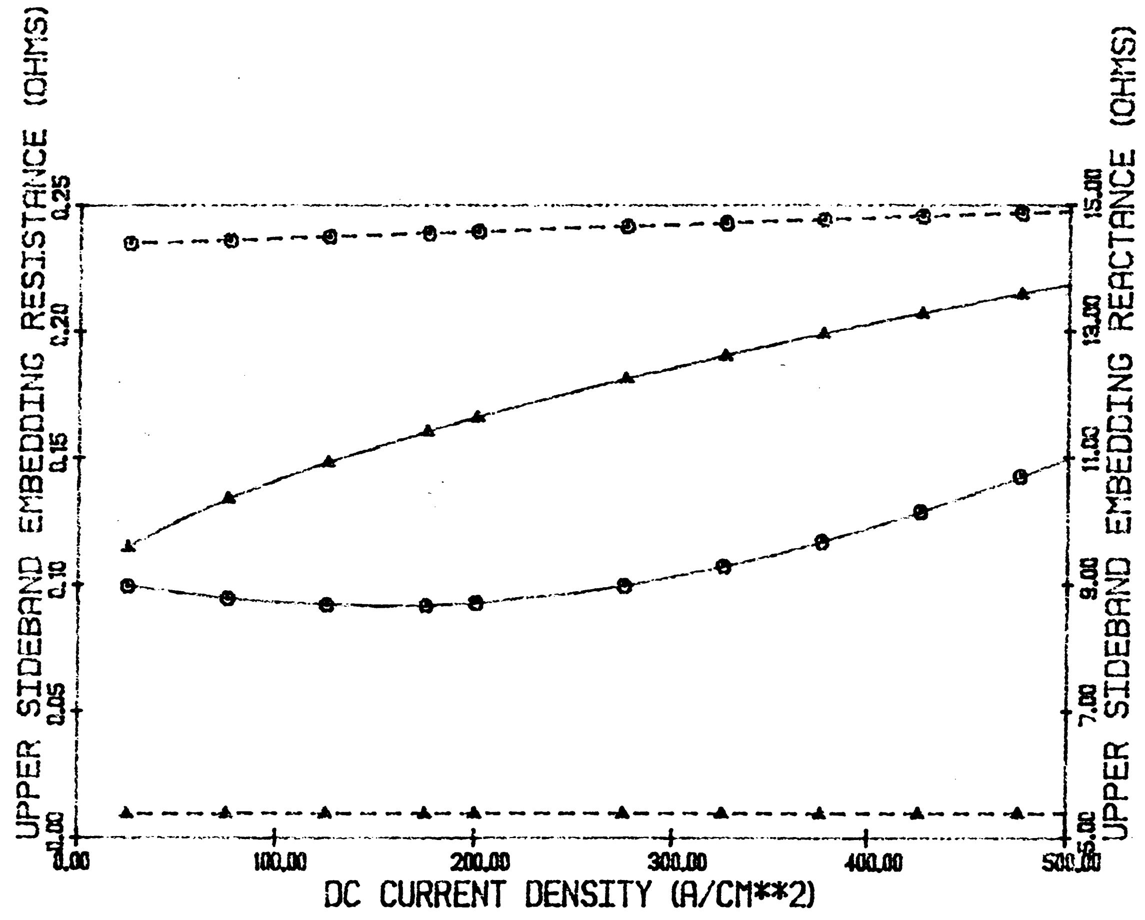

FIG. 5.25 THE SIGNAL FREQUENCY EMBEDDING CIRCUIT TERMINATION USED IN FIG. 5.22 PLOTTED AS A FUNCTION OF DC CURRENT DENSITY.

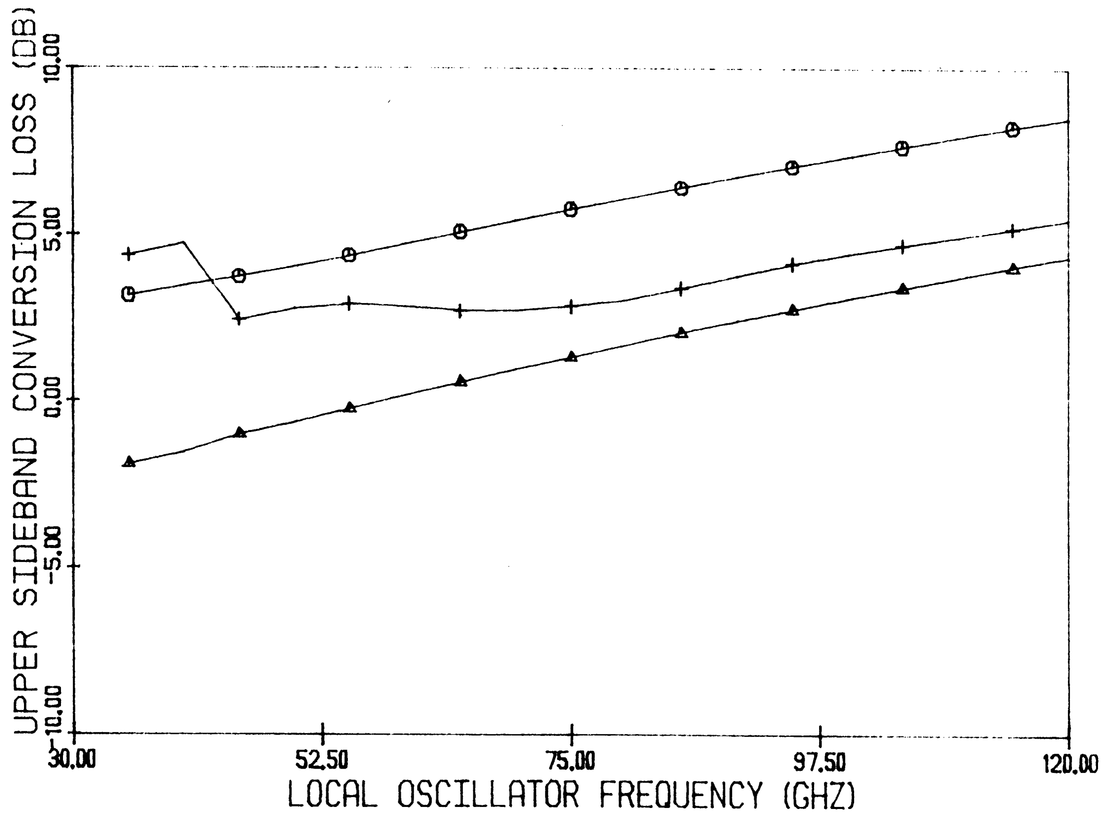

FIG. 5.26 CONVERSION LOSS OF BARITTS 1, 6 AND 12 PLOTTED AS A FUNCTION OF LO FREQUENCY. THIS PLOT IS IDENTICAL WITH FIG. 5.16 EXCEPT THAT HERE THE MINIMAL NOISE FIGURE TERMINATION IS USED.

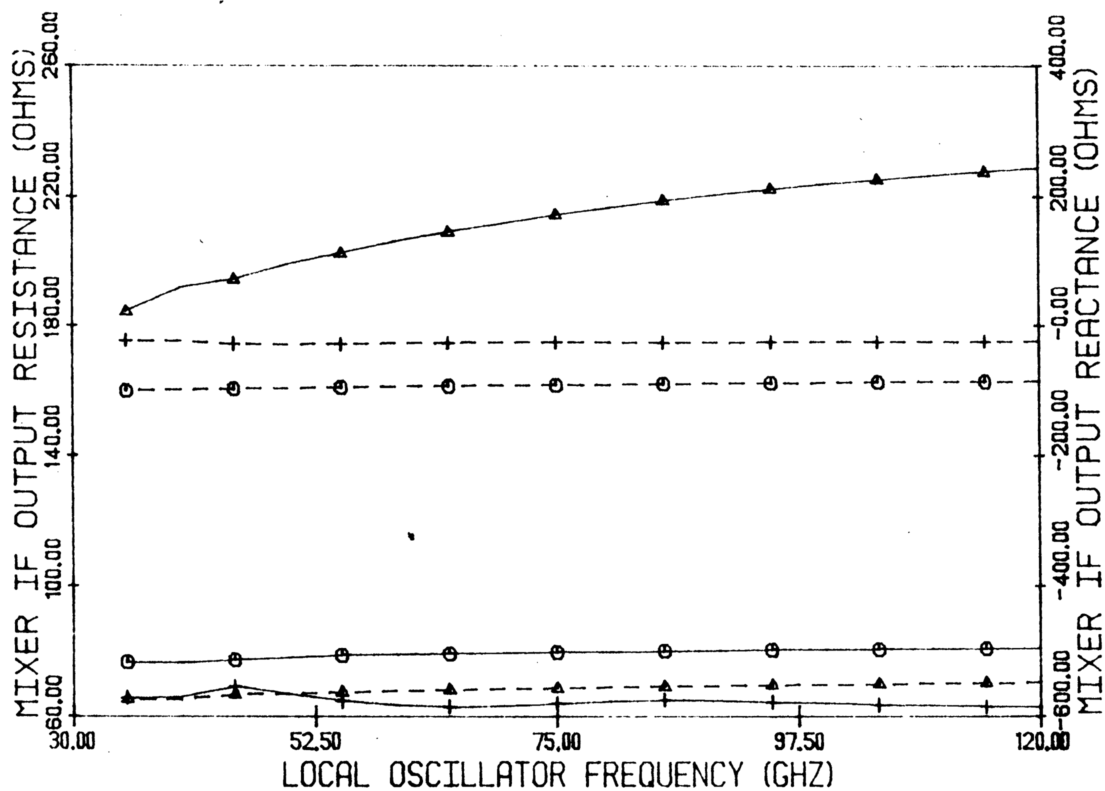

FIG. 5.27 MIXER IF OUTPUT IMPEDANCE FOR BARITTS 1, 6, AND 12 PLOTTED AS FUNCTIONS OF DC CURRENT DENSITY. BARITT 12 WAS BIASED AT 175 A/cm^2 WHILE THE OTHER TWO DEVICES WERE BIASED AT 25 A/cm^2. THE IF FREQUENCY IS 4 GHz AND THE LO DRIVE IS $4V_T$. CIRCLES DESIGNATE BARITT 1 WHILE TRIANGLES DESIGNATE BARITT 6 AND THE PLUSES DESIGNATE BARITT 12.

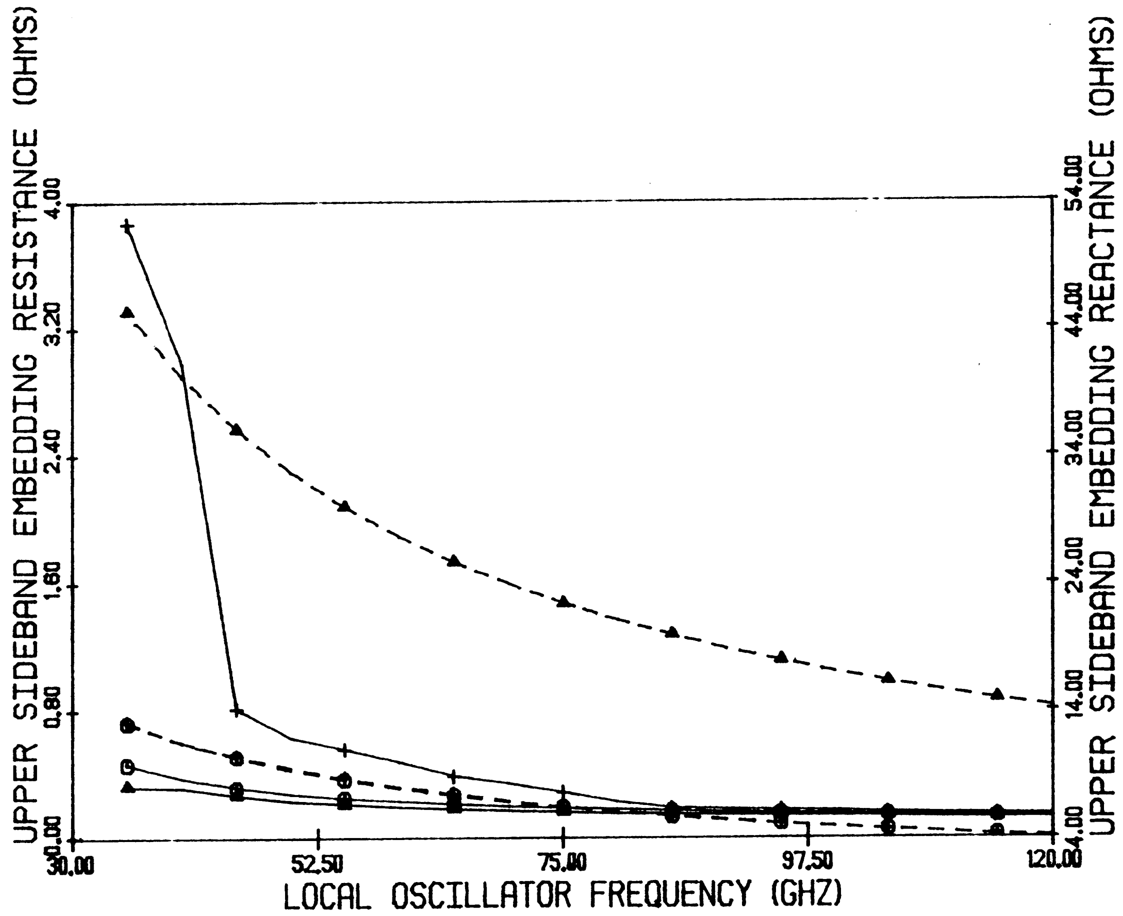

FIG. 5.28 THE SIGNAL FREQUENCY EMBEDDING IMPEDANCE (OPTIMIZES NOISE FIGURE) WHICH CORRESPONDS TO FIG. 5.27.

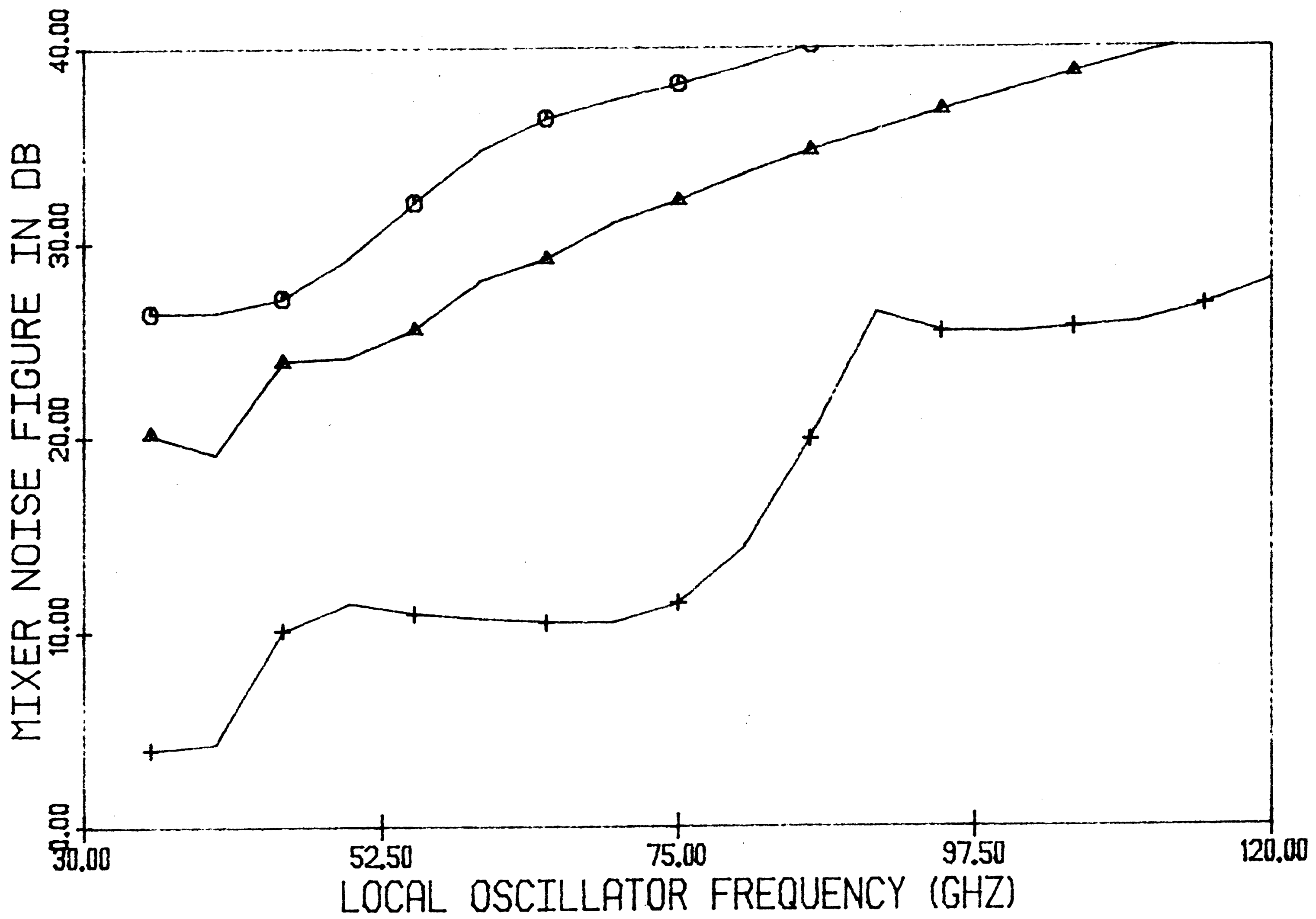

FIG. 5.29 THE MIXER NOISE FIGURE FOR THE CASE OF FIGS. 5.26 THROUGH 5.28.

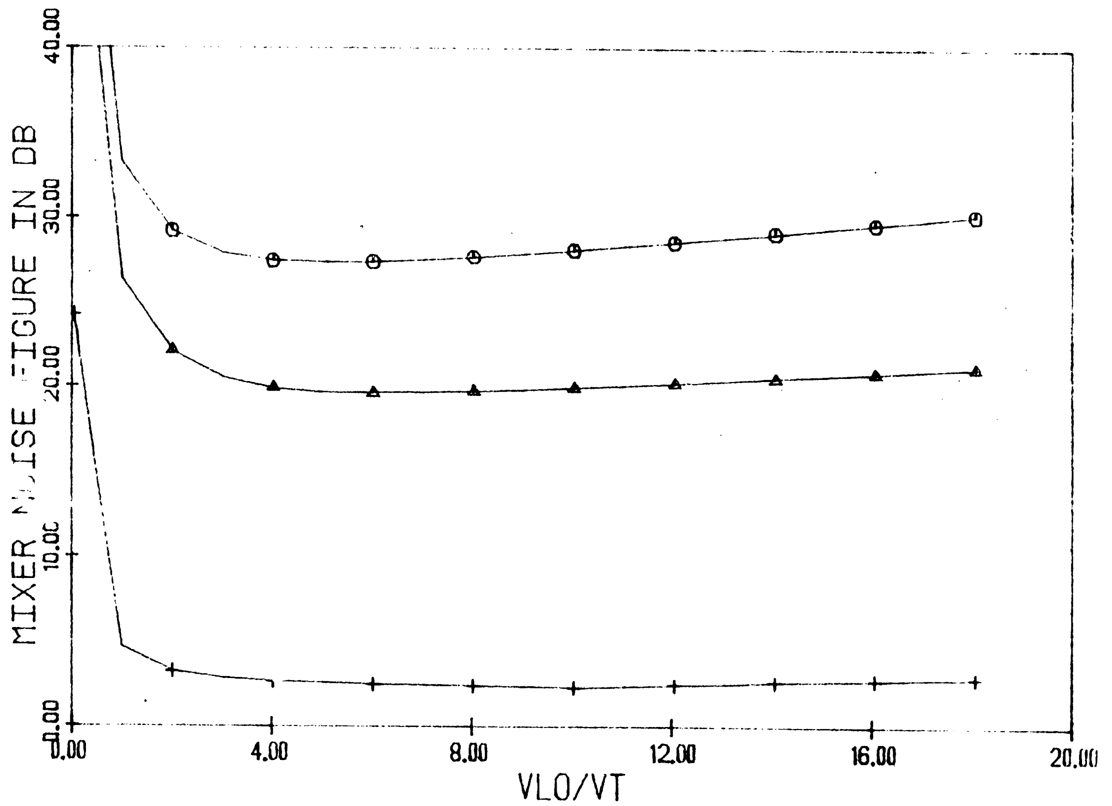

FIG. 5.30 MIXER NOISE FIGURE IN BARITT 1 AS A FUNCTION OF LO DRIVE LEVEL. THE BIAS AND IF CONDITIONS ARE IDENTICAL WITH THOSE OF FIGS. 5.26 THROUGH 5.29. THE CIRCLES DESIGNATE BARITT 1 WHILE THE TRIANGLES DESIGNATE BARITT 6 AND THE PLUSES DESIGNATE BARITT 12.

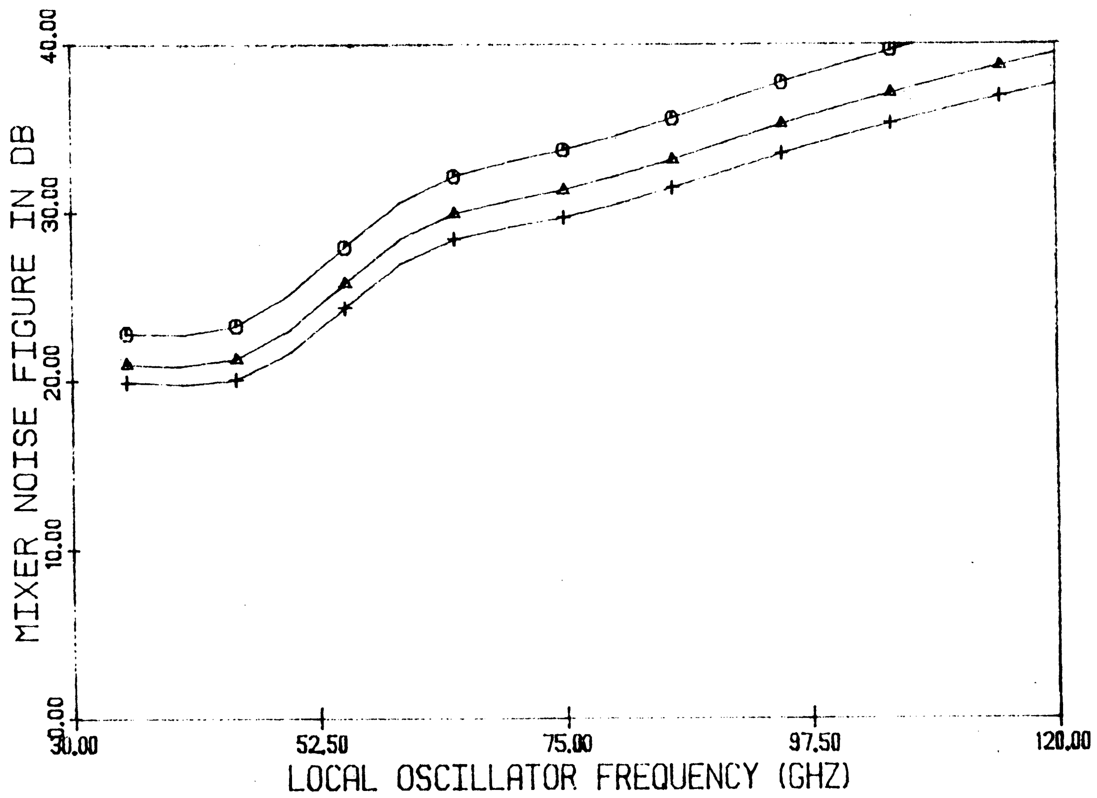

FIG. 5.31 NOISE FIGURE AS A FUNCTION OF LO FREQUENCY FOR BARITT 1 WITH DC CURRENT DENSITY AS A PARAMETER. THE LO DRIVE IS $4V_T$ AND THE IF IS 4 GHz. THE CIRCLES DESIGNATE 50 A/cm^2; THE TRIANGLES, 75 AND THE PLUSES, 100.

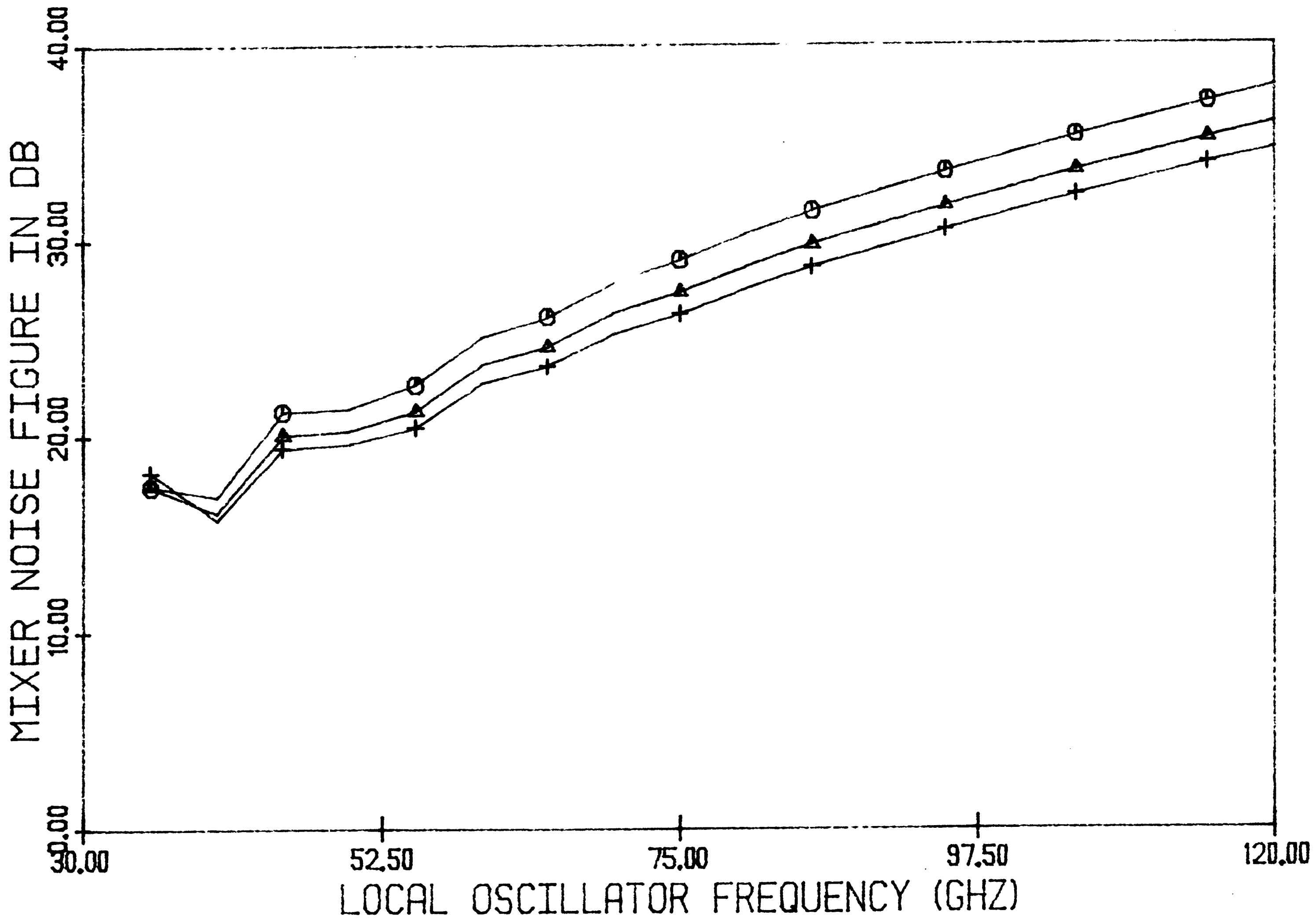

FIG. 5.32 NOISE FIGURE FOR BARITT 6 AS A FUNCTION OF LO FREQUENCY WITH CURRENT DENSITY AS A PARAMETER.

ALL OTHER PARAMETERS AND SYMBOLS ARE IDENTICAL WITH THOSE OF FIG. 5.31.

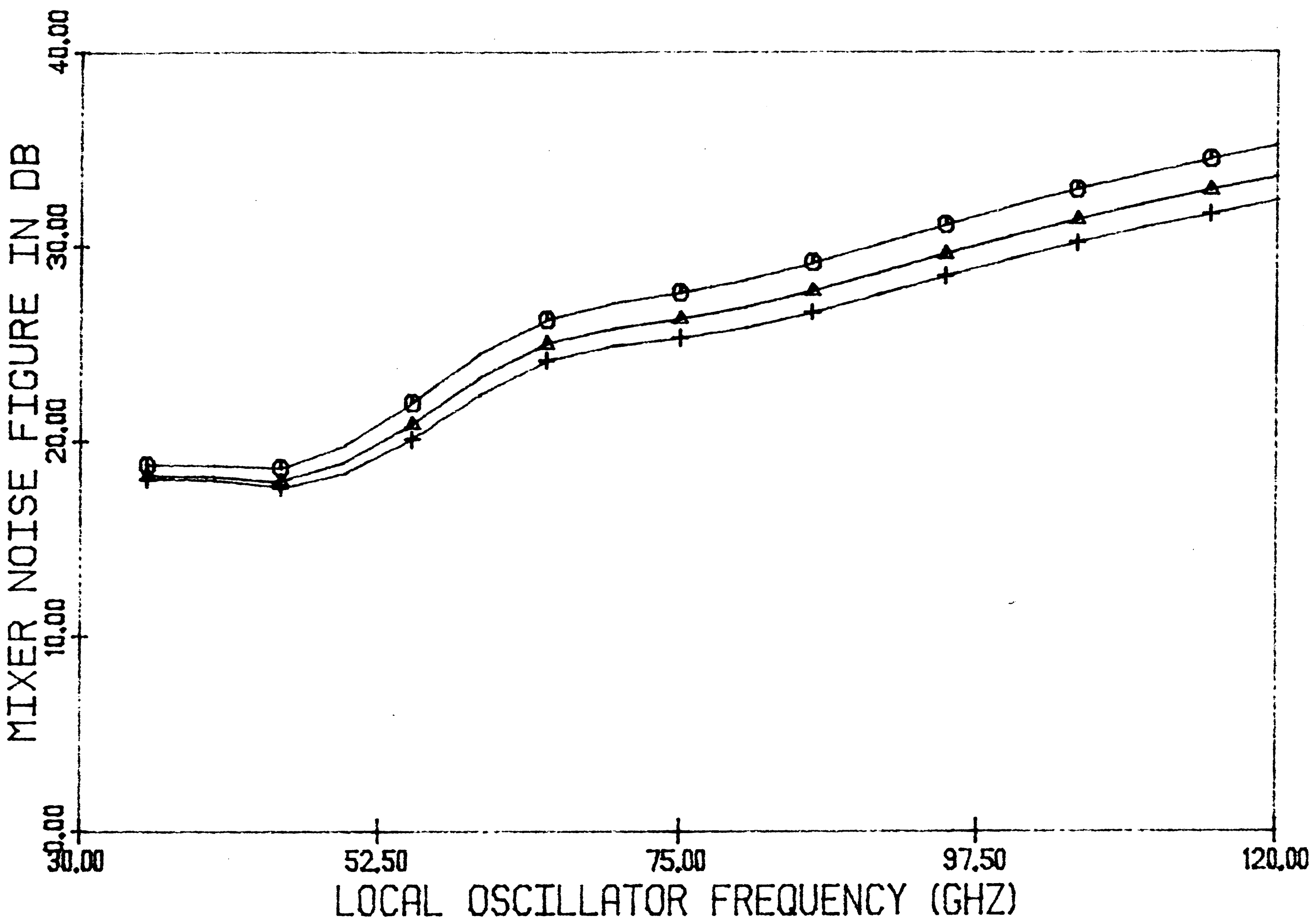

FIG. 5.33 NOISE FIGURE FOR BARITT 1 AS A FUNCTION OF LO FREQUENCY WITH CURRENT DENSITY AS A PARAMETER. THE CIRCLES DESIGNATE 150 A/cm^2; THE TRIANGLES, 200 AND THE PLUSES, 250.

in Fig. 5.33, it is shown that for somewhat higher current densities the improvement ceases.

The essential difference between the BARITTs with acceptable noise figures and those with unacceptable noise figures is that shot noise dominates in the bad diodes while velocity fluctuation noise dominates in the good diodes. Since good performance is predicted for Schottky-barrier diodes using the exact same formulation for the injection-region shot noise correlation matrix, the effect is a result of the transformation of the shot noise through the drift region to the device terminals. Examination of the detailed computer output indicates that the existence of low shot noise is associated with a very small negative or a positive imaginary part of the drift region transport factor Γ_D, when evaluated at the signal frequency.

In Figs. 5.34 through 5.36, the imaginary part of Γ_D as obtained in the small-signal studies of Chapter IV is plotted. These results do not significantly differ from those obtained in the mixer analysis. The shape of the Γ_D curves closely tracks the shape of the noise figure curves. Due to the complexity of the correlation matrix analysis presented in Chapter III, it is difficult to pin down exactly why Γ_D is important. However, physically it is not surprising. Γ_D is the complex transport factor which multiplies the injected particle current. Therefore, it plays a critical role in determining the drift region response to the injected shot noise.

To some extent the results presented here can be compared with the results of McCleer.[30] He obtained good noise figures in a self-oscillating mixer at microwave frequencies. The diffusion noise dominated this mixer. He also presented one calculation of the noise

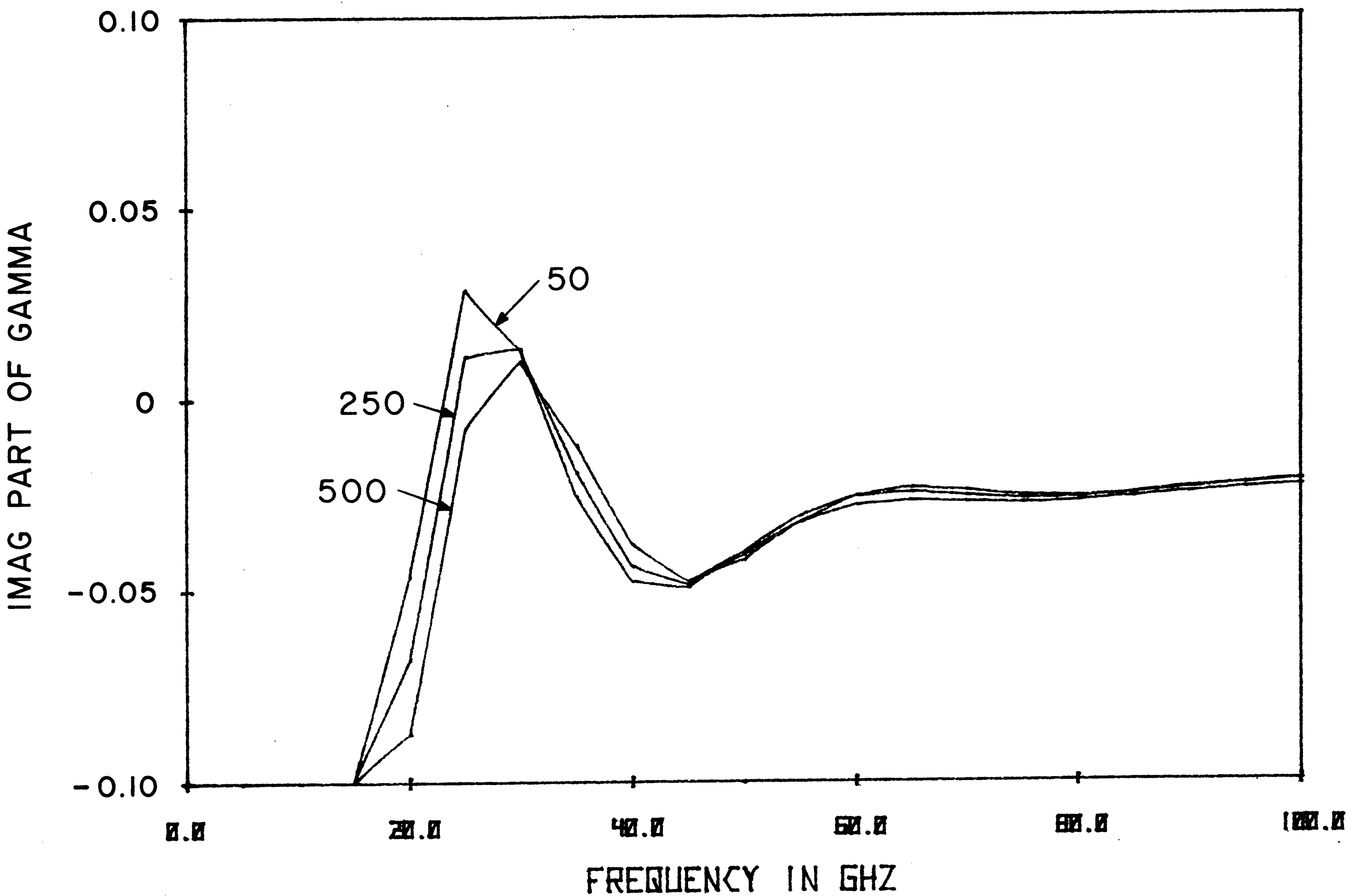

FIG. 5.34 IMAGINARY PART OF Γ_D FOR BARITT 1 AS A FUNCTION OF FREQUENCY WITH CURRENT DENSITY AS A PARAMETER.

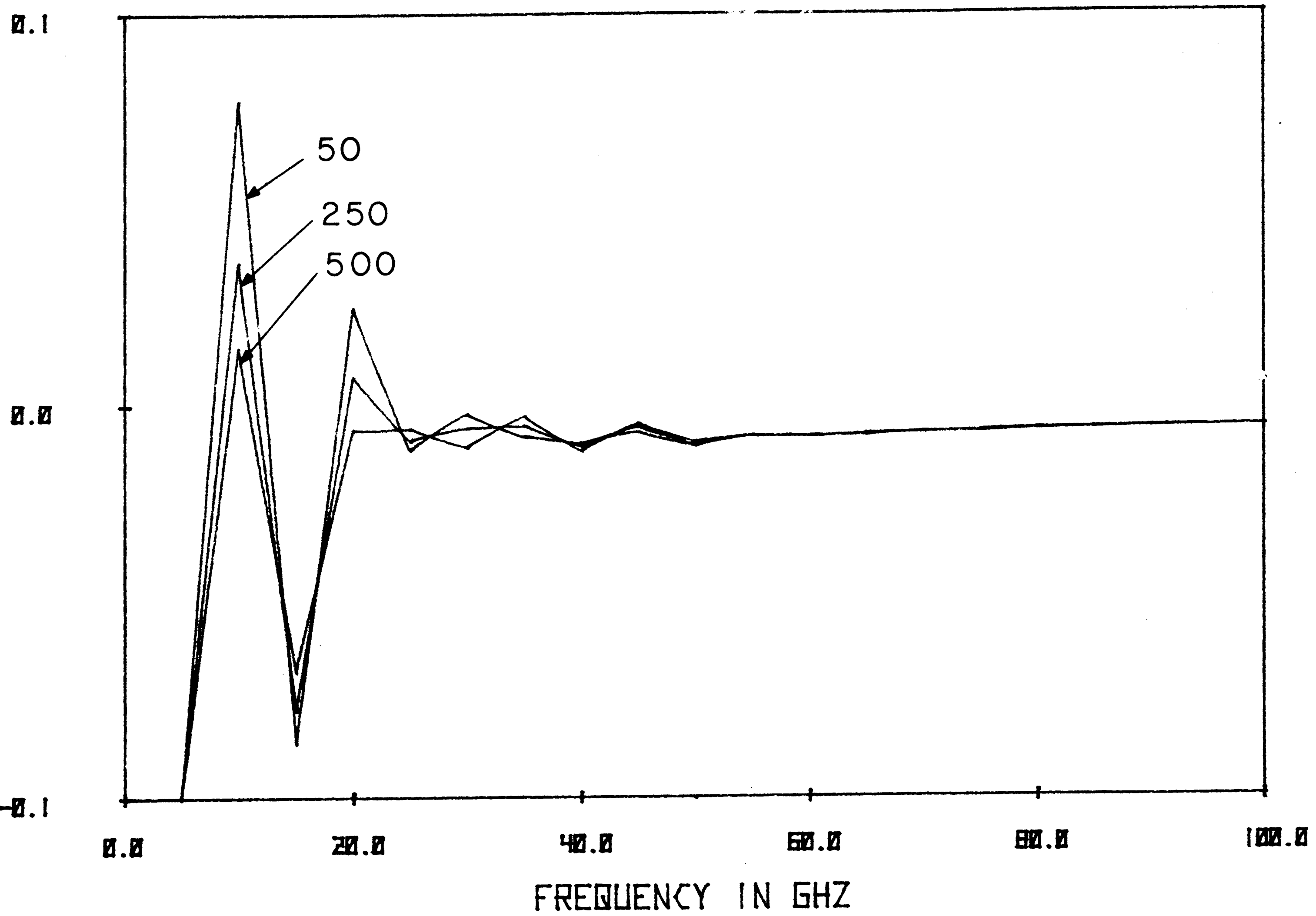

FIG. 5.35 IMAGINARY PART OF Γ_D FOR BARITT 6 AS A FUNCTION OF FREQUENCY WITH CURRENT DENSITY AS A PARAMETER.

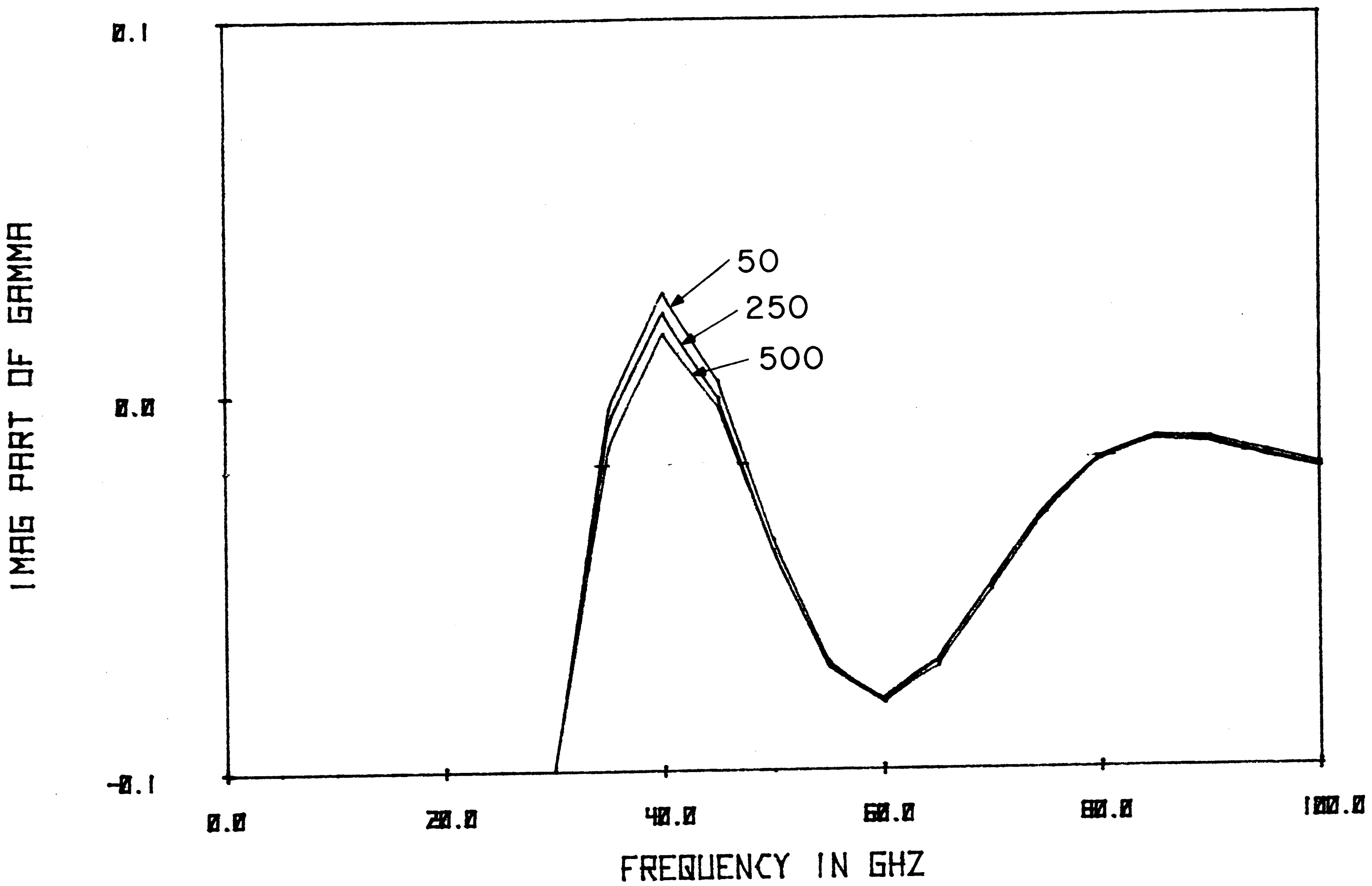

FIG. 5.36 IMAGINARY PART OF Γ_D FOR BARITT 12 AS A FUNCTION OF FREQUENCY WITH CURRENT DENSITY AS A PARAMETER.

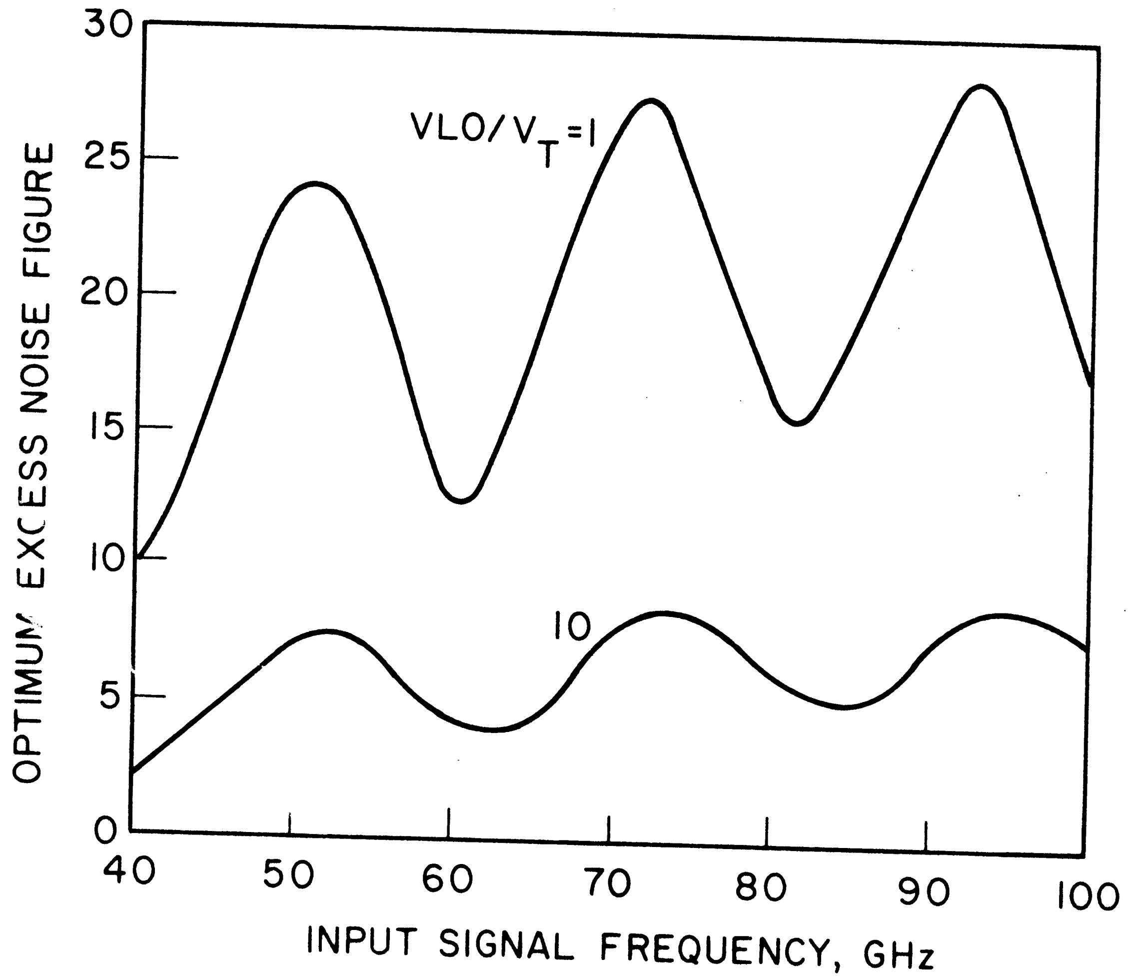

FIG. 5.37 OPTIMUM EXCESS NOISE FIGURE FOR MC CLEER'S DC MAXIMUM POWER STRUCTURE NO. 2. THIS CORRESPONDS TO FIG. 7.21 OF MC CLEER.[30]

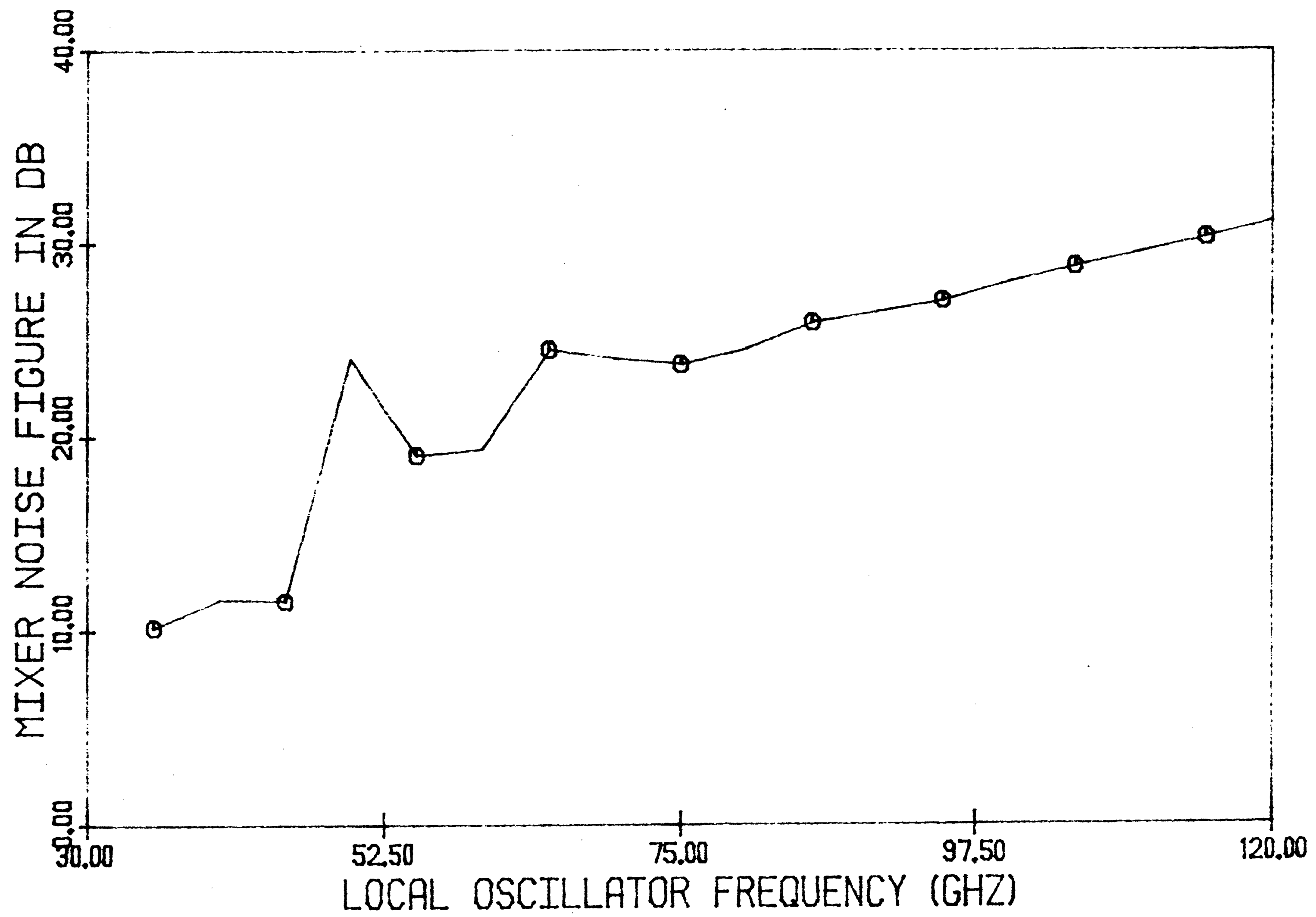

FIG. 5.38 THE SAME CALCULATION AS IS SHOWN IN FIG. 5.37 OBTAINED USING THE ANALYSIS PRESENTED HERE. (VLO = 10 V_T)

figure for a millimeter-wave mixer. This is shown in Fig. 5.37. The corresponding result obtained from the program used here is shown in Fig. 5.38. The transit-time rippling is comparable, but the noise figure obtained here is substantially higher than the noise figure of McCleer. Since the shot noise dominates the noise figure, the difference between the two approximate velocity fluctuation noise models is not responsible for the difference in the noise figure. Unfortunately, the two mixer analyses have a substantially different language. While here a matrix formulation is used throughout, McCleer uses a large coupled circuit to represent the three-frequency mixer. As a result it is difficult to ascertain where and why the models differ. However, adjustments of details of the device models can reduce the difference seen.

5.4 Summary

In this chapter a variety of mixer calculations were presented. First, a series of Schottky-barrier calculations were presented. These showed that the mixer analysis provides reasonable results. Some errors in the 3- to 4-dB range, however, might be evident. This is unavoidable unless exact device-circuit interactions are considered at a great number of frequencies.

Next, the performance of BARITTs as mixers was studied. It was found that BARITTs usually yielded good conversion losses and even in some situations, conversion gains. The only actual instabilities found were in situations where the IF frequency fell in the negative-resistance band. This, however, may be more a consequence of operation in the millimeter-wave region than it is of BARITTs. The results also

indicated that self-oscillating mixer operation is possible in heavily doped short structures with small parasitics. Good noise figures can be attained in such a mixer. In general, however, BARITTs do not seem to be low noise mixers. In order for a BARITT to be a low noise mixer it is necessary to have the proper drift region parameters or the terminal shot noise is high.

CHAPTER VI. MONTE CARLO STUDIES OF NOISE AND TRANSPORT IN GaAs

6.1 Introduction

Throughout this investigation, the drift-diffusion transport model has been used, and it has been assumed that the velocity fluctuation noise source spectral density was white. In this chapter, Monte Carlo techniques are used to examine the validity of these assumptions. Since they are virtually universally used in semiconductor device modeling, the results of the investigations presented in this chapter are applicable not only to the device models used here but also to a wide variety of other device models as well.

Monte Carlo investigations provide a detailed study of band structure dependent transport processes in the quasi-free-particle approximation. These transport processes play an important role in determining the device impedance and upper frequency limits to various physical mechanisms and are directly connected with velocity fluctuation noise. The investigations presented in this chapter have two important goals. The first investigation explores the role of transient carrier transport in GaAs millimeter-wave transit-time device drift regions. The second investigation is directed at establishing the proper procedures which must be followed in Monte Carlo estimates of velocity fluctuation noise spectra.

6.2 The Monte Carlo Model and Method

6.2.1 The Monte Carlo Method.

In this section, the basic Monte Carlo procedure is described. Monte Carlo programs are

essentially statistical experiments based on a random flight model of carrier transport. A Monte Carlo program repeats a basic accelerate-scatter iteration shown in Fig. 6.1 many times. The results are then analyzed to yield statistical estimates of quantities of interest.

This statistical process always yields results which have some variance. This variance can be reduced by various techniques, the most fundamental of which is the compilation of more raw data (more electrons and longer total times) for averaging. In practice this typically requires that the cost of the data production be increased by a factor of four to reduce the variance to one half the original level. Therefore throughout this work, variance in the results is tolerated provided it does not obscure the basic gross features of carrier transport and noise.

The basic accelerate-scatter iteration shown in Fig. 6.1 proceeds as follows. First, a random number is generated to determine a time during which the electron is ballistically accelerated by the applied field. During this acceleration the electron moves from an initial state k_a to a final state k_i. This transformation is uniquely determined by the flight time, the field, and the band structure. A second random number is then generated to determine the type of scattering event experienced by the electron. The relative probability of the various scattering events is controlled by k_i. A final sequence of random numbers is then generated to determine the change in carrier energy and momentum produced by the scattering event. This sequence is dependent on k_i and the type of scattering event. The resulting final state k_b is assumed to be instantaneously achieved and can then be used as the k_a of the next iteration.

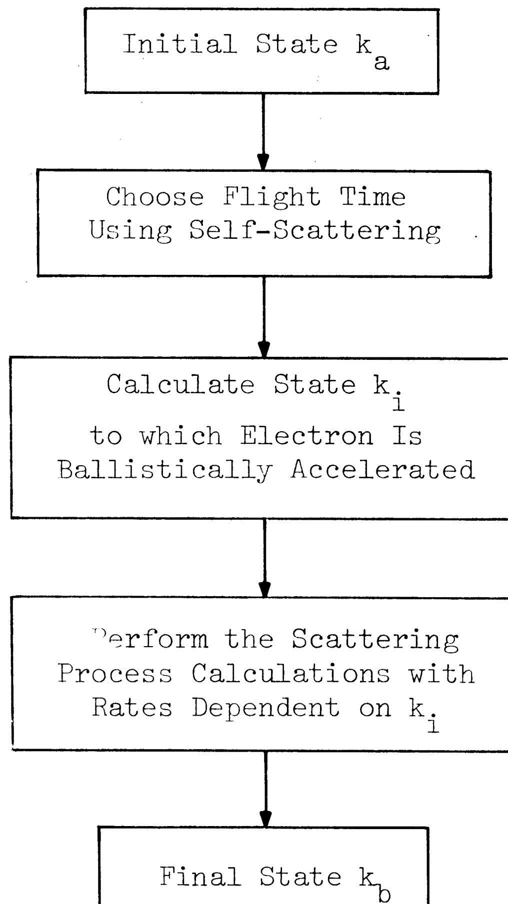

FIG. 6.1 THE BASIC ACCELERATE-SCATTER ITERATION OF THE MONTE CARLO METHOD.

The programs used here were written by Peter Blakey and implement the Fawcett[163,164] two-valley model of GaAs with band non-parabolicity neglected. The various scattering rates are plotted as functions of carrier energy in Figs. 6.2 and 6.3. These figures show that the physical scattering rates are strongly dependent on the electron state k_i. This dependency greatly complicates the selection of the first random number in Fig. 6.1, the ballistic acceleration time. To simplify this process and thereby greatly reduce the computational cost, a fictional scattering process called self-scattering is introduced. In a self-scattering event the state k_b is identical to the state k_i. The electron is not really scattered. The dependency of this fictional scattering rate on k_i is selected to provide an arbitrary total (real plus self-scattering) rate which is constant over k_i. The ballistic acceleration time then is exponentially distributed and easily selected.

It is interesting to note that if the scattering rates, energy band structure, and field are all known, a Monte Carlo program can be written in complete ignorance of the Boltzmann transport equation. Yet it is commonly asserted the Monte Carlo techniques represent a numerical solution of the Boltzmann equation. Fawcett[163] showed that for steady-state calculations the two methods agree in the limit of infinite flight times. Ferry et al.[165] assert that the Boltzmann transport equation and ensemble Monte Carlo methods are not consistent for transient problems, and that the ensemble Monte Carlo method is the more accurate of the two. However, the absence of alternative numerical solutions to the basic transport problem does make this type of discussion somewhat academic.

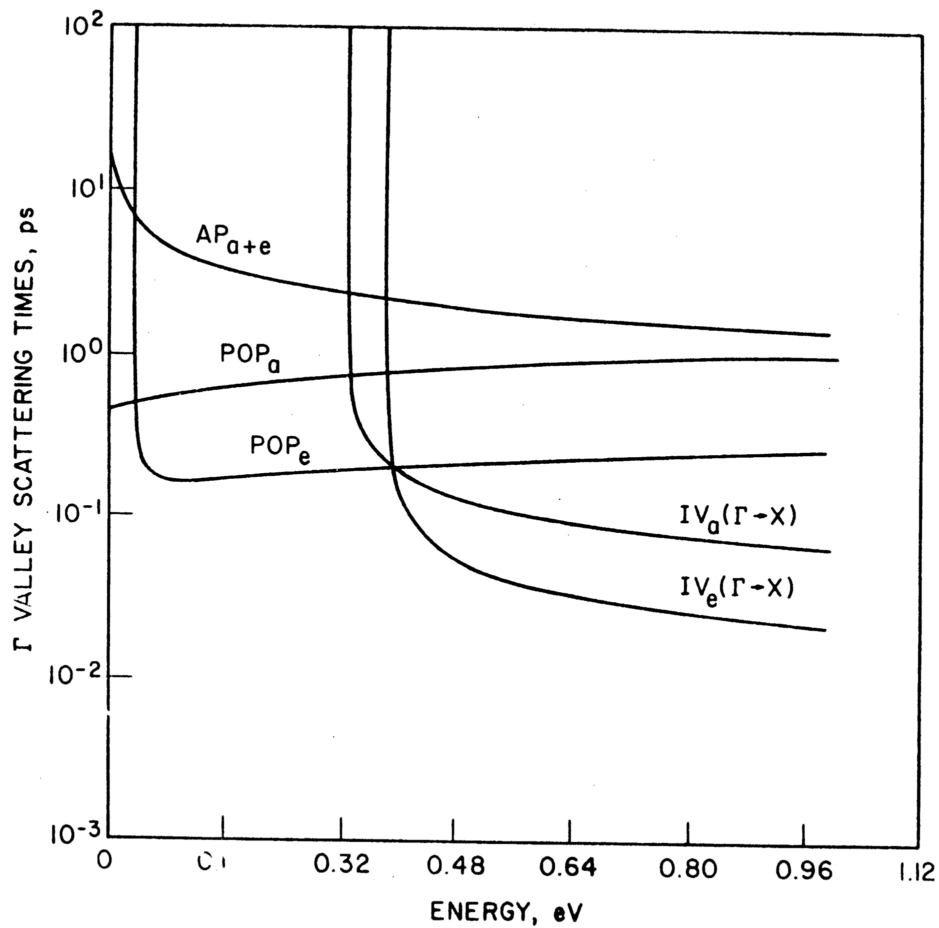

FIG. 6.2 SCATTERING RATES FOR THE CENTRAL VALLEY. (AP_{a+e} = ACOUSTIC PHONON ABSORPTION PLUS EMISSION; $POP_{a,e}$ = POLAR OPTIC PHONON ABSORPTION AND EMISSION, RESPECTIVELY; $IV_{a,e}$ = INTER-VALLEY ABSORPTION AND EMISSION, RESPECTIVELY)

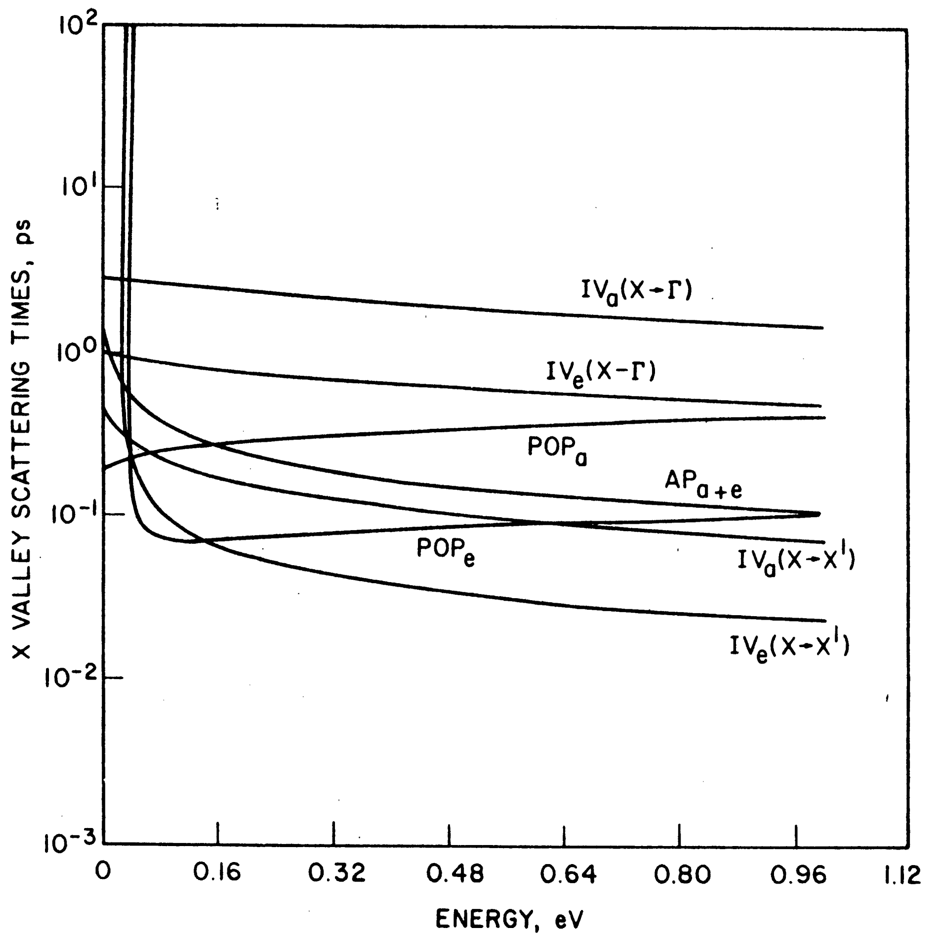

FIG. 6.3 SCATTERING RATES FOR THE SATELLITE VALLEY. (AP_{a+e} = ACOUSTIC PHONON ABSORPTION PLUS EMISSION; $POP_{a,e}$ = POLAR OPTIC PHONON ABSORPTION AND EMISSION, RESPECTIVELY; $IV_{a,e}$ = INTERVALLEY ABSORPTION AND EMISSION, RESPECTIVELY)

6.2.2 The Physical Model. In this section some general comments concerning the physical model used in the Monte Carlo simulation are made. Further details are available elsewhere.[98,163,164] Here the focus is on several assumptions made in the model. These are the neglect of band nonparabolicity, the neglect of intra-collisional field effects, and the use of a two-valley model instead of a three-valley model.

Neglecting band nonparabolicity has the advantage of greatly reducing the computational cost. Although this would seem to produce inaccuracies, trial runs with and without nonparabolicity show that neglecting it produces little error for fields up to 20 kV/cm in GaAs. Evidently the effects of nonparabolicity on the effective mass and on the scattering rates (introduced by warping the density of states) tend to counteract.

Intracollisional field effects occur because of the finite duration of the actual collisions in time and space. The resulting field acceleration during the collision or scattering event tends to reduce the thresholds for the various scattering mechanisms somewhat. However, it is difficult to specify the extent to which the thresholds are reduced, especially when the electric field is a function of time. The main effect of neglecting the intracollisional field effect is again a restriction of the model to low fields. Here the model will always be used at field levels of 20 kV/cm or less.

The last question concerns the use of a two-valley model instead of a three-valley model. The justification for using a two-valley model is that it works for transport problems. This is a result of the great similarity of the two nonequivalent valleys

(the L and X valleys) in effective mass and energy. Any differences between a two- and three-valley model in terms of transport features are largely eliminated by the fact that the coupling constants in each model are adjusted to match experimental steady-state transport data.

The discussion in this section illustrates an often overlooked fact. Although Monte Carlo calculations represent the best first-principles transport model that actually provides numerical results, *any* transport model is based on a number of assumptions and physical parameters. In some instances these parameters cannot be experimentally measured or theoretically calculated. They are used as adjustable parameters, and their values are selected to provide a good match to experimental transport data. It is, therefore, doubtful that the fine details of carrier transport under transient conditions can actually be resolved by the Monte Carlo model or any other model at present. This provides additional justification for stopping the process of data accumulation at the point where the gross features are clearly visible even though noticeable statistical jitter is still present.

6.3 Dynamic Transport Transients and Consequences for GaAs Transit-Time Device Properties

6.3.1 Introduction.

It has long been known that the electron velocity in GaAs does not respond to rapid field variations in accordance with the static velocity-electric field characteristic. The importance of such nonstationary or transient carrier dynamics has been explored to some extent in Gunn devices and in short channel

FETs. The influence of transient carrier transport on GaAs transit-time device properties has received little attention however. This influence is the subject of this discussion.

Transient carrier transport has two primary forms. When the field is stepped up, the velocity does not track the electric field in accordance with the static velocity-field curve, but instead starts from its initial value and rapidly overshoots the expected final value and then relaxes back to the expected final value. Alternatively, when the field is stepped down, instead of tracking the static velocity-field curve, the velocity often first undershoots the expected final value and then relaxes to its final value.

Three main ways by which such transport transients can change transit-time device behavior will be discussed. First, a particle current waveshaping mechanism will be described. Second, the role of transient transport in establishing upper frequency limits to premature collection mode operation is considered. Lastly, transient transport in the undepleted epitaxial portions of a transit-time device is discussed.

6.3.2 Transient Carrier Dynamics. Transport in transit-time devices is conventionally modeled by a Brownian motion type of drift-diffusion equation in which the transport coefficients are determined by the local instantaneous field (a quasi-static pseudo-local approximation). Both the drift-diffusion equation and the quasi-static pseudo-local approximation are based on the assumption that the carrier distribution function in phase space instantaneously relaxes to the steady-state distribution appropriate to the local

instantaneous field. Transient carrier transport becomes important in situations where this assumption is invalid.

A basic type of transient transport phenomena is the velocity overshoot illustrated in Fig. 6.4. In Fig. 6.4 the experiment performed switches an electric field on at t = 0 and observes the time response of a collection of mutually independent electrons. For time frames on the picosecond level, the carrier velocity can overshoot its expected steady-state final value by several hundred percent. During this overshoot, as is illustrated in Fig. 6.5, the carriers can travel several tenths of a micron.

The opposite experiment, that of turning the field off at t = 0, is illustrated in Figs. 6.6 and 6.7. As is shown in Fig. 6.6, it takes several picoseconds for the electrons to be stopped. This basic inertial behavior is more clearly illustrated in Fig. 6.7. It should be noted that for some cases the mean carrier velocity can become negative. Such negative velocities have been reported in other Monte Carlo studies, but cannot result from an energy-momentum model based on equations such as those of Blotekjaer.[166]

The origins of velocity undershoots lie in the finite relaxation times and in a preferential Jones-Rees effect as illustrated in Fig. 6.8. The electrons must shift from the satellite valley to the central valley. Electrons scatter into the central valley with an initially high energy. They may have either positive or negative velocities. Electrons which enter the central valley with positive velocities (e.g., point a) gain energy from the field. As a result they tend to remain above the threshold for intervalley scattering and rapidly scatter back to a satellite valley. Electrons which

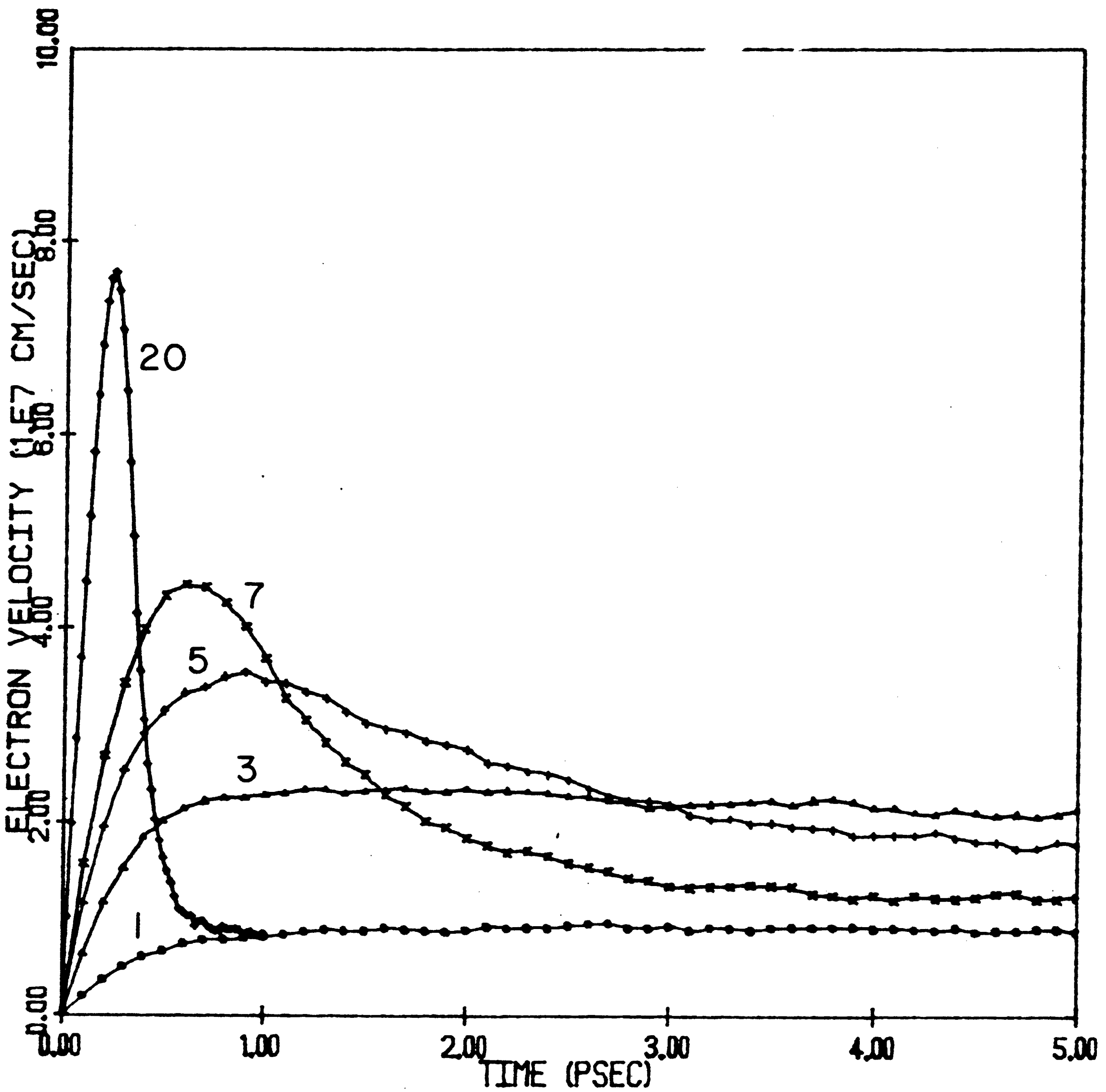

FIG. 6.4 A VELOCITY OVERSHOOT STUDY. THE PARAMETER IS THE FINAL ELECTRIC FIELD IN kV/cm.

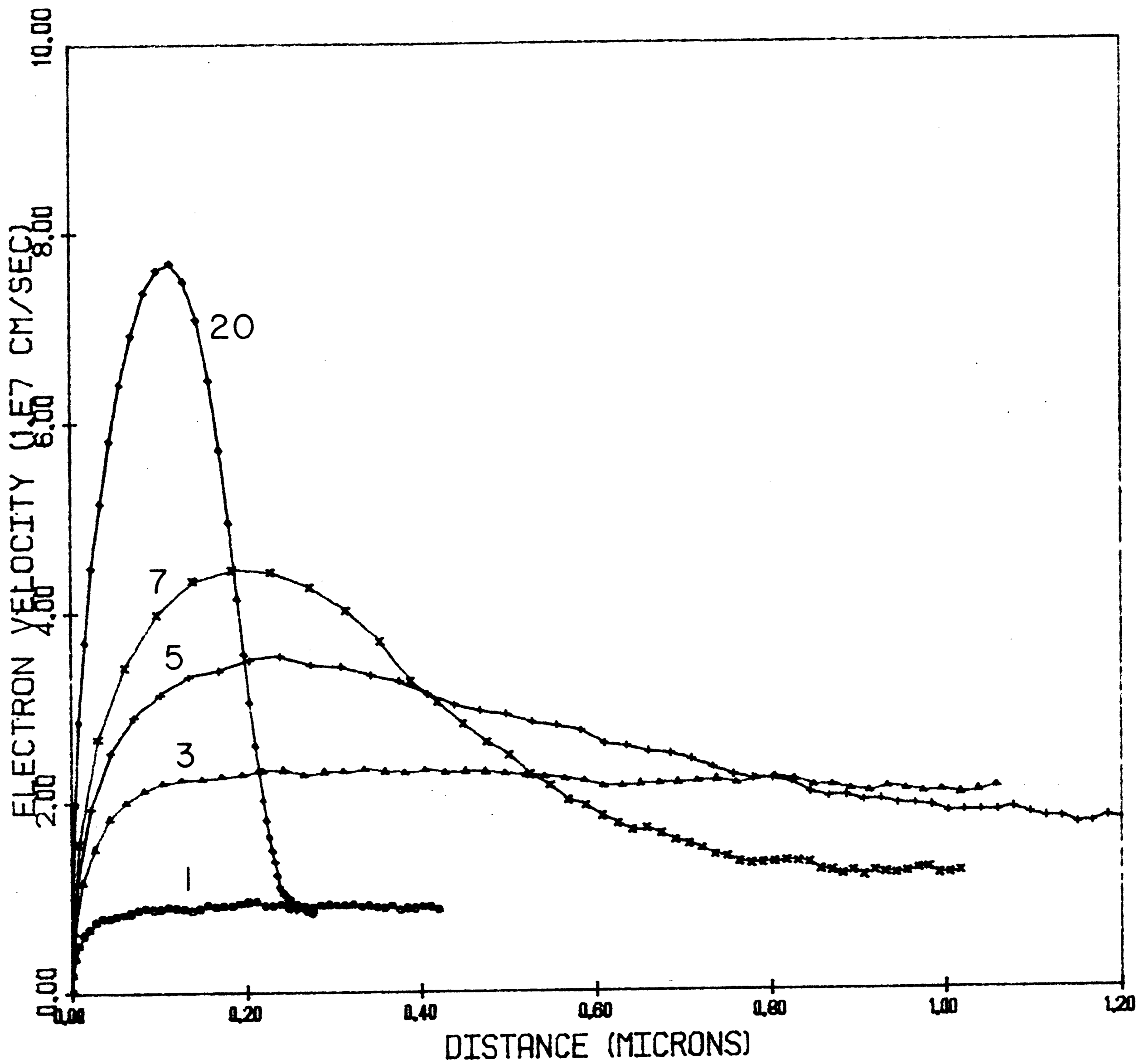

FIG. 6.5 THE VELOCITY OVERSHOOT OF FIG. 6.4 PLOTTED AS A FUNCTION OF MEAN DISTANCE TRAVELED.

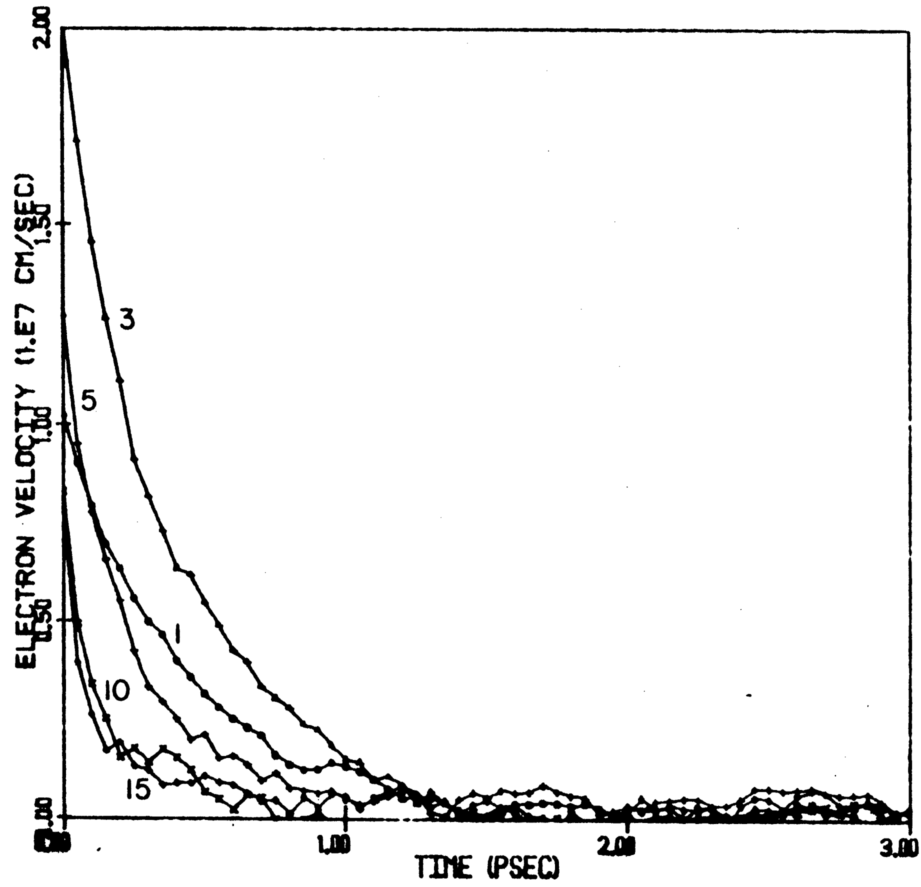

FIG. 6.6 THE VELOCITY COLLAPSE FOLLOWING AN INSTANTANEOUS SWITCH OF THE FIELD TO ZERO. THE PARAMETER IS THE INITIAL FIELD IN kV/cm.

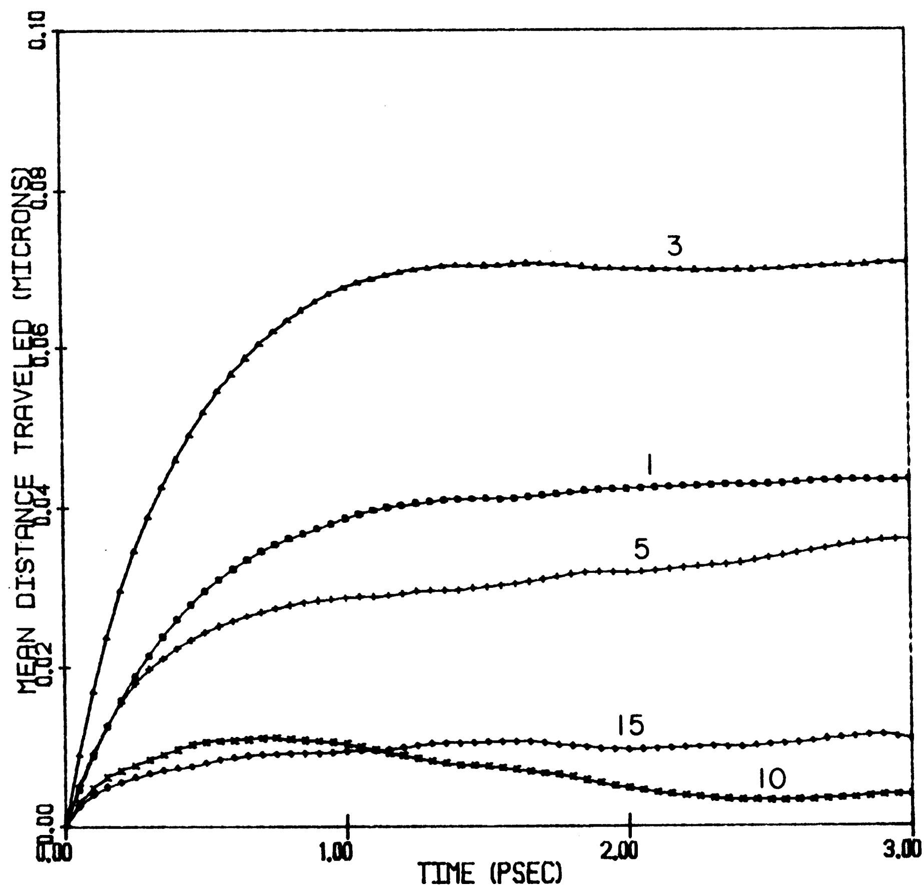

FIG. 6.7 THE MEAN DISTANCE TRAVELED AS A FUNCTION OF TIME AFTER THE FIELD IS SHUT OFF. THE PARAMETER IS THE INITIAL FIELD IN kV/cm.

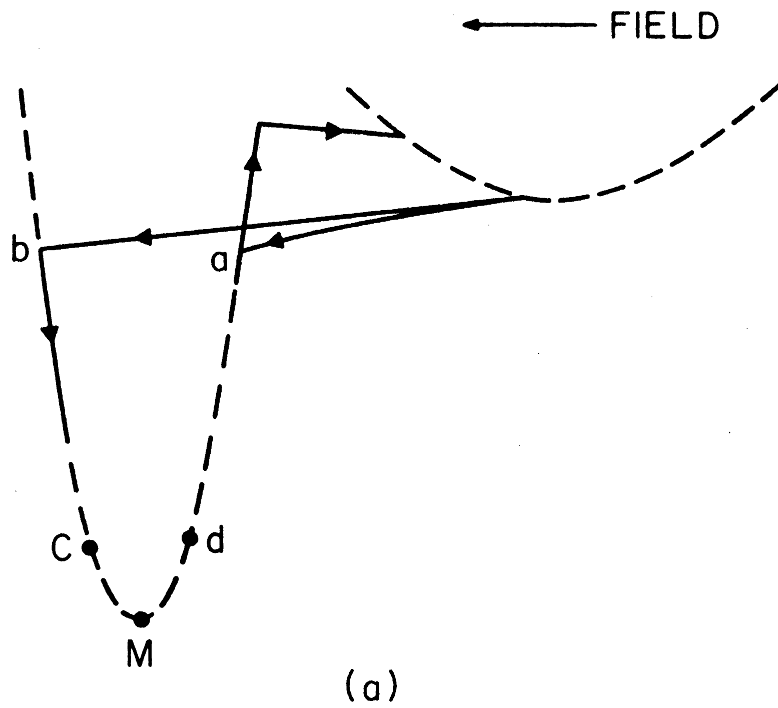

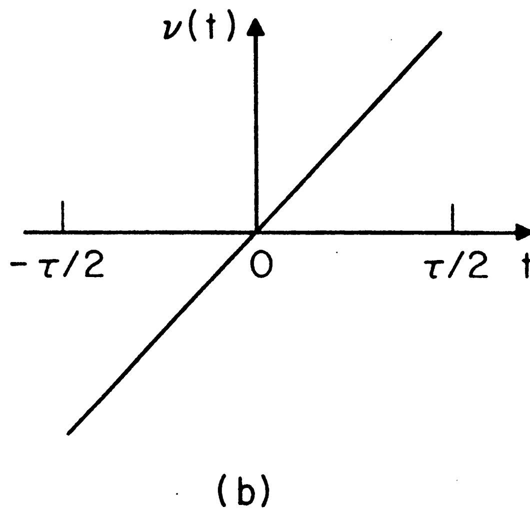

FIG. 6.8 THE JONES-REES CENTRAL VALLEY BEHAVIOR. (a) MOMENTUM SPACE BEHAVIOR AND (b) VELOCITY AS A FUNCTION OF TIME FOR A BALLISTIC FLIGHT ACROSS THE CENTRAL VALLEY.

enter the central valley with negative velocities (e.g., point b) lose energy to the field. As a result they tend to move below the threshold for intervalley scattering and remain in the central valley. This is known as the Jones-Rees effect[167] whose important in Gunn devices is well known. It also affects the nature of velocity fluctuation noise and diffusion. The role played by this effect is to selectively overload the carrier distribution with electrons having a negative velocity for a short time following the field change.

Similar transients occur in the mean carrier energy. The central valley energy is shown as a function of time in Fig. 6.9 and space in Fig. 6.10 for the case in which the field is turned on. Although no undershoots or overshoots occur, there is a prolonged transient. In Fig. 6.11 the mean satellite valley energy is plotted as a function of position for the case in which a field of 20 kV/cm is turned on. A rather dramatic overshoot occurs. The central and satellite valley energies for the experiment in which the field is turned off are shown in Figs. 6.12 and 6.13, respectively. Here, although no overshoots or undershoots are seen, there is a slow thermalization of the carrier distribution.

These energy transients have several important consequences. First they reflect the basic nature of the response. While the carrier acceleration by the field can respond instantaneously to a change in field, the scattering environment cannot change instantaneously. This is closely related to the question of the validity of ballistic transport. (Particularly for low energy electrons, it is <u>not</u> true that acoustic phonon scattering and optical phonon absorption are negligible as is sometimes assumed in ballistic transport discussions.) A second

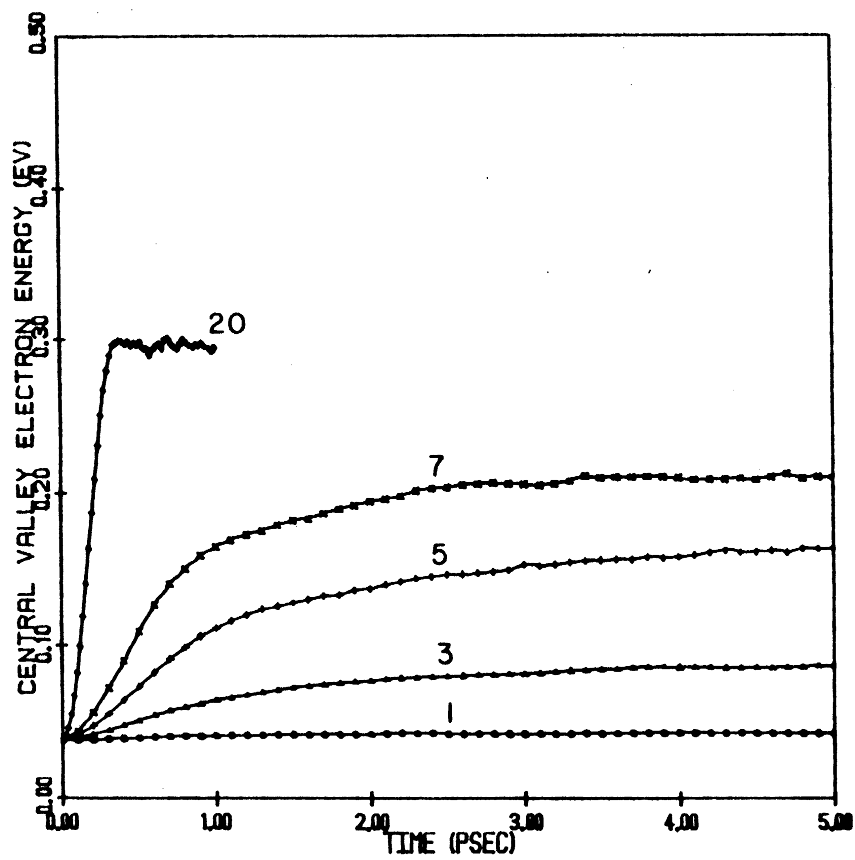

FIG. 6.9 CENTRAL VALLEY ENERGY TRANSIENTS FOLLOWING A SUDDEN APPLICATION OF AN ELECTRIC FIELD. THE PARAMETER IS THE FINAL OR APPLIED FIELD IN kV/cm.

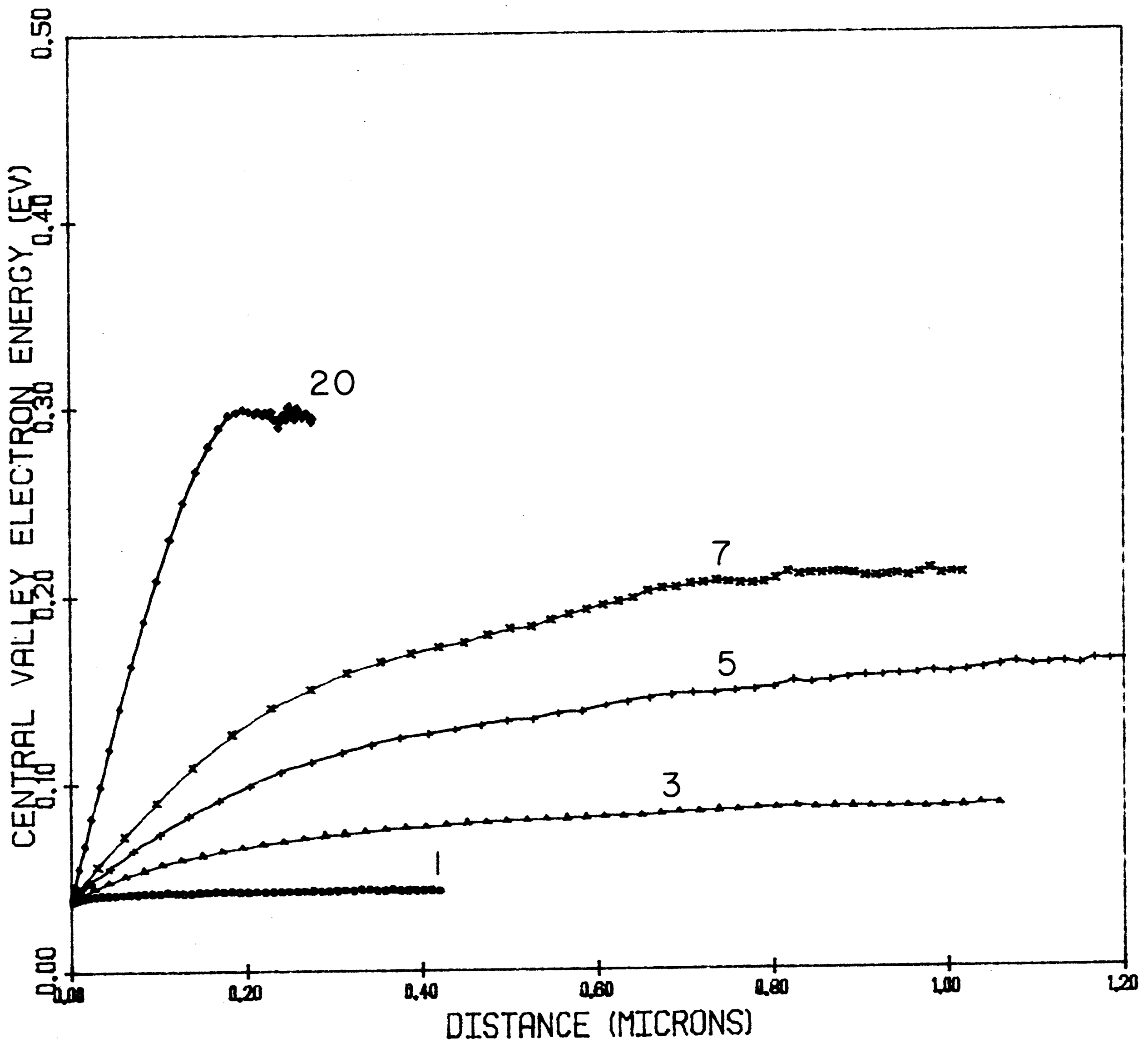

FIG. 6.10 CENTRAL VALLEY ENERGY TRANSIENT OF FIG. 6.9 AS A FUNCTION OF MEAN DISTANCE TRAVELED.

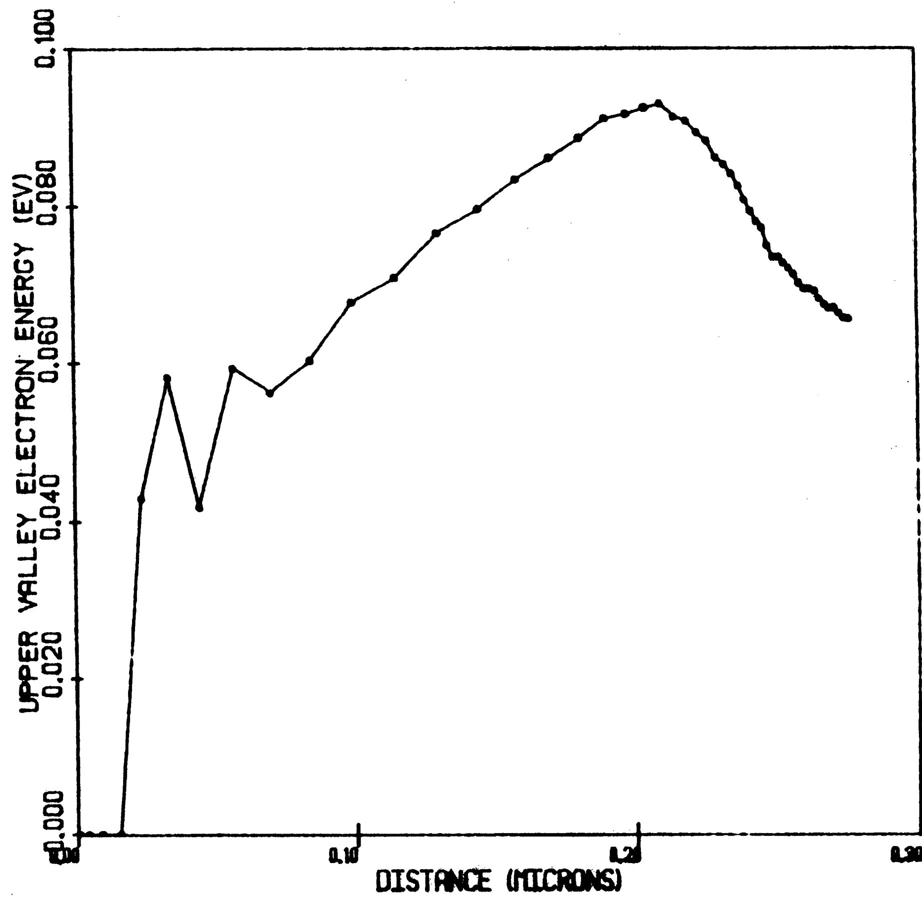

FIG. 6.11 SATELLITE VALLEY ENERGY TRANSIENT CORRESPONDING TO THE CASE OF FIG. 6.9 AS A FUNCTION OF MEAN DISTANCE TRAVELED.

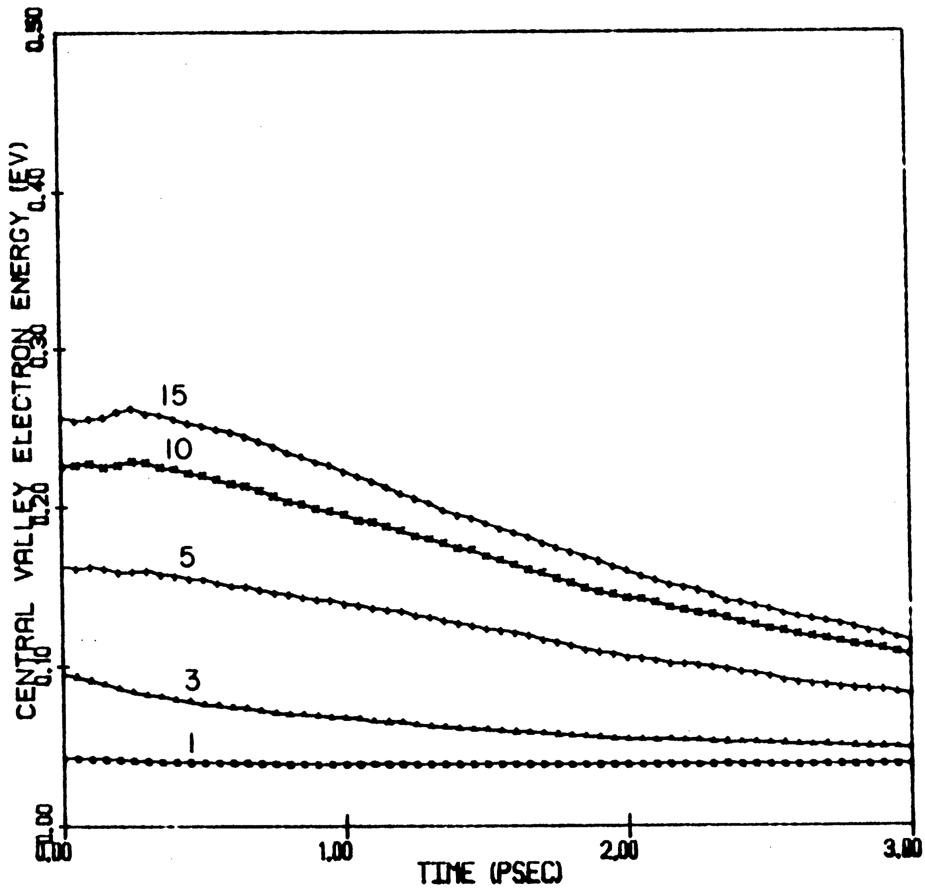

FIG. 6.12 CENTRAL VALLEY ENERGY TRANSIENTS FOLLOWING A FIELD SHUT OFF. THE PARAMETER IS THE INITIAL FIELD IN kV/cm.

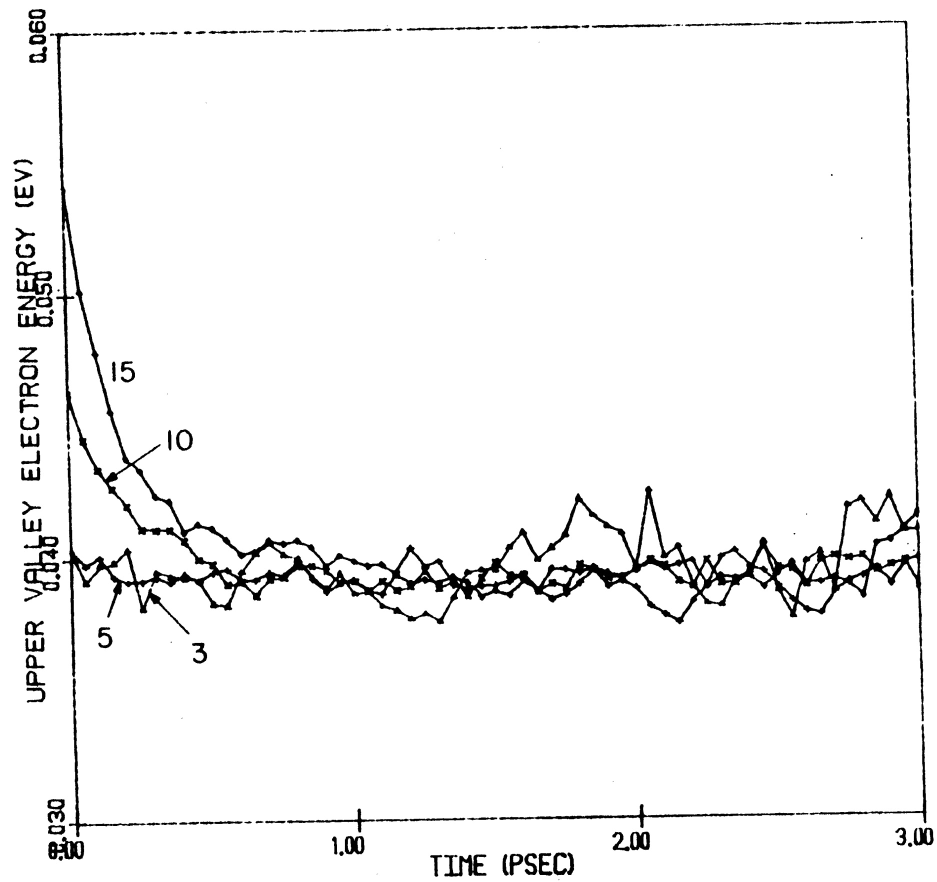

FIG. 6.13 UPPER VALLEY ENERGY TRANSIENTS FOLLOWING THE FIELD SHUT OFF. THE PARAMETER IS THE INITIAL FIELD IN kV/cm.

consequence is that spatial variations in carrier energy should be accompanied by spatial variations in velocity fluctuations. Such variations have in fact been reported[168] and may have great importance in short gate GaAs FET noise modeling.

6.3.3 Efficiency Enhancement and Degradation Through Transient Carrier Transport. In this section mechanisms by which velocity overshoots and undershoots could alter the particle current or induced current waveform in a transit-time device are described. The pertinent transients are illustrated in Fig. 6.14 and 6.15. In Fig. 6.14 the field is switched from a level of 10 to 6 kV/cm while in Fig. 6.15 the field is switched from 6 to 10 kV/cm. A switch down in field results in a velocity undershoot while a switch up in field results in a velocity overshoot even when both the initial and final fields are definitely above the peak field of the static velocity-field curve.

The possible role of these transients in GaAs transit-time devices is now considered. The carriers are injected into a "low" field drift region from a high field avalanche or tunneling region. Furthermore, for an IMPATT, this occurs near the 180-degree phase point in the RF cycle, a point at which the magnitude of the terminal voltage has a large negative derivative, and the fields in the device must be generally decreasing. Under these conditions a velocity undershoot is expected. Such an undershoot would depress the current waveform. Later in the cycle, near 270 degrees of RF phase angle, the voltage and fields begin to increase. This increase, especially in structures where the field is elevated in front of the drifting carrier pulse, can result in a velocity overshoot. Depending on the relative phasing and magnitudes of these overshoots, the efficiency may be either reduced or,

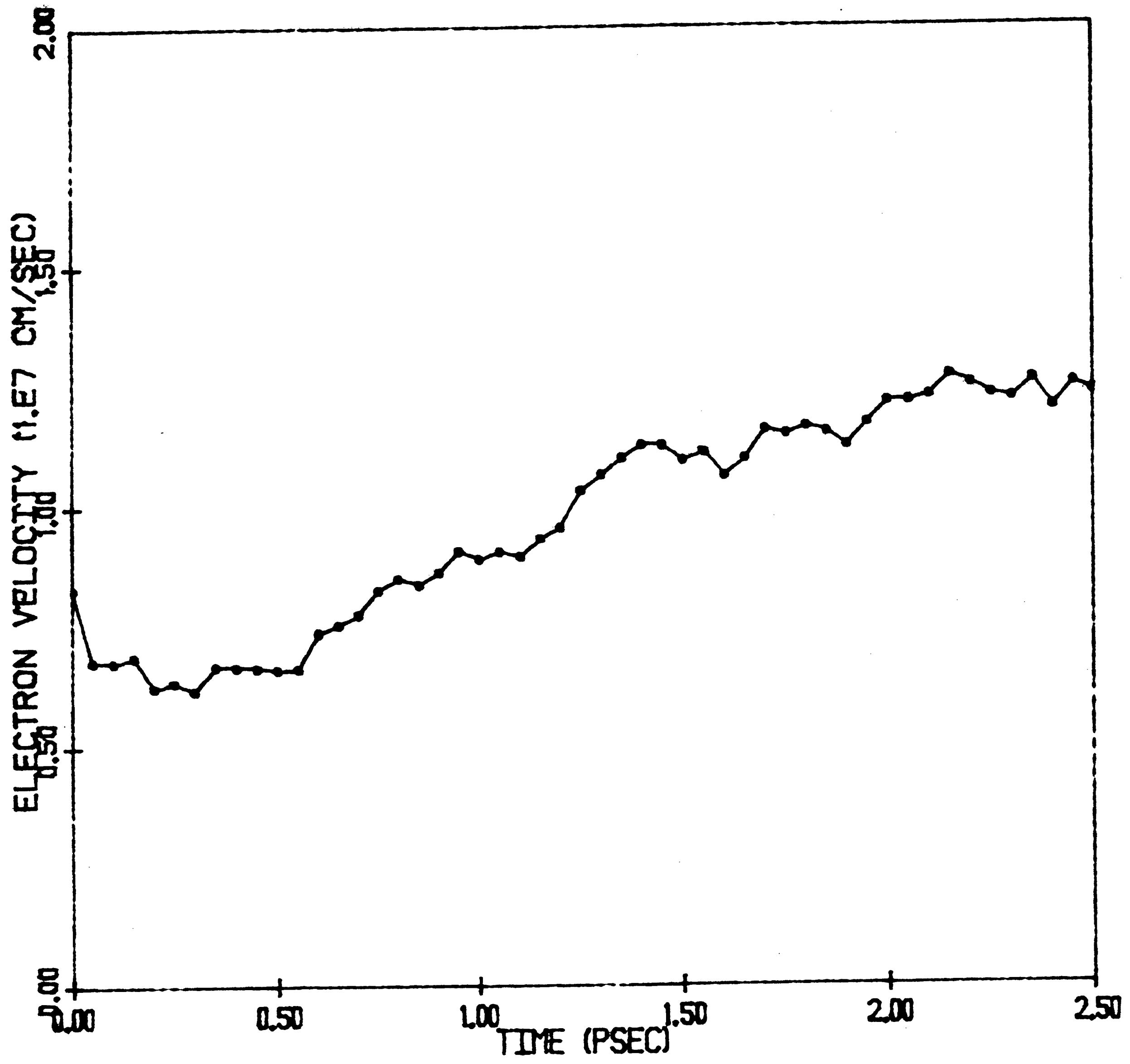

FIG. 6.14 VELOCITY TRANSIENT FOR THE CASE OF A SWITCH FROM 10 kV/cm TO 6 kV/cm.

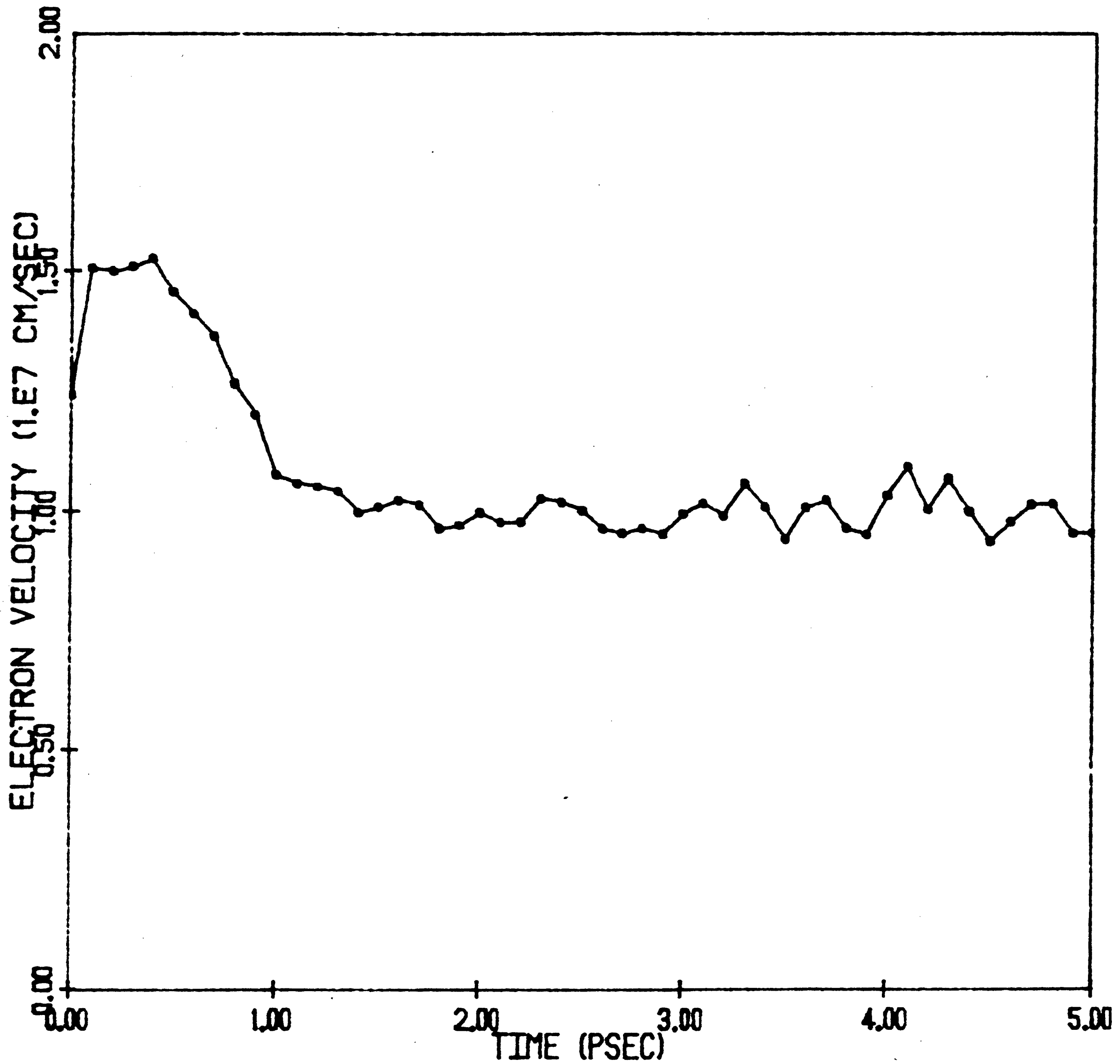

FIG. 6.15 VELOCITY TRANSIENT FOR THE CASE OF A SWITCH FROM A FIELD OF 6 kV/cm TO 10 kV/cm.

more interestingly enhanced. The enhancement would occur by producing a waveform similar to that shown in Fig. 6.16.

The question which will now be addressed is the specification of circumstances under which these transient transport effects would be expected to enhance the transit-time device oscillation efficiency. Since 1 to 2 ps are needed for the velocity overshoots and undershoots, a drift half-cycle length of at least several picoseconds would be needed. This corresponds to an upper frequency limit of 100 to 200 GHz. On the other hand, as the drift half-cycle length is increased, the relative importance of these effects is reduced. It seems doubtful that they would be important in devices designed for operation below 20 to 30 GHz.

Several points can be made concerning the device doping profile. First, it would be desirable to have the electric field sharply drop from the avalanche region to the drift region. Therefore, some type of high-low or low-high-low structure is desired. Second, a punch-through structure would also be desirable. In such structures space-charge interactions can keep the field in front of the drifting carrier pulse higher than the field in the pulse.

6.3.4 Premature Collection at Millimeter-Wave Frequencies. Premature collection operation of transit-time devices is important in high-efficiency operation at microwave frequencies. Attempts to scale these structures to millimeter-wave operation have not succeeded well to date. One possible explanation is that the avalanche process in GaAs has an anomalously long intrinsic response time.[10] Recent work indicates that the drift velocity in GaAs may be somewhat lower at high fields then was earlier expected. This would provide a longer

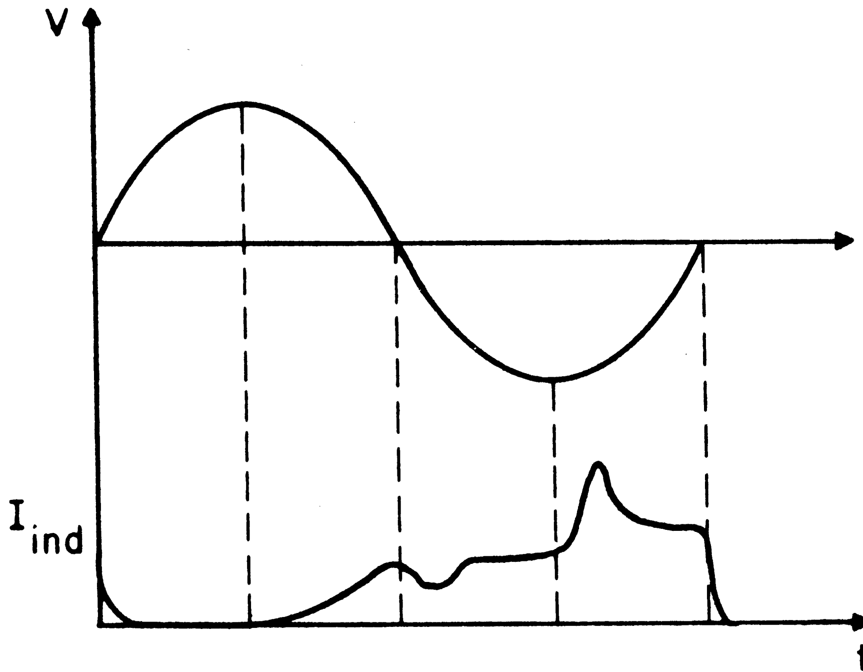

FIG. 6.16 INDUCED CURRENT WAVEFORM TAILORING BY VELOCITY TRANSIENTS WHICH COULD ENHANCE THE OSCILLATION EFFICIENCY. THE TERMINAL VOLTAGE WAVEFORM IS SHOWN FOR REFERENCE. THE INDUCED CURRENT DIP FOLLOWING THE 180-DEGREE PHASE POINT IS A RESULT OF A VELOCITY UNDERSHOOT WHILE THE PEAK IN THE LAST QUARTER CYCLE IS A RESULT OF A VELOCITY OVERSHOOT.

intrinsic response time in GaAs without introducing any anomalous effects. Here a second limitation is suggested. This new limitation involves an upper frequency limit to premature collection which arises from transient carrier transport.

Premature collection occurs when the depletion-layer edge in an n-type GaAs transit-time device moves in from the nn^+ collecting contact and prematurely intercepts the drifting carrier pulse. The efficiency is enhanced by both improving the phasing of the collection and by contributions made by carriers in the undepleted region to the induced current. The central point of the discussion here is that both the carriers in the injected current pulse and in the undepleted region contribute to a velocity undershoot which starts with the pulse interception and lasts for several picoseconds. This velocity undershoot should lead to a dip in the induced current at the interception point which lies near the 270-degree phase point. Such a dip will degrade the device efficiency.

In Fig. 6.17 the velocity is shown as a function of time for a sequence of field steps down from an initial field of 6 kV/cm to final fields of 5, 4, 3, 2 and 1 kV/cm. The basic response is a severe velocity undershoot which lasts for 1 to 2 ps. In Fig. 6.18 the corresponding ratio of satellite to central valley electron population ratio is shown. The valley population ratio responds much more slowly than the velocity. As electrons in the injected carrier pulse experience such a sudden field drop, they are expected to contribute to a velocity and current undershoot.

Carriers in the undepleted layer undergo a somewhat similar phenomena. The trajectory which they follow in momentum space is

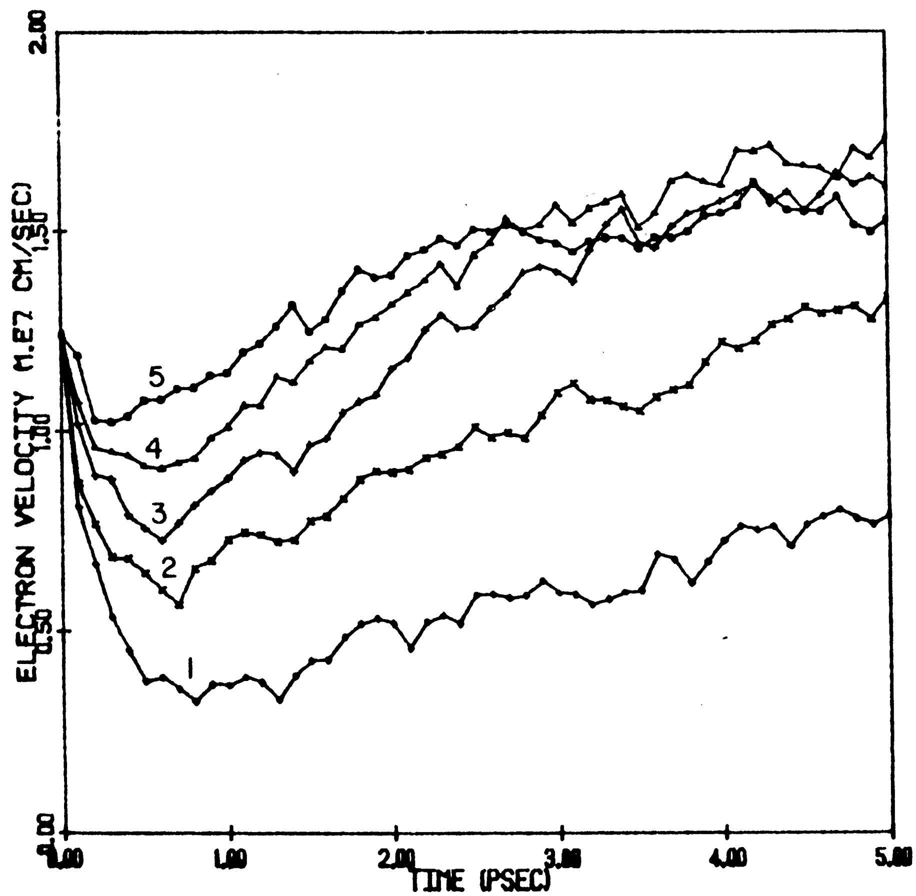

FIG. 6.17 VELOCITY TRANSIENTS FOR A STEP DOWN IN FIELD. THE INITIAL FIELD IS 6 kV/cm AND THE PARAMETER IS THE FINAL FIELD IN kV/cm.

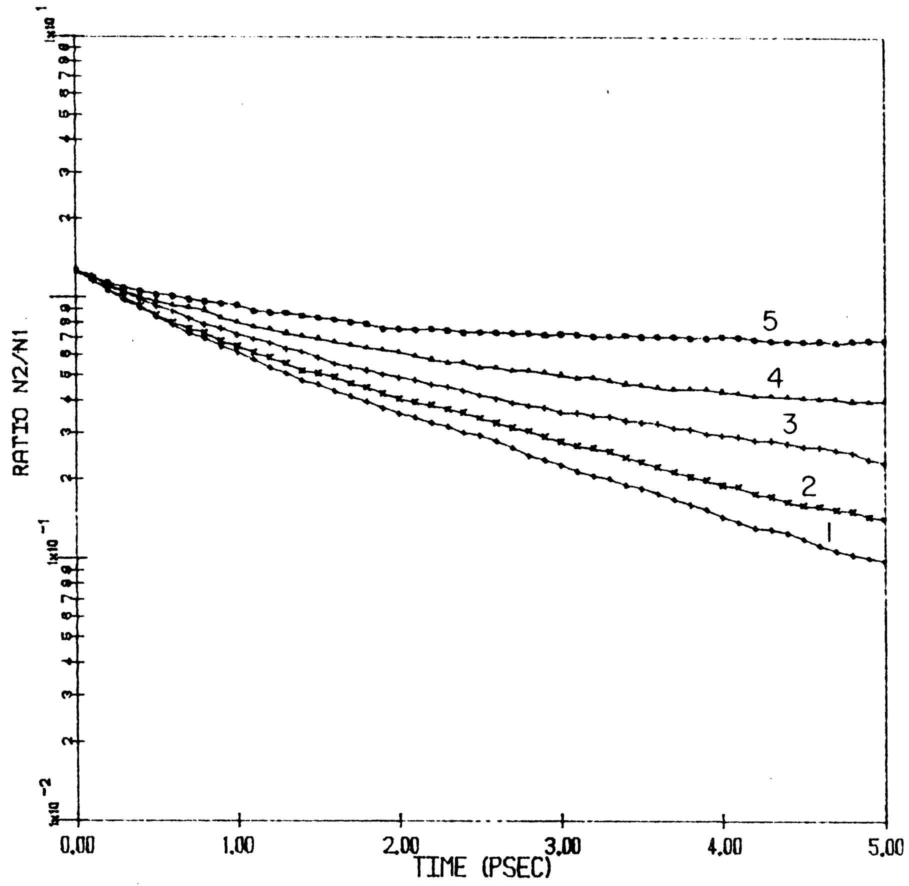

FIG. 6.18 RATIO OF SATELLITE VALLEY POPULATION (N2) TO CENTRAL VALLEY POPULATION (N1) AS A FUNCTION OF TIME FOR THE FIELD STEPS OF FIG. 6.17.

also illustrated in Fig. 6.8. Initially they move away from the nn^+ contact. During the pulse interception they reverse their direction of travel. In Fig. 6.8 this is the trajectory cmd. Since this also takes some time, these carriers will also contribute to the velocity undershoot. The above discussion provides several strong arguments for the existence of a dip in the induced current which may last for 1 to 2 ps immediately following the pulse interception. At 10 GHz, this dip would be inconsequential. The drift half-cycle at 10 GHz is 50 ps long, and there is ample time for the carriers to equilibrate to an elevated velocity (in accordance with the static velocity-electric field characteristic) after the dip. It is precisely this elevated velocity which leads to the well-established efficiency enhancement obtained by premature collection in X-band devices. At 40 GHz, however, the drift half-cycle is only 12.5 ps long. A 1-ps dip near the crucial 270-degree phase point is therefore much more significant, and there will only be several picoseconds available after the dip for the velocity elevation to occur. At 80 GHz the drift half-cycle is only 6.25 ps long, and it seems doubtful that premature collection, as conventionally understood, is possible.

The mechanisms discussed here can be partially included in a standard drift-diffusion model by utilizing a realistic field-dependent diffusion coefficient. The diffusion coefficient in GaAs rises to very high levels for field values around the peak field in the velocity-electric field characteristic. This peak is a direct result of the intervalley scattering physics discussed here. In a standard simulation, this high diffusion coefficient will result in

a substantial broadening of the pulse. This pulse broadening will degrade the efficiency.[169] It becomes particularly important in millimeter-wave devices because they are much shorter than X-band devices. Conventional simulations show that diffusion effects are sufficiently adverse in GaAs millimeter-wave devices that, unlike the situation at X-band, it is preferred to keep the active region of the device depleted throughout the cycle.[170]

6.3.5 Carrier Inertial Effects in Undepleted Regions. It has long been known that losses in undepleted regions limit the power and efficiency of IMPATTs. The role played by transient carrier dynamics in determining these losses in undepleted bulk GaAs has recently been studied by Blakey et al.[130] Here it is shown that these effects can cause the losses to be larger than anticipated in GaAs transit-time devices.

The key concept here is that the carrier velocity is no longer in phase with the RF field. Rather, the velocity has both an in-phase and a quadrature-phase component. A sample result is shown in Fig. 6.19. Here the in-phase and quadrature-phase velocity components are shown as functions of RF field amplitude. The RF frequency is 250 GHz and the dc field is zero. The in-phase component of velocity decreases for large drives thereby increasing the losses. This is anticipated from the static velocity-field characteristic. What is not anticipated in these conventional models is the quadrature-phase component. This component is inductive at low drives but becomes capacitive for very high drives. The effect of an inductive quadrature-phase component is to counteract the capacitive displacement current flow. This means that larger RF fields are required to

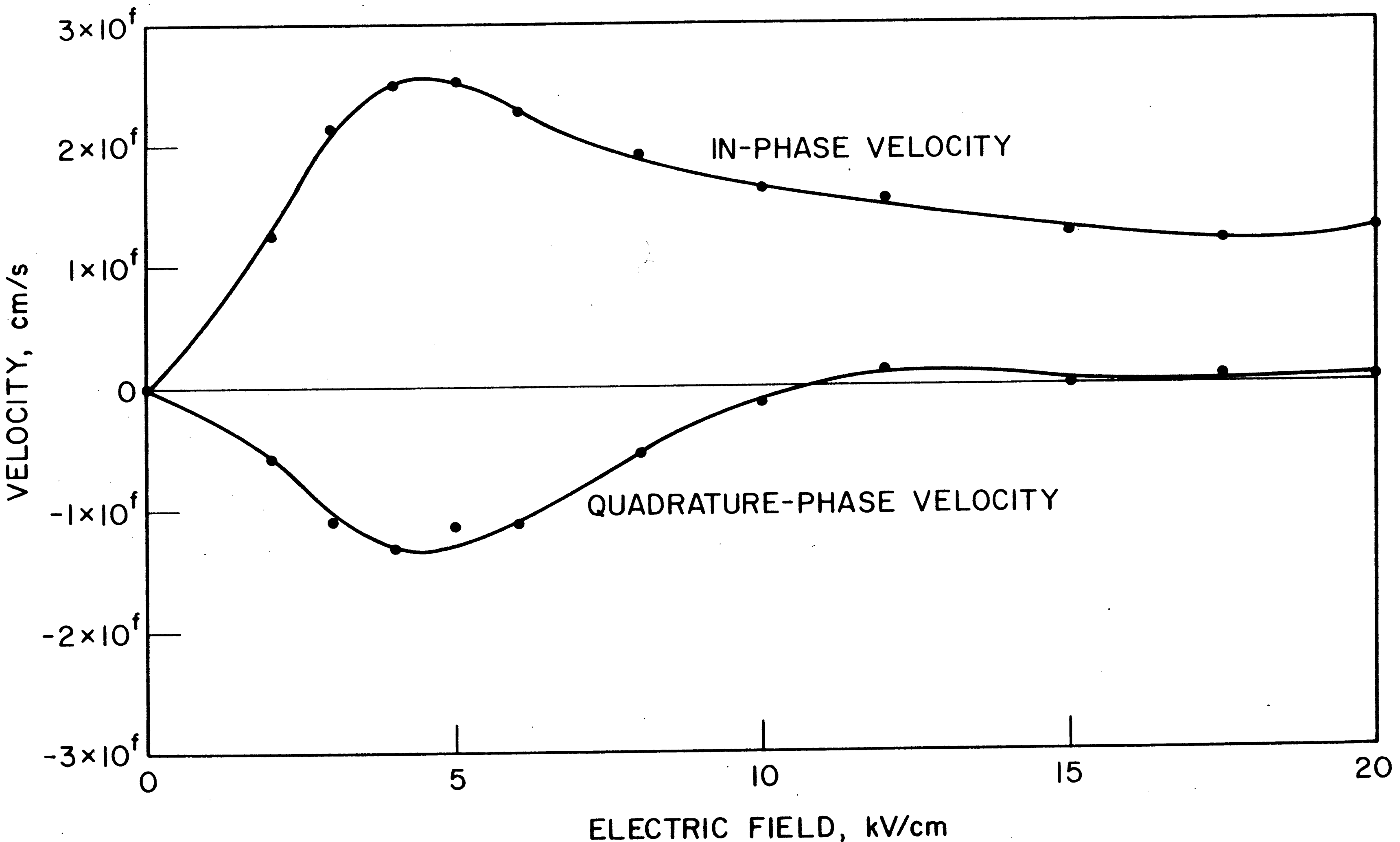

FIG. 6.19 IN-PHASE AND QUADRATURE-PHASE VELOCITY COMPONENTS AT 250 GHz AS FUNCTIONS OF RF DRIVING FIELD LEVEL. THE DC FIELD WAS ZERO.

maintain the same total RF current thereby increasing the losses.

The effects discussed here are essentially a large-signal plasma resonance effect. There is a characteristic scattering or relaxation time τ, and the in-phase mobility μ_r (as determined by the slope in the in-phase velocity component at low drive levels) is

$$\mu_r = \frac{\mu_o}{1 + (\omega\tau)^2} , \tag{6.1}$$

while the quadrature-phase mobility is

$$\mu_i = \frac{\mu_o \omega\tau}{1 + (\omega\tau)^2} , \tag{6.2}$$

where ω is the radian frequency and μ_o is the dc mobility. It should be noted that the in-phase mobility is a decreasing function of frequency.

Zimmermann et al.[171] have performed a related investigation for Si IMPATTs. They found a similar frequency and drive dependent mobility with in-phase and quadrature-phase components. They considered the effects of the mobility in the high field region under a standard small-signal analysis and argued that it would lead to a decrease in efficiency. Another related argument was presented by Doumbia et al.[172] who arrived at a similar conclusion with a more qualitative argument. Neither group considered the effects in the undepleted regions. Champlin and Eisenstein[129] have included plasma resonance effects in the undepleted region in an analysis of millimeter- and submillimeter-wave mixer diodes. They found that such effects can result in a substantial improvement in mixer behavior at submillimeter-wave frequencies.

6.4 The Theory and Practice of Monte Carlo Noise Experiments

6.4.1 Introduction.

The noise properties of semiconductor devices are extremely important in many applications. As a result, considerable effort is expended on modeling semiconductor device noise behavior, using a variety of techniques of varying sophistication and applicability.[173]

The noise theories are all based, implicitly or explicitly, on assumptions regarding the microscopic behavior of charge carriers in the semiconductor. While it is essentially impossible to check these assumptions experimentally, many may be checked (at least within the limitations of the quasi-free-particle approximation) and more general results may be obtained using statistical simulations of carrier transport, i.e., Monte Carlo "experiments." These experiments are particularly appropriate for investigating millimeter- and submillimeter-wave noise properties and are likely to be increasingly applied in the context of submicron device noise theory. This section is concerned with the theory and practice of using such Monte Carlo experiments.

The most important microscopic assumptions concern the shapes of the noise source spectrum and autocorrelation functions. Monte Carlo estimation of these quantities has been attempted by various workers[174-177] with some success. However, the procedures involved are generally not well understood, and certain problems and accuracy limitations which can be encountered are not fully recognized. (This is in contrast to the situation regarding Monte Carlo-based estimates of steady-state transport coefficients, such as drift velocities and diffusion coefficients.[178]) Here, techniques relevant to the

application of Monte Carlo experiments to noise investigations are discussed. A sample time series for the case of electron transport in GaAs is then analyzed using the techniques, and significant new results and insights are obtained.

The organization of this section is as follows. Section 6.4.2 contains a brief review of the physical and mathematical background of the problem under consideration and Section 6.4.3 contains a review and discussion of relevant statistical procedures. The results of the analysis of a sample time series are presented and discussed in Section 6.4.4.

6.4.2 Physical and Mathematical Background. The problem under consideration is the estimation of the velocity fluctuation spectrum in multivalley semiconductors in the presence of a constant electric field. The computer results are obtained in Section 6.4.4 for GaAs modeled by a central valley and a set of equivalent satellite valleys (the "two-valley" model of Fawcett et al.[163,164]), but the extension to three or more valleys is straightforward so this choice is not restrictive.

The microscopic random processes of interest describe the velocity and valley of a single electron as a function of time. The velocity process is

$$v(t) = E[v] + \Delta v(t) \quad , \qquad (6.3)$$

where $E[v]$ is the expected or mean value of v and Δv is a random fluctuation about this mean. The mean is constant since the electric field seen by the electron is constant. The valley process is developed by assigning the numerical identifier "1" to the central valley

and "2" to satellite valleys. The valley random variable val(t) is assigned the identifier of the valley occupied by the electron at time t.

In the Monte Carlo experiments being considered, estimates of the autocovariance and spectrum of the velocity and valley random processes may be obtained. The autocovariance of the velocity process is

$$K_v(t_1,t_1 + \tau) = E\left\{\{v(t_1) - E[v(t_1)]\}\{v(t_1 + \tau) - E[v(t_1 + \tau)]\}\right\} , \qquad (6.4)$$

which is also the autocovariance of the velocity fluctuation process. The autocovariance of the valley process is

$$K_{val}(t_1, t_1 + \tau) = E\{\langle val(t_1) - E[val(t_1)]\rangle\langle val(t_1 + \tau) - E[val(t_1 + \tau)]\rangle\} , \qquad (6.5)$$

which may be expressed as (for either i = 1 or i = 2)

Pr(electron is in valley i at both time t_1 and time $t_1 + \tau$)

- Pr(electron is in valley i at any time)^2 =

Pr(electron is in valley i at time t_1)

$\cdot${Pr(electron is in valley i at time $t_1 + \tau$ given that it is in valley i at time t_1) - Pr(electron is in valley i at time t_1)} ,

where Pr(x) is the probability of event x occurring. A positive valley autocovariance means that it is more likely that the electron is in equivalent valleys at the two times than the unconditional

probability of finding the electron in the original valley i at time $t + \tau$.

The velocity fluctuation spectrum is given by the Fourier transform of the velocity fluctuation autocovariance with respect to the lag time,

$$S_v(f) = \int_{-\infty}^{\infty} K_v(t_1, t_1 + \tau) e^{-j2\pi f\tau} \, d\tau \quad . \tag{6.6}$$

If the spectrum is to be useful, the dependence of K_v on the absolute time t_1 must be known. The usual assumption of stationarity (that K_v is independent of t_1) is adopted here.

The fluctuating velocity component Δv leads to two measurable physical phenomena, diffusion and noise. The common physical origin explains why the label "diffusion noise" is often applied to velocity fluctuation noise. There is a simple relationship between the conventional diffusion coefficient D and the zero-frequency value of the velocity fluctuation spectrum[179,180]

$$D = \frac{1}{2} S_v(0) \quad . \tag{6.7}$$

(When this relationship is used it is possible to use noise measurements as an experimental means of obtaining values for diffusion coefficients.[179]) The velocity fluctuation is related to the velocity fluctuation noise source spectrum $S_j(f)$ used in noise modeling by[179]

$$S_j(f) = q^2 n S_v(f) \quad , \tag{6.8}$$

where n is the carrier density and q is the magnitude of electronic charge. A useful division of the total spectrum in multivalley semiconductors was suggested by Shockley et al.[180] In a two-valley

semiconductor, three components may be considered: one due to electron motion in the first valley, one due to electron motion in the second valley, and a "partition noise" spectrum due to the random partition of the electrons between the two valleys.

6.4.3 Statistical Procedures. Autocovariances and spectra are quite commonly estimated in time series analysis. The basic techniques are described in textbooks on time series analysis,[181-183] and computer programs for their evaluation are available.[184,185] The discussion in this section therefore concentrates mainly on the particular methods and problems associated with time series analysis of Monte Carlo generated data pertaining to hot carrier transport in semiconductors. The discussion is divided into three parts: first, a general discussion of time series analysis, then of window function properties, and finally of the selection of time series length and sampling rate.

A crude Monte Carlo estimation of an autocovariance may be obtained by first generating k independent realizations or time series of the basic Monte Carlo experiment and then averaging the quantities $\Delta v(t_1)\Delta v(t_1 + \tau)$ over each realization. Under fairly weak conditions, this ensemble average converges (almost surely) to the actual autocovariance. Alternatively, a single time series can be used with the additional assumption of ergodicity to obtain an estimate of the same autocovariance. In particular, if the time series is observed at intervals Δt with $r\Delta t = \tau$, then[181]

$$\lim_{L \to \infty} \frac{1}{L} \sum_{j=M}^{M+L-r} \Delta v(j)\Delta v(j + r) = K_{\Delta V}(\tau) \quad , \qquad (6.9)$$

where M is some starting value, L is the number of time points for which data is available, and equality means convergence with probability one.

The corresponding estimate of the spectrum from the same single time series is the periodogram which is defined by[181]

$$I_v(f) = \frac{\Delta t}{N} \left| \sum_{n=-(N/2)}^{n=(N/2)-1} v(t) \exp^{-j2\pi f \Delta t} \right|^2 , \quad -\frac{1}{2\Delta t} \leq f \leq \frac{1}{2\Delta t} , \tag{6.10}$$

where $v(t)$ is sampled at N data points with spacing Δt running from $-N\Delta t/2$ to $[(N/2) - 1]\Delta t$. The inverse transform of $I_v(f)$ is the time average autocovariance of the data set. [In practice it is computationally more efficient to use fast Fourier transforms (FFTs) to calculate and invert $I_v(f)$ than it is to calculate $K_{v_t}(\tau)$ directly from the time average.]

It is important to note that even for an ergodic process

$$\lim_{T\to\infty} I_v(f) \neq S_v(f) , \tag{6.11}$$

i.e., <u>the periodogram does not limit to the spectrum</u>, as is sometimes assumed intuitively.[174,176] (A convincing demonstration of this inequality is given by Jenkins and Watts.[181]) The left-hand side of Eq. 6.11 is actually a random variable whose variance is proportional to $S_v^2(f)$. Ths means that increasing the time series length has <u>no effect</u> on the variance or mean square error of the periodogram estimate of $S_v(f)$. Increasing the time series length improves the <u>resolution</u> (it makes each periodogram point an estimate of the power in a narrower frequency band) without improving the <u>accuracy</u> of the estimate.

As is demonstrated in Section 6.4.4, the periodogram is a very noisy estimate of $S_v(f)$. Two approaches have previously been used to reduce the variance in estimates of $I_v(f)$ obtained from Monte Carlo generated time series. One approach is to average many periodograms,[174] while the other is to Fourier transform a truncated velocity fluctuation autocorrelation function.[175] Both of these procedures are actually particular cases of a more general smoothing procedure in which the periodogram is smoothed by the use of a "lag window."

In the window smoothing procedure (which is described in detail by Jenkins and Watts[181]), the spectral estimate is obtained by the Fourier transform

$$\int_{-\infty}^{\infty} K_v(\tau)w(\tau)\ \exp^{-j2\pi f\tau}\ d\tau \quad ,$$

where $w(\tau)$ is the lag window function. Averaging many periodograms is equivalent to using a Bartlett window,[181] while truncating the autocorrelation is equivalent to imposing a rectangular window. The finite length of the time series is also equivalent to imposition of a rectangular window. Once it is realized that a window smoothing is implicitly or explicitly involved, it becomes an obvious procedure (and a necessary one if the quality of the estimate is to be assessed) to understand and, where possible, exploit the effect of the window on the estimate. The present work, in fact, uses certain advantageous properties of the Parzen window.

The functional forms of the rectangular, Bartlett and Parzen windows are given in Table 6.1 and plotted in Fig. 6.20. (Details of other windows are given in Jenkins and Watts.[181]) Since time domain

Table 6.1

Lag and Spectral Window Functions

Window Name	Lag Window Function	Spectral Window Function
Rectangular	$w_R(u) = \begin{cases} 1 & \|u\| \leqq M \\ 0 & \|u\| > M \end{cases}$	$W_R(f) = 2M \sin(2\pi f M)/2\pi f M$
Bartlett	$w_B(u) = \begin{cases} 1 - (\|u\|/M) & \|u\| \leqq M \\ 0 & \|u\| > M \end{cases}$	$W_B(f) = M[(\sin \pi f M)/\pi f M]^2$
Parzen	$w_P(u) = \begin{cases} 1 - 6(u/M)^2 + 6(\|u\|/M)^3 & \|u\| \leqq (M/2) \\ 2[1 - (\|u\|/M)]^3 & (M/2) < \|u\| \leqq M \\ 0 & \|u\| > M \end{cases}$	$W_p(f) = \frac{3}{4} M[(\sin \pi f M/2)/(\pi f M/2)]^4$

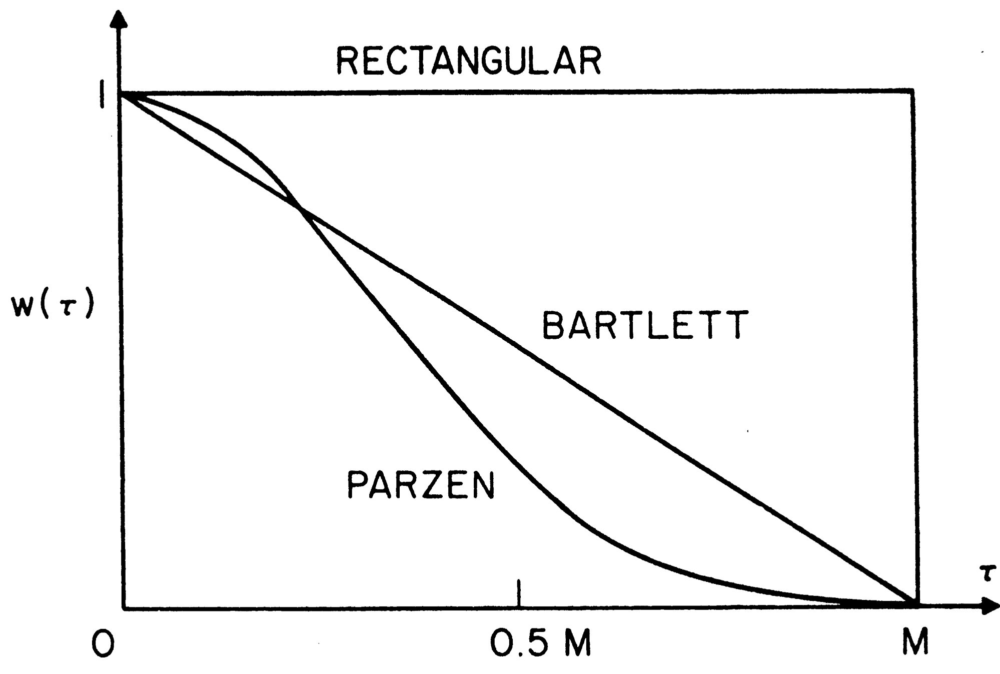

FIG. 6.20 THREE LAG WINDOWS.

multiplication corresponds to frequency domain convolution,* the Fourier transforms of the three windows are shown in Fig. 6.21. The Parzen window has the particular advantage of having reduced side-lobes, thereby decreasing one mechanism (leakage) by which spurious artifacts can be introduced into the spectrum. The Parzen window also has the property that it will not provide negative estimates. The Bartlett and rectangular windows also have this property, but some windows (e.g., the Tukey window[181]) do not.

In Table 6.2 several figures of merit for the various windows are provided. The bandwidth represents the minimum size spectral structure which can be resolved by the estimate. The bias and the variance are quantities possessed by all statistical estimates. Since any statistical estimate will yield different values for different time series, a statistical estimate can be viewed as a random variable which will have an expected or average result and a variance describing the mean square or standard deviation of the estimate from its expected value. The estimated bias is the difference between the actual quantity and the expected or average estimation result and is, therefore, a measure of the average or expected error. The variance describes the expected spread or "noise" of the estimate. The variance ratio shown in Table 6.2 is the ratio of the smoothed spectral estimate variance to the variance of the unsmoothed periodogram [which is proportional to $S_V(f)$]. The bias is proportional to the second derivative of $S_V(f)$ with respect to frequency, so the

---

* Rees[186] has used a similar convolution to eliminate unphysically long time constants in an indirect Monte Carlo calculation of transferred-electron devices.

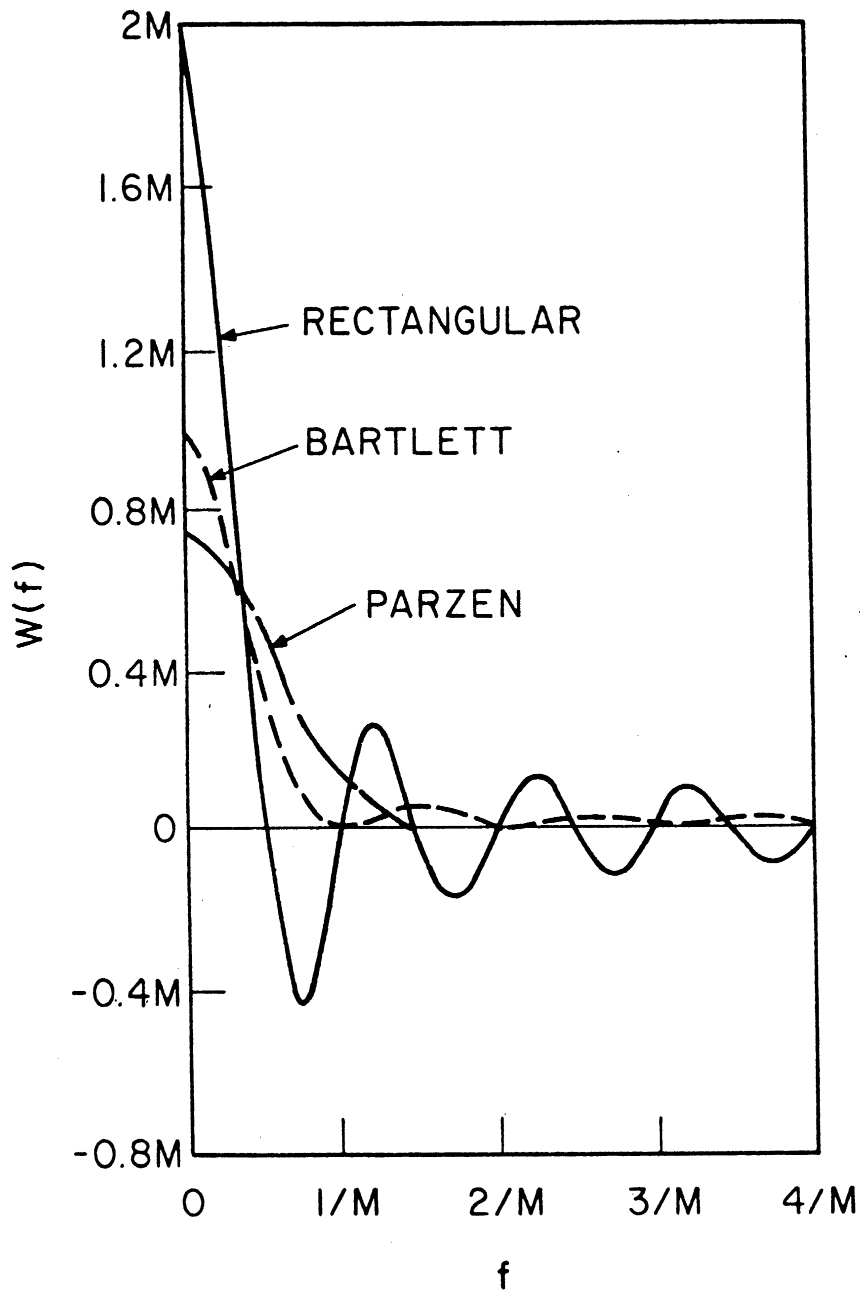

FIG. 6.21 THREE SPECTRAL WINDOWS.

Table 6.2

Properties of Spectral Window Estimates

Window Name	Bandwidth	Bias*	Variance Ratio
Rectangular	0.5/M	**	2M/T
Bartlett	1.5/M	order 1/M	0.667M/T
Parzen	1.86/M	$(0.152/M^2)S^{(2)}(f)$***	0.539M/T

---

* The bias of all the windows is proportional to the second derivative of the real spectrum with respect to frequency.

** A convolution integral expression is provided by Jenkins and Watts.[181]

*** $S^{(2)}(f)$ is the second derivative of S(f) with respect to frequency.

spectrum tends to be underestimated around peaks and overestimated around troughs. Ideally both the bias and variance would be zero. In practice, there is a trade-off between the two. Table 6.2 shows that increasing the window width M decreases the bias but increases the variance. The optimum M is found by performing a window closing experiment in which the time series is analyzed using increasing values of M. The window length is increased until the resulting spectrum contains all the structures which are known to be present, and no additional structures which cannot be explained. A more useful criterion does not exist.

There are two considerations involved in choosing a lower bound for the time series length T. The first is that the finite length of the time series itself imposes a window (the data window) implying a window convolution integral of the form[181]

$$S_{obs}(f) = \int_{-\infty}^{\infty} S_v(f) \frac{T \sin \pi(f - g)T}{\pi(f - g)T} dg \quad . \tag{6.12}$$

Therefore, T should be chosen such that $S_v(f)$ is constant over the main sinc function lobe, e.g.,

$$\frac{0.5}{T} \leq \Delta f_{flat} \quad , \tag{6.13}$$

where Δf_{flat} is the smallest frequency band across which the spectrum can be approximated as flat. Based on results obtained elsewhere,[174-177] a good choice for Δf_{flat} is 20 to 30 GHz. The corresponding time series length is 20 ps or longer. The other factor is the desirability of ensuring that the behavior with the longest associated time constant repeats often enough to be adequately modeled statistically. A variety of factors including relaxation times, high-frequency

fall-off of negative differential mobilities, difficulties in diffusion coefficient estimation, and some results presented in Section 6.4.4 indicate that time constants in the 2 to 10 ps range can be associated with electron transport in GaAs, and thus the minimum time series length should be in the 50 to 100 ps range.

The time step chosen (or, equivalently, sampling rate) can play a critical role. The process of sampling the data at a fixed rate, every Δt, alters the spectrum to

$$S_{alias}(f) = \frac{1}{\Delta t} \sum_{n=-\infty}^{\infty} S_v\left(f - \frac{n}{\Delta t}\right) \quad . \tag{6.14}$$

If Δt is not small enough to ensure that $S_v(f) << S_v[f - (1/2\Delta t)]$ for all $f \geqq (2\Delta t)^{-1}$, then significant spectral power will be transferred from high frequencies to low frequencies by the sampling process (this is the well-known phenomenon of aliasing). Intuitively the spectral power is expected to become small only at frequencies in excess of the most rapid scattering rates. The inverse of the scattering rates used to obtain the results in Section 6.4.4 are shown in Figs. 6.2 and 6.3. From these it would seem reasonable to expect significant spectral power out to several THz, and that time steps in excess of a few hundredths of a picosecond could lead to significant aliasing problems. This assessment of the significance of the spectral power in the THz frequency range is supported by results obtained elsewhere[174-177] and in Section 6.4.4.

One final consideration is that the combination of long T and short Δt can require analysis of a large number of data points. The storage capacity of some FFT routines may be exceeded, and mass storage FFT techniques[184] may be required. The minimum number of

data points based on a minimum T of 50 ps and a maximum Δt of 2.5×10^{-2} ps is approximately 2000, and significantly more are generally desirable.

6.4.4 An Example of a Time Series Analysis. In this section results of a sample analysis of a time series are presented and discussed. The Monte Carlo simulation program can provide the instantaneous electron state at a user specified rate. The particular data analyzed represents an electron flight in GaAs, with impurity scattering neglected, at an electric field of 10 kV/cm and a temperature of 300°K.

The time series length, sampling rate, and lag window were chosen according to the criteria established in Section 6.4.3. The choices of time series length and sampling rate were limited by a 16,000 point limitation on the FFT employed,[185] although as previously noted the limitation could be overcome by use of a mass storage FFT. The imposed compromise between time series length T and sampling time step Δt was chosen to be T = 80 ps and $\Delta t = 5 \times 10^{-3}$ ps. The Parzen window was chosen to reduce the danger of introducton of spurious artifacts into the spectrum.

The window length was established by performing a window closing experiment which, as stated previously, involves adjusting the window length until the resulting spectrum contains all the structures which are known to exist and none which cannot be explained. From a previous computation it was known that the dc diffusion coefficient at 10 kV/cm is approximately 60 $cm^2 s^{-1}$ which, in Eq. 6.7, sets $S_v(0)$. Also, from earlier analysis,[174,175] it was expected that the velocity fluctuation spectrum would peak at approximately 650 GHz at

an electric field of 10 kV/cm. The results of the window closing experiment are shown in Fig. 6.22. The optimum lag window length is in the range of 5 to 6 ps. A value of 5 ps (which corresponds to a bandwidth of 350 GHz) was used for subsequent analysis.

The results obtained using this window are shown in Figs. 6.23 and 6.24. Figure 6.23 is a convincing demonstration of the advantages of using a window-smoothed spectrum as opposed to a simple periodogram. The smoothed spectrum of Fig. 6.23 also demonstrates the major features of the velocity fluctuation spectrum--an increase from the dc value with peaks at approximately 400 and 650 GHz, followed by a decline which is interrupted by a peak at approximately 1400 GHz. This behavior is more clearly shown with the scale change employed in Fig. 6.24.

Completion of the window closing experiment requires that the calculated structure be explained. The first step is identification of the overall spectrum structures which are the result of processes within individual valleys. This is done by using the individual valley spectra which are also shown in Fig. 6.24. These are calculated by ignoring all data points for which the electron was in the other valley. The results show that while there is no dominant structure in the satellite valley spectrum, two of the spectral peaks (at 650 and 1450 GHz) correspond to peaks in the central valley spectrum. It is therefore assumed that they result from central valley phenomena. The peak at approximately 400 GHz does not correspond to features in either valley spectrum and so can provisionally

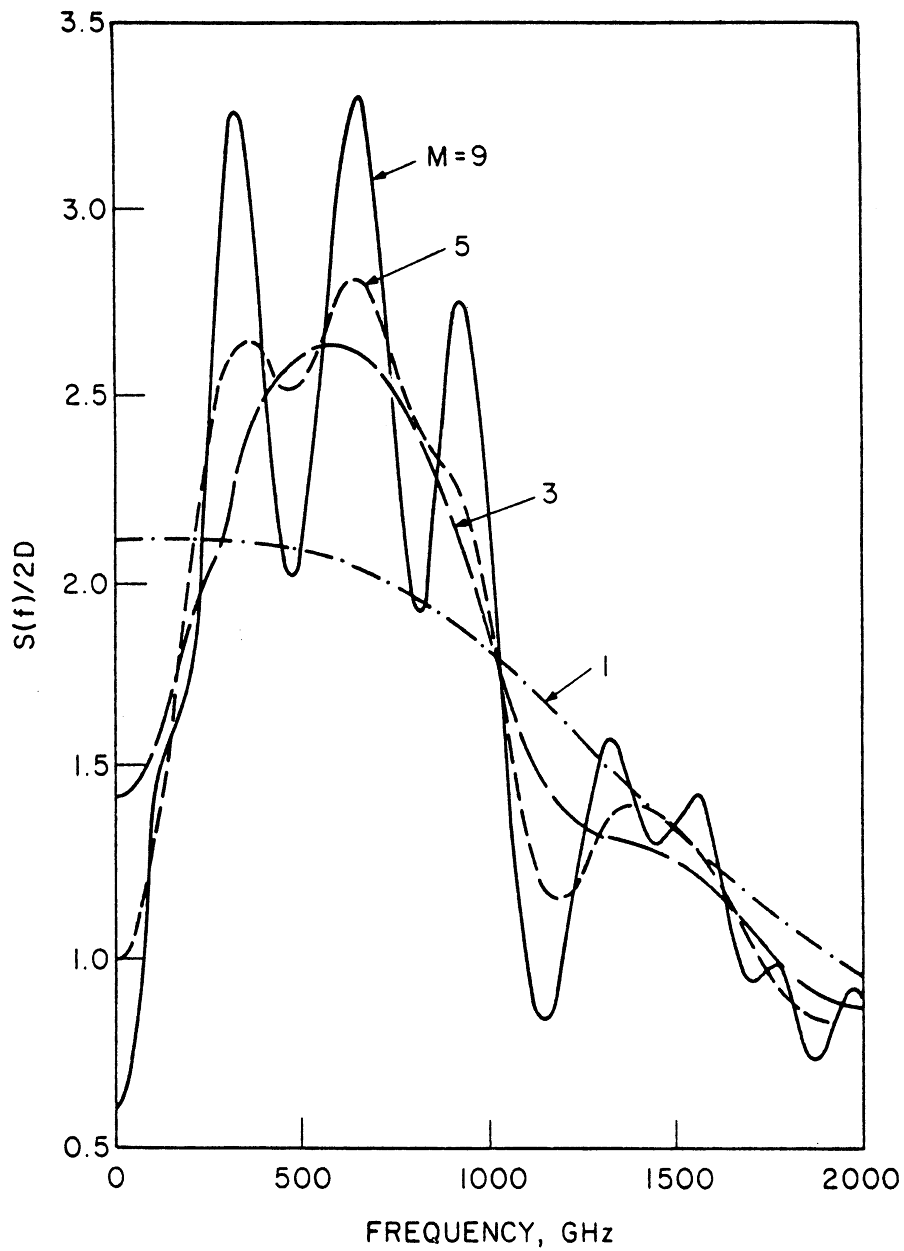

FIG. 6.22 WINDOW CLOSING EXPERIMENT FOR ROOM TEMPERATURE UNDOPED GaAs AT A FIELD OF 10 kV/cm. A DC NORMALIZED SPECTRAL COMPONENT OF ONE CORRESPONDS TO A DIFFUSION COEFFICIENT OF 62 cm^2/s.

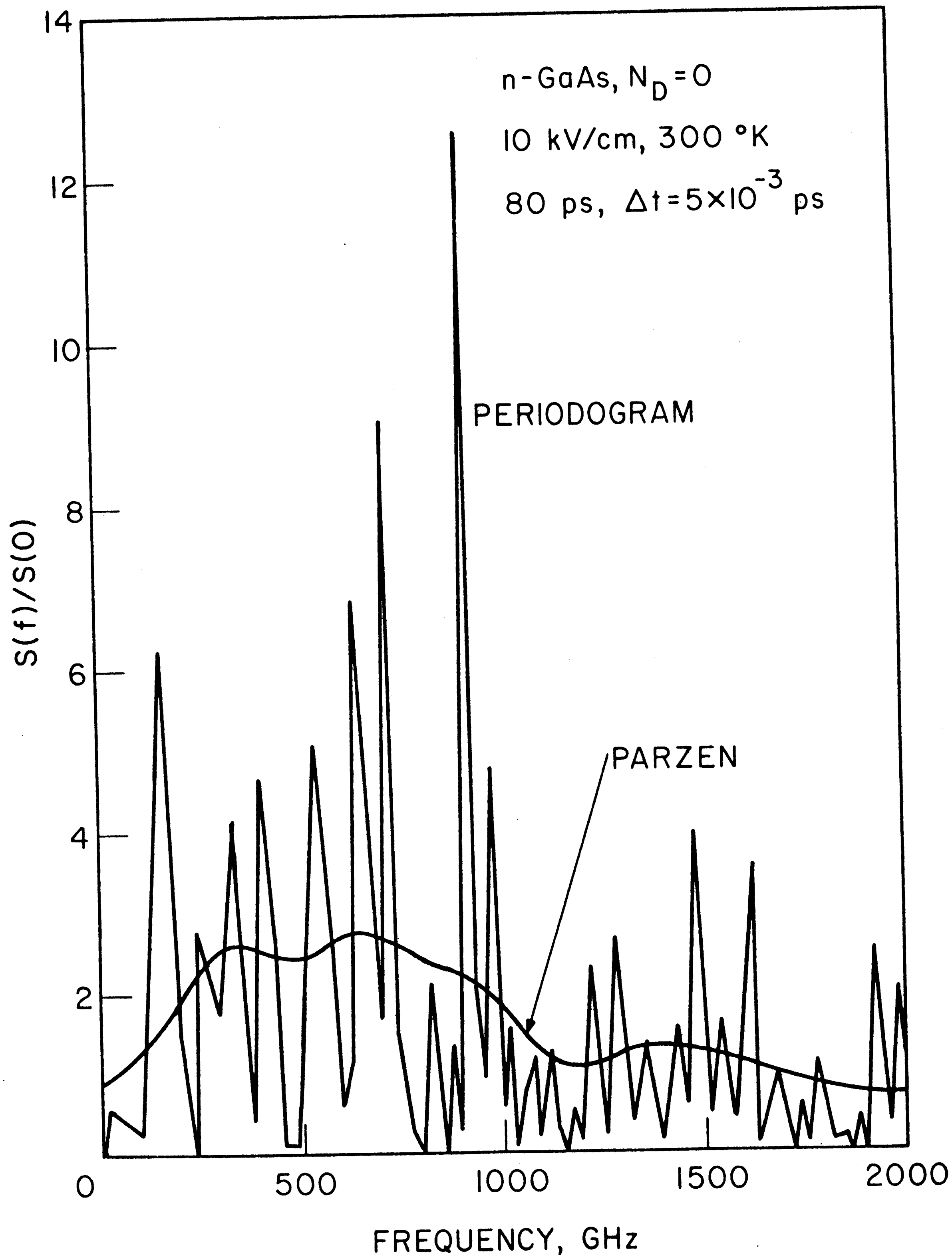

FIG. 6.23 COMPARISON OF SMOOTHED AND UNSMOOTHED PERIODOGRAMS.

[S(0) = 2D WHERE D = 62 cm^2/s]

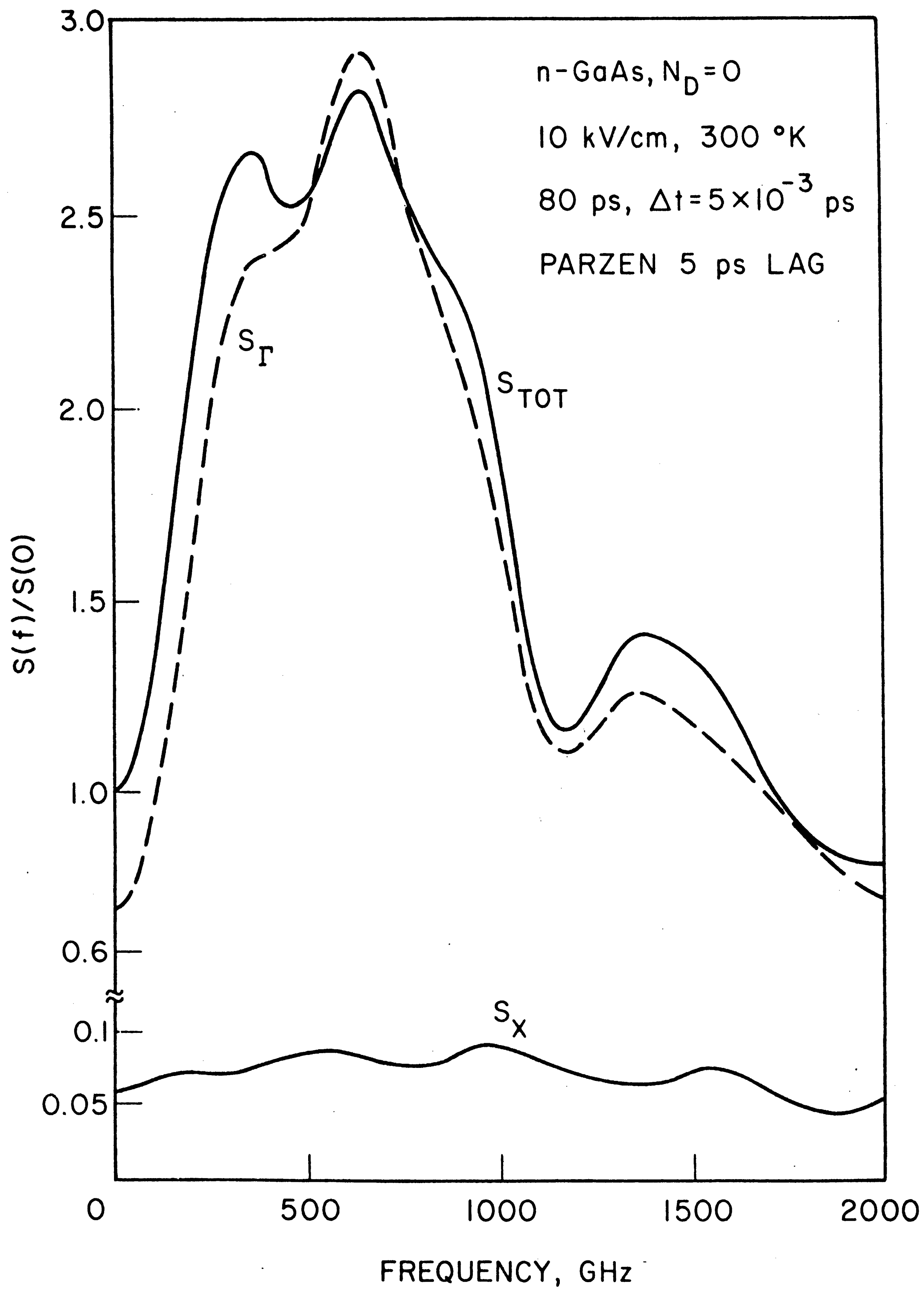

FIG. 6.24 TOTAL AND INDIVIDUAL VALLEY VELOCITY FLUCTUATION NOISE SPECTRA. [S(0) = 2D WHERE D = 62 cm²/s]

be identified as a partition noise peak. These three peaks are now considered in turn.

The peak near 650 GHz has already been discovered and explained by Hill et al.[174] The underlying mechanism is shown in Fig. 6.8. For fields above a few kV/cm, the electron spends a significant time in the central valley, mainly on occasions when it is scattered into the central valley at points similar to point b in Fig. 6.8. On these occasions the electron starts with a large negative velocity, is accelerated by the field through the valley minimum to a large positive velocity, and then scatters back to the satellite valley. An electron which is scattered into the central valley with a positive velocity (point a in Fig. 6.8) will normally spend a much shorter time in the central valley before scattering back to the satellite valley. Hill et al.[174] demonstrated that a ballistic flight of duration τ produces a spectral peak at $\omega\tau = 4$. For ballistic flight across the central valley, with the conditions present in the simulation, the peak is expected to lie near 650 GHz.

The peak near 1400 GHz can also be attributed to a type of ballistic flight. The $\omega\tau = 4$ criterion for the 1400-GHz peak corresponds to a flight time of approximately 0.5 ps, which is close to the Γ-valley rate for polar optical phonon scattering. (Polar optical phonon scattering is the dominant scattering mechanism for electrons in the Γ-valley at energies below the threshold required for intervalley scattering.) The 1400-GHz peak can therefore be attributed to subthreshold scattering processes.

The 360-GHz peak has been attributed by a process of elimination to partition noise. Such a peak was not anticipated by

Shockley et al.[180] who anticipated a partition noise spectrum with a simple $[1 + (\omega\tau)^2]^{-1}$ form. Insight into the origins of the 360-GHz peak requires detailed examination of the velocity autocovariance functions shown in Figs. 6.25 and 6.26 and the valley autocovariance function shown in Fig. 6.27. These are now discussed.

Figures 6.25 and 6.26 show that the Γ-valley behavior dominates the overall velocity autocovariance behavior. The Γ-valley velocity autocovariance exhibits three important features: the initial swing into the negative region, the inflection point at approximately 0.5 ps, and the swing back into the positive region at approximately 3 ps.* The initial swing into the negative region indicates an expected change in sign of the velocity fluctuation. This is reasonable since the physical processes involved are acceleration by the field (only the perpendicular velocity component is being considered here) and scattering. The field acceleration tends to change negative velocity fluctuations into positive fluctuations. Since the net effect of scattering is to counteract the field acceleration (otherwise the velocity would not have a time constant mean), the scattering tends to change positive velocity fluctuations into negative fluctuations. The initial downswing of the velocity autocovariance can be attributed to the field acceleration. The inflection point near 0.5 ps indicates a point at which the scattering has disrupted the previously nearly

---

* Price[187] anticipated the first two of these features. A common error is to regard the electron as having a constant velocity between collisions which yields an exponential decay. Although this is true perpendicular to the electric field,[175] parallel to the electric field the electron is being accelerated between collisions, thereby eliminating a simple exponential decay form for the autocorrelation function.

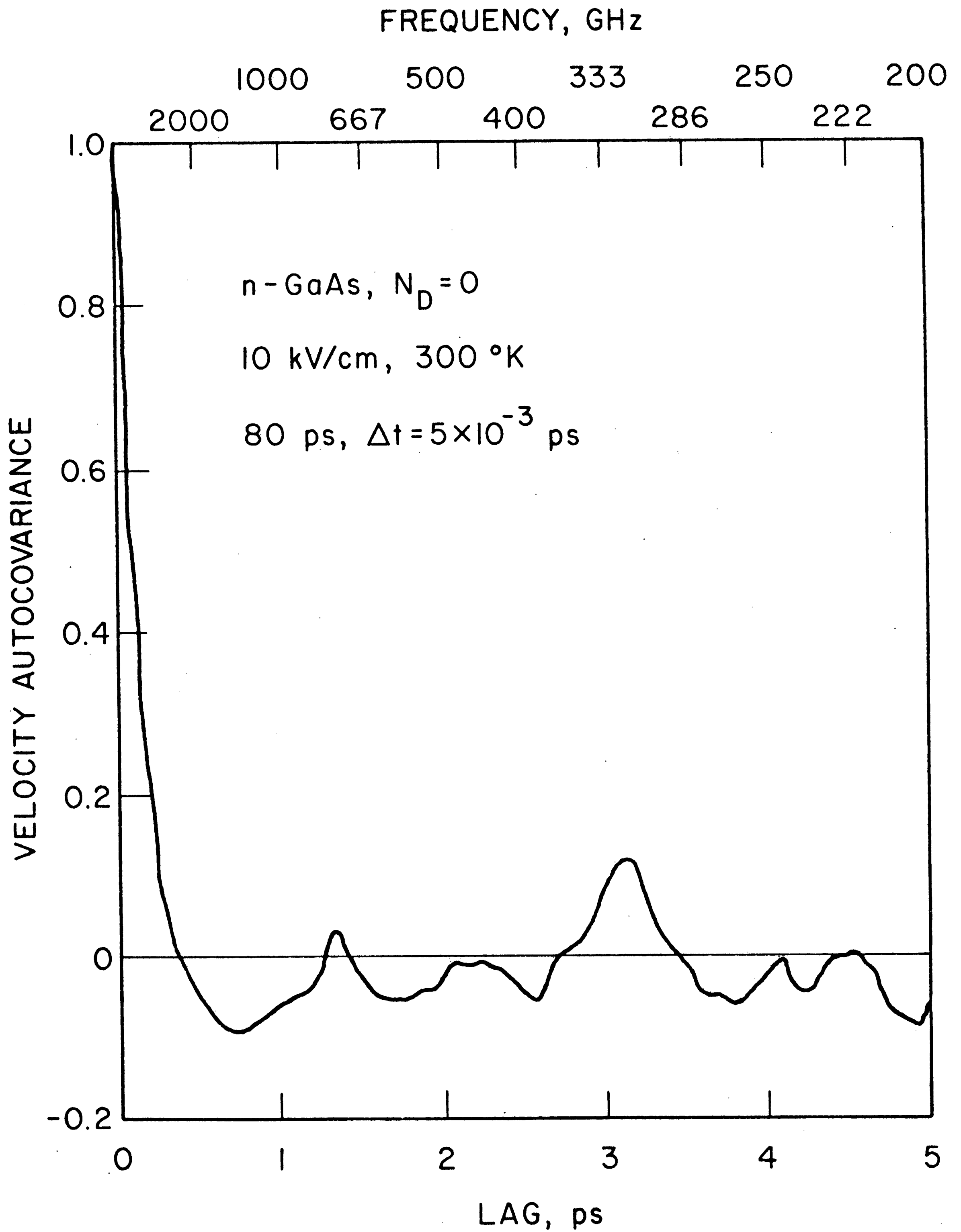

FIG. 6.25 OVERALL VELOCITY AUTOCOVARIANCE OR VELOCITY FLUCTUATION AUTOCORRELATION.

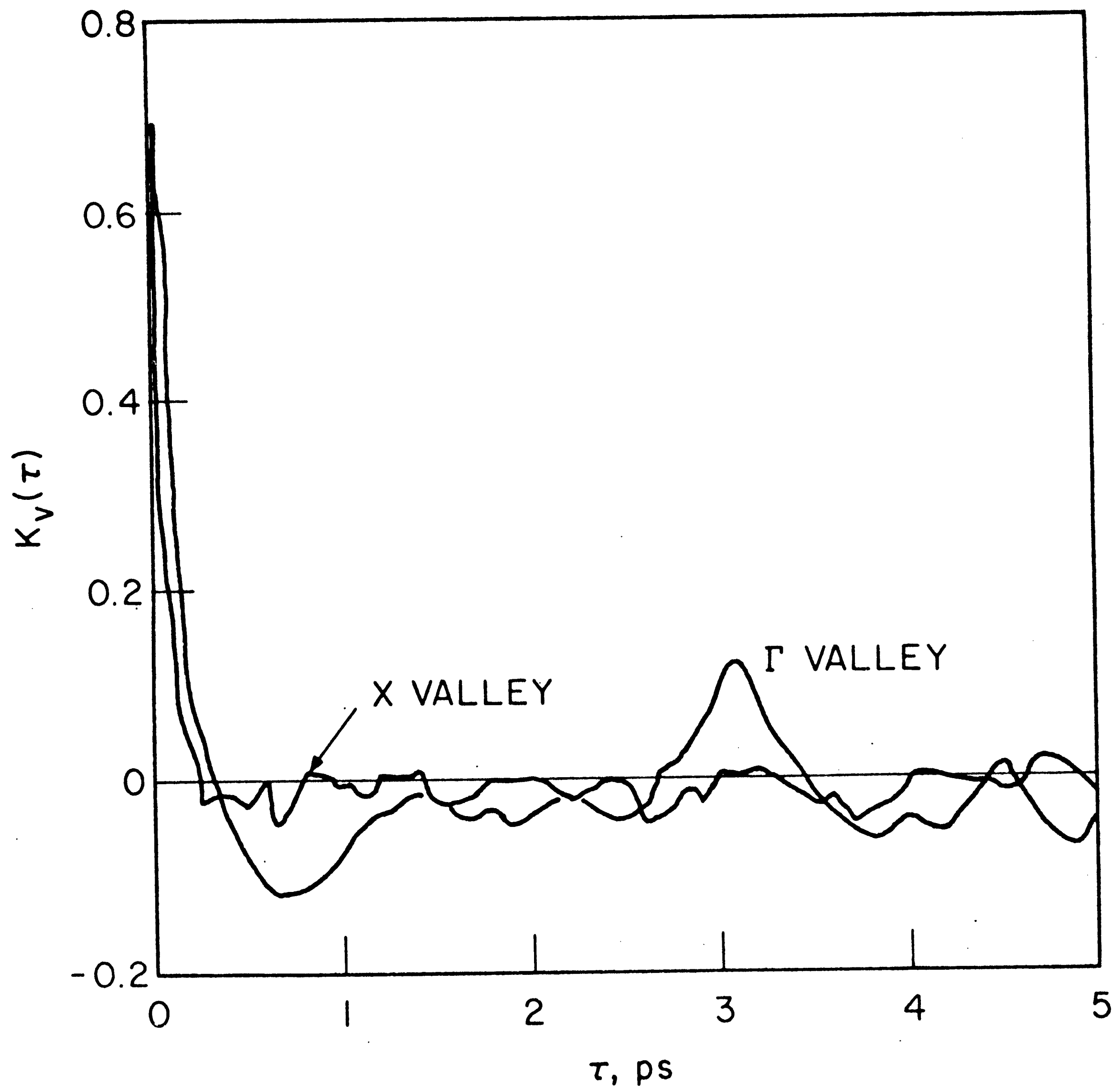

FIG. 6.26 INDIVIDUAL VALLEY VELOCITY AUTOCOVARIANCE FUNCTIONS.

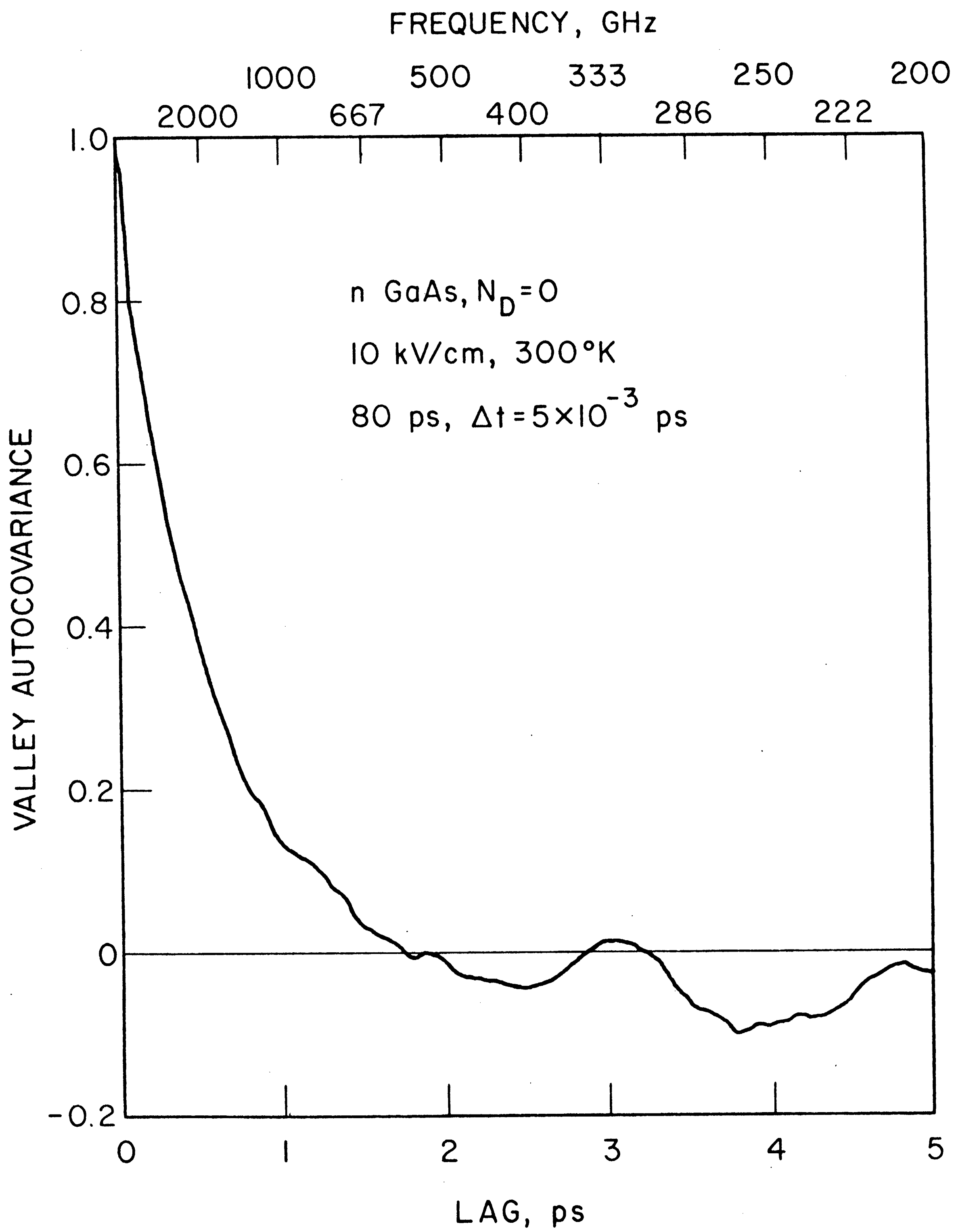

FIG. 6.27 VALLEY RANDOM PROCESS AUTOCOVARIANCE FUNCTION ESTIMATE.

linear field-induced behavior. A representative scattering time for Γ-valley electrons is indeed 0.5 ps. Another factor which contributes to the observed short time behavior is the electrons which scatter into the Γ-valley at a point such as a in Fig. 6.8. These electrons generally undergo short flights before being scattered to the satellite valley. A change in sign of velocity fluctuation is often associated with intervalley scattering.

The origin of the positive swing near 3 ps in the velocity autocovariance can be deduced from the valley autocovariance function plotted in Fig. 6.27. In Section 6.4.2 it was noted that a change in the sign of this function indicates that the electron is expected to be in nonequivalent valleys at times t and $t + \tau$. Figure 6.27 thus shows a tendency for a 3-ps "round trip" in which the electron starts in one valley, scatters to a nonequivalent valley, and then scatters back to the original valley. This round-trip behavior is believed to provide the structure at 3 ps in the velocity autocovariance and to be responsible for the 400-GHz "partition noise" peak. (Previous estimates which used an autocorrelation function truncated at 2 ps[175] could not observe this structure.)

This 3-ps round-trip time is longer than the time constants which might be intuitively associated with carrier transport in GaAs (although when working with effective relaxation times, the <u>energy</u> relaxation time is often calculated to be of the order of a few ps even though the momentum relaxation time is much less). The round-trip correlation time may be responsible for a well-known problem associated with diffusion coefficient estimation using Monte Carlo simulation.[174,175,188-190] Such estimates typically use an ensemble

time average, but exhibit the property that for short time series lengths (less than 5 to 8 ps in GaAs) the estimated diffusion coefficient becomes a function of the individual time series length.* It is reasonable to expect that the valley round-trip correlation time would affect the results for time series which are not significantly longer than the correlation time, in which case examination of the valley autocorrelation function should provide a useful guide for selecting the time series length to be employed for Monte Carlo estimation of diffusion coefficients in multivalley semiconductors. [A related point is the question of the circumstances (space and time scales, boundary conditions, etc.) in which the "conventional" diffusion coefficient (which assumes Fick's law and an infinite medium) can be useful. Some initial work regarding this topic has appeared in the literature.[174,175,177,188,191]]

The quality of the spectral estimate can be assessed using Table 6.2. The variance of the estimate is reduced to 3.3 percent of the variance of the unsmoothed periodogram which explains the striking difference between the two estimates in Fig. 6.23. The bias around 640 GHz, where the second differential of the spectrum with respect to frequency is large, may be as high as 20 percent but through most of the spectrum it will be much lower. Overall, the estimated spectrum probably deviates from the "real" spectrum <u>of the model</u> within the bandwidth stated by less than 10 percent on average. (Discrepancies introduced by any failure of the two-valley model to correctly represent GaAs are, of course, no reflection on the

---

* Hill et al.[174] interpreted this in terms of Eq. 6.12.

estimation procedures employed.) Previous work[174-176] did not assess the accuracy of the estimates presented and did not present sufficient information to allow this to be done with Table 6.2. It is felt that the results presented here are of at least comparable accuracy and were produced using considerably less raw data and significantly more efficient (inexpensive) analysis procedures.

6.4.5 General Discussion. The results illustrate the potential of Monte Carlo experiments designed to investigate hot carrier noise phenomena. A reasonably good estimate of the behavior of the spectrum at millimeter- and submillimeter-wave frequencies can be obtained quite economically from relatively little Monte Carlo generated data. This is worth doing as the departures from the widely assumed "white" noise spectrum are clearly significant at millimeter- and submillimeter-wave frequencies. The absolute accuracy of the estimate is limited, but presently adequate bearing in mind the approximations inherent in all current Monte Carlo models of carrier transport.

Although the actual computations involved can be routinely performed, the interpretation phase of the experiment requires care. The division of observed structure by valley and identification of structure not associated with a particular valley as partition noise is quite straightforward, but identification of the physical processes within a valley which are responsible for observed structure can be less certain. The valley autocovariance function has proved a useful aid to interpretation of what physical processes are associated with partition noise and may well prove to have other uses in the theory of carrier transport in multivalley semiconductors.

Overall, the procedures are sufficiently economical to permit systematic investigations of the velocity fluctuation noise spectrum as a function of electric field, temperature, and doping density. The results are directly applicable to the noise modeling of millimeter- and submillimeter-wave devices, both in the drift region of transit-time devices and in the undepleted epitaxial material/series resistance of devices in general. The results can also be applied to FET and transferred-electron device noise modeling (less sophisticated noise temperature estimations by Monte Carlo techniques have already been used in FET modeling[192,193]). Although there are considerable difficulties in experimental measurements of the noise spectrum in the millimeter- and submillimeter-wave regions, such measurements would provide a useful tool for investigating band structure and scattering processes.

Some possible extensions of the work may be of interest. It should be possible to repeat this type of study using position in a device instead of time as the independent variable. A step in this direction was reported by Zimmermann et al.[168] who found that the magnitude of the velocity fluctuations in a short gate FET is a strong function of position (this is a noise analog of the velocity overshoot effect). Recently Zimmermann and Constant[194] extended this approach to the calculation of terminal noise voltages or currents in unipolar one-dimensional structures. The next step would be to check the spatial correlation function of the velocity fluctuations. FET noise models generally assume a spatial grid in which the velocity fluctuation noise sources in the various grid elements are mutually uncorrelated.[195,196] Another interesting

result of a study of velocity fluctuation as a function of position would be in the estimation of the spatial velocity frequency spectrum. Jacoboni has previously indicated the importance of this information in a study of the validity of the drift-diffusion equation in small semiconductor devices.[191]

6.4.6 Hot Carrier Noise in Mixer Diodes. As discussed in Chapter III the noise sources typically retained in a Schottky-barrier mixer noise calculation are shot and thermal noise. Held and Kerr[101] found that it was necessary to slightly elevate the assumed noise source temperature for the thermal resistance to achieve agreement between theory and experiment for an 85-GHz Schottky-barrier mixer. They hypothesized that this elevated noise source temperature was due to scattering noise, and that it had a spectral density function which was flat out to 80 to 100 GHz after which it fell off. The results presented in this section, and in several of the references, provide additional insight into this elevated temperature. These insights are based on the assumption that the noise source temperature elevation in the thermal resistance is due to hot carrier or velocity fluctuation noise.

Several features of velocity fluctuation noise are pertinent to the mixer noise problem. The first such feature is that the dc spectral noise power component is proportional to the carrier diffusion coefficient. The diffusion coefficient for electrons in GaAs increases for low fields to a peak near 3 to 5 kV/cm associated with intervalley scattering. The diffusion coefficient then declines for higher fields. The small field present in the undepleted portion of the mixer diode therefore leads to an additional

noise component. It should be noted that, when pumped, the peak field in this region[101] can approach 2 kV/cm, and that the effective fields present in this region may in fact be substantially higher than the dc field.

The second feature of velocity fluctuation noise which is pertinent to the mixer noise problem is the peak seen in the spectral density function at high millimeter- and submillimeter-wave frequencies. Velocity fluctuation noise therefore should be more important at these high frequencies than it is at 85 GHz.

The last factor which should be mentioned is the correlation effects discussed in Chapter III. Such correlation effects are typically neglected in thermal noise calculations (and were neglected in this work as well). No procedure for specifying the correlation matrix elements for the off-diagonals presently exists. These effects may very well be important enough to mask the other effects of velocity-fluctuation noise in the undepleted region, and therefore additional study of this question is needed.

6.5 Summary and Conclusions

In this chapter Monte Carlo methods were used to test various assumptions made in the device physical model. It was argued that transient carrier transport effects such as velocity overshoots and undershoots were expected in GaAs transit-time device regions. Such transient effects could either degrade or enhance the device response. It was argued that they may enhance the oscillation efficiency in high-low or low-high-low structures designed for operation in the 50- to 200-GHz region. Possible effects of such

transients on premature collection were also considered and found to represent an upper frequency boundary of approximately 80 GHz past which premature collection, as conventionally understood, probably does not occur. The role of transient carrier transport in the undepleted region was also discussed and shown to lead to an additional loss component at high drives in GaAs millimeter-wave devices.

The design of a Monte Carlo investigation of noise spectra was also described. Procedures by which such a test could be systematically designed and executed were demonstrated. It was found that strong peaks are expected at high millimeter-wave and low submillimeter-wave frequencies in GaAs. The importance of such peaks and velocity fluctuation noise in GaAs mixer diodes was discussed.

CHAPTER VII. CONCLUSIONS AND SUGGESTIONS FOR FUTURE STUDY

7.1 Introduction

In the course of this investigation many equations were derived, several computer programs written and a variety of numerical studies made. In this chapter the important conclusions are reviewed and some suggestions for future study are offered.

7.2 Conclusions

This report has three main sections. In Chapters II and III a general mixer analysis is derived. In Chapters IV and V the performance of BARITT devices as frequency converters in the 30- to 120-GHz range was studied. In Chapter VI Monte Carlo methods were used to investigate several aspects of carrier transport and noise in these devices.

Frequency converters have been studied for at least 50 years now. As a result any contributions made in the analytical chapters are largely in technical detail. The possible exception is the development of an explicitly defined general framework for studying frequency conversion and noise correlation in a wide variety of structures. The general technique underlying this analysis is to first subdivide the system into an active portion (the intrinsic diode in this work) and a passive portion (e.g., the parasitics and circuit). The active portion is then further subdivided into a nonlinear region and a linear portion. This general order of

subdivision was found to be of great use in avoiding technical difficulties and may be useful in the study of other systems such as FET mixers.

Several other comments can be made concerning the material presented in the first portion of this dissertation. It is the first application of Saleh's notation and, more importantly, noise correlation matrices in transit-time devices. Additionally, a heuristic argument was presented for the existence of correlation effects in velocity fluctuation noise, and the general identity of noise correlation in periodically pumped nonlinear systems such as mixers and oscillators was also explicitly stated. Lastly, the matrix reduction technique which was obtained by generalizing the three-frequency to two-frequency case of Peterson[141] should prove useful in mixer design and analysis.

The second portion of this dissertation is the numerical studies presented in Chapters IV and V. In Chapter IV the emphasis was on unpumped diodes. Methods of designing BARITT mixers were discussed. BARITTs were also shown to be competitive in video detection operation with Schottky devices. It was also shown that in the 30- to 120-GHz band, there is little performance advantage in building a long BARITT.

In Chapter V the emphasis was on mixers. BARITTs were found to be useful frequency converters near 35 GHz in both externally pumped and self-oscillating configurations. While good conversion losses are reported throughout the range, and conversion gains in many instances, the noise performance is usually not good. This is a result of the transformation of the injection region shot noise through the drift region to the device terminals. Unless the proper

biases, drive levels and structures are used, the result is a high IF noise voltage. It should be noted, however, that the Shottky-barrier tests presented indicated that 3 to 4 dB of drift may be present in the results. This drift is unfortunately unavoidable unless the device-circuit interaction at a great number of frequencies is considered. This, of course, is impossible in a survey such as that presented here.

The last portion of the dissertation used Monte Carlo techniques to examine several aspects of carrier transport in GaAs devices. Velocity overshoots and undershoots were explored, and mechanisms by which they could enhance or degrade transit-time device oscillators were outlined. In particular, it was suggested that a velocity undershoot followed by a velocity overshoot could, if properly timed, enhance the operation of punch-through low-high-low or high-low GaAs transit-time devices for frequencies in the 40- to 200-GHz range. Premature collection was also studied from the point of view of the preferential Jones-Rees effect. This effect was found to lead to a probable velocity undershoot immediately following the pulse interception in premature collection operation. While unimportant at microwave frequencies due to their long RF periods, this undershoot should substantially alter the role of premature collection in transit-time devices operated at millimeter-wave frequencies.

The last sequence of results presented were concerned with the proper design of Monte Carlo estimations of noise spectral densities. The existing ad hoc procedures were replaced by a more systematic procedure whose statistical estimation properties are well understood. Velocity fluctuation noise was used as an example, and the

resulting spectrum contained several new features. Additionally, the possibility of valley round-trip effects in GaAs was considered. Such effects could include spectral peaks and difficulties in diffusion coefficient estimation.

7.3 Suggestions for Future Studies

The most immediate need in the frequency converter area is for a comparison of theory and experiment. The program used here could be used in such a comparison provided the necessary circuit impedance levels could either be measured, calculated or established by some scaling procedure.

One limitation of this work was the approximate model used for velocity fluctuation noise calculations. More exact models can be formulated and would have been used if time considerations allowed. Such models should be implemented and used in future work in this area.

Generally speaking, the model developed here can, with appropriate modifications, be applied to studies of noise and frequency conversion in a wide range of structures not considered here. Such structures include npn BARITTs, TUNNETTs and, most importantly, IMPATT devices. Such investigations, especially when based on a common mathematical framework, may provide additional insights into the relative advantages and disadvantages of these devices in frequency conversion applications. They also can be used to evaluate parametric stability.

The results obtained here show several areas in which transient transport can affect device behavior. They are also in substantial

agreement with a large existing body of transport calculations. What is missing at this point is actual device calculations based on higher-order transport models. It should be noted, however, that models based on the drift-diffusion transport model may produce results similar to those of higher-order models in many instances. This can happen because *any* model based on the quasi-free-particle approximation will include Poisson's equation, the carrier continuity equations, and the spatial conservation of electrical current as is discussed in Chapter IV. Furthermore, any model will also contain the same cold-capacitance, some form of drift-region transit-time effects, and injection phase delays if avalanching is present. It is expected that a primary role of the results presented here is to provide guidance in selecting test cases in which the drift-diffusion and higher-order model results may differ significantly. These results also show that such effects may in fact be beneficial. If this proves to be true, then the benefits can be maximized only by the use of models in which some form of transient carrier transport is allowed to occur.

APPENDIX A. MATERIAL PARAMETERS

In this appendix the material parameters used in the investigation are tabulated. This will be done for Si first and then for GaAs.

A.1 Silicon Parameters

The Si parameters were used in a study of Si pnp BARITTs and therefore no tunneling rates were used. Additionally, the electron transport factors (velocity and diffusion coefficient) were not needed. The parameters used were:

$$D_p = 0.0259\ (T/300)\ \mu_p\ \mathrm{cm^2/s}$$

and

$$v_p = v_{sp}/[1 + (v_{sp}/\mu_p)/E]\ \mathrm{cm/s} \quad ,$$

where the mobility is

$$\mu_p = 480\ (T/300)^{-2.6}\ \mathrm{cm^2/(V\text{-}s)} \quad ,$$

and the saturated velocity is

$$v_{sp} = 10^7\ [1 - (T - 300)/1000]\ \mathrm{cm/s} \quad .$$

Electrical permittivity is

$$\varepsilon = 11.8 \times (8.854 \times 10^{-14})\ \mathrm{F/cm} \quad ,$$

intrinsic carrier concentration is

$$n_i = 1.5 \times 10^{10} \times (T/300)^{1.5} \times \exp\,[FAC300 - E_g/(2T \times 0.0259/300)]\ \mathrm{cm^{-3}} \quad ,$$

where

$$FAC300 = (1.16 - 7.02 \times 10^{-4} \times 90000/1408)/(2.0 \times 0.0259) \quad ,$$

and the energy band gap is

$$E_g = 1.16 - 7.02 \times 10^{-4}\ T^2/(T + 1108)\ \text{eV} \quad .$$

The thermal parameters are

$$\rho_m = 2.328\ \text{g-cm}^{-3} \quad ,$$

$$C_s = 0.165 - 2.46 \times 10^{-4}\ T_{cen}(1 - 5.32 \times 10^{-7}\ T_{cen}T_{cen})$$
$$+ 4.44 \times 10^{-10}\ T^3_{cen}\ \text{Wsg}^{-1}\ {}^{\circ}\text{K}^{-1} \quad ,$$

$$K_s = 1.381 - 5.98 \times 10^{-3}\ T_{cen}\{1.0 - 3.06 \times 10^{-3}\ T_{cen}$$
$$\cdot\ [1.0 - 1.78 \times 10^{-3}\ T_{cen}(1.0 - 7.6 \times 10^{-4}\ T_{cen})]\}\ \text{W}^{\circ}\text{K}^{-1}\ \text{cm}^{-1} \quad ,$$

where T_{cen} is the temperature in degrees centigrade.

A.2 Gallium Arsenide Parameters

The GaAs parameters were used in several calculations. The GaAs devices were n-type and therefore electron transport coefficients were used instead of hole coefficients. The parameters used were:

$$D_n = 20.0\ \text{cm}^2\text{s}^{-1}$$

and

$$v_n = [\mu_n E + v_{sn} F_1/(1 + F_1)]\ \text{cm/s} \quad ,$$

where

$$F_1 = (E/4.0 \times 10^3)^4 \quad ,$$

the mobility is

$$\mu_n = 2.25 \times 10^6/T \ cm^2V^{-1}s^{-1} \quad ,$$

and the saturated velocity is

$$v_{sn} = 7.5 \times 10^6 \times (300/T)^{0.7} \ cm \ s^{-1} \quad .$$

Electrical permittivity is

$$\varepsilon = 12.5 \times 8.854 \times 10^{-14} \ F \ cm^{-1} \quad .$$

The thermal parameters are

$$\rho_m = 5.32 \ g \ cm^{-3} \quad ,$$

$$C_s = 0.36 \ Wsg^{-1} \ {}^oK^{-1} \quad ,$$

and

$$K_s = 0.451 - 1.664 \times 10^{-3} \ T_{cen}[1.0 - 2.36 \times 10^{-3} \ T_{cen} (1.0 - 8.56 \times 10^{-4} \ T_{cen})] \quad .$$

The Si velocity parameters are essentially those used by Sjolund[60] and are obtained by fitting the data of Seidel and Scharfetter[197] to the expression used here. The GaAs velocity data is that of Kramer and Mircea.[198] The thermal parameters are obtained from Olson[199] while the remaining parameters are available in Sze.[74]

APPENDIX B. DOCUMENTATION OF COMPUTER PROGRAM

In this appendix the basic structure of a computer solution to the mixer problem as described in Chapters II, III, and IV is outlined. The program was developed by modifying and extending a Schottky-barrier mixer analysis program developed at NASA Goddard Space Flight Center.[117] The main structure of the program is flowcharted in Fig. B.1. The MAIN program begins with a call to a subroutine (START) which reads input data and performs various initializations. Typically the execution continues with the performance of a large-signal solution. This is done by a call to subroutine DRIVE where the large-signal analysis of Chapter IV is implemented. DRIVE returns the Fourier components needed for the small-signal mixer analysis. (In another option these Fourier components can be read in from an external data file, and the execution of subroutine DRIVE is skipped.)

The small-signal mixer analysis described in Chapter II is then implemented by calling subroutine SMSIG. The structure of this subroutine is flowcharted in Fig. B.2. It begins by calling subroutine YINJ in which the injection region conversion admittance is formed. For transit-time devices, the program continues with the formation of the intrinsic diode conversion admittance matrix. This is done by inverting the injection region conversion matrix (call to CMINV) and then forming the intrinsic diode conversion impedance matrix (call to ZID). This conversion impedance matrix is then inverted by calling CMINV to form the intrinsic diode conversion

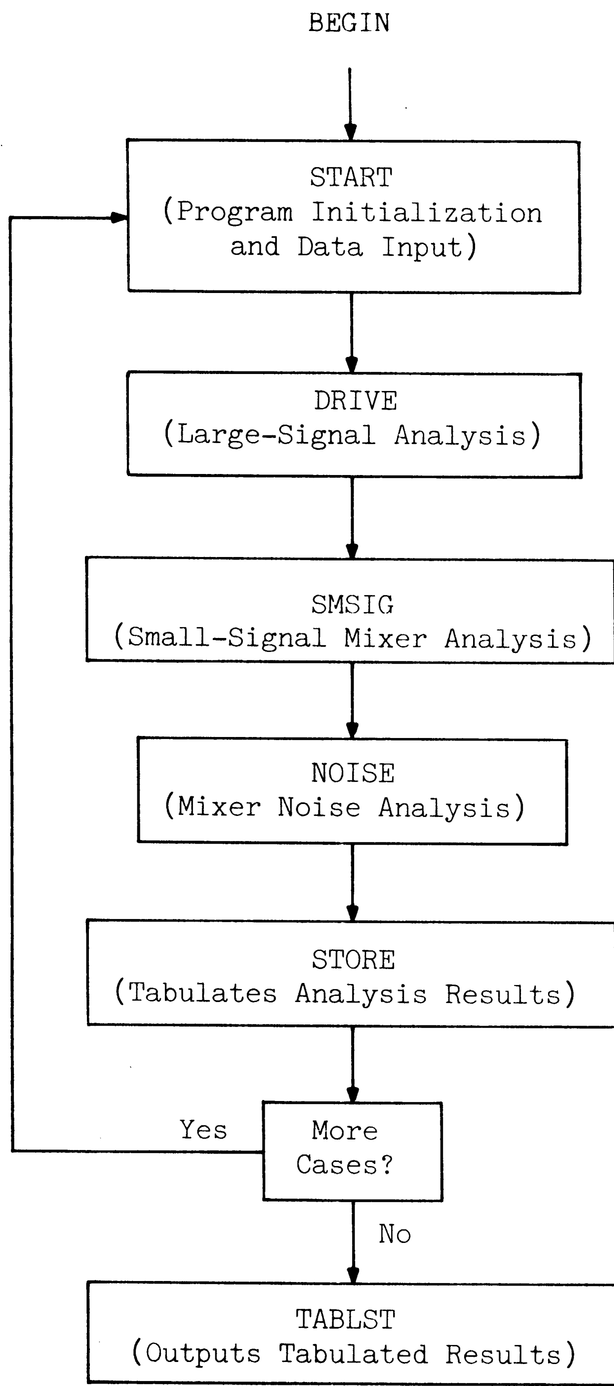

FIG. B.1 FLOW CHART OF MIXER ANALYSIS PROGRAM.

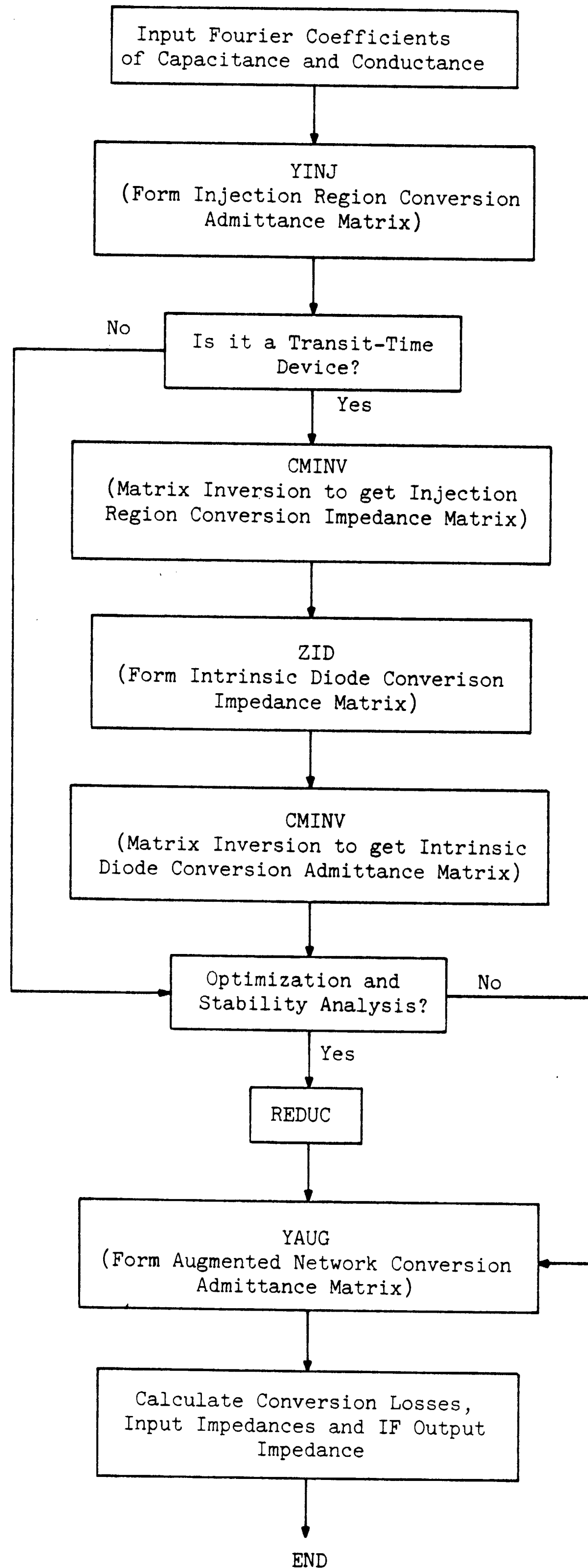

FIG. B.2 FLOW CHART OF SUBROUTINE SMSIG.

admittance matrix. If the optimal conversion loss is desired, the analysis of Section 2.4 is implemented by a call to subroutine REDUC. SMSIG ends by calculating and printing the various mixer input impedances and conversion losses using the augmented network conversion admittance formed in a call to subroutine YAUG.

The MAIN program (Fig. B.1) follows the small-signal analysis of SMSIG by the mixer noise analysis implemented in subroutine NOISE. NOISE is flowcharted in Fig. B.3. It starts by calling subroutine CORREL which forms the injection region correlation matrix as described in Chapter III. If it is a transit-time device, the intrinsic diode shot-noise correlation matrix is formed by calling subroutine SHOTID. The shot-noise mixer-noise temperature contribution is then calculated by calling subroutine TMIX. TMIX solves Eqs. 3.59 and 3.60. The thermal noise contribution to the mixer correlation matrix is then calculated in a call to subroutine TNOISE. The thermal contribution to the mixer noise temperature is calculated by calling TMIX a second time. For transit-time devices, the velocity fluctuation noise contribution to the noise correlation matrix is formed in a call to subroutine TVFCAL. The velocity fluctuation noise contribution to the mixer noise temperature is calculated by a third call to subroutine TMIX.

The MAIN program then calls a subroutine STORE which stores various important parameters in a set of output tables. It checks to see if all the cases of interest have been run and, if they have, it proceeds to print the tabulated output by calling subroutine TABLST. If additional cases remain, it returns to START. Up to 20 cases are allowed before the output tables are filled. This

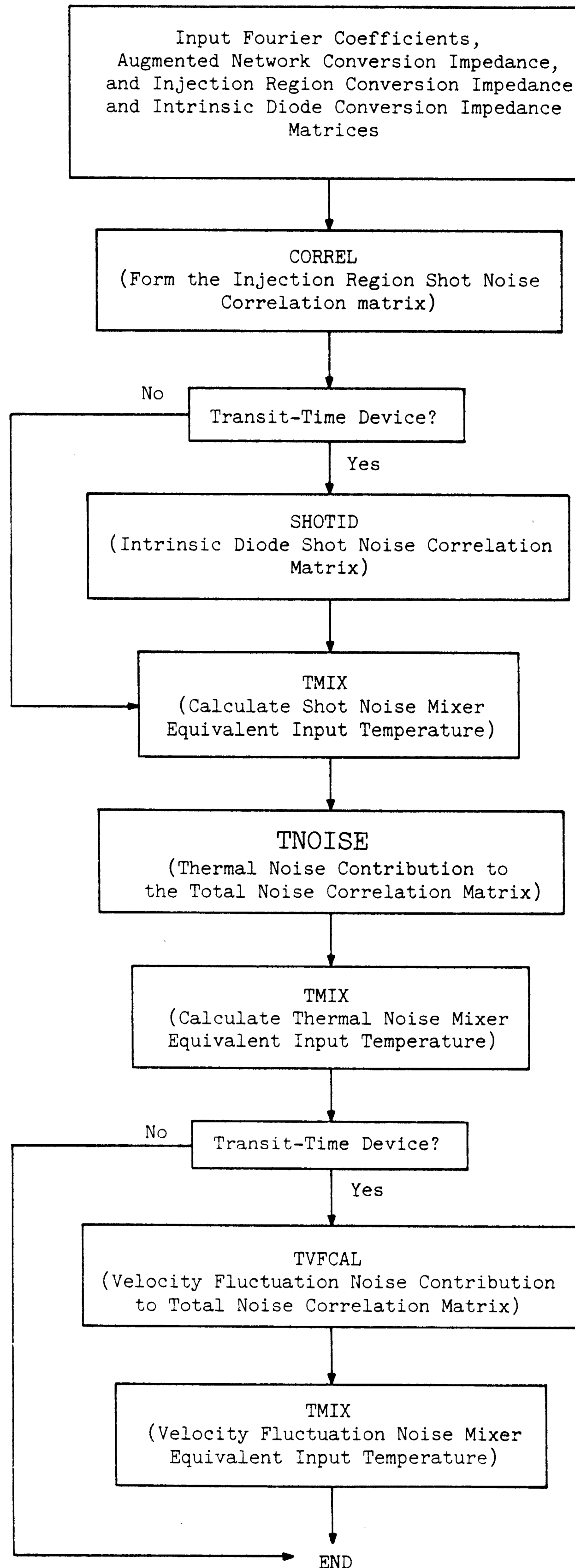

FIG. B.3 FLOW CHART OF SUBROUTINE NOISE.

tabulated form can also be written onto an external file and used as the input data to an external plotting routine.

The dc and small-signal device analysis for transit-time devices is required at several points in the solution. At these points an interfacing program called TTDEV is used. It calls the proper dc solution procedure (BARDC for BARITTs and TUNDC for TUNNETTs) which in turn uses the general dc drift region solution described in Chpater IV. This dc drift region solution is implemented by calling subroutine DRIFDC. TTDEV continues by forming an array of frequencies of interest, e.g., harmonics of the local oscillator or sideband frequencies. It then feeds this array into subroutine SMASIG which controls the transit-time device small-signal solution. SMASIG first sets up the material parameters used in the small-signal solution described in Chapter IV. It then loops through the provided frequency array. It calculates the various small-signal device parameters at each frequency by calling subroutine DEVSS. DEVSS in turn calls subroutine DRIFSS where the small-signal drift region solution and noise analysis described in Chapter IV are implemented. The various transit-time device subroutines are flowcharted in Fig. B.4.

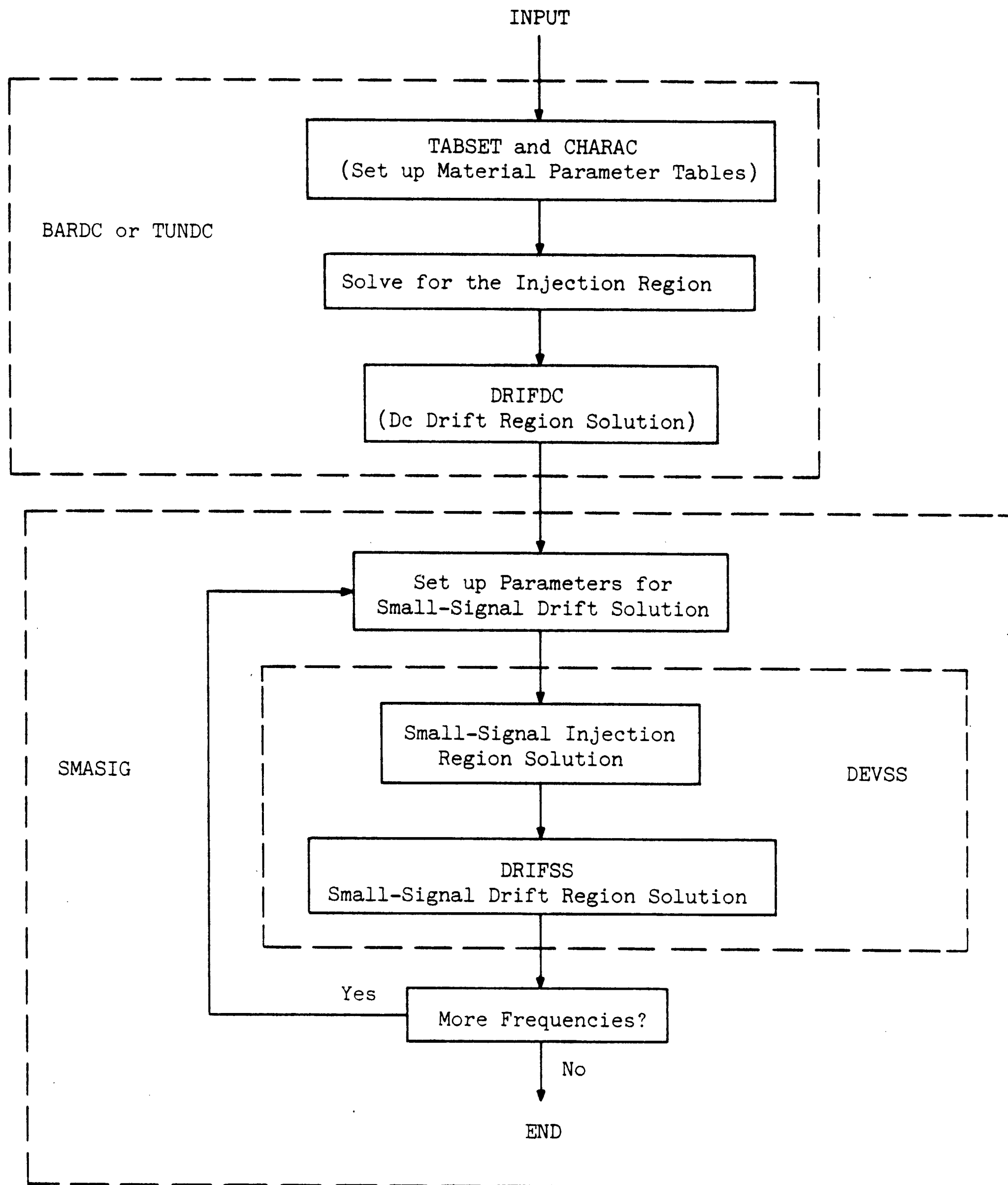

FIG. B.4 FLOW CHART OF SUBROUTINE TTDEV.

APPENDIX C. NOISE FACTOR MINIMIZATION

In this appendix the noise factor optimization procedure used in Chapter V is described. McCleer[30] previously used this procedure in BARITT mixer analysis and it essentially was originally developed by an IRE standards committee.[200] The procedure is described in some detail for the sake of completeness.

The procedure minimizes the noise factor which is the ratio of the input signal-to-noise ratio to the output signal-to-noise ratio when the input is thermal noise at room temperature. If a network gain G is defined, the noise factor is

$$F = 1 + \frac{N_e}{GN_{in}} , \qquad (C.1)$$

where N_e is the excess noise due to the network alone and N_{in} is the input thermal noise. The excess noise factor then is

$$F_e = F - 1 . \qquad (C.2)$$

F_e is minimized by applying the idealized mixer representation shown in Fig. C.1. Here the mixer is described by a noiseless two-port (signal and intermediate frequencies) and two partially correlated noise sources. The noiseless mixer corresponds to the total diode and is described by the ABCD parameters A_{TD}, B_{TD}, C_{TD} and D_{TD}. V_n and I_n are noise sources. Z_{e_1} is the signal frequency embedding circuit impedance or source impedance.

The correlation between the two noise sources is described by dividing V_n into

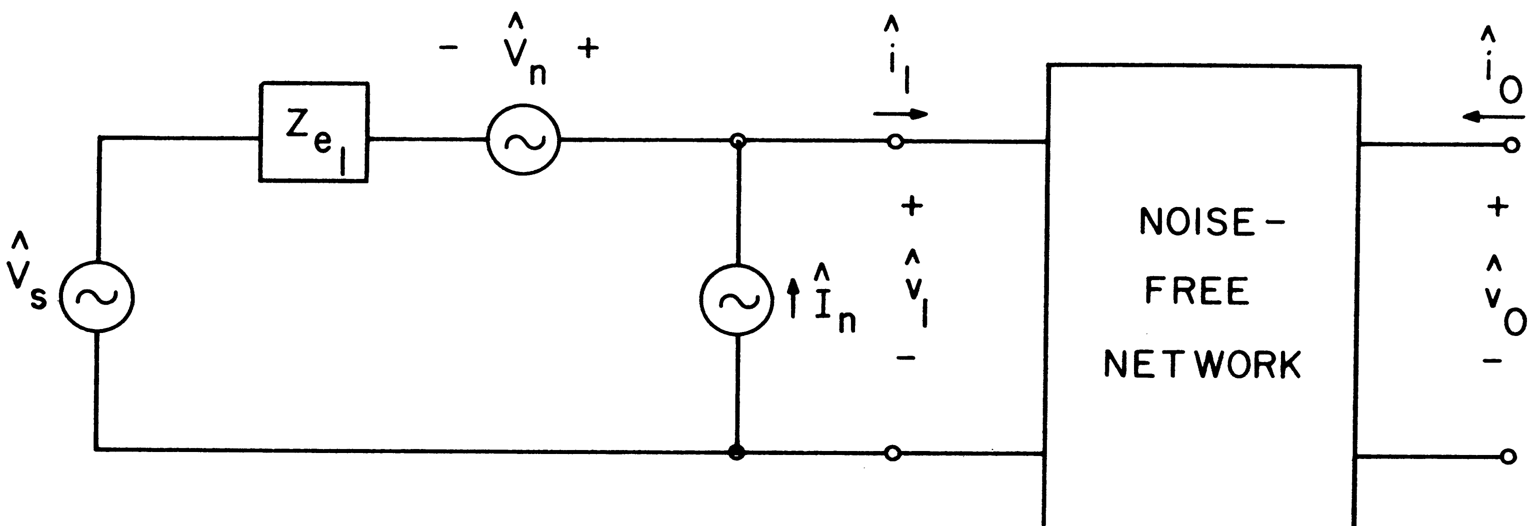

FIG. C.1 REPRESENTATION OF A LINEAR TWO-PORT NETWORK WITH ALL INTERNAL NOISE SOURCES EXPRESSED AS EQUIVALENT INPUT NOISE SOURCES $\hat{V}_n$ AND $\hat{I}_n$.

$$V_n = V_{nu} + V_{nc} \quad , \tag{C.3}$$

where V_{nu} and I_n are uncorrelated, while V_{nc} and I_n are correlated. A correlation impedance Z_γ is defined. Z_γ satisfies the following relations:

$$V_{nu} = V_n - Z_\gamma I_n \quad , \tag{C.4}$$

and in terms of statistical expectations or averages,

$$Z_\gamma = \frac{E(|V_n I_n^*|)}{E(|I_n|^2)} = R_\gamma + jX_\gamma \quad . \tag{C.5}$$

The goal is to find the value of Z_{e_1} which minimizes F_e. Haus et al.[200] have shown that the optimum Z_{e_1} has an imaginary part $X_{e_1 opt} = - X_\gamma$ and a real part

$$R_{e_1 opt} = \left(\frac{R_u + G_n R_\gamma^2}{G_n}\right)^{1/2} , \tag{C.6}$$

where

$$R_u = \frac{E(|V_{nu}|^2)}{4qV_{TH}} \quad , \tag{C.7}$$

$$G_n = \frac{E(|I_n|^2)}{4qV_{TH}} \quad , \tag{C.8}$$

and V_{TH} is the thermal voltage kT/q. The optimum excess noise factor is

$$F_{e,opt} = 2G_n(R_\gamma + R_{e_1,opt}) \quad . \tag{C.9}$$

To determine the optimum Z_{e_1}, the four quantities R_γ, X_γ, R_u and G_n must be determined. This is done by applying four different test values for Z_{e_1} to a mixer with an open circuit termination at the IF port. The open-circuit noise voltage at the IF terminals is "measured" for each test Z_{e_1}. It should be noted that since the IF port is open circuited, neither B_{TD} nor D_{TD} appear in the final results.

The first test Z_{e_1} is a short circuit. This test result is

$$|A_{TD}|^2 E(|V_s|^2) = E(|V_n|^2) , \qquad (C.10)$$

where V_s is the resulting IF terminal voltage.

The next test Z_{e_1} is an open circuit. This test result is

$$|C_{TD}|^2 E(|V_o|^2) = E(|I_n|^2) , \qquad (C.11)$$

where V_o is the resulting IF terminal voltage.

In the third test Z_{e_1} is set to an arbitrary finite pure resistance R_{st}. The basic test result is

$$(A_{TD} + C_{TD}R_{st})V_R = V_n + R_{st}I_n , \qquad (C.12)$$

where V_R is the IF terminal voltage. If each side of this equation is multiplied by its complex conjugate and then averaged, the result is

$$|A_{TD} + C_{TD}R_{st}|^2 E(|V_R|^2) = E(|V_n|^2) + R_{st}^2 E(|I_n|^2) + R_{st}E(I_nV_n^* + V_nI_n^*) . \qquad (C.13)$$

Since A + A* = 2 Re(A), Eqs. C.5, C.10 and C.11 can be used to obtain

$$|A_{TD} + C_{TD}R_{st}|^2 E(|V_R|^2) = |A_{TD}|^2 E(|V_s|^2) + R_{st}^2 |C_{TD}|^2 E(|V_o|^2)$$

$$+ 2R_{st}\ \mathrm{Re}[Z_\gamma |C_{TD}|^2 E(|V_o|^2)] \quad (C.14)$$

or

$$R_\gamma = \frac{1}{|C_{TD}|^2 E(|V_o|^2)} \frac{1}{2R_{st}} [|A_{TD} + C_{TD}R_{st}|^2 E(|V_R|^2) - |A_{TD}|^2 E(|V_s|^2)$$

$$- R_{st}^2 |C_{TD}|^2 E(|V_o|^2)] \quad . \quad (C.15)$$

In the fourth and final test, Z_{e_1} is set to finite pure reactance jX_{st}. The basic result is

$$(A_{TD} + jX_{st}C_{TD})V_X = V_n + jX_{st}I_n \quad , \quad (C.16)$$

where V_X is the IF terminal voltage. Proceeding as was done in the third test, both sides are multiplied by their complex conjugate and then averaged. The result is

$$|A_{TD} + jX_{st}C_{TD}|^2 E(|V_X|^2) = E(|V_n|^2) + X_{st}^2 E(|I_n|^2)$$

$$+ jX_{st} E(I_n V_n^* - I_n V_n^*) \quad . \quad (C.17)$$

Since $A - A^* = j2\mathrm{Im}(A)$, Eqs. C.5, C.10 and C.11 can be used to obtain

$$|A_{TD} + jX_{st}C_{TD}|^2 E(|V_X|^2) = |A_{TD}|^2 E(|V_s|^2) + X_{st}^2 |C_{TD}|^2 E(|V_o|^2)$$

$$- 2X_{st}\ \mathrm{Im}[Z_\gamma^* |C_{TD}|^2 E(|V_o|^2)] \quad (C.18)$$

or

$$X_\gamma = \frac{1}{|C_{TD}|^2 E(|V_o|^2)} \frac{1}{2X_{st}} [|A_{TD} + jX_{st}C_{TD}|^2 E(|V_X|^2) - |A_{TD}|^2 E(|V_s|^2) - X_{st}^2 |C_{TD}|^2 E(|V_o|^2)] \quad . \qquad (C.19)$$

The only remaining parameter yet undetermined is V_{nu}. Multiplying both sides of Eq. C.4 by their complex conjugate and averaging yields

$$E(|V_{nu}|^2) = E(|V_n|^2) + |Z_\gamma|^2 E(|I_n|^2) - Z_\gamma E(I_n V_n^*) - Z_\gamma^* E(I_n^* V_n) \quad . \qquad (C.20)$$

With the use of Eq. C.5, this can be rewritten as

$$E(|V_{nu}|^2) = E(|V_n|^2) - |Z_\gamma|^2 E(|I_n|^2) \quad . \qquad (C.21)$$

With the use of Eqs. C.10 and C.11, this can then be rewritten as

$$E(|V_{nu}|^2) = |A_{TD}|^2 E(|V_s|^2) - |Z_\gamma|^2 |C_{TD}|^2 E(|V_o|^2) \quad . \qquad (C.22)$$

Computationally the procedure is to first determine the ABCD parameters of the total diode two-frequency mixer. The four test terminations are then applied and the voltages V_s, V_o, V_R and V_X are found. Equations C.11, C.15, C.19 and C.22 are then used to determine $E(|I_n|^2)$, R_γ, X_γ and $E(|V_{nu}|^2)$. X_γ determines $X_{e_1 opt}$ and Eqs. C.6 through C.8 can then be used to find $R_{e_1 opt}$. The optimum excess noise factor is calculated using Eq. C.9.

In the remaining portion of this appendix, the ABCD parameters of the total diode two-port in Saleh's notation are related to the y-parameters of the conversion admittance matrix obtained by

applying the reduction technique as was done in the stability analysis of Chapter II. The parameter A_{TD} is defined as

$$A_{TD} = \left. \frac{V_1}{V_0} \right|_{I_0=0} = -\frac{Y_{00}}{Y_{01}} , \qquad (C.23)$$

where $I_0 = 0$ implies that $Y_{01}V_1 + Y_{00}V_0 = 0$. The parameter B_{TD} is defined as

$$B_{TD} = \left. \frac{V_1}{I_0} \right|_{V_0=0} = \frac{1}{Y_{01}} , \qquad (C.24)$$

where $V_0 = 0$ implies $I_1 = Y_{11}V_1$ and $I_0 = Y_{01}V_1$. The parameter C_{TD} is defined by

$$C_{TD} = \left. \frac{I_1}{V_0} \right|_{I_0=0} = Y_{10} - \frac{Y_{11}Y_{00}}{Y_{01}} , \qquad (C.25)$$

where the basic relation between I_1, the voltages, and the y-parameters is used in addition to the implication used to obtain Eq. C.23. The parameter D_{TD} is defined by

$$D_{TD} = \left. \frac{I_1}{I_0} \right|_{V_0=0} = \frac{Y_{11}}{Y_{01}} \qquad (C.26)$$

as a result of the same implications of $V_o = 0$ which underlie Eq. C.24.

LIST OF REFERENCES

1. Torrey, H. C. and Whitmer, C. A., Crystal Rectifiers, McGraw-Hill Book Co., Inc., New York, 1948.

2. Cowley, A. M. and Sorensen, H. O., "Quantitative Comparison of Solid-State Microwave Detectors," IEEE Trans. on Microwave Theory and Techniques, vol. MTT-14, No. 12, pp. 588-602, December 1966.

3. Anand, Y. and Moroney, W. J., "Microwave Mixer and Detector Devices," Proc. IEEE, vol. 58, No. 8, pp. 1182-1190, August 1971.

4. Shockley, W., "Negative Resistance Arising from Transit Time in Semiconductor Diodes," Bell System Tech. J., vol. 33, No. 4, pp. 799-826, July 1954.

5. Coleman, D. J., Jr. and Sze, S. M., "A Low-Noise Metal-Semiconductor-Metal (MSM) Microwave Oscillator," Bell System Tech. J. (Brief), vol. 50, No. 5, pp. 1695-1699, May-June 1971.

6. Read, W. J., "A Proposed High Frequency Negative Resistance Diode," Bell System Tech. J., vol. 37, No. 2, pp. 401-446, March 1958.

7. Lee, C. A., Batdorf, R. L., Wiegmann, W. and Kaminsky, G., "The Read Diode--An Avalanching, Transit-Time, Negative-Resistance Oscillator," Appl. Phys. Letters, vol. 6, No. 5, pp. 89-91, 1 March 1965.

8. Misawa, T., "Negative Resistance in p-n Junctions Under Avalanche Breakdown Conditions, Parts I and II," IEEE Trans. on Electron Devices, vol. ED-13, No. 1, pp. 137-151, January 1966.

9. Johnston, R. L., DeLoach, B. C., Jr. and Cohen, B. G., "A Silicon Diode Microwave Oscillator," Bell System Tech. J., vol. 44, No. 2, pp. 369-372, February 1965.

10. Elta, M. E. and Haddad, G. I., "High Frequency Limitations of IMPATT, MITATT and TUNNETT Mode Devices" (Invited Paper), IEEE Trans. on Microwave Theory and Techniques, vol. MTT-27, No. 5, pp. 442-449, May 1979.

11. Lee, C. A., Berenz, J. and Dalman, G. C., "Determination of GaAs Intrinsic Avalanche Response Time from Noise Measurements," Proc. Sixth Biennial Cornell Electrical Engineering Conf., Ithaca, NY, pp. 233-245, August 1977.

12. Nishizawa, J. I., Motoya, K. and Okuno, Y., "GaAs TUNNETT Diodes," IEEE Trans. on Microwave Theory and Techniques, vol. MTT-26, No. 12, pp. 1029-1035, December 1978.

13. Hishizawa, J., Motoya, K. and Okuno, Y., Results presented at the 1979 European Microwave Conference, Quoted in Microwaves, vol. 18, No. 8, p. 21, August, 1979.

14. Elta, M. E., Fetterman, H. R., Macropoulos, W. V. and Lambert, J. J., "150-GHz GaAs MITATT Source," IEEE Electron Device Letters, vol. EDL-1, No. 6, pp. 115-116, June 1980.

15. Kim, C. S., "Tunnel-Diode Converter Analysis," IEEE Trans. on Electron Devices, vol. ED-8, No. 9, pp. 394-405, September 1961.

16. Gabriel, W. F., "Tunnel-Diode Low-Level Detection," IEEE Trans. on Microwave Theory and Techniques, vol. MTT-15, No. 10, pp. 538-553, October 1967.

17. Nagano, S. and Akaiwa, Y., "Behavior of Gunn Diode Oscillator with a Moving Reflector as a Self-Excited Mixer and a Load Variation Detector," IEEE Trans. on Microwave Theory and Techniques, vol. MTT-19, No. 12, pp. 906-910, December 1971.

18. Kwok, S. P., Nguyen-Ba, H. and Haddad, G. I., "Properties and Potential of BARITT Devices," Presented at the 1974 Int. Solid-State Circuits Conf., Philadelphia, PA, February 1974.

19. Iijima, Y., East, J. R. and Haddad, G. I., "Solid-State Devices for Low-Frequency Doppler Detectors," IEEE Trans. on Microwave Theory and Techniques (Tech. Note), vol. MTT-26, No. 2, pp. 132-133, February 1978.

20. Grace, M. I., "Down Conversion and Sideband Translation Using Avalanche Transit-Time Oscillators," Proc. IEEE (Letters), vol. 54, No. 11, pp. 1570-1571, November 1966.

21. Evans, W. J. and Haddad, G. I., "Frequency Conversion in IMPATT Diodes," IEEE Trans. on Electron Devices, vol. ED-16, No. 1, pp. 78-87, January 1969.

22. Chao, C. and Haddad, G. I., "Characteristics of the Avalanche Diode in a Self-Mixing Doppler Radar System," in Avalanche Transit-Time Devices, G. I. Haddad (Ed.), Artech House, Inc., Dedham, MA, 1973.

23. Gupta, M. S., Lomax, R. J. and Haddad, G. I., "Noise Considerations in Self-Mixing IMPATT Diode Oscillators for Short-Range Doppler Radar Applications," IEEE Trans. on Microwave Theory and Techniques, vol. MTT-22, No. 1, pp. 37-43, January 1974.

24. Hines, M. E., "Large-Signal Noise Frequency Conversion and Parametric Instabilities in IMPATT Diode Networks," Proc. IEEE, vol. 60, No. 12, pp. 1534-1548, December 1972.

25. Gonda, J. and Schroeder, W. E., "IMPATT Diode Circuit Design for Parametric Stability," IEEE Trans. on Microwave Theory and Techniques, vol. MTT-25, No. 5, pp. 343-352, May 1977.

26. Peterson, D. F., "Circuit Conditions to Prevent Second-Subharmonic Power Extraction in Periodically Driven IMPATT Diode Networks," IEEE Trans. on Microwave Theory and Techniques, vol. MTT-22, No. 8, pp. 784-790, August 1974.

27. Vanoverschelde, A., Salmer, G., Ramaut, J. and Meignant, D., "The Use of Punch-Through Diodes in Self-Oscillating Mixers," J. Phys. D.: Appl. Phys., vol. 8, No. 9, pp. 1108-1114, 1975.

28. East, J. R., Nguyen-Ba, H. and Haddad, G. I., "Design, Fabrication, and Evaluation of BARITT Devices for Doppler System Applications," IEEE Trans. on Microwave Theory and Techniques, vol. MTT-24, No. 12, pp. 943-948, December 1976.

29. East, J. R., McCleer, P. J. and Haddad, G. I., "K-Band BARITT Doppler Detectors," 1977 IEEE MTT-S Int. Microwave Symp. Digest, San Diego, CA, pp. 88-91, June 1977.

30. McCleer, P. J., "Frequency Conversion in Punch-Through Semiconductor Devices," Technical Report No. 143, Electron Physics Laboratory, Department of Electrical and Computer Engineering, The University of Michigan, Ann Arbor, August 1978.

31. McCleer, P. J. and Haddad, G. I., "BARITT Diode Video Detectors," 1978 IEEE MTT-S Int. Microwave Symp. Digest, pp. 372-374, Ottawa, Canada, June 1978.

32. J. Chen et al., "Millimeter-Wave BARITT Diode Mixers and Detectors," 1982 IEEE MTT-S Int. Microwave Symp., Dallas, TX (to be presented).

33. Ramo, S., "Currents Induced by Electron Motion," Proc. IRE, vol. 27, No. 9, pp. 584-585, September 1939.

34. Shockley, W., "Currents to Conductors Induced by a Moving Point Charge," J. Appl. Phys., vol. 9, p. 635, October 1938.

35. Haddad, G. I., Greiling, P. T. and Schroeder, W. E., "Basic Principles and Properties of Avalanche Transit-Time Devices," IEEE Trans. on Microwave Theory and Techniques, vol. MTT-18, No. 11, pp. 752-772, November 1970.

36. Schroeder, W. E. and Haddad, G. I., "Nonlinear Properties of IMPATT Devices" (Invited Paper), Proc. IEEE, vol. 61, No. 2, pp. 153-182, February 1973.

37. Blakey, P., Culshaw, B. and Giblin, R. A., "Comprehensive Models for the Analysis of High-Efficiency GaAs IMPATTs," IEEE Trans. on Electron Devices, vol. ED-25, No. 6, pp. 674-682, June 1978.

38. Culshaw, B., Giblin, R. A. and Blakey, P. A., Avalanche Diode Oscillators, Taylor and Francis, Ltd., London, England, 1978.

39. Haddad, G. I. (Ed.), Avalanche Transit-Time Devices, Artech House, Inc., Dedham, MA, 1973.

40. Culshaw, B., "Graphical Optimization of the Doping Profile of Transit-Time Devices," Proc. IEEE (Letters), vol. 63, No. 2, pp. 321-323, February 1975.

41. Scharfetter, D. L. and Gummel, H. K., "Large-Signal Analysis of a Silicon Read Diode Oscillator," IEEE Trans. on Electron Devices, vol. ED-16, No. 1, pp. 64-77, January 1969.

42. Kim, C. K. and Matthei, W. G., "GaAs Read IMPATT Diode Oscillators," Proc. Fourth Biennial Cornell Electrical Engineering Conf., Ithaca, NY, pp. 299-305, August 1973.

43. Bauhahn, P. E. and Haddad, G. I., "IMPATT Device Simulation and Properties," IEEE Trans. on Electron Devices, vol. ED-24, No. 6, pp. 634-642, June 1977.

44. Blakey, P. A., Giblin, R. A. and Seeds, A. J., "Large-Signal Time-Domain Modeling of Avalanche Diodes," IEEE Trans. on Electron Devices, vol. ED-26, No. 11, pp. 1718-1728, November 1979.

45. Blakey, P. A., Culshaw, B. and Giblin, R. A., "Efficiency Enhancement in Avalanche Diodes by Depletion-Region-Width Modulation," Electronics Letters, vol. 10, No. 21, pp. 435-436, 17 October 1974.

46. Kuvas, R. L. and Schroeder, W. E., "Premature Collection Mode in IMPATT Diodes," IEEE Trans. on Electron Devices, vol. ED-22, No. 8, pp. 549-558, August 1975.

47. Kramer, B. and Balzano, C., "Observation of a Peak in the Negative-Resistance/R.F.-Voltage Curve for High-Low GaAs IMPATT Diodes," Electronic Letters, vol. 11, No. 21, pp. 509-511, 16 October 1975.

48. Statz, H., Haus, H. A. and Pucel, R. A., "Large-Signal Dynamic Loss in Gallium Arsenide Read Avalanche Diodes," IEEE Trans. on Electron Devices, vol. ED-25, No. 1, pp. 22-33, January 1978.

49. Culshaw, B., Blakey, P. A. and Giblin, R. A., "Charge-Limited Domain in Gallium Arsenide Avalanche Diodes," Electronics Letters, vol. 11, No. 5, pp. 102-103, 6 March 1975.

50. Hirachi, Y., Kobayashi, K., Ogasawara, K. and Toyama, Y., "A New Concept for High Efficiency Operation of High-Low-Type GaAs IMPATT Diodes," IEEE Trans. on Electron Devices, vol. ED-25, No. 6, pp. 666-674, June 1978.

51. Culshaw, B., Blakey, P. A. and Giblin, R. A., "Design Criteria for Gallium Arsenide High Efficiency Avalanche Diodes," Proc. Fifth Biennial Cornell Electrical Engineering Conf., Ithaca, NY, pp. 355-366, August 1975.

52. Brackett, C. A., "The Elimination of Tuning-Induced Burnout and Bias-Circuit Oscillations in IMPATT Oscillators," Bell System Tech. J., vol. 52, No. 3, pp. 271-306, March 1973.

53. Blakey, P. A., Culshaw, B. and Giblin, R. A., "Criterion for the Optimum Punchthrough Factor of Gallium Arsenide IMPATT Diodes," Electronics Letters, vol. 12, No. 11, pp. 284-286, 27 May 1976.

54. van Iperen, B. B. and Tjassens, H., "Influence of Carrier Velocity Saturation in the Unswept Layer on the Efficiency of Avalanche Transit-Time Diodes," Proc. IEEE (Letters), vol. 59, No. 6, pp. 1032-1033, June 1971.

55. Gilden, M. and Hines, M. E., "Electronic Tuning Effects in the Read Microwave Avalanche Diode," IEEE Trans. on Electron Devices, vol. ED-13, No. 1, pp. 169-175, January 1966.

56. Elta, M. E., "High Frequency Calculations of IMPATT and TUNNETT Diodes," Seventh Biennial Conf. on Active Microwave Semiconductor Devices and Circuits, Ithaca, NY, pp. 401-411, August 1979.

57. Elta, M. E., "The Effects of Mixed Tunneling and Avalanche Breakdown on Microwave Transit-Time Diodes," Tech. Report No. 142, Electron Physics Laboratory, Department of Electrical and Computer Engineering, The University of Michigan, Ann Arbor, June 1978.

58. Elta, M. E. and Haddad, G. I., "Large-Signal Performance of Microwave Transit-Time Devices in Mixed Tunneling and Avalanche Breakdown," IEEE Trans. on Electron Devices, vol. ED-26, No. 6, pp. 941-948, June 1979.

59. Elta, M. E. and Haddad, G. I., "Mixed Tunneling and Avalanche Mechanisms in p-n Junctions and Their Effects on Microwave Transit-Time Devices," IEEE Trans. on Electron Devices, vol. ED-25, No. 6, pp. 694-702, June 1978.

60. Sjölund, A., "Small-Signal Analysis of Punch-Through Injection Microwave Diodes," Solid-State Electronics, vol. 16, No. 5, pp. 559-569, May 1973.

61. Oakes, J. G. and Lee, C. A., "An Inductive Phase Delay in the Retarding Field Region of Schottky Barrier BARITT Diodes," Int. Electron Devices Meeting Tech. Digest, Washington, DC, pp. 479-482, December 1973.

62. Ruegg, H. W., "A Proposed Punch-Through Microwave Negative-Resistance Diode," IEEE Trans. on Electron Devices, vol. ED-15, No. 8, pp. 577-585, August 1968.

63. Vanoverschelde, A. and Salmer, G., "Silicon BARITT Diodes as Millimetre Wavelength Oscillators," IEE Solid-State and Electron Devices, vol. 2, No. 4, pp. 115-120, July 1978.

64. Vanoverschelde, A. and Salmer, G., "GaAs and InP Punchthrough Diodes as Oscillators in the Millimetre-Wave Range," IEE Solid-State and Electron Devices, vol. 3, No. 4, pp. 94-98, July 1979.

65. Nguyen-Ba, H. and Haddad, G. I., "Effects of Doping Profile on the Performance of BARITT Devices," IEEE Trans. on Electron Devices, vol. ED-24, No. 9, pp. 1154-1163, September 1977.

66. Delagebeauderf, D., "Punchthrough Injection Structures for Low Voltage Oscillation and Low Noise Amplification," Presented at the Fourth European Microwave Conf., Montreux, Switzerland, September 1974.

67. Eknoyan, O., Yang, E. S. and Sze, S. M., "Multilayered Ion-Implanted BARITT Diodes with Improved Efficiency," Solid-State Electronics, vol. 20, No. 4, pp. 291-295, April 1977.

68. Wright, G. T., "Transit-Time Oscillator with Velocity-Limited Injection," Electronics Letters, vol. 7, No. 16, pp. 449-451, 12 August 1971.

69. Sitch, J. E., Majerfield, A., Robson, P. N. and Hagesawa, F., "Transit-Time-Induced Microwave Negative Resistance in $Ga_{1-x}Al_xAs$-GaAs Heterostructure Diodes," Electronics Letters, vol. 11, No. 19, pp. 457-458, 18 September 1975.

70. Adlerstein, M. G. and Statz, H., "Double-Velocity IMPATT Diodes," IEEE Trans. on Electron Devices, vol. ED-26, No. 5, pp. 817-819, May 1979.

71. Kwok, S. P. and Haddad, G. I., "Power Limitations in BARITT Devices," Solid-State Electronics, vol. 19, No. 9, pp. 795-807, September 1976.

72. Braun, F., "Uber die Stromleitung Durch Schwefelmetalle," Ann Physik Chem., vol. 153, pp. 556, 1874.

73. Mott, N. F., "Note on the Contact Between a Metal and an Insulator or Semiconductor," Proc. Cambridge Phil. Soc., vol. 34, pp. 568, 1938.

74. Sze, S. M., Physics of Semiconductor Devices, Wiley-Interscience, New York, 1969.

75. Henisch, H. K., Rectifying Semiconductor Contacts, Oxford at the Clarendon Press, Oxford, England, 1957.

76. Dascalu, D., Electronic Processes in Unipolar Solid-State Devices, Abacus Press, Kent, England, 1977.

77. Rhoderick, E. H., Metal-Semiconductor Contacts, Clarendon Press, Oxford, England, 1978.

78. Edwards, R., Ciccolella, D. F., Misawa, T., Iglesias, D. E. and Decker, V., "Millimeter-Wave Silicon IMPATT Diodes," Presented at the 1969 IEEE Int. Electron Devices Meeting, Washington, DC, October 1969.

79. Gilden, M. and Moroney, W., "High-Power Pulsed Avalanche Diode Oscillators for Microwave Frequencies," Proc. IEEE (Correspondence), vol. 55, No. 1, pp. 1227-1228, July 1967.

80. Ying, R. S., English, D. L., Weller, K. P., Nakaji, E. M., Lee, D. H. and Bernick, R. L., "Millimeter-Wave Pulsed IMPATT Diode Oscillators," Proc. Fifth Biennial Cornell Electrical Engineering Conf., Ithaca, NY, pp. 377-388, August 1975.

81. Seidel, T. E., Niehaus, W. C. and Iglesias, D. E., "Double-Drift Silicon IMPATTs at X-Band," IEEE Trans. on Electron Devices, vol. ED-21, No. 8, pp. 523-531, August 1974.

82. Pfund, G., Snapp, C. and Podell, A., "Pulsed and CW Double-Drift Silicon IMPATTs," Presented at the 1974 IEEE/GMTT Int. Microwave Symp., Atlanta, GA, June 1974.

83. Niehaus, W. C., Seidel, T. E. and Iglesias, D. E., "Double-Drift IMPATT Diodes Near 100 GHz," IEEE Trans. on Electron Devices, vol. ED-20, No. 9, pp. 765-771, September 1973.

84. Ishibashi, T. and Ohmori, M., "200 GHz 50 mW CW Oscillator with Silicon IMPATT Diodes," IEEE Trans. on Microwave Theory and Techniques, vol. MTT-24, No. 11, pp. 858-859, November 1976.

85. Chao, C., Bernick, R. L., Ying, R. S., Weeler, K. P., Lee, D. H. and Nakaji, E. M., "Pulsed IMPATT Diode Oscillators Above 200 GHz," IEEE Int. Solid-State Circuits Conf. Digest, Philadelphia, PA, pp. 130-131, February 1977.

86. Midford, T. A. and Bernick, R. L., "Millimeter-Wave CW IMPATT Diodes and Oscillators," IEEE Trans. on Microwave Theory and Techniques, vol. MTT-27, No. 5, pp. 483-492, May 1979.

87. Ohmori, M., Ishibashi, T. and Ono, S., "Dependency of the Highest Harmonic Oscillation Frequency on Junction Diameter of IMPATT Diodes," IEEE Trans. on Electron Devices, vol. ED-24, No. 12, pp. 1323-1329, December 1977.

88. Bowman, L. S. and Burrus, C. A., Jr., "Pulse-Driven Silicon p-n Junction Avalanche Oscillators for the 0.9 to 20 mm Band," IEEE Trans. on Electron Devices, vol. ED-14, No. 8, pp. 411-418, August 1967.

89. Ino, M., Ishibashi, T. and Ohmori, M., "C.W. Oscillation with p^+-p-n^+ Silicon IMPATT Diodes in the 200 GHz and 300 GHz Bands," Electronics Letters, vol. 12, No. 6, pp. 148-149, March 1976.

90. Ishibashi, T., Ino, M., Makimura, T. and Ohmori, M., "Liquid-Nitrogen-Cooled Submillimetre-Wave Silicon IMPATT Diodes," Electronics Letters, vol. 13, No. 10, pp. 299-300, 12 May 1977.

91. Schwarz, R. I. and Bonek, E., "Current-Tuned GaAs Schottky-Barrier IMPATT Diodes for 60 to 96 GHz Operation," Electronics Letters, vol. 14, No. 25, pp. 812-813, December 1978.

92. Chen, W. T., "A High Power, High Efficiency Millimeter Wave IMPATT Diode," Proc. Fifth Biennial Cornell Electrical Engineering, Conf., Ithaca, NY, pp. 389-396, August 1975.

93. Gibbons, G., Purcell, J. J., Wickens, P. R. and Gokgor, H. S., "50 GHz Gallium Arsenide IMPATT Oscillator," Electronics Letters, vol. 8, No. 21, pp. 513-514, 19 October 1972.

94. Goldwasser, R. E., Long, S. I. and Terzian, P., "Highly Reliable Pulse GaAs Read Diodes," Proc. Fifth Biennial Cornell Electrical Engineering Conf., Ithaca, NY, pp. 367-376, August 1975.

95. Adlerstein, M. G., Wallace, R. N. and Steele, S. R., "Millimeter-Wave GaAs Read IMPATT Diodes," IEEE Trans. on Electron Devices, vol. ED-25, No. 9, pp. 1151-1156, September 1978.

96. Masse, D., Chu, G., Johnson, K. and Adlerstein, M. G., "High Power GaAs Millimeter Wave IMPATT Diodes," Microwave J., vol. 22, No. 6, pp. 103-105, June 1979.

97. Scharfetter, D. L., "Power-Impedance-Frequency Limitations of IMPATT Oscillators Calculated from a Scaling Approximation," IEEE Trans. on Electron Devices, vol. ED-18, No. 8, pp. 536-543, August 1971.

98. Bauhahn, P. E., "Properties of Semiconductor Materials and Microwave Transit-Time Devices," Technical Report No. 140, Electron Physics Laboratory, The University of Michigan, Ann Arbor, October 1977.

99. Haydl, W. H., Smith, R. S. and Bosch, R., "50-110 GHz Gunn Diodes Using Molecular Beam Epitaxy," IEEE Electron Device Letters, vol. EDL-1, No. 10, pp. 224-226, October 1980.

100. Weinreb, S. and Kerr, A. R., "Cryogenic Cooling of Mixers for Millimeter and Centimeter Wavelengths," IEEE J. of Solid-State Circuits, vol. SC-8, No. 1, pp. 58-63, February 1973.

101. Held, D. N. and Kerr, A. R., "Conversion Loss and Noise of Microwave and Millimeter-Wave Mixers: Parts I and II," IEEE Trans. on Microwave Theory and Techniques, vol. MTT-26, No. 2, pp. 49-61, February 1978.

102. Anand, Y. and Christou, A., "Millimeter High Burnout GaAs Schottky Barrier Diodes," 1979 Int. Electron Devices Meeting Tech. Digest, Washington, DC, pp. 402-404, December 1979.

103. Christou, A., Anderson, W. T., Jr., Davey, J. E., Bark, M. L. and Anand, Y., "High Performance Millimetre Ge-GaAs Mixer Diode for Low LO Power Applications," Electronics Letters, vol. 16, No. 7, pp. 254-256, 27 March 1980.

104. Anand, Y., Christou, A. and Day, H., "Ideality and Noise Figure Characteristics of R.F. Sputtered Millimetre GaAs Diodes," Electronics Letters, vol. 16, No. 15, pp. 581-583, 17 July 1980.

105. Bernues, F. et al., "GaAs or Si: What Makes a Better Mixer Diode?" Microwaves, vol. 15, No. 3, pp. 46-55, March 1976.

106. Keen, N. J., "Low-Noise Millimetre-Wave Mixer Diodes: Results and Evaluation of a Test Programme," IEE Proc., Pt. I, Solid-State and Electron Devices, vol. 127, No. 4, pp. 188-198, August 1980.

107. Schneider, M. V., Linke, R. A. and Cho, A. Y., "Low-Noise Millimeter-Wave Mixer Diodes Prepared by Molecular Beam Epitaxy (MBE)," Appl. Phys. Letters, vol. 31, No. 3, pp. 219-221, 1 August 1977.

108. Vizard, D. R., Keen, N. J., Kelly, W. M. and Wrixon, G. T., "Low Noise Millimeter Wave Schottky Barrier Diodes with Extremely Low Local Power Requirements," 1979 IEEE MTT-S Int. Microwave Symp. Digest, Orlando, FL, pp. 81-83, April-May 1979.

109. Keen, N., Haas, R. and Berchtold, E., "Very Low Noise Mixer at 115 GHz Using a Mott Diode Cooled to 20 K," Electronics Letters, vol. 14, No. 25, pp. 825-827, 7 December 1978.

110. McColl, M. and Millea, M. F., "Advantages of Mott Barrier Mixer Diodes," Proc. IEEE, vol. 61, No. 4, pp. 499-500, April 1973.

111. Linke, R. A., Schneider, M. V. and Cho, A. Y., "Cryogenic Millimeter-Wave Receiver Using Molecular Beam Epitaxy Diodes," IEEE Trans. on Microwave Theory and Techniques, vol. MTT-26, No. 12, pp. 935-938, December 1978.

112. Cohn, M., Degenford, J. E. and Newman, B. A., "Harmonic Mixing with an Antiparallel Diode Pair," IEEE Trans. on Microwave Theory and Techniques, vol. MTT-23, No. 8, pp. 667-673, August 1975.

113. Henry, P. S., Glance, B. S. and Schneider, N. V., "Local-Oscillator Noise Cancellation in the Subharmonically Pumped Down-Converter," IEEE Trans. on Microwave Theory and Techniques, vol. MTT-24, No. 5, pp. 254-257, May 1976.

114. McMaster, T. F., Schneider, M. V. and Snell, W. W., Jr., "Millimeter-Wave Receivers with Subharmonic Pump," IEEE Trans. on Microwave Theory and Techniques, vol. MTT-24, No. 12, pp. 948-952, December 1976.

115. Carlson, E. R., Schneider, M. V. and McMaster, T. F., "Subharmonically Pumped Millimeter-Wave Mixers," IEEE Trans. on Microwave Theory and Techniques, vol. MTT-26, No. 10, pp. 706-715, October 1978.

116. Brackett, C. A., "The Elimination of Tuning-Induced Burnout and Bias-Circuit Oscillations in IMPATT Oscillators," Bell System Tech. J., vol. 52, No. 3, pp. 271-306, March 1973.

117. Siegel, P. H. and Kerr, A. R., "A User Oriented Computer Program for the Analysis of Microwave Mixers, and a Study of the Effects of the Series Inductance and Diode Capacitance on the Performance of Some Simple Mixers," NASA Technical Memorandum 80324, Goddard Space Flight Center, Greenbelt, MD, July 1979.

118. Bhatia, C. S. and van der Ziel, A., "The Effect of Capacitive Mixing and Detection in Schottky-Barrier Diodes at High, Intermediate, or Modulation Frequencies," IEEE Trans. on Electron Devices, vol. ED-27, No. 1, pp. 83-87, January 1980.

119. Strutt, M.J.O., "Noise Figure Reduction in Mixer Stages," Proc. IRE, vol. 34, No. 12, pp. 942-950, December 1946.

120. Uhlir, A., Jr., "Shot Noise in p-n Junction Frequency Converters," Bell System Tech. J., vol. 37, No. 4, pp. 951-958, July 1958.

121. van der Ziel, A. and Watters, R. L., "Noise in Mixer Tubes," Proc. IRE, vol. 46, No. 7, pp. 1426-1427, July 1958.

122. Dragone, C., "Analysis of Thermal and Shot Noise in Pumped Resistive Diodes," Bell System Tech. J., vol. 47, No. 11, pp. 1883-1902, November 1968.

123. Keen, N. J., "Evidence for Coherent Noise in Pumped Schottky-Diode Mixers," Electronics Letters, vol. 13, No. 10, pp. 282-284, 12 May 1977.

124. Convert, G., "Sur la Theorie du Bruit des Diodes a Avalanche," Revue Technique Thomson-CSF, vol. 3, No. 3, pp. 419-471, September 1971.

125. Scherer, E. F., "Investigations of the Noise Spectra of Avalanche Oscillators," IEEE Trans. on Microwave Theory and Techniques, vol. MTT-16, No. 9, pp. 781-788, September 1968.

126. Goedbloed, J. J. and Vlaardingerbroek, M. T., "Theory of Noise and Transfer Properties of IMPATT Diode Amplifiers," IEEE Trans. on Microwave Theory and Techniques, vol. MTT-25, No. 4, pp. 324-332, April 1977.

127. Kuvas, R. L., "Nonlinear Noise Theory for IMPATT Diodes," IEEE Trans. on Electron Devices, vol. ED-23, No. 4, pp. 395-411, April 1976.

128. Fikart, J. L., "AM and FM Noise of BARITT Oscillators," IEEE Trans. on Microwave Theory and Techniques, vol. MTT-22, No. 5, pp. 517-523, May 1974.

129. Champlin, K. S. and Eisenstein, G., "Cutoff Frequency of Submillimeter Schottky-Barrier Diodes," IEEE Trans. on Microwave Theory and Techniques, vol. MTT-26, No. 1, pp. 31-34, January 1978.

130. Blakey, P. A., East, J. R., Mains, R. K. and Rothman, E. D., "Monte Carlo Calculation of the Large-Signal Admittance of Bulk Gallium Arsenide at Millimeter- and Submillimeter-Wave Frequencies" (to be submitted for publication).

131. Saleh, A.A.M., Theory of Resistive Mixers, M.I.T. Press, Cambridge, MA, 1971.

132. Blakey, P. A., Froelich, R. K., Grondin, R. O., Mains, R. K. and Haddad, G. I., "Millimeter-Wave IMPATT Diode Modeling," Presented at the Eighth Biennial Cornell Electrical Engineering Conference, Ithaca, NY, August 1981.

133. van der Ziel, A., "Infrared Detection and Mixing in Heavily Doped Schottky-Barrier Diodes," J. Appl. Phys., vol. 47, No. 5, pp. 2059-2068, May 1976.

134. Tsang, D. W. and Schwarz, S. E., "Transport Theory of High-Frequency Rectification in Schottky Barriers," J. Appl. Phys., vol. 50, No. 5, pp. 3459-3471, May 1979.

135. Tsang, D. W. and Schwarz, S. E., "Detection of 10-μ Radiation with Point-Contact Schottky Diodes," Appl. Phys. Letters, vol. 30, No. 6, pp. 263-265, 15 March 1977.

136. Mouthaan, K., "Characterization of Nonlinear Interactions in Avalanche Transit-Time Oscillators, Frequency Multipliers and Frequency Dividers," IEEE Trans. on Microwave Theory and Techniques, vol. MTT-18, No. 11, pp. 853-862, November 1970.

137. Blakey, P. A., East, J. R. and Haddad, G. I., "Impact of Submicron Technology on Microwave and Millimeter-Wave Devices," VLSI Electronics: Microstructure Science, Einspruch, N. (Ed.), Academic Press, Inc., New York, vol. 2, Chap. 4, 1981.

138. Froelich, R. K. and Blakey, P. A., "Energy and Momentum Conserving Simulation of Millimeter-Wave IMPATT Diodes," Presented at the Second Int. Conference on the Numerical Analysis of Semiconductor Devices and Integrated Circuits, Dublin, Ireland, June 1981.

139. McCleer, P. J., Snyder, D. E., Grondin, R. O. and Haddad, G. I., "Analytic Modeling of Transit-Time Device Drift Regions with Field-Dependent Transport Coefficients," Solid-State Electronics, vol. 24, No. 1, pp. 37-48, January 1981.

140. Held, D. N., "Analysis of Room Temperature Millimeter-Wave Mixers Using Gallium Arsenide Schottky Barrier Diodes," Sc.D. Dissertation, Columbia University, 1977.

141. Peterson, D. F., Private communication.

142. Linvill, J. G. and Gibbons, J. R., Transistors and Active Circuits, McGraw-Hill Book Co., Inc., New York, 1961.

143. Rollett, J. M., "Stability and Power-Gain Invariants of Linear Twoports," IRE Trans. on Circuit Theory, vol. CT-9, No. 1, pp. 29-32, March 1962.

144. Taur, Y., "Josephson-Junction Mixer Analysis Using Frequency-Conversion and Noise-Correlation Matrices," IEEE Trans. on Electron Devices, vol. ED-27, No. 10, pp. 1921-1928, October 1980.

145. Kerr, A. R., "Shot Noise in Resistive-Diode Mixers and the Attenuator Noise Model," IEEE Trans. on Microwave Theory and Techniques, vol. MTT-27, No. 2, pp. 135-140, February 1979.

146. Sjolund, A., "Noise at Large RF Amplitudes in IMPATT Oscillators," Int. J. Elec., vol. 34, No. 4, pp. 551-564, April 1973.

147. Snyder, D. L., Random Point Processes, John Wiley and Sons, Inc., New York, 1975.

148. Grondin, R. O., Blakey, P. A., East, J. R. and Rothman, E. D., "Monte Carlo Estimation of Hot Carrier Noise at Millimeter- and Submillimeter-Wave Frequencies," IEEE Trans. on Electron Devices, vol. ED-28, No. 8, pp. 914-923, August 1981.

149. Nougier, J. P., "Noise and Diffusion of Hot Carriers," Physics of Nonlinear Transport in Semiconductors, Ferry, D. K., Barker, J. R. and Jacoboni, C. (Eds.), Plenum Press, New York, 1980.

150. Statz, H., Pucel, R. A. and Haus, H. A., "Velocity Fluctuation Noise in Metal-Semiconductor-Metal Diodes," Proc. IEEE, vol. 60, No. 5, pp. 644-645, May 1972.

151. Rees, H. D., "Calculation of Distribution Functions by Exploiting the Stability of the Steady State," J. Phys. Chem. Solids, vol. 30, No. 3, pp. 643-655, March 1969.

152. Barker, J. R., "Quantum Transport Theory," Physics of Nonlinear Transport in Semiconductors, Ferry, D. K., Barker, J. R. and Jacoboni, C. (Eds.), Plenum Press, New York, 1980.

153. Barker, J. R. and Ferry, D. K., "On the Physics and Modeling of Small Semiconductor Devices-I," Solid-State Electronics, vol. 23, No. 6, pp. 519-530, June 1980.

154. Kroemer, H., "Hot-Electron Relaxation Effects in Devices," Solid-State Electronics, vol. 21, No. 1, pp. 61-67, January 1978.

155. Stratton, R., "Semiconductor Current-Flow Equations (Diffusion and Degeneracy)," IEEE Trans. on Electron Devices, vol. ED-19, No. 12, pp. 1288-1292, December 1972.

156. East, J. R., Private communication.

157. McCleer, P. J., Private communication.

158. Gummel, H. K. and Blue, J. L., "A Small-Signal Theory of Avalanche Noise in IMPATT Diodes," IEEE Trans. on Electron Devices, vol. ED-14, No. 9, pp. 569-580, September 1967.

159. McCleer, P. J. and Haddad, G. I., "On the Base-Region Minority Carrier Concentration in Narrow-Base Transistors," IEEE Trans. on Electron Devices, vol. ED-25, No. 3, pp. 382-384, March 1978.

160. Bjorkman, G. and Snapp, C. P., "Small-Signal Noise Behaviour of Companion p^+-n-p^+ and p^+-n-ν-p^+ Punchthrough Microwave Diodes," Electronic Letters, vol. 8, No. 20, pp. 501-503, 5 October 1972.

161. Weller, K. P., "Small-Signal Theory of a Transit-Time Negative Resistance Device Utilizing Injection from a Schottky Barrier," RCA Rev., vol. 32, No. 3, pp. 372-382, September 1971.

162. Snapp, C. P. and Weissglas, P., "On the Microwave Activity of Punchthrough Injection Transit-Time Structures," IEEE Trans. on Electron Devices, vol. ED-19, No. 10, pp. 1109-1118, October 1972.

163. Fawcett, W., "Non-Ohmic Transport in Semiconductors," Electrons in Crystalline Solids, International Atomic Energy Agency, Vienna, 1973.

164. Fawcett, W., Boardman, A. D. and Swain, S., "Monte Carlo Determination of Electron Transport Properties in Gallium Arsenide," J. Phys. Chem. Solids, vol. 31, pp. 1963-1990, September 1970.

165. Ferry, D. K., Lugli, P. and Zimmermann, J., "On the Physics and Modeling of Small Semiconductor Devices-IV. Generalized Retarded Transport in Ensemble Monte Carlo Techniques" (to be published).

166. Blotekjaer, K., "Transport Equations for Electrons in Two-Valley Semiconductors," IEEE Trans. on Electron Devices, vol. ED-17, No. 1, pp. 38-47, January 1970.

167. Jones, D. and Rees, H. D., "A Reappraisal of Instabilities Due to the Transferred-Electron Effect," J. Phys. C., vol. 6, pp. 1781-1793, 24 May 1973.

168. Zimmermann, J., Leroy, Y., Kaszynski, A. and Carnez, B., "Monte Carlo Calculation of Nonsteady-State Hot Electron Noise in Very Short Channel n-Si and n-GaAs Devices," Proc. Fifth Int. Conf. on Noise in Physical Systems, Bad Nauheim, Germany, Springer Series on Electrophysics, Wolf, D. (Ed.), Springer-Verlag, New York, vol. 2, 1978.

169. Culshaw, B., "Effect of Carrier Diffusion on Operation of Avalanche Diodes," Electronics Letters, vol. 10, No. 9, pp. 143-145, 2 May 1974.

170. Blakey, P. A., Unpublished work.

171. Zimmermann, J., Leroy, Y. and Constant, E., "Monte Carlo Calculation of Microwave and Far Infrared Hot Carrier Mobility in N-Si: Efficiency of Millimeter Transit-Time Oscillators," J. Appl. Phys., vol. 49, No. 6, pp. 3378-3383, June 1978.

172. Doumbia, I., Salmer, G. and Constant, E., "High Frequency Limitation on Silicon IMPATT Diode: Velocity Modulation," J. Appl. Phys., vol. 46, No. 4, pp. 1831-1833, April 1975.

173. van Vliet, K. M., Friedmann, A., Zijlstra, R.J.J., Gisolf, A. and van der Ziel, A., "Noise in Single Injection Diodes, I. A Survey of Methods," J. Appl. Phys., vol. 46, pp. 1804-1813, April 1975.

174. Hill, G., Robson, P. N. and Fawcett, W., "Diffusion and the Power Spectral Density of Velocity Fluctuations for Electrons in InP by Monte Carlo Methods," J. Appl. Phys., vol. 50, pp. 356-360, January 1979.

175. Fauquembergue, R., Zimmermann, J., Kaszynski, A., Constant, E. and Microondes, G., "Diffusion and the Power Spectral Density and Correlation Function of Velocity Fluctuation for Electrons in Si and GaAs by Monte Carlo Methods," J. Appl. Phys., vol. 51, pp. 1065-1071, February 1980.

176. Kaszynski, A., "Etude des Phenomenes de Transport dans les Materiaux Semiconducteurs par les Methodes de Monte Carlo: Application a l'Arseniure de Gallium de Type N," Thesis Docteur Ingeniur, L'Universite des Sciences et Techniques de Lille, 1979.

177. Ferry, D. K. and Barker, J. R., "Generalized Diffusion, Mobility, and the Velocity Autocorrelation Function for High Field Transport in Semiconductors," J. Appl. Phys., vol. 52, No. 2, pp. 818-824, February 1981.

178. Price, P. J., "Monte Carlo Calculation of Electron Transport in Solids," Semiconductors and Semimetals, Willardson, R. K. and Beer, A. C. (Ed.), Academic Press, Inc. New York, vol. 14, 1979.

179. Nougier, J. P., "Noise and Diffusion of Hot Carriers," Physics of Nonlinear Transport in Semiconductors, Ferry, D. K., Barker, J. R. and Jacoboni, C. (Eds.), Plenum Press, New York, 1980.

180. Shockley, W., Copeland, J. A. and James, R. P., "The Impedance Field Method of Noise Calculation in Active Semiconductor Devices," Quantum Theory of Atoms, Molecules and the Solid State, Lowdin, P.-O. (Ed.), Academic Press, Inc., New York, 1966.

181. Jenkins, G. M. and Watts, D. G., Spectral Analysis and Its Applications, Holden-Day, San Francisco, 1968.

182. Kendall, M., Time Series , 2nd Edition, Hafner Press, New York, 1976.

183. Schwartz, M. and Shaw, L., Signal Processing, Discrete Spectral Analysis, Detection and Estimation, McGraw-Hill Book Co., Inc., New York, 1975.

184. Programs for Digital Signal Processing, Digital Signal Processing Committee (Eds.), IEEE Press, Inc., New York, 1980.

185. Fox, D. J. and Guire, K. E., Documentation for MIDAS, 3rd Ed., Statistical Research Laboratory, The University of Michigan, Ann Arbor, 1976.

186. Rees, H. D., "Intrinsic Noise of Transferred-Electron Amplifiers" (Invited Paper), IEE Solid-State and Electron Devices, vol. 1, pp. 165-179, November 1977.

187. Price, P. J., "Fluctuations of Hot Electrons," Fluctuation Phenomena in Solids, Burgess, R. E. (Ed.), Academic Press, Inc., New York, 1966.

188. Fawcett, W. and Rees, H. D., "Calculation of the Hot Electron Diffusion Rate for GaAs," Phys. Letters, vol. 29A, pp. 578-579, 11 August 1969.

189. Abe, M., Yanagisawa, S., Wada, O. and Takanashi, H., "Monte Carlo Calculations of Diffusion Coefficients of Hot Electrons in n-Type GaAs," Appl. Phys. Letters, vol. 25, pp. 674-675, 1 December 1974.

190. Quaranti, A. A., Borsari, V., Jacoboni, C. and Zanarini, G., Electron Diffusion in CdTe," Appl. Phys. Letters, vol. 22, pp. 103-105, 1 February 1973.

191. Jacoboni, C., "Generalization of Fick's Law for Non-local Complex Diffusion in Semiconductors," Phys. Stat. Sol. B, vol. 65, pp. 61-65, 1 September 1974.

192. Frey, J., "Effects of Intervalley Scattering on Noise in GaAs and InP Field-Effect Transistors," IEEE Trans. on Electron Devices, vol. ED-23, No. 12, pp. 1298-1303, December 1976.

193. Golio, J. M. and Trew, R. J., "Compound Semiconductors for Low-Noise Microwave MESFET Applications," IEEE Trans. on Electron Devices, vol. ED-27, No. 7, pp. 1256-1262, July 1980.

194. Zimmermann, J. and Constant, E., "Application of Monte Carlo Techniques to Hot Carrier Diffusion Noise Calculation in Unipolar Semiconducting Components," Solid-State Electronics, vol. 23, pp. 915-925, September 1980.

195. van Vliet, K. M., "The Transfer Impedance Method for Noise in Field-Effect Transistors," Solid-State Electronics, vol. 22, pp. 233-236, March 1979.

196. Pucel, R. A., Haus, H. A. and Statz, H., "Signal and Noise Properties of Gallium Arsenide Microwave Field-Effect Transistors," Advances in Electronics and Electron Physics, vol. 38, Academic Press, Inc., New York, pp. 195-265, 1975.

197. Seidel, T. E. and Scharfetter, D. L., "Dependence of Hole Velocity upon Electric Field and Hole Density for p-Type Silicon," J. Phys. Chem. Solids, vol. 28, No. 12, pp. 2563-2574, December 1967.

198. Kramer, B. and Mircea, A., "Determination of Saturated Electron Velocity in GaAs," Appl. Phys. Letters, vol. 26, No. 11, pp. 623-625, June 1975.

199. Olson, H. M., "Temperature Transients in IMPATT Diodes," IEEE Trans. on Electron Devices, vol. ED-23, No. 5, pp. 494-503, May 1976.

200. Haus, H. A. et al., "Representation of Noise in Linear-Twoports," Proc. IRE, vol. 48, No. 1, pp. 69-74, January 1960.

UNIVERSITY OF MICHIGAN
3 9015 03027 7043